A Search for Leptoquarks Coupling to τ Leptons and Bottom Quarks in Proton-Proton Collisions at the CMS Experiment

Dissertation

zur

Erlangung der naturwissenschaftlichen Doktorwürde
(Dr. sc. nat.)

vorgelegt der

Mathematisch-naturwissenschaftlichen Fakultät

der

Universität Zürich

von

Izaak W. Neutelings

aus

den Niederlanden

Promotionskommission

Prof. Dr. Ben Kilminster (Vorsitz)

Prof. Dr. Florencia Canelli

Prof. Dr. Nicola Serra

Prof. Dr. Gino Isidori

Zürich, 2023

Abstract

Despite the many remarkable successes of the Standard Model (SM) of particle physics, there are both theoretical and experimental reasons that imply the SM is not the final and most fundamental theory of nature. Some anomalies have emerged in measurements of semileptonic B hadron decays that could reveal the violation of lepton flavor universality. Models that propose a new particle called the leptoquark (LQ) are strongly motivated as a possible explanation, and could reveal the underlying connection between quarks and leptons and explain the observed flavor symmetries, as well as the hierarchical mass pattern.

This thesis presents a search for the single and pair production of LQs that decay exclusively to a τ lepton and a bottom quark, as well as a novel search for the exchange of an LQ by b quarks that produces a τ lepton pair. This is done by targeting the $\tau\tau$ decay channels, and creating several event categories based on the number of jets and heavy-flavored jets. The search uses a data set of pp collisions corresponding to an integrated luminosity of $138\,\mathrm{fb}^{-1}$, collected at a center-of-mass energy of $13\,\mathrm{TeV}$, and recorded with the CMS detector. Preliminary results are presented: Upper limits are set on the production cross section of third-generation scalar and vector LQs as a function of the LQ mass, and results are compared with theoretical predictions to obtain lower limits on the LQ mass. At 95% confidence level, third-generation LQs decaying to a τ lepton and a b quark with unit coupling are excluded for masses below $1.25\,\mathrm{TeV}$ for a scalar model, and below 1.53 $(1.86)\,\mathrm{TeV}$ for a vector model with nonminimal coupling $\kappa = 0$ (1). At $\lambda = 2.5$, the lower limits are $1.37\,\mathrm{TeV}$ for a scalar model, and 1.86 $(1.96)\,\mathrm{TeV}$ for a vector model with $\kappa = 0$ (1). Upper limits are also set on the coupling strength of such LQs as a function of their mass. Due to the inclusion of the nonresonant LQ exchange processes, this analysis is able to set constraints on LQs with masses up to $10\,\mathrm{TeV}$, much higher than can be produced directly at the LHC. For a representative LQ mass of 2 TeV and a coupling strength of 2.5, an excess with a significance of 3.4 standard deviations above the standard model expectation is observed in the data. Consequently, the observed upper limits on the LQ production cross section are about three times larger than expected for this benchmark.

As hadronic decays of the τ lepton (τ_h) are an important part of this search, this thesis also presents the reconstruction and identification algorithms used in CMS, as well as the measurements of its performance and the corrections to simulated τ_h candidates that are needed to ensure good modeling of the data.

Acknowledgements

I want to thank the great people in the UZH group and the CMS Collaboration that have helped me along the way, and with whom it was a great privilege and pleasure to work on diverse projects and push the limits of our understanding of Nature.

Special thanks go to my supervisor, Prof. Dr. Ben Kilminster, who kept me on track while trusting me to learn and grow in my own way; Dr. Yuta Takahashi, for teaching me the way of the τ, while challenging and encouraging me with great patience; Dr. Arne Reimers, for helping me finish the analysis with no nonsense; Janik Andrejkovič, for his great contribution with the $j \to \tau_{\mathrm{h}}$ estimation and thorough studies; Kyle Cormier, for the stimulating and clarifying conversations; Gino Isidori and his group, for providing inspiration and motivation that guided our experimental work.

I would also like to express my deepest gratitude for my dedicated parents and my loving family, for supporting me throughout my studies in all the different ways, whether it be with finances and administration, helping me move between cities, or allowing me to focus on my studies and work during Christmas holidays. Without their continuous understanding, patience, and moral support, I would not have been able to complete this challenging yet rewarding journey of my studies.

Contents

1 Introduction

Over the last 100 years, physicists have made large strides in understanding the natural laws that govern the universe as we know it. The smallest building blocks of matter and the way they interact at small scales have been encoded in the Standard Model (SM) of particle physics. Despite its many remarkable successes, there are both theoretical and experimental reasons that imply the SM is not the final and most fundamental theory of nature.

One of the most striking features of the SM is that it neatly orders quarks and leptons into three distinct generations. Except for mass, each generation of fermions seems to be a copy of the others. In particular, the SM gauge interactions cannot differentiate between different lepton flavors, even though there is no fundamental symmetry protecting them from mixing. The observed fermion masses vary by many orders of magnitudes, and this pattern does not seem natural or accidental. It instead appears very hierarchical, which could suggest something about the underlying physics that we have yet to uncover.

On the experimental side, many tests of the universality of lepton flavor have been made by studying the decays of various particles. In the last decade, several anomalies have appeared in precision measurements that could help uncover the violation of this universality. In particular, the evidence seems suggest some new physics interactions that couple preferentially to the third generations of fermions like bottom quarks and τ leptons. Models that propose a new particle called the leptoquark (LQ) have recently received considerable theoretical interest as a possible explanation for these flavor anomalies.

Due to record-high collision energies and integrated luminosities, as well as state-of-the-art detectors, the experiments at the Large Hadron Collider (LHC) are able to offer a diverse physics program that can explore the topic of flavor in many unique ways. LQs could be directly created or exchanged in proton-proton collisions at the LHC, which motivates the search for these signatures in multipurpose detectors like CMS. This thesis presents a combined search for single and pair production of LQs that decay exclusively to a τ lepton and a bottom quark, as well as nonresonant production of a τ lepton pair through the t-channel exchange of an LQ. Single and pair production have a resonant final state that includes two τ leptons and at least one heavy-flavored jet. Nonresonant production will also have a final state with two τ leptons and a distribution of jets produced in association by gluon splitting or initial state radiation. The search is based on a data sample of proton-proton collisions at a center-of-mass energy of 13 TeV recorded by the CMS experiment in 2016–2018, corresponding to a data set with an integrated luminosity of about $138\,\mathrm{fb}^{-1}$. This analysis was the first at the LHC to incorporate a search for nonresonant LQ production, which has the benefit of being sensitive to LQs with masses larger than the energy exchanged in the collisions.

A τ lepton may decay to an electron (e) or muon (μ), each accompanied by two undetected neutrinos (ν), or it may decay to hadrons (τ_h) and a neutrino. We reconstruct both hadronic and leptonic decays of the two τ leptons, classifying events into exclusive channels denoted by the measured particles: fully hadronic ($\tau_\mathrm{h}\tau_\mathrm{h}$), semileptonic ($\mathrm{e}\tau_\mathrm{h}$, $\mu\tau_\mathrm{h}$), and fully leptonic channels ($\mathrm{e}\mu$, $\mu\mu$). Due to the large branching fraction, the semileptonic and fully hadronic channels are the most sensitive to an LQ signal with two τ leptons, while the events with two light leptons ($e\mu$, $\mu\mu$) are used to constrain SM backgrounds.

The hadronic decay modes make up about 64.8% of τ lepton decays, and are therefore crucial in the statistically limited search for LQs. I have therefore contributed to dedicated algorithms to reconstruct and identify τ_h decays with good accuracy and efficiency, while suppressing the large background of objects that are misreconstructed or misidentified. Furthermore, corrections to simulated τ_h candidates need to be measured to ensure good understanding and modeling of the data. These algorithms and corrections, including a significant fraction of my own work as well as work I helped supervise as co-convener of the CMS Tau ID Group, will also be presented in this thesis.

This dissertation first describes the state-of-the-art theoretical and experimental approaches used in this thesis (Chapters 2 to 5), followed by an in-depth explanation of the analysis I developed and executed in order to complete the thesis (Chapters 6 to 14). It has the following structure: Chapter 2 discusses the SM and its flavor symmetries, after which Chapter 3 motivates the search for hypothetical particles like LQs, which are beyond the SM. Chapter 4 describes the LHC accelerator, CMS detector and the collection of proton-proton collision data. Chapter 5 describes the way physics objects that are relevant for this thesis are reconstructed in CMS, while Chapter 6 focuses mainly on the reconstruction and identification of hadronically decayed τ leptons. Chapter 7 describes the data sets and the simulation of both the background processes and the signal model. Chapter 8 and Chapter 9 then discuss how corrections are derived and applied to the simulation of background processes to account for mismodeling. After these, Chapter 10 discusses the common preselection of events that are compatible with the decay channels of the pair of τ leptons, and the optimized final selections targeting the LQ $\to$ bτ signal and nonresonant LQ signals. Chapter 11 discusses the estimations of relevant background processes. Chapter 12 explains the way a hypothetical signal is extracted from data with systematic uncertainties. Chapter 13 presents the preliminary results. A summary is given in Chapter 14.

2 The Standard Model

This chapter introduces the Standard Model (SM) of particle physics that encapsulates the behavior of matter and its interplay with the strong, weak, and electromagnetic forces. Section 2.1 discusses experimental observations, which have led to the mathematical formulation of the SM laid out in Section 2.2. Section 2.2.3 lays out the unexplained features of flavor symmetry, which will motivate the subject of this thesis. Finally, Section 2.3 will explain the physics of proton-proton (pp) collisions.

2.1 Experimental observations & building the Standard Model

In the past century, physicists have slowly puzzled together our current understanding of the fundamental nature of matter from a series of experimental observations and theoretical considerations. To understand how the theoretical framework of the SM of particle physics laid out in Section 2.2 was finally constructed, this section will highlight several important observations and insights. More detailed historical discussions can be found in Refs. [1–3]. A rough timeline of the experimental discovery of particles is given by Fig. 2.1.

2.1.1 The electromagnetic interaction

By the 1930s, the electron (e^-), proton (p^+), and neutron (n^0) were discovered, and were enough to describe the composition of ordinary matter that surrounds us in daily life. Quantum mechanics was successful in describing the hydrogen atom and its emission spectrum, but small deviations were found between theory and experiment in the energy levels of hydrogen, as well as the magnetic moment of the electron. This led to the development of *quantum electrodynamics* (QED), which can very precisely and accurately compute the observed anomalous magnetic moment of the electron with perturbation theory, and became the fundamental theory for the electromagnetic interaction, with the photon as mediator between particles with electric charge.

The mathematical structure and methods of QED also inspired the later theories of other interactions. One important principle guiding the formulation of interactions between particles, is *gauge symmetry*, which requires that the theory is invariant under the *local transformations* of a certain symmetry group. Gauge symmetry implies conservation of charge and one or more *gauge bosons*, which are bosons with spin 1 that mediate a force. For QED, the gauge symmetry is given by a local $\mathrm{U}(1)_{\mathrm{EM}}$ symmetry that generates a coupling between charged particles and the photon. More detail will be given in Section 2.2.1.

2.1.2 The discovery of exotic particles

As experimental techniques improved, many other types of matter particles that were completely unexpected were observed in cosmic rays and fixed-target experiments. In 1936, the muon ($\mu^\pm$) was discovered, which is a particle that has the same properties as the electron, except it is unstable and has a mass that is approximately 206.7 larger than that of the electron. In the

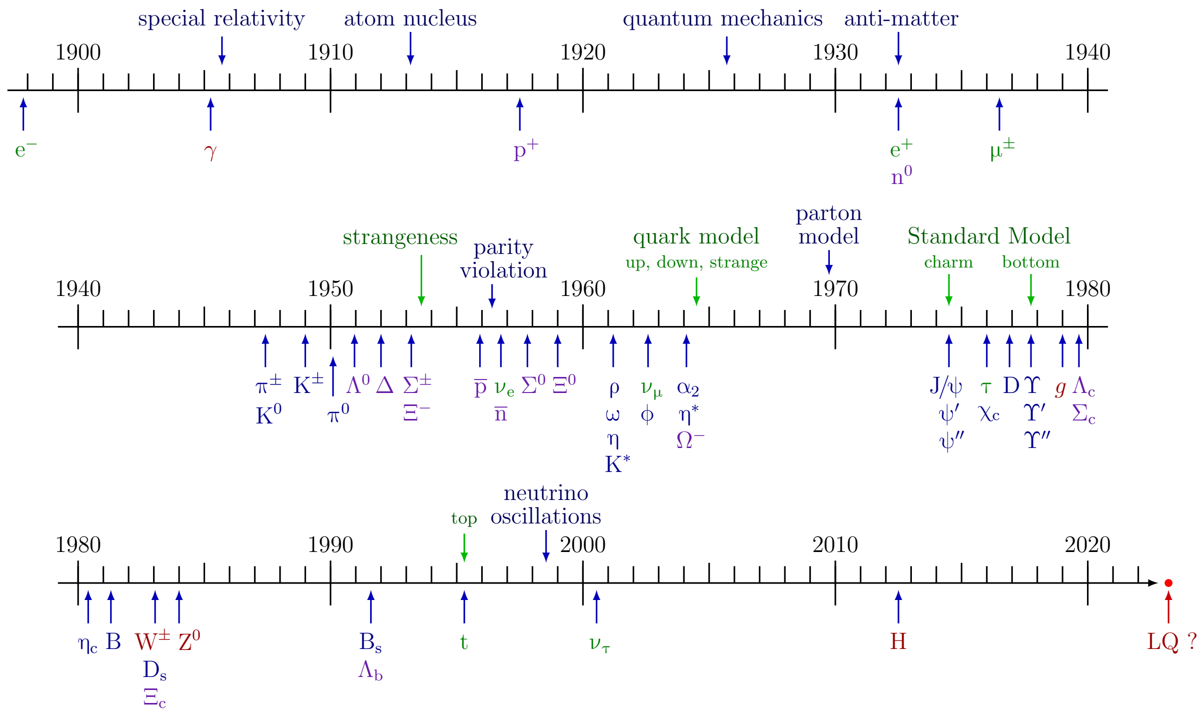

Figure 2.1: A timeline of particle physics in the last 130 years. Some of the most important experimental discoveries of subatomic particles are indicated below the timeline. Leptons and quarks are highlighted in green. Mesons and baryons are indicated in blue and purple, respectively, and are hadrons, which are the bound state of two or three quarks, respectively. Finally, fundamental bosons are shown in red. Note that some particles, like the positron (e^+), pion (π), neutrino (ν), Ω^-, Υ, gluon, top quark, and Higgs boson, were predicted before experimental observation. The leptoquark (LQ) is a hypothesized boson. Figure inspired by Ref. [4].

years after World War II, new particles were observed in collisions of cosmic rays with protons and neutrons. They included the pions ($\pi^\pm$, π^0), the kaons ($K^\pm$, K^0), the Δ particles, and the hyperons (Λ, Σ, Ξ). Because these particles are easy to produce in large numbers, but decay relatively slowly, it was recognized that their production mechanism must be mediated by the *strong force*, which also holds together protons and neutrons in the nucleus of the atom, while their decay is most often mediated by the *weak force*, which is also responsible for beta decay of radioactive nuclei and the neutron [3, 5]. These types of particles that can be produced in strong interactions are referred to as *hadrons*. These include the proton and neutron. In contrast, *leptons* like the electron, muon, and neutrino (ν) do not participate in the strong interaction, but can interact through the electromagnetic and weak force.

2.1.3 The quark model

It is now understood that hadrons are composite particles. This realization was achieved by finding certain patterns in the observed properties of the hadrons. In analogy to the SU(2) symmetry of spin, the concept of *isospin* was used to group together hadrons of identical spin and similar mass into the same isospin multiplets according to the observed value of the electrical charge. Furthermore, to explain why certain hadrons like kaons and hyperons are always produced in pairs, a new quantum number called *strangeness* was postulated, which, like isospin, is conserved by the strong force. This eventually led to the *quark model* proposed by Gell-Mann [6] and Zweig [7] in 1964, who suggested the existence of a new type of strongly-interacting particle with fractional charge, called the *quark*. Like the leptons, they have spin 1/2, and are therefore also *fermions*. These quarks came in three species, or *flavors*: the up (u), down (d), and strange quark (s). By ordering the hadrons into multiplets of an SU(3) flavor symmetry, Gell-Mann successfully predicted the existence of the Ω^- baryon, which was discovered later in 1964 [8]. The quark model was later extended in 1974 with the charm quark (c) after the discovery of J/ψ, a $c\bar{c}$ state [9, 10]. When later the Υ, a $b\bar{b}$ state, was discovered [11], the bottom quark (b) was also included, which implied, due to flavor symmetry, the existence of the top quark (t) long before its discovery.

Most observed hadrons are classified as either *mesons* or *baryons*, which are bound states of two or three quarks, respectively. This picture is a bit more complicated by the *parton model*, which will be discussed in Section 2.3.1. Almost all (free) hadrons are unstable. The notable exception is the proton, for which the Super-Kamiokande experiment has set a lower limit on the lifetime of $\tau_{\mathrm{p}} > 2.4 \times 10^{34}$ years at a 90% confidence level [12]. The decay chain of all other baryons end with the proton, which is the lightest baryon. This implies a law of *conservation of baryon number B*. Protons and neutrons, for example, have $B = +1$, and their antiparticles ($\bar{\mathrm{p}}$, $\bar{\mathrm{n}}$) have $B = -1$. Since this is an additive number, quarks are assigned baryon number $B = +1/3$, while anti-quarks must have $B = -1/3$.

2.1.4 The strong interaction

Quarks of the same flavor can form bound states like the Δ^{++} baryon, which is a uuu state and should violate the Pauli exclusion principle if quarks have indeed spin 1/2. To explain the observation of such states with the quark model, the concept of *color charge* was introduced. Each quark is assigned a red, blue, or green color charge, while antiquarks must have anti-red, anti-blue, or anti-green. In this way, three quarks of the same flavor but different color charge can form a bound state without violating the exclusion principle. The mathematical structure of color charge can also be given by an $\mathrm{SU}(3)_{\mathrm{C}}$ color symmetry, analogous to the SU(3) flavor symmetry. This fact helped to formulate the theory of *quantum chromodynamics* (QCD), which is the fundamental theory of strong interactions. When using $\mathrm{SU}(3)_{\mathrm{C}}$ as a gauge symmetry, the theory also implies the existence of the gluon, a massless vector boson that mediates the strong interaction between objects with color charge. Gluons can also self-interact, and therefore carry color. While they are massless, their strong self-interaction ensures they have a short range, in line with observations of nuclei and hadrons.

Another initial problem for the quark model was that quarks were never observed as isolated particles. The idea of *color confinement* was formulated, which stated that strongly interacting particles must form colorless states like hadrons, wherein the color charge of the constituent quarks cancel each other when combined. The mechanism for color confinement was only explained much later by QCD. However, the discovery of new hadrons like J/ψ and Υ, and experiments probing the substructure of the proton, provided more experimental evidence in favor of the quark model (see Section 2.3.1). Furthermore, quarks and gluons can explain the phenomena of the production of so-called *jets* of hadrons in particle colliders, which is discussed in Section 5.1. Quarks and their color charge are also confirmed by the observed rate of hadron creation in electron-positron collision data. For example, the ratio of production cross sections of the hadrons with respect to pairs of muons can be roughly approximated by

$$R(s) = \frac{\sigma(\mathrm{e^+e^-} \to \mathrm{hadrons})}{\sigma(\mathrm{e^+e^-} \to \mu^+\mu^-)} \approx N_{\mathrm{C}} \sum_f Q_f^2, \tag{2.1}$$

where $N_{\mathrm{C}} = 3$ is the number of color charges, $Q_f = -1/3$ or $+2/3$ is the electric charge of the quark with flavor f, and s is square of the center-of-mass collision energy [3, p. 278; 13, Section 9.2.1]. Without color, $N_\mathrm{C} = 1$, and this ratio would be three times smaller than observed.

2.1.5 The weak interaction

The weak interaction is responsible for most hadron decays, for example, the beta decay of the neutron, $\mathrm{n}^0 \to \mathrm{p}^+\mathrm{e}^-\overline{\nu}_\mathrm{e}$. In 1933, Fermi proposed a simple model where these four particles with spin 1/2 interact in a single point. For this, he postulated the existence of the neutrino, whose existence was confirmed later in 1956 using the neutrino flux from nuclear reactors [14]. The strength of this *contact interaction* was given by the *Fermi constant* $G_\mathrm{F} \approx 1.1638 \times 10^{-5}\,\mathrm{GeV}^{-2}$.

In order to explain why the weak interaction has such a short range and is many orders of magnitude weaker than the electromagnetic and strong interactions, one needs a theory wherein the weak force is mediated by a massive vector boson that is exchanged between two pairs of fermions. This was accomplished by Glashow, Weinberg, and Salam in the 60s, in what is now called the *electroweak theory*. Their model included two charged $\mathrm{W}^\pm$ bosons and one neutral Z^0 boson, for which Weinberg derived a simple formula in his seminal paper [15] that related the masses of these *weak bosons*. In 1983, both the W and Z bosons were directly observed in proton-antiproton collisions at CERN [16, 17]. With the combined success of the electroweak theory and QCD, the SM of particle physics was formed.

The weak interaction has several unique and nontrivial properties, which helped formulate the final structure of the SM. In 1956, Wu observed that *parity symmetry* was violated in weak decays [18]. In her famous experiment, she measured the beta decay of cobalt 60 nuclei that were polarized in a magnetic field, and observed that electrons were preferentially emitted in the direction opposite of the nuclei spin, violating parity. In comparison, parity violation has not been observed in electromagnetic or strong processes, after many rigorous tests. Experimentally, it turns out that the violation of parity by the weak interaction is maximal. Neutrinos, which are only known to interact through the weak force, always have a *left-handed helicity* (i.e., the spin is anti-parallel with the momentum), while antineutrinos always have a *right-handed helicity* (i.e., the spin is parallel with the momentum). Clear evidence for this is seen in, for example, the measured helicity of the muon in pion decay, $\pi^+ \to \mu^+\nu_\mu$ [19, 20], or the angular distribution of the electron in muon decay, $\mu^+ \to \mathrm{e}^+\nu_\mathrm{e}\overline{\nu}_\mu$ [21]. Furthermore, the maximal violation of parity can quantitatively describe why the observed decay rate of $\pi^+ \to \mathrm{e}^+\nu_\mathrm{e}$ is heavily suppressed compared to that of the muonic decay, such that their ratio is $\Gamma(\pi^+ \to \mathrm{e}^+\nu_\mathrm{e})/\Gamma(\pi^+ \to \mu^+\nu_\mu) \approx 1.2 \times 10^{-4}$ [22]. If parity were conserved, this ratio would be about 5.5 instead due to the small electron mass compared to that of the muon.

The theory of weak interactions describes the interaction between the weak bosons and two quarks or two leptons. Each pair belongs to a different generation. For example, the first generation has couplings W-$\mathrm{e}\nu_\mathrm{e}$ or W-ud, while the second generation has couplings W-$\mu\nu_\mu$ or W-sc. These are responsible for decays where charge is exchanged, i.e., *charged currents*. However, there is some mixing between quark generations in charged currents, as explained below. *Neutral currents* are given by Z-$f\bar{f}$ couplings, where f is any fermion, and $\bar{f}$ is the corresponding antiparticle of the same flavor but opposite charge. No mixing is found in these couplings. It was realized that these pairs form doublets under an $\mathrm{SU}(2)_\mathrm{L}$ symmetry, where the label L represents the fact that the fermions interacting with the W boson must have a left-handed chirality, while antifermions must be right-handed because of maximal parity violation. The weak bosons then, form a triplet, and are the gauge bosons with $\mathrm{SU}(2)_\mathrm{L}$ as a gauge symmetry.

While the strong interaction conserves the number of each quark flavor, the weak interaction does not as evidenced by observed hadron decays like $\mathrm{K}^{\pm} \to \pi^{\pm}\pi^{0}$, which violates strangeness. This can be explained if one assumes that the quark eigenstate that participates in the weak interaction do not align with the quark mass eigenstates [23]. The kaon decay to two pions must then involve an $\mathrm{s} \to \mathrm{d}$ transition. This can be expressed with the simple rotation matrix

$$\begin{pmatrix} d' \\ s' \end{pmatrix} = \begin{pmatrix} \cos\theta_{\mathrm{C}} & \sin\theta_{\mathrm{C}} \\ -\sin\theta_{\mathrm{C}} & \cos\theta_{\mathrm{C}} \end{pmatrix} \begin{pmatrix} d \\ s \end{pmatrix}, \tag{2.2}$$

where $|d'\rangle$ and $|s'\rangle$ represent the weak eigenstates, which are linear combinations of the mass eigenstates $|d\rangle$ and $|s\rangle$. The mixing of the down and strange states is quantified with the *Cabibbo angle* θ_{C}, which is measured to be about $\theta_{\mathrm{C}} \approx 13.04°$. To explain the suppressed decay rate of $\mathrm{K}^0 \to \mu^+\mu^-$, Glashow, Iliopoulos, and Maiani used this mixing matrix and proposed the existence of the charm quark as a partner to the strange quark in 1970, several years before the discovery of J/ψ [24]. This is referred to as the *Glashow–Iliopoulos–Maiani* (GIM) *mechanism.*

One consequence of quark mixing can be seen in the *oscillations of the neutral kaon system* ($\mathrm{K}^0 \rightleftharpoons \overline{\mathrm{K}}^0$) that decays through the weak eigenstates $\mathrm{K_S}$ and $\mathrm{K_L}$, which have distinct lifetimes [25]. These eigenstates were expected to also be eigenstates of the *CP symmetry*, which combines charge conjugation and parity reversal. However, evidence for a small violation of CP violation was found in the experiment performed by Cronin and Fitch at Brookhaven in 1964 [26]. In 1973, Kobayashi and Maskawa recognized that CP violation could not be accommodated in a four-quark model and postulated the existence of a third generation of quarks [27]. They generalized the Cabibbo matrix Eq. (2.2) to

$$\begin{pmatrix} d' \\ s' \\ b' \end{pmatrix} = \begin{pmatrix} V_{ud} & V_{us} & V_{ub} \\ V_{cd} & V_{cs} & V_{cb} \\ V_{td} & V_{ts} & V_{tb} \end{pmatrix} \begin{pmatrix} d \\ s \\ b \end{pmatrix}, \tag{2.3}$$

where the matrix is the so-called *Cabbibo-Kobayashi-Maskawa* (CKM) *matrix*, denoted by V_{CKM}. Several years later, the Υ was discovered, which was direct evidence for the bottom quark. The bottom quark implied the existence of its partner with charge $+2/3$, the top quark, which was indeed observed from its decay much later in 1995 at the Tevatron collider in Fermilab [28, 29]. Most of the elements of the CKM matrix have been measured to good precision, primarily from hadron decays and the oscillations of neutral meson systems [13, Section 12]. The size of the diagonal elements are close to one, while $|V_{ud}|$ and $|V_{ud}|$ are about roughly 0.22, and the size of the other off-diagonal elements are smaller than 0.042.

2.1.6 Fermion generations

In 1975, a third charged lepton called the τ lepton was discovered. It has a mass m_τ of 1.776 GeV, almost 17 times larger than that of the muon. Direct evidence that the τ neutrino (ν_τ) existed and is distinct from the electron neutrino (ν_{e}) and muon neutrino (ν_μ) was announced by the DONUT experiment in 2000 [30]. No evidence for more quarks or leptons has so far been found. Precision measurements of the decay width of the Z boson are consistent with three generations of neutrinos, as long as the new neutrinos have a mass lower than $M_{\mathrm{Z}}/2 \approx 45\,\mathrm{GeV}$ [31]. The observation of the top quark and τ neutrino therefore officially completed the known matter content in Nature. The current SM of particle physics counts six quark flavors and six lepton flavors that are organized into three generations of two flavors each. The charged leptons with $Q = -1$ are known as the electron, muon, and τ lepton, and for each lepton generation there is a corresponding neutrino without electric charge, i.e., $Q = 0$. The quarks come in three generations of up-type quarks with charge $Q = +2/3$; the up, charm, and top quark, and in three generations of down-type quarks with charge $Q = -1/3$; the down, strange, and bottom quark. The antiparticles of the fermions have the opposite quantum numbers, including electric charge Q. There is a clear hierarchy in the observed mass, which allows the generations to be ordered from small to large mass. Leptons and quarks, as well as the gauge bosons and Higgs boson, have no substructure, and are presumed to be fundamental particles that are not further composed of new types of particles [32]. Figure 2.3 summarizes the observed particles of the SM with their respective properties.

2.1.7 The Higgs boson & Yukawa interactions

As mentioned above, the weak bosons need to be massive to explain the weakness and short-range of the weak force. However, gauge bosons with nonzero mass spoil the gauge invariance of the theory. To get around this, one can instead assume that the $\mathrm{SU}(2)_\mathrm{L}$ gauge symmetry of the electroweak theory is spontaneously broken. *Spontaneous symmetry breaking* (SSB) can be achieved with a new scalar boson (i.e., spin 0), called the *Higgs boson*, that interacts with the gauge bosons and generates mass and has a nonzero *vacuum expectation value* (vev). This is called the *Higgs mechanism*, proposed in 1964 [35, 36]. The Higgs boson was long sought for, and its discovery was finally announced in 2012 [37–40]. A single Higgs boson is the simplest and most minimal solution, although it is possible to achieve SBB with more than one Higgs boson. No evidence of additional Higgs bosons have been found so far [41].

The Higgs boson also couples to fermions with so-called *Yukawa couplings*, and can be used to generate gauge invariant fermion masses in the theory. The fermion masses are proportional to the coupling strength of their coupling to the Higgs. Contrary to the W and Z boson masses, these Yukawa couplings are parameters of the theory and need to be measured in experiment from the fermion masses and Higgs vev, which is measured from the lifetime of weak decays. With a mass of $m_\mathrm{t} \approx 172.8\,\mathrm{GeV}$ [13, p. 32], the top quark is by far the heaviest fermion. Due to its large Yukawa coupling, it becomes important in quantum corrections of observables like the masses of the weak bosons. Theorists used this fact to accurately predict the mass of the top quark with the SM, using precision electroweak measurements and special theoretical techniques [43]. Similarly, the mass of the Higgs boson was not known from theory beforehand, but it was possible to constrain it very well with an SM fit to precision measurements at the Tevatron and LEP of the top quark, and the W and Z bosons [44]. Many measurements of the production and decay of the Higgs boson at the LHC have been made, and so far the measured coupling strengths between the Higgs boson and both weak bosons and the heaviest fermions agree well with the SM predictions [33, 45], as shown in Fig. 2.2.

2.1.8 Neutrinos

Even though neutrinos are very hard to detect because they are light and only interact via the weak force, physicists have been able to learn quite a lot about them. As already mentioned, neutrinos always have left-handed helicity, while anti-neutrinos have right-handed helicity. Other experiments have shown that neutrinos are different from their antiparticles, and that they come

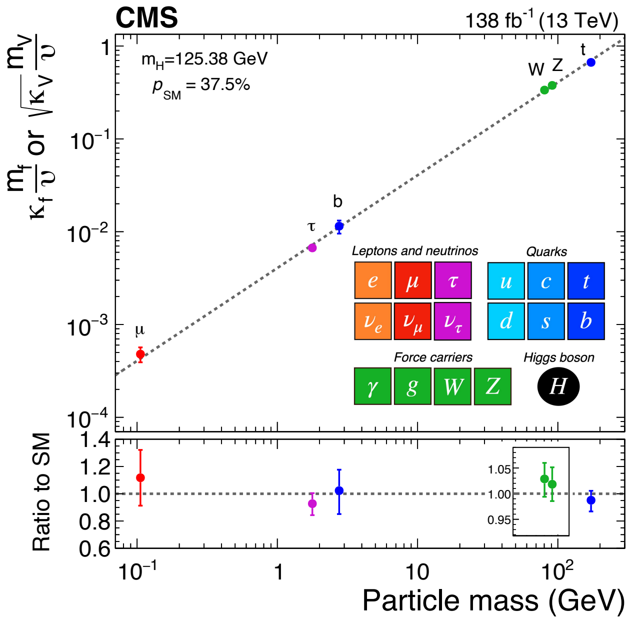

Figure 2.2: Measurements of the Higgs boson coupling strengths as measured by the CMS experiment as a function of mass [33]. The coupling strengths are represented by the reduced coupling strength modifiers $\kappa_f m_f/v$ ($\sqrt{\kappa_f} m_V/v$) for Higgs couplings to the fermions (gauge bosons), where $v \approx 246\,\mathrm{GeV}$ is the vev of the Higgs field. The SM prediction corresponds to coupling strength modifiers $\kappa_i = 1$. Note that the coupling strengths for fermions are proportional to mass, as expected for Yukawa couplings. Figure take from from Ref. [34].

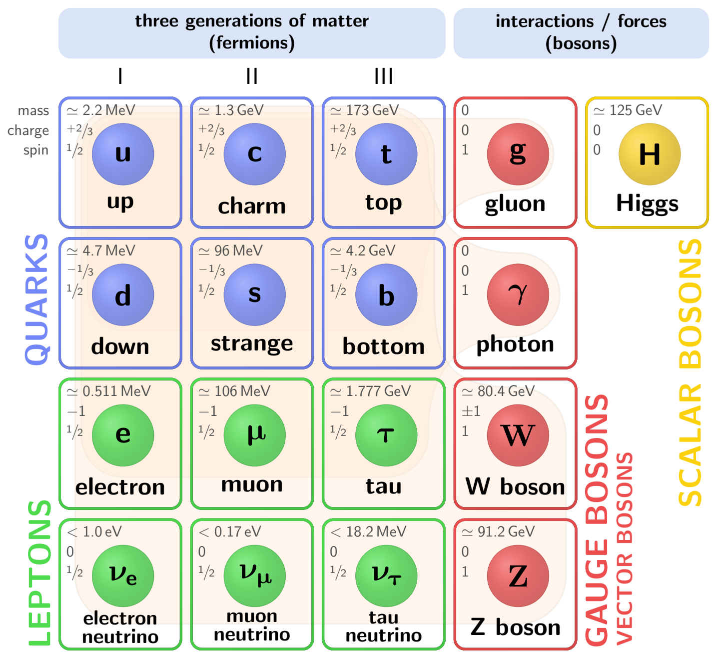

Figure 2.3: A table of the particles in Standard Model of particle physics and their properties. Matter is given by fermions, and interactions mediated by vector bosons (i.e., spin 1). The fermions are elementary particles with spin 1/2 and comprise of quarks, which can interact with the strong force, and leptons, which cannot. Each species, or *flavor*, of fermion can be distinguished by their mass and interactions. There are six flavors of quarks and six flavors of leptons, which are organized into three generations of two flavors because of the symmetrical way in which they interact with the weak force mediated by the $W^{\pm}$ and Z bosons. Note that the generations are ordered by increasing mass. The vector bosons are called gauge bosons. The Higgs boson is the only (fundamental) scalar boson (i.e., spin 0) in this model. Figure adapted from Ref. [42].

in three flavors, the electron neutrino, muon neutrino, and τ neutrino. These observed properties lead to the concept of *conservation of lepton number* L, where each lepton carries a number $L = +1$, and their antiparticle carries $L = -1$, and which is conserved in all SM processes [46]. Furthermore, processes like $\mu^{\pm} \to e^{\pm}\gamma$ have never been observed, even though they are allowed by conservation of charge and lepton number. This led to the idea of splitting lepton number in to one conserved lepton number per generation: $L = L_e + L_\tau + L_\tau$ [47, 48].

It was long believed neutrinos were massless. The SM is constructed on this assumption because implementing masses for left-handed neutrinos in the same way as for the charged fermions requires the existence of a right-handed neutrino, whose existence is uncertain. This will be discussed in Section 2.2.2. Nevertheless, the observation of *neutrino oscillations* implies that neutrinos do have mass [49], which requires the SM to be extended. The oscillations imply that neutrino flavors mix because the neutrino's mass eigenstates are different than the weak eigenstates, similar to quarks. The mixing is quantified by a 3×3 unitary matrix called the *Pontecorvo-Maki-Nakagawa-Sakata* (PMNS) *matrix*, which is the analogue of the CKM matrix. This mixing of neutrinos is in fact experimental proof of the violation of the numbers of individual lepton flavor, and can technically allow the *lepton-flavor violating* decay $\mu^{\pm} \to e^{\pm}\gamma$, although it is extremely suppressed as discussed in Section 2.2.3.

2.2 The Standard Model of particle physics

In the SM, matter is composed of elementary particles with spins of 1/2 referred to as fermions, while forces occur due to the exchange of elementary particles with spins of 1 called gauge bosons. Although it is rarely referred to as a force because it has a spin of 0, the Higgs boson interacts with fermions giving rise to their mass. The SM is a quantum field theory (QFT), which describes matter and the forces as quantum fields, and particles as excited states of these fields. The *kinematics*, or the momentum and energy of particles, and *dynamics*, or the interactions between particles, are encoded in the *SM Lagrangian density.* The terms of the Lagrangian density can be grouped into three separate *sectors*:

$$\mathcal{L}_{\mathrm{SM}} = \mathcal{L}_{\mathrm{gauge}} + \mathcal{L}_{\mathrm{Higgs}} + \mathcal{L}_{\mathrm{Yukawa}}. \tag{2.4}$$

The *gauge sector* $\mathcal{L}_{\mathrm{gauge}}$ describes the kinetics of the fermion and gauge boson fields, as well as the strong, weak and electromagnetic interactions between them. The *Higgs sector* $\mathcal{L}_{\mathrm{Higgs}}$ describes the kinetics of the scalar Higgs field and its interaction with itself and the gauge boson fields. Finally, the *Yukawa sector* $\mathcal{L}_{\mathrm{Yukawa}}$ contains the Yukawa interactions between the fermion and Higgs fields. The Lagrangian density, or Lagrangian for short, gives all the mathematical terms to derive the equations of motion and the interactions between the different fields, and allows us to compute cross sections and decay rates. Most physical observable are computed with perturbation theory, which expands the calculation into a power series in the coupling strength. This works if the coupling strength is small enough for the series to converge. The more terms of higher order are included, the higher the accuracy should become. The accuracy of observables calculated with perturbation theory are often indicated by *leading order* (LO), *next-to-leading order* (NLO), *next-to-next-to-leading order* (NNLO), etc.

The terms of the SM Lagrangian are constrained by three conditions. Firstly, the SM must be *Lorentz invariant* such that the Lagrangian has the same form between two inertial reference frames, in accordance with special relativity. The terms are therefore often a product of fields and their space-time derivatives, which are called *local operators*. The fields themselves themselves are the irreducible representations of the double cover of the Poincaré group, such that they can describe particles with spin 0 (scalar bosons), 1/2 (fermions), or 1 (vector bosons) [50, 51]. It should be noted, however, that the SM does violate the discrete symmetries of parity (P), charge-conjugation (C), and time-reversal (T), which are part of the Lorentz group. Nevertheless, for the SM to be a consistent Lorentz invariant QFT, the combined application of C, P, and T operations must lead to invariant descriptions of all physical phenomena, a theorem known as the *CPT theorem*. As mentioned in Section 2.1.5, violations of P, C, and CP have been observed in weak interactions. CPT symmetry has never been observed to be violated and has been confirmed experimentally [52–55].

Secondly, the SM is a *gauge theory*: It has an internal symmetry that corresponds to the local $\mathrm{SU}(3)_\mathrm{C} \times \mathrm{SU}(2)_\mathrm{L} \times \mathrm{U}(1)_\mathrm{Y}$ symmetry group, where the labels C, L, Y refer to the charges of the three subgroups, namely color charge, weak isospin, and weak hypercharge, respectively. Each term in the Lagrangian must be invariant under the local transformations of this group, and the SM fields must belong to a representation of this group. Each subgroup of the $\mathrm{SU}(3)_\mathrm{C} \times \mathrm{SU}(2)_\mathrm{L} \times \mathrm{U}(1)_\mathrm{Y}$ gauge group is associated with a gauge field, which must also be a vector boson. Gauge fields are in the adjoint representation, which means that for the $\mathrm{SU}(N)$ groups, it forms a multiplet with $N^2 - 1$ components. Gauge fields of a $\mathrm{SU}(N)$ gauge symmetry can self-interact, which is a consequence of the fact that $\mathrm{SU}(N)$ is a *non-Abelian* group. A fermion field may be *charged* under a gauge group if the group transforms one of it properties, otherwise the field is referred to as a singlet. If a fermion field is charged under a gauge group with dimension N, it must be in the fundamental representation of this group, such that is forms a multiplet with N components. Importantly, at low energies the SM gauge group is spontaneously broken to

$$\mathrm{SU}(3)_\mathrm{C} \times \mathrm{SU}(2)_\mathrm{L} \times \mathrm{U}(1)_\mathrm{Y} \xrightarrow{\mathrm{SSB}} \mathrm{SU}(3)_\mathrm{C} \times \mathrm{U}(1)_\mathrm{EM} \tag{2.5}$$

by the nonzero vev of the Higgs field, where $\mathrm{U}(1)_\mathrm{EM}$ is the gauge symmetry group for QED. The color group $\mathrm{SU}(3)_\mathrm{C}$ is the basis for the fundamental theory of the strong interaction, QCD. This will be discussed in more detail below.

Finally, the SM is required to be *renormalizable*, so that physical observables converge in perturbative calculations. The condition of renormalizability in four space-time dimensions limits the total mass dimension of the local operators in Lagrangian terms to $d = 4$, where the *mass dimension* of a local operator is the sum of the mass dimensions its composing fields, which takes values $d = 1$ for a boson field with spin 0 or 1 and $d = 3/2$ for a fermion field with spin 1/2, while each derivative adds an extra $d = 1$. In the view of Effective Field Theory (EFT), however, models beyond the SM can introduce new terms of higher-order dimensions that are suppressed with some cut-off scale Λ. This will be discussed in more detail later in this Section 3.3.

In addition to these three conditions, we need to specify the field content, which is the set of fermion fields that explains the observed elementary matter particles, and pattern of SSB of $\mathrm{SU}(2)_\mathrm{L}$. As discussed in Section 2.1.6, experiment shows there are in total six quark flavors and six leptons that come in three generations of two flavors each. Because they are spin-1/2 fermions, they enter the SM Lagrangian as *spinor fields*. The vector bosons such as gluons and the weak bosons emerge naturally by requiring $\mathrm{SU}(3)_\mathrm{C} \times \mathrm{SU}(2)_\mathrm{L} \times \mathrm{U}(1)_\mathrm{Y}$ as a gauge symmetry. As discussed in Section 2.1.7, only one scalar boson that is consistent with a Higgs boson has been observed. We therefore implement SSB in the SM with a single Higgs field, which is a scalar field that forms a doublet under $SU(2)_L$. The nonzero vev of the Higgs field breaks the $SU(2)_L$ symmetry and generates mass terms for the weak bosons and fermions.

Before discussing other symmetries of the SM to better understand flavor, we first need to introduce how matter and their interactions in the gauge and Yukawa sectors are formulated in the SM.

2.2.1 The gauge sector

Let us have a closer look at how the gauge sector describes the motion and gauge interactions of matter and the gauge bosons. It can be written as

$$\mathcal{L}_{\text{gauge}} = \sum_f \sum_{\psi_f} \overline{\psi}_f i\gamma^\mu D_\mu \psi_f - \frac{1}{4} G^a_{\mu\nu} G^{\mu\nu}_a - \frac{1}{4} W^i_{\mu\nu} W^{\mu\nu}_i - \frac{1}{4} B^{\mu\nu} B^{\mu\nu}, \tag{2.6}$$

in natural units $c = \hbar = 1$ [56], and where $a = 1, ..., 8$ and $i = 1, 2, 3$. In the first term, matter is given by five fermion fields ψ_f in three generations $f = 1, 2, 3$;

$$Q^f_{\text{L}} = \begin{pmatrix} u^f_{\text{L}} \\ d^f_{\text{L}} \end{pmatrix}, \quad u^f_{\text{R}}, \quad d^f_{\text{R}}, \quad L^f_{\text{L}} = \begin{pmatrix} \nu^f_{\text{L}} \\ e^f_{\text{L}} \end{pmatrix}, \quad e^f_{\text{R}}. \tag{2.7}$$

Their Dirac adjoints are given by $\overline{\psi}_f = \psi^\dagger_f \gamma^0$. They have opposite quantum numbers, such that the local operator in the first term of Eq. (2.6) has no charge of any kind. Besides their generation, the different fermion fields are identified by their representation and quantum numbers for the $SU(3)_C \times SU(2)_L \times U(1)_Y$ gauge group. Because of the $SU(2)_L$ gauge symmetry, the SM is a chiral gauge theory, meaning it distinguishes left- and right-handed fermion fields. The left-handed fermion fields form a weak isospin doublet that contains two components that are left-handed spinors, while each right-handed fermion field is a single spinor that is a singlet under $SU(2)_L$. Right-handed neutrinos ν_R canonically are not included in the SM because the weak interaction couples only to left-handed neutrinos ν_L, and the neutrinos are often assumed massless as explained in Section 2.2.2. Each quark field also forms a color triplet under $SU(3)_C$, but color indices are suppressed here for brevity. The representations of the SM fields under the SM gauge group and corresponding quantum numbers are summarized in Table 2.1 and visualized in Fig. 2.4.

In the last three terms of Eq. (2.6), the field strength tensors $G^a_{\mu\nu}$, $W^i_{\mu\nu}$, and $B_{\mu\nu}$ correspond to, respectively, the eight-component gluon field G^a_μ of $SU(3)_C$, the three-component weak gauge field W^i_μ of $SU(2)_L$, and the hypercharge field B_μ of $U(1)_Y$. These terms describe both the kinetics and self-interactions of these three vector fields.

The kinetics of the fermions and their interactions with gauge bosons are given by the covariant derivative

$$D_\mu = \partial_\mu + ig_{\text{s}} t_a G^a_\mu + igT_i W^i_\mu + ig' \frac{Y}{2} B_\mu \tag{2.8}$$

where T_i and t_a and are the generators for $SU(2)_L$ and $SU(3)_C$, respectively, and Y is the weak hypercharge of the field that D_μ acts on. For weak isospin doublets, $T_i = \sigma_i/2$, with the usual three Pauli matrices σ_i, while for color triplets, $t_a = \lambda_a/2$, with the eight Gell-Mann matrices λ_a. Meanwhile, the second term disappears for color singlets like the leptons since $t_a \psi_f = 0$, and similarly, the third term will vanish for right-handed fermion fields since $T_i \psi^f_{\text{R}} = 0$.

Table 2.1: Summary of SM fields and their representation of the $\mathrm{SU}(3)_\mathrm{C} \times \mathrm{SU}(2)_\mathrm{L} \times \mathrm{U}(1)_\mathrm{Y}$ gauge group with the corresponding quantum numbers T_3 of $\mathrm{SU}(2)_\mathrm{L}$ and hypercharge Y of $\mathrm{U}(1)_\mathrm{Y}$, as well as the electric charge Q of $\mathrm{U}(1)_\mathrm{EM}$. Bold numbers indicate the dimension of the representation under the respective gauge group: **1** is a singlet, **2** is a doublet, **3** is a triplet, and **8** is an octet. For the fermions, the generational and color indices are omitted. The weak gauge field is written in the weak isospin eigenbasis with $W^\pm_\mu = (W^1_\mu \mp iW^2_\mu)(\sqrt{2})$. The Dirac adjoint of each spinor field has the opposite quantum numbers.

Field name	Symbol	Representations		Quantum numbers		
		$\mathrm{SU}(3)_\mathrm{C}$	$\mathrm{SU}(2)_\mathrm{L}$	T_3	$Y/2$	$Q = T_3 + Y/2$
Quark doublet	$Q_\mathrm{L} = \begin{pmatrix} u_\mathrm{L} \\ d_\mathrm{L} \end{pmatrix}$	**3**	**2**	$\begin{pmatrix} +\frac{1}{2} \\ -\frac{1}{2} \end{pmatrix}$	$+\frac{1}{6}$	$\begin{pmatrix} +\frac{2}{3} \\ -\frac{1}{3} \end{pmatrix}$
Up-quark singlet	u_R	**3**	**1**	$+\frac{2}{3}$	$+\frac{2}{3}$	$+\frac{2}{3}$
Down-quark singlet	d_R	**3**	**1**	$-\frac{1}{3}$	$-\frac{1}{3}$	$-\frac{2}{3}$
Lepton doublet	$L_\mathrm{L} = \begin{pmatrix} \nu_\mathrm{L} \\ e_\mathrm{L} \end{pmatrix}$	**1**	**2**	$\begin{pmatrix} +\frac{1}{2} \\ -\frac{1}{2} \end{pmatrix}$	$-\frac{1}{2}$	$\begin{pmatrix} 0 \\ -1 \end{pmatrix}$
Lepton singlet	e_R	**1**	**1**	0	-1	-1
Gluon field	G^a_μ	**8**	**1**	0	0	0
Weak gauge field	$W^i_\mu = \begin{pmatrix} W^+_\mu \\ W^-_\mu \\ W^3_\mu \end{pmatrix}$	**1**	**3**	$\begin{pmatrix} +1 \\ -1 \\ 0 \end{pmatrix}$	0	$\begin{pmatrix} +1 \\ -1 \\ 0 \end{pmatrix}$
Hypercharge field	B_μ	**1**	**1**	0	0	0
Higgs doublet	$\Phi = \begin{pmatrix} \phi^+ \\ \phi^0 \end{pmatrix}$	**1**	**2**	$\begin{pmatrix} +\frac{1}{2} \\ -\frac{1}{2} \end{pmatrix}$	$+\frac{1}{2}$	$\begin{pmatrix} +1 \\ 0 \end{pmatrix}$
Conjugate Higgs doublet	$\Phi^\mathrm{c} = \begin{pmatrix} \phi^{0*} \\ \phi^- \end{pmatrix}$	**1**	**2**	$\begin{pmatrix} +\frac{1}{2} \\ -\frac{1}{2} \end{pmatrix}$	$-\frac{1}{2}$	$\begin{pmatrix} 0 \\ -1 \end{pmatrix}$

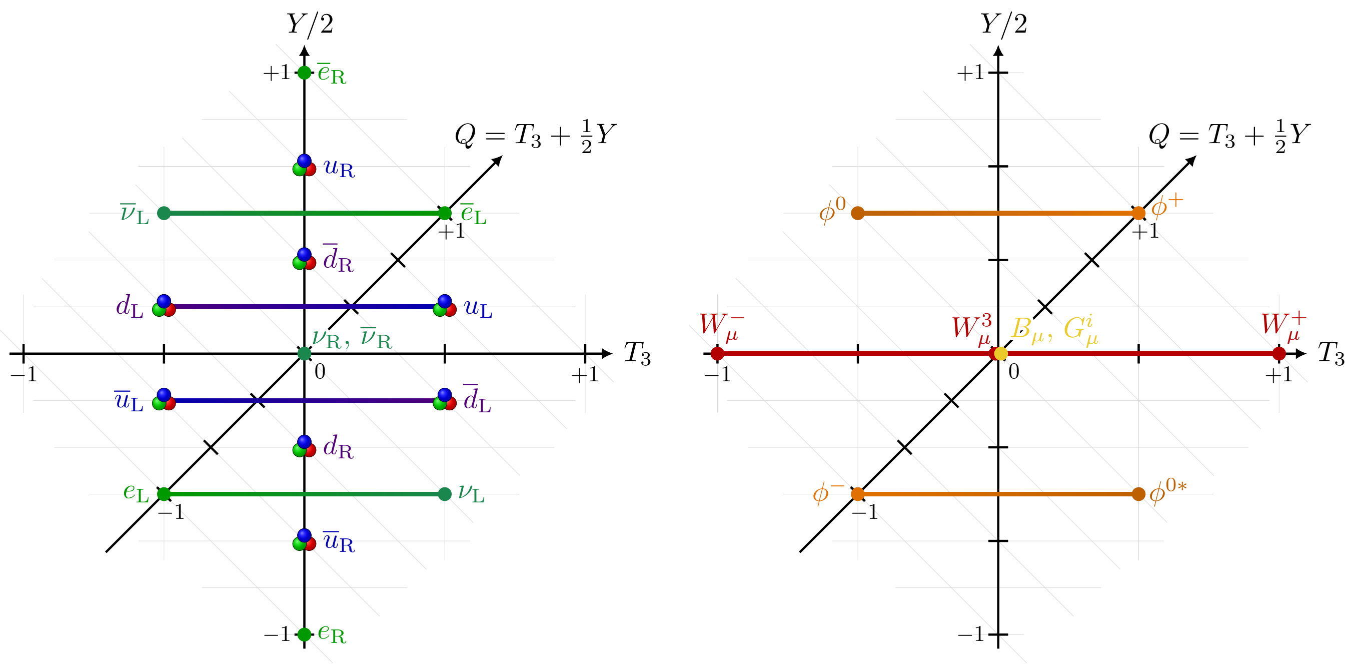

Figure 2.4: Graph of the $\mathrm{SU}(2)_\mathrm{L} \times \mathrm{U}(1)_\mathrm{Y}$ quantum numbers $(T_3, Y/2)$ of the fermion (left) and boson (right) fields in the SM. The quarks are shown as a color triplet (red, blue, green). Note that right-handed neutrinos ν_R are not included in the SM.

As mentioned above, the gauge group is spontaneously broken due to the nonzero Higgs vev. Through the Higgs mechanism, the gauge bosons acquire mass and mix into the mass eigenstates

$$W_\mu^\pm = \frac{W_\mu^1 \mp iW_\mu^2}{\sqrt{2}}, \quad Z_\mu = W_\mu^3 \cos\theta_{\mathrm{W}} + B_\mu^3 \sin\theta_{\mathrm{W}}, \quad A_\mu = W_\mu^3 \sin\theta_{\mathrm{W}} - B_\mu^3 \cos\theta_{\mathrm{W}}, \tag{2.9}$$

where $W_\mu^\pm$ are the charged W boson fields, Z_μ is the neutral Z boson field, A_μ is the photon field, and θ_{W} is the Weinberg angle given by $\sin\theta_{\mathrm{W}} = g'/\sqrt{g^2 + g'^2}$. After mixing, the new covariant derivative becomes

$$D_\mu = \partial_\mu + ig_{\mathrm{s}} t_a G_\mu^a + i\frac{g}{\sqrt{2}} T^+ W_\mu^+ + i\frac{g}{\sqrt{2}} T^- W_\mu^- + i\frac{g}{\cos\theta_{\mathrm{W}}} \left(T_3 - \sin^2\theta_{\mathrm{W}}\, Q\right) Z_\mu + ieQA_\mu, \tag{2.10}$$

such that the ladder operators $T^\pm = T_1 \pm iT_2$ couple up-type quarks to down-type anti-quarks and vice versa in the charged weak interaction. The photon field A_μ is the gauge field that belongs to $\mathrm{U}(1)_{\mathrm{EM}}$ with coupling strength e, and gives rise to the conserved quantity $Q = T_3 + Y/2$, which is familiar as the electric charge.

2.2.2 The Yukawa sector

In order to explain mass of the fermions, we need to add *Dirac mass terms*, which are of the form

$$-m\overline{\psi}\psi = -m\left(\overline{\psi}_{\mathrm{R}}\psi_{\mathrm{L}} + \overline{\psi}_{\mathrm{L}}\psi_{\mathrm{R}}\right), \tag{2.11}$$

where ψ is a full Dirac spinor, and $\psi_{\mathrm{L}} = \frac{1}{2}(1-\gamma^5)\psi$ and $\psi_{\mathrm{R}} = \frac{1}{2}(1+\gamma^5)\psi$ with $\gamma^5 = i\gamma^0\gamma^1\gamma^2\gamma^3$ are its left- and right-handed projections, respectively. However, this term cannot be gauge invariant under $\mathrm{SU}(2)_{\mathrm{L}}$ because it mixes fields of different chirality. As is the case for the gauge bosons, the solution is to use the SSB of the Higgs sector. Following the previously mentioned conditions for terms in the Lagrangian, one can include the following interaction terms between a complex Higgs doublet Φ and fermions:

$$\mathcal{L}_{\mathrm{Yukawa}} = -Y_d^{fg}\overline{Q}_{\mathrm{L}}^f \Phi d_{\mathrm{R}}^g - Y_u^{fg}\overline{Q}_{\mathrm{L}}^f \Phi^{\mathrm{c}} u_{\mathrm{R}}^g - Y_e^{fg}\overline{L}_{\mathrm{L}}^f \Phi e_{\mathrm{R}}^g + \text{h.c.}, \tag{2.12}$$

with the conjugate Higgs doublet $\Phi^{\mathrm{c}} = i\sigma_2\Phi^\dagger$, and unitary Yukawa matrices Y_d^{fg}, Y_u^{fg}, Y_e^{fg} that mix the fermion generations in generation space U(3). As Φ is a scalar field that forms a weak isospin doublet,

$$\Phi = \begin{pmatrix} \phi^+ \\ \phi^0 \end{pmatrix}, \tag{2.13}$$

the terms (2.12) are manifestly Lorentz and gauge invariant, and have mass dimension four. The Higgs-fermion interactions are not obtained through the gauge principle, and as a consequence, the Yukawa matrices are unitary matrices that can generally mix the various flavors and introduce CP violation.

Because the Higgs vev is nonzero, we can fix the $\mathrm{SU}(2)_{\mathrm{L}}$ gauge. It is convenient to choose the unitary gauge

$$\Phi = \frac{1}{\sqrt{2}}\begin{pmatrix} 0 \\ v + h \end{pmatrix}, \tag{2.14}$$

with the vev $v \approx 246\,\mathrm{GeV}$, a real constant, and the neutral Higgs field h, a (real) scalar.

Therefore, after SSB, we are left with

$$\mathcal{L}_{\text{Yukawa}} = -\frac{Y_d^{fg}}{\sqrt{2}}\overline{d}_{\text{L}}^f(v+h)d_{\text{R}}^g - \frac{Y_u^{fg}}{\sqrt{2}}\overline{u}_{\text{L}}^f(v+h)u_{\text{R}}^g - \frac{Y_e^{fg}}{\sqrt{2}}\overline{e}_{\text{L}}^f(v+h)e_{\text{R}}^g + \text{h.c.} \tag{2.15}$$

In the next section, we will see how the Yukawa matrices can be diagonalized to obtain the mass eigenstates with mass coefficients of the form $m^f = vY^{ff}/\sqrt{2}$.

The SM assumes that neutrinos are massless. Nevertheless, the observation of neutrino oscillations imply that neutrinos do have mass [49]. The problem with the Dirac mass terms (2.11) is that it is not known if right-handed neutrinos exist. Alternately, if one assumes the neutrino is its own antiparticle, one could build a *Majorana mass term* from a different combination with the Higgs field without a right-handed neutrino, but the resulting local operator would be of mass dimension five, making it nonrenormalizable [56].

2.2.3 Flavor symmetry

To construct the SM Lagrangian, we started from the general conditions of Lorentz invariance, gauge invariance under $\text{SU}(3)_\text{C} \times \text{SU}(2)_\text{L} \times \text{U}(1)_\text{Y}$, and renormalizability, after which we put in all the particle content Eq. (2.7) observed in experiment. With just these assumptions, we find that the SM has more symmetries that were not imposed beforehand. These symmetries are therefore called *accidental*. In particular, the gauge sector (2.6) by itself is highly symmetric. Without changing the physics of this sector, one can perform unitary transformations within the three generation of each fermion type

$$\psi_f \to \psi'_f = U^{fg}\psi_g, \tag{2.16}$$

where $U_{gf} \in \text{U}(3)$ is a unitary matrix with 3×3 generational indices. Because there are five fermion fields, the gauge sector therefore has a very large global $G_{\text{gauge}}^{\text{global}} = \text{U}(3)^5$ symmetry [57, 58]. Each U(3) group can be decomposed into $\text{SU}(3) \times \text{U}(1)$:

$$G_{\text{gauge}}^{\text{global}} = \text{SU}(3)_{Q_\text{L}} \times \text{SU}(3)_{d_\text{R}} \times \text{SU}(3)_{u_\text{R}} \times \text{SU}(3)_{L_\text{L}} \times \text{SU}(3)_{e_\text{R}} \tag{2.17}$$

$$\times\, \text{U}(1)_{Q_\text{L}} \times \text{U}(1)_{d_\text{R}} \times \text{U}(1)_{u_\text{R}} \times \text{U}(1)_{L_\text{L}} \times \text{U}(1)_{e_\text{R}}, \tag{2.18}$$

such that each SU(3) represents a transformation in generation space,

$$Q_\text{L}^f \to V_Q^{fg}Q_\text{L}^g, \quad u_\text{R}^f \to V_u^{fg}u_\text{R}^g, \quad d_\text{R}^f \to V_d^{fg}d_\text{R}^g, \quad L_\text{L}^f \to V_L^{fg}L_\text{L}^g, \quad e_\text{R}^f \to V_e^{fg}e_\text{R}^g, \tag{2.19}$$

with special unitary matrices $V^{fg} \in \text{SU}(3)$, whereas each U(1) is a simple complex phase rotation.

There is no reason that these global symmetries should hold generally. Indeed, the structure of the Yukawa sector (2.12) explicitly breaks a large part of these symmetries, because the Yukawa matrices can mix the different flavors if there is no global flavor symmetry imposed. Such a global symmetry would require the Yukawa matrices to be proportional to the identity matrix, implying the each generation would all have the same mass. This is evidently not the case, as the fermion masses are different and span several orders of magnitude. $G_{\text{gauge}}^{\text{global}}$ is thus not a good symmetry of the SM because of the Yukawa sector, and it gets explicitly broken to

$$G_{\text{gauge}}^{\text{global}} \xrightarrow{\text{Yukawa}} G_{\text{SM}}^{\text{global}} = \text{U}(1)_\text{B} \times \text{U}(1)_\text{e} \times \text{U}(1)_\mu \times \text{U}(1)_\tau, \tag{2.20}$$

where the first factor indicates the conservation of baryon number B, while the last three factors denote the conservation of the number of each individual lepton flavor L_{e}, L_{μ}, L_{τ}, which add up to the total lepton number L [59, 60]. Note that these symmetries, which are observed experimentally (see Sections 2.1.3 and 2.1.8), emerge naturally from the formulation of the SM.

Although the SU(3) factors in Eq. (2.17) are not a symmetry of the SM, they can still be used for a change of basis in which the Yukawa matrices are diagonal. For leptons, one can find transformations V_L, $V_e \in \mathrm{SU}(3)$ such that the Yukawa matrix becomes

$$Y_e \to V_L Y_e V_e^\dagger = \mathrm{diag}(y_e, y_\mu, y_\tau), \tag{2.21}$$

with y_f real and positive [62]. This is the mass basis for charged leptons with masses $m_f = vy_f/\sqrt{2}$. These transformations still cancel in the gauge sector, so lepton generations do not mix in the SM. This corresponds to the conservation of the individual lepton flavors. Since neutrino oscillations have been observed to occur in Nature, it is clear that lepton flavor is actually not a conserved quantity. And in addition, conversation of the total lepton number is violated by anomalies due to nonperturbative effects at the quantum level [60, 62, 63]. Still, both these effects are extremely suppressed for processes involving the charged leptons [64–67]. Two examples of lepton-flavor violating decays are shown in Fig. 2.5. Therefore, $\mathrm{U}(1)_{\mathrm{e}} \times \mathrm{U}(1)_{\mu} \times \mathrm{U}(1)_{\tau}$ is still an excellent approximate symmetry. Furthermore, leptons are treated equally by each of the gauge interactions, which is referred to as *lepton flavor universality* (LFU). The violation of LFU in observables like production cross sections or decay rates would be a clear hint of new physics beyond the SM.

For quarks, there are two Yukawa matrices, but only three independent transformations available. It is a common convention to make Y_d diagonal while factorizing Y_u into a unitary and real diagonal matrix so that

$$Y_d \to V_Q Y_d V_d^\dagger = \mathrm{diag}(y_d, y_s, y_b), \tag{2.22}$$

and

$$Y_u \to V_Q Y_u V_u^\dagger = V_{\mathrm{CKM}}^\dagger \mathrm{diag}(y_u, y_c, y_t), \tag{2.23}$$

where $m_f = vy_f/\sqrt{2}$ are the quark masses, and V_{CKM} is the CKM matrix introduced in Section 2.1.5. Most generally, V_{CKM} is a unitary matrix with three real angles and six complex phases, but thanks to the residual flavor symmetry, one can still rotate the phases of the six quark flavors to eliminate five out of six complex phases. This leaves the V_{CKM} with just four physical parameters: three real angles that mix the up-type quarks, and one complex phase that introduces CP violation [56, 62]. Note that if there were only two generations, there would only be one mixing angle, and no complex phase causing CP violation, like in the Cabibbo matrix (2.2). To obtain a full quark mass basis with both Y_d and Y_u diagonal, one can redefine the up-type components of the quark doublets, such that V_{CKM} is moved to the gauge sector,

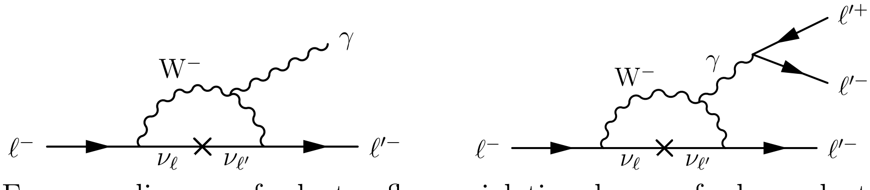

Figure 2.5: Feynman diagrams for lepton flavor violating decays of a heavy lepton, $\ell^- \to \ell^- \gamma$ and $\ell^- \to \ell^- \ell^- \ell^+$, if one adds neutrino masses to the SM. These are extremely suppressed due to the small neutrino masses, with a branching fraction that is several orders of magnitude less than 10^{-50} [61].

where it will only appear in the charged weak interactions in Eq. (2.10). The electromagnetic and strong interactions will still conserve the C, P, T, and flavor symmetries thanks to their structure (2.10) and the unitarity of the CKM matrix. The neutral weak interaction through Z-boson exchange violates C and P, but it still respects CP and flavor conservation. Therefore, decays with *flavor-changing neutral currents* (FCNCs) in the SM can only happen at loop-level involving W-boson exchange. Besides being at loop level at LO, the rates of such decays will also be heavily suppressed by the GIM mechanism, which makes them a good probe for testing the SM, as it would be more sensitive to new physics.

If one extends the SM with nonzero neutrino masses, it is necessary to introduce the PMNS matrix to explain neutrino oscillations. This extended SM has twelve fermion masses, six mixing angles, and two CP phases emerging from the Yukawa sector, which makes up 20 of the 26 parameters of the SM, which need to be experimentally determined. So most of the SM free parameters come from the Yukawa sector. Moreover, the pattern of the fermion masses appears very hierarchical across the generations, spanning several orders of magnitude. At the same time, while CKM matrix has nontrivial mixing of quark generations, it is not too far off from the identity matrix. This begs the question why matter comes in three generations, and what mechanism can explain the pattern of mass and mixing. The mass hierarchy could suggest that new physics somehow prefers the higher generations, which motivates studying physics that involve τ leptons, bottom or top quarks.

In summary, the gauge sector is highly flavor-symmetric, and the only source of flavor mixing and CP violation in the SM comes from the the Yukawa sectors. Additionally, we can tell apart the different flavors through their Yukawa couplings to the Higgs and therefore their masses. Good ways to test the SM is in observables where we expect strict LFU, or to look for decays violating charged lepton flavor [68].

2.3 The physics of proton-proton collisions

Modern particle physics has long used particle accelerators to study Nature in a controlled experiment. By colliding two beams of particles head-on, or letting a beam hit a fixed target, we can create interactions at higher energies and thereby probe physics at smaller scales. In this way, we can test the predictions of the SM and look for new phenomena. The largest and most powerful collider today is the LHC, which accelerates two proton beams up to record energies and collides them head-on inside of four large detectors. The LHC will be described in a later chapter.

2.3.1 The proton substructure

Unlike leptons and quarks, which are elementary particles (as far as we know), protons are composite particles. Protons are a bound state between quarks and gluons. The substructure of the proton has been carefully studied in deep inelastic scattering (DIS) experiments at SLAC [70, 71] and DESY [72], which collided electrons or positrons with protons. If large enough momentum is transferred between the proton and a colliding particle, the proton will break apart into secondary hadrons. These experiments showed that at the short distance scale, or equivalently short time scale, of DIS, one can treat protons as a loosely bound group of constituents. The constituents are referred to as *partons*. This is a consequence of *asymptotic freedom* in QCD, which follows from the non-Abelian nature of $\mathrm{SU}(3)_\mathrm{C}$, which means that gluons

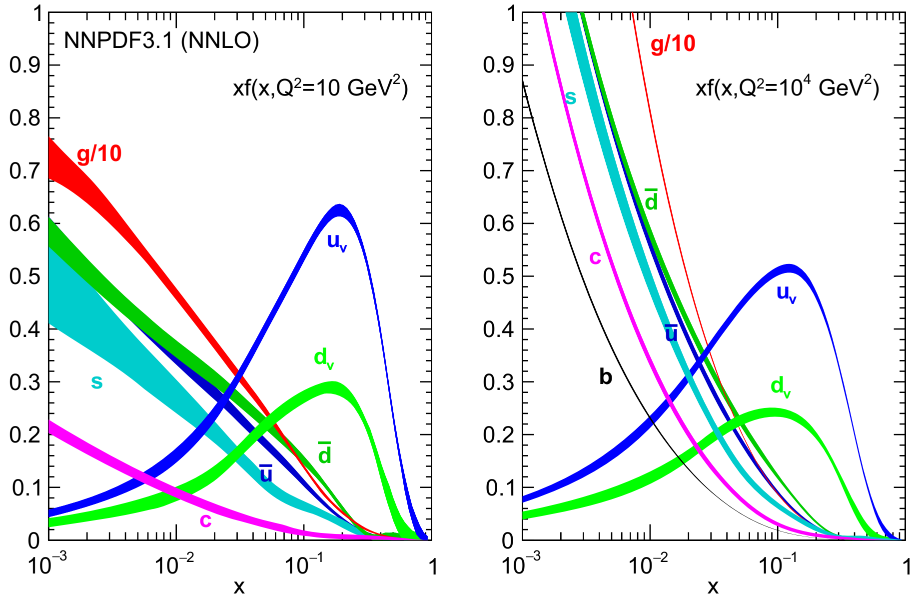

Figure 2.6: Plot of the proton PDF $f_p(x,Q^2)$ times the momentum fraction x as calculated by NNPDF3.1 at NNLO accuracy in perturbation theory for $Q^2 = 10\,\mathrm{GeV}^2$ (left) and $Q^2 = 10^4\,\mathrm{GeV}^2$ (right). Adapted from [69].

are self-interacting. To a good approximation, the scattering in such a collision happens with just a single parton to which all the momentum is transferred, while ignoring its interactions with the other constituents in the proton. The partons are either quarks or antiquarks with fractional electrical charge and spin 1/2, or electrically neutral gluons with spin 1.

In the parton model, *parton distribution functions* (PDFs) describe the probability of finding a parton of type p with momentum fraction x in a collision at some momentum scale Q as a function of the form $f_p(x,Q^2)$ [73–77]. The proton can be thought of as a bound state involving two up and one down quark, called *valence quarks*, plus an admixture of quark-antiquark pairs, called *sea quarks*, which are created by quantum fluctuations from the strong QCD fields present in the proton. To reflect the proton quantum numbers, the PDFs of the up- and down-type (anti)quarks are normalized so that, for any given Q^2,

$$\int_0^1 \left[f_\mathrm{u}(x,Q^2) - f_{\bar{\mathrm{u}}}(x,Q^2)\right] \mathrm{d}x = 2, \quad \int_0^1 \left[f_\mathrm{d}(x,Q^2) - f_{\bar{\mathrm{d}}}(x,Q^2)\right] \mathrm{d}x = 1, \tag{2.24}$$

while all others must be zero.

The PDFs can be extracted in different ways from experimental data (mainly DIS) [76]. One such set of PDFs that has been used in the simulation of proton collisions and is calculated at next-to-next-leading order (NNLO) accuracy in perturbation theory is shown in Fig. 2.6. Notice that the PDFs attributed to quarks heavier than the up and down quark are nonnegligible, especially at higher Q^2. This contribution is noteworthy, because it makes processes with bottom quarks in the initial state, like the signal model of this thesis, also possible. Still, the PDFs of heavier quarks are considerably suppressed. While at high Q^2, heavy-quark PDFs become more important, another considerable source is *gluon splitting* $g \to q\bar{q}$, where a gluon "splits" into a quark-antiquark pair. This will add an extra parton to the final state, although it tends to be softer and more forward.

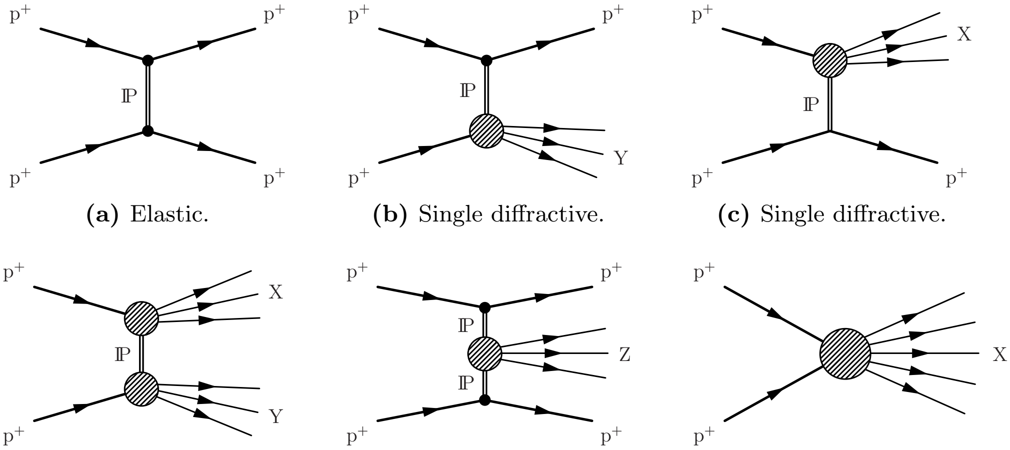

(a) Elastic. (b) Single diffractive. (c) Single diffractive.
(d) Double diffractive. (e) Central diffractive. (f) Nondiffractive.

Figure 2.7: The dominant processes in proton-proton collisions: Elastic and inelastic scattering at leading order. The inelastic processes can be further divided into diffractive (about 25%) and nondiffractive (75%) [78].

2.3.2 Proton-proton collisions at the LHC

Most of the times when the proton beams cross in the LHC, little of interest happens. Even with the record beam intensities that the LHC provides, most of the protons in the beams do not interact. When they do, they exchange only small amounts of momentum and gain only small momentum in the transverse direction. This is called *soft scattering* and corresponds to long-distance interactions. The total cross section of pp collisions at 13 TeV has been measured to be roughly $\sigma_{\mathrm{pp}}^{\mathrm{tot}} \approx 100\,\mathrm{mb}$, where $1\,\mathrm{barn} = 100\,\mathrm{fm}^2$, or $10^{-28}\,\mathrm{m}^2$. The main contributions are elastic scattering where both protons stay intact, and inelastic scattering, where at least one proton breaks up in the interaction. Elastic scattering makes up approximately 25% of the total cross section, while inelastic scattering, 75%. These results at 13 TeV are reported in Ref. [79–81]. The inelastic processes can be further divided into diffractive and nondiffractive [78]. Diffractive processes are not understood from first principles by the current theory of the strong interaction, QCD, because these interactions cannot be calculated perturbatively. Instead, Regge Theory [82–84] is used. In this framework a colorless object called the *Pomeron*, carries the transferred momentum between the protons. All of these types of interactions are shown in Fig. 2.7.

To measure electroweak processes, study the Higgs boson, or search new physics, however, one is interested in pp collisions with a *hard process*, where two partons directly exchange a large amount of momentum. This kind of process is illustrated in Fig. 2.8, where the right diagram shows a concrete example of the Drell-Yan process, in which a fermion-antifermion pair are created through quark-antiquark annihilation. Just as in DIS, the hard process will happen at time scales much shorter than those of the strong interactions between the proton's constituents. Therefore, the PDFs from lepton-proton data can be used for each of the two proton to quantify the probability of finding these partons. This follows from the factorization theorem [85, 86], which provides a formula to calculate the cross sections of a hard process with an integral of the form

$$\sigma(\mathrm{pp} \to X + Y) = \sum_{i,j} \int_0^1 \int_0^1 f_i(x_1, Q^2) f_j(x_2, Q^2) \hat{\sigma}_{ij\to X}(x_1, x_2, Q^2)\,\mathrm{d}x_1\,\mathrm{d}x_2\,, \tag{2.25}$$

where $\sigma_{ij\to X}(x_1, x_2, Q^2)$ is the parton-level cross section of the hard process, $i + j \to X$, and parton i (j) carries a fraction x_1 (x_2) of the momentum of its mother proton. Fig. 2.9 compares

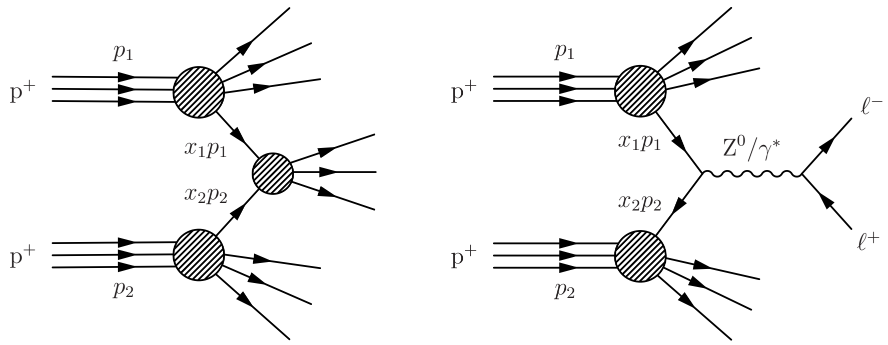

Figure 2.8: Left: Feynman diagrams of a pp collision with a generic hard process represented by a blob in the middle. The groups of three lines coming from the left represent the proton with its substructure. The hard process is effectively a collision of two partons $i = 1, 2$ emerging from each proton and carrying a fraction x_i of their mother proton's total momentum p_i [75]. The rest of the proton becomes debris, and continues along the beamline. **Right**: Simple example of a hard process: Drell-Yan at tree level, which involves a virtual photon γ^* or Z boson from quark-antiquark annihilation creating a lepton-antilepton pair.

the theoretical cross sections of some of the main processes for different center-of-mass energies $\sqrt{s}$. Notice the orders of magnitude difference between the hard processes and the total cross section. Hard processes make up a tiny fraction of the inelastic processes, show in Fig. 2.7f. Figure 2.10 compares the predicted and measured cross sections of several SM processes involving the production of top quarks as measured by CMS at $\sqrt{s} = 7$, 8, and 13 TeV.

Collisions with hard processes are characterized by a large momentum exchange of more than a few GeV between the protons [89]. The remnants of the protons will mostly disappear in the beamline, while particles created in the hard process will typically have relatively large transverse momenta, such that they transverse the geometric acceptance of the detector. Therefore, pp collision *events* are often selected based on the presence of particles with large transverse momenta, instead of just the total momentum p_i. In this way, they can be distinguished from uninteresting soft scattering.

The production of particles in the hard process will be boosted along the z-direction. This is because typically only one *parton* (quark or gluon) emerges from each proton to take part in the main collision process. Each parton will carry some fraction x_i of that hadron's total momentum, which is almost completely in the z-direction. The boost will therefore depend on their difference in momentum (see Fig. 2.8). This means that the total momentum of the hard collision in the transverse plane should be zero, while the boost in the z direction will be unknown if some part of the momentum is carried away by invisible particles not captured by the detector, or if multiple simultaneous collisions obscure the final state particles necessary to reconstruct the boost.

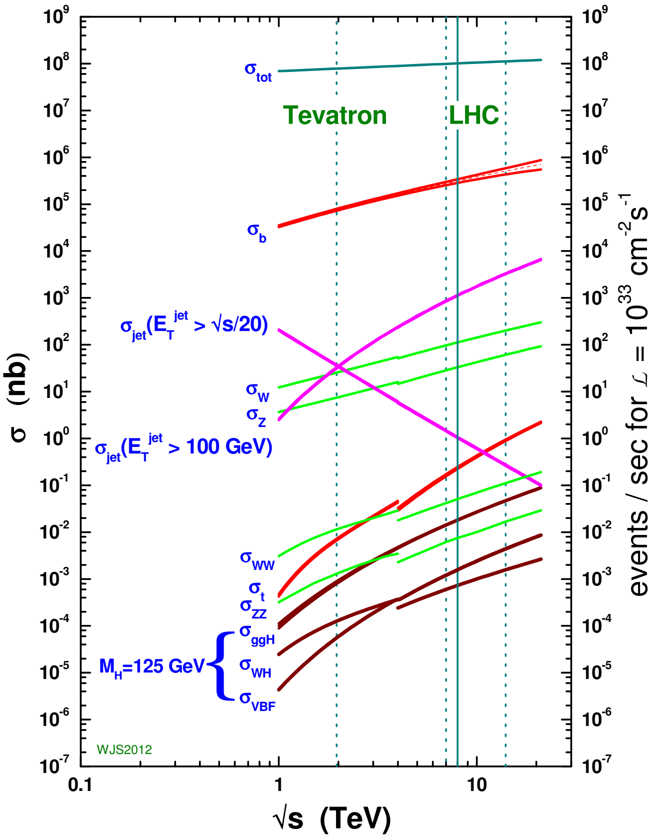

Figure 2.9: Plot of the most common processes in proton-proton collisions and their cross sections numerically calculated at NLO or NNLO accuracy in perturbation theory of QCD with MSTW2008 PDFs [77]. Taken from [87].

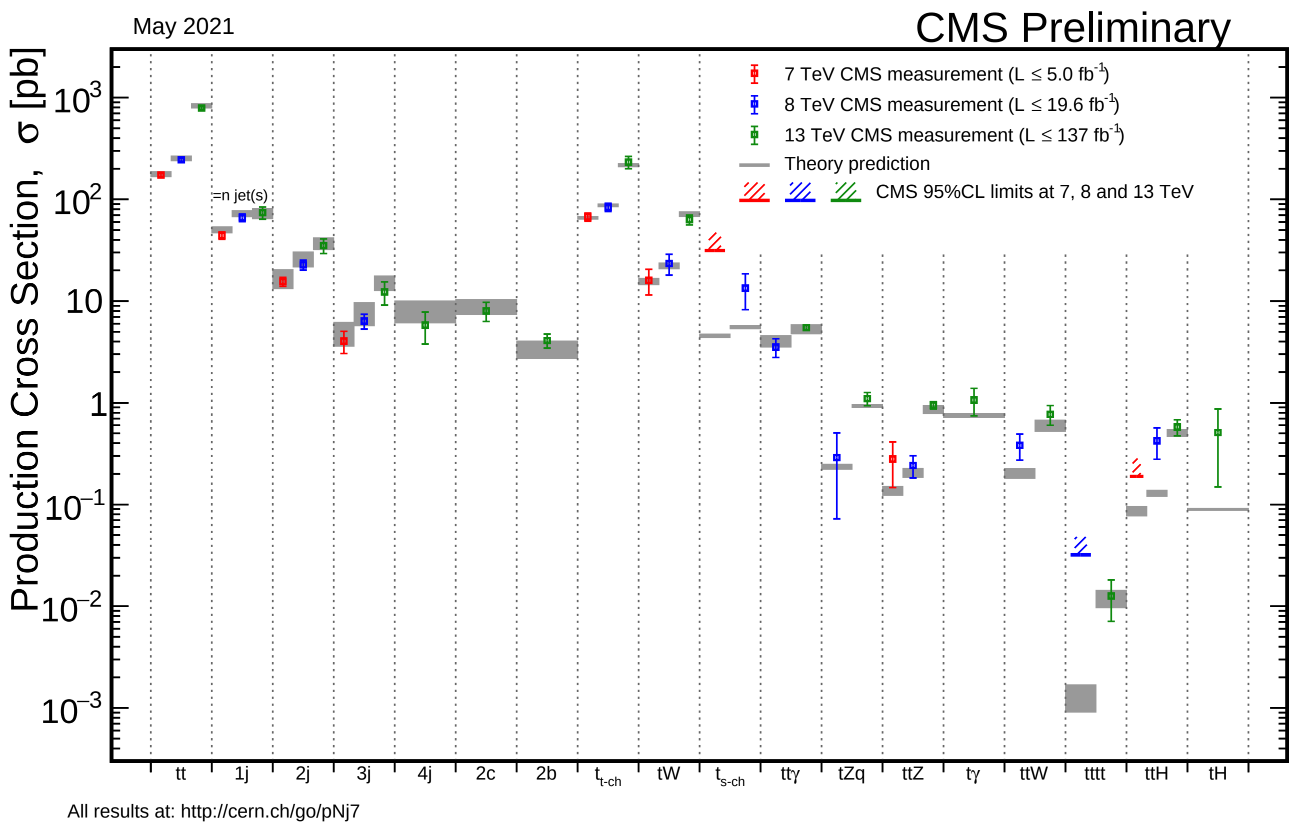

Figure 2.10: Predicted and measured cross sections for a variety of SM processes wherein one or more top quarks are produced in pp collisions at center-of-mass energies of $\sqrt{s}$ = 7, 8, and 13 TeV, as measured by the CMS Collaboration. The x axis denotes the process. The cross section for the production of a pair of top quarks ($t\bar{t}$) is shown inclusively, as well as separately for production with additional jets (j), bottom quark (b), or charm quark (c). "s-ch" and "t-ch" refer to s-channel or t-channel production of a single top quark, respectively. Taken from [88].

3 Beyond the Standard Model

The SM of particle physics is remarkably successful in describing matter and its fundamental interactions. The mathematical theory behind the SM provides some of the most precise predictions, which have been confirmed with tests of unprecedented precision. The strength of the electromagnetic force given by the fine-structure constant $\alpha = e^2/4\pi$ for example, has been calculated with up to twelve digits and agrees with measurement up to ten [90–93]. In 2012, the discovery of a major missing piece, the Higgs boson was announced by the ATLAS and CMS experiments at the CERN LHC [37–40], more than 47 years after its prediction [35, 36]. Despite its many successes, there are both theoretical and experimental reasons that imply the SM is not complete and is not the final and most fundamental theory of nature. The following section highlights several examples of open questions in physics. After that, Section 3.2 will discuss tests of LFU. Finally, a possible solution for some anomalous experimental measurements is proposed in Section 3.4

3.1 Shortcomings of the Standard Model

Most obviously, the SM does not offer a description for gravity. The SM can explain very well and predict behavior of the electromagnetic, weak, and strong interactions at the energy scales we have covered in experiments so far. At these same scales, gravity is many orders of magnitude weaker than the weak interaction, and its effects are therefore neglected at the scales probed by the SM. Quantum effects of gravity are expected to play a role at the Planck scale $\Lambda_{\text{Planck}} = 1.22 \times 10^{19}$ GeV, which is many orders of magnitude higher than what current particle accelerators can achieve, as shown in Fig. 3.1. The big question that remains is if gravity can be quantized like the other interactions, which would imply the existence of a force-carrying particle called the graviton. To be consistent with Einstein's theory of relativity, this new particle should be a massless boson with spin-2. However, there is no clear path to fit it consistently in a QFT like that of the SM, because one quickly runs into issues of renormalization when performing perturbative calculations. This might indicate the need of a new mathematical framework that supersedes QFT. One such candidate is string theory.

The last chapter already mentioned that the SM assumes neutrinos are massless. There are several possibilities to add neutrino mass terms to the SM Lagrangian, but the exact nature of neutrinos has yet to be revealed by experiment.

Another theoretical puzzle is the so-called *strong CP-problem*. In the most general Lorentz and gauge-invariant SM Lagrangian, one would also expect a CP-violating term in the gauge sector (2.6) coming from the gluon fields. Nevertheless, CP violation has only been observed in weak interactions so far, and there is no confirmed reason why strong interactions should respect CP symmetry [62].

One glaringly missing piece in the SM is *dark matter*. From astronomical observations, it appears that there exists about five times more matter than the kinds that are part of the SM [95–97]. Independent pieces of evidence for this unknown kind of matter include inconsistencies in

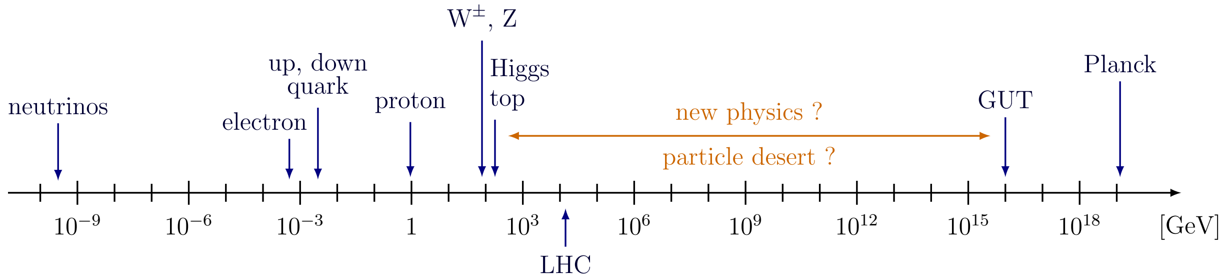

Figure 3.1: Logarithmic scale of different energy scales in particle physics. Some particle masses $m = E/c^2$ are indicated for reference. The SM reaches approximately up to the top quark mass. New physics may appear at the LHC around the TeV scale. If not, a *particle desert* may lie ahead with no new physics until the scale of a Grand Unification Theory (GUT), where the SM interactions are expected to unify [94]. Beyond the GUT scales lies the Planck scale where quantum gravitational effects are expected to become important.

the rotation curves of galaxies [98, 99], the localization of matter through lensing in the Bullet Cluster [100, 101], and the precise measurement of the angular power spectrum of the cosmic microwave background (CMB) [95, 96]. If this is indeed a new type of matter, the big question is how it interacts with "normal" SM matter, if at all. There are many experiments that try to find evidence of such interactions, including dedicated dark matter detectors, as well as searches in proton-proton collision data at the ATLAS & CMS experiments.

The same measurements of the CMB point to another big conundrum. They found that 68.3% of the energy content in the observable universe is an unknown form of energy, referred to as *dark energy*. In the standard model of cosmology, this type of energy is expressed as the cosmological constant, and can be ascribed to the vacuum energy which uniformly permutes all of space. While the SM offers amazingly precise agreement with the measured electron magnetic moment, the calculation of the energy density of the vacuum presents one of the worst quantitative predictions in physics: It underestimates the observed value by up to 120 orders of magnitude [102]. This is a huge discrepancy that needs to be investigated.

For the reasons mentioned above and more, the SM clearly cannot be the end of the story, and physicists need to look for a new fundamental theory of Nature. There are many extensions of the SM and full new theories that have been proposed. Such models often predict new particles that can be directly produced in high-energy collisions, such as those at the Large Hadron Collider (LHC). While the discovery of such a new particle would be clear-cut and exciting evidence of new physics, the new hypothetical particles may be too heavy or weakly coupled to discover with present colliders or data sets, and it is not always clear in what phase space to explore without making model-dependent assumptions. In the case of no discovery, it is still possible to put exclusion limits on model parameters like coupling and mass to constrain the model. Complementary to direct searches, physicists are looking for indirect evidence of new physics by precisely measuring physical observables that can be be calculated in the SM in order to find any notable deviations from SM predictions. Such observables are typically total, fiducial, and differential cross sections and decay rates. These directions of research can also offer a systematic and model-independent way of probing beyond the SM. One popular framework for this is that of the EFT, which will be discussed in Section 3.3.

Section 2.2.3 argues that the observation of LFU violation (LFUV) or lepton flavor violation (LFV) in Nature would be a clear sign of physics beyond the SM. Physicists have looked directly for LFV decays, but found no evidence so far. Strong limits have been set on forbidden decays of the muon [103, 104], the τ lepton [105], B hadrons [106–109], and quarkonia [110], but also on leptonic decays of Z and Higgs bosons [111] that violate lepton flavor. In the next decade, several experiments could reach sensitivity to decay rates predicted by some new physics models [105, 112, 113]. For testing LFU in the SM, it is important to precisely measure ratios of decay rates or production cross sections. Some signs of LFUV have in fact emerged in the semileptonic decays of B hadrons, which the next section will present in more detail. Other discrepancies that could hint at LFUV have been found in the anomalous magnetic momentum of the muon. Combined, they deviate with respect to the SM with a significance of 4.2 standard deviations [114, 115], although some of the discrepancy could be related to theoretical predictions for the hadronic vacuum polarization [116–118]. These flavor anomalies could be explained by models that hypothesize the existence of a new type of particle called the leptoquark (LQ). Section 3.4 will introduce the basic phenomenology of LQs, which motivates the search presented in this thesis.

3.2 Tests of lepton flavor universality

LFU has been experimentally confirmed in numerous decays at both low and high energy [119]. The most stringent tests of the universality between electrons and muons (e/μ universality) in charged currents come from the measurement of the decay rates of leptonic decays of the pion and kaon

$$R^{h}_{\mathrm{e}/\mu} = \frac{\Gamma\left(h^- \to \mathrm{e}^- \overline{\nu}_{\mathrm{e}}\right)}{\Gamma\left(h^- \to \mu^- \overline{\nu}_{\mu}\right)}, \tag{3.1}$$

with $h = \pi$, K, and where the inclusion of charge-conjugated decays is implied. This ratio can be calculated down to a precision of 10^{-4}, because the dynamics of strong interactions cancel out to a first approximation, and only appear in the electroweak corrections [119]. The values $R^{\pi}_{\mathrm{e}/\mu}$ and $R^{\mathrm{K}}_{\mathrm{e}/\mu}$ are measured with a precision of around 0.2% [22, 120, 121], and are in excellent agreement with the SM. Additionally, the ratio of $\Gamma\left(\mathrm{K}^- \to \pi\ell^-\overline{\nu}_\ell\right)$ from semileptonic kaon decays show similar agreement [119, 122].

Other strong bounds on e/μ universality in charged currents are obtained from the ratio of the fully leptonic decays of the τ lepton [119, 123]. Similarly, stringent constraints on μ/τ universality have been set by a comparison of the decays of the muon and τ lepton to an electron plus neutrinos, as well as by the decays $\tau^- \to h^-\overline{\nu}_\tau$ and $h^- \to \mu^-\overline{\nu}_\mu$, again with $h = \pi$, K. Moreover, the comparison of τ-lepton decays to muons and muon decays to electrons has tested e/τ universality to almost 0.1% precision.

The BESIII Collaboration has also been able to confirm LFU in the charm sector by analyzing $\mathrm{e}^+\mathrm{e}^-$ collisions at the BEPCII, which ran at the right center-of-mass energies to produce copious amounts of J/ψ mesons and D meson pairs. Their analyses of purely leptonic J/ψ decays [124] and $\mathrm{e}^+\mathrm{e}^- \to \ell^+\ell^-$ production [125] has allowed BESIII to test LFU in neutral currents at energies around the J/ψ mass. Furthermore, they have measured decay ratios of both fully leptonic and semileptonic decays of $\mathrm{D}_{(\mathrm{s})}$ mesons [126–129].

At higher center-of-mass energies, the experiments operating at the electron-positron colliders at the SLC and LEP colliders have confirmed LFU in Z boson decays by measuring the partial widths to the level of about 0.2% [130]. The LEP experiments have also measured the branching fractions of W bosons from ee → WW production to the percent level, and reported an excess of the branching fraction $\mathcal{B}(\mathrm{W} \to \tau\overline{\nu}_\tau)$ with respect to the other leptons, that amounts to 2.6 standard deviations [131]. This has recently been resolved by both ATLAS [132] and CMS [133], who made measurements of branching fractions and their ratios with improved precision. This is shown in Fig. 3.2.

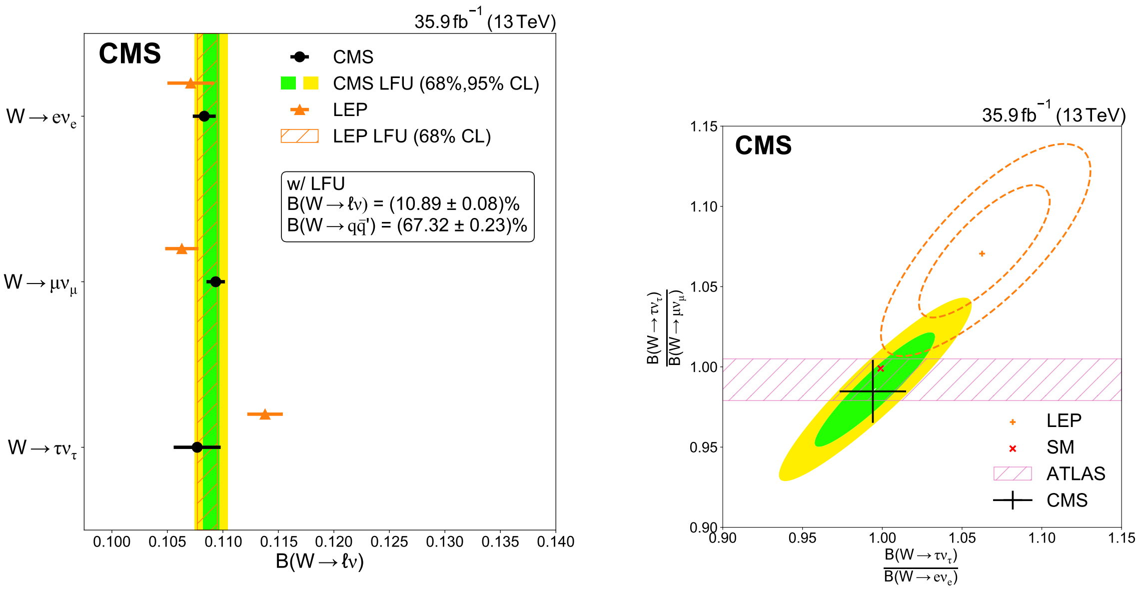

Figure 3.2: Tests of LFU in the decay of the W boson. **Left**: Measurement of the leptonic branching ratios by CMS compared to the corresponding LEP results [131] (orange). The vertical green (yellow) band shows the extracted branching fraction at a 68% (95%) confidence level (CL) assuming strict LFU. **Right**: Two dimensional comparison of the ratios of branching fraction, with results from LEP (orange point and dashed lines), ATLAS [132] (pink band), and CMS (green-yellow ellipse with the black cross as one-dimensional projections). The SM expectation is shown as a red cross. Both figures are taken from Ref. [133].

The tests discussed above involved processes with either purely leptonic transitions, or semileptonic transitions involving only the lightest two quark generations. However, several experiments that study B hadron decays have reported discrepancies with the SM predictions that could give the first hints of LFUV.

3.2.1 B anomalies

The main three experiments that have been specifically designed to study the properties and behavior of B hadron decays are BaBar, Belle, and LHCb. The BaBar experiment [134] at the PEP-II collider at SLAC in California, United States, and the Belle experiment [135] at the KEKB collider in Tsukuba, Japan are referred to as "B factories" because they have recorded e^+e^- collisions with center-of-mass energies tuned to the $\Upsilon(4S)$ resonance peak to create vast amounts of B meson pairs. The LHCb experiment [136–138], on the other hand, has one of the four large detectors at the LHC at CERN near Geneva, Switzerland, and recorded proton-proton collisions. The LHCb detector covers the very forward direction, close to the beam, to capture mainly B hadrons that are produced in QCD processes and subsequently decay in the detector. These three experiments have reported several anomalies in the rates and angular distributions of leptonic and semileptonic B-hadron decays. The significance of several of these anomalies are compared in the left plot of Fig. 3.3. In the following, we will discuss two important cases of semileptonic decays that have garnered a lot of attention in the last decade.

First, LFU has been tested in the $b \to s\ell^+\ell^-$ transition by looking at the ratio of decay rates

$$R(\mathrm{K}^{(*)}) = \frac{\Gamma\left(\mathrm{B} \to \mathrm{K}^{(*)}\mu^+\mu^-\right)}{\Gamma\left(\mathrm{B} \to \mathrm{K}^{(*)}e^+e^-\right)}, \tag{3.2}$$

where the B meson and kaon can be neutral or charged. This observable is often integrated in one or more regions of q^2, the squared invariant mass of the dilepton system in order to avoid

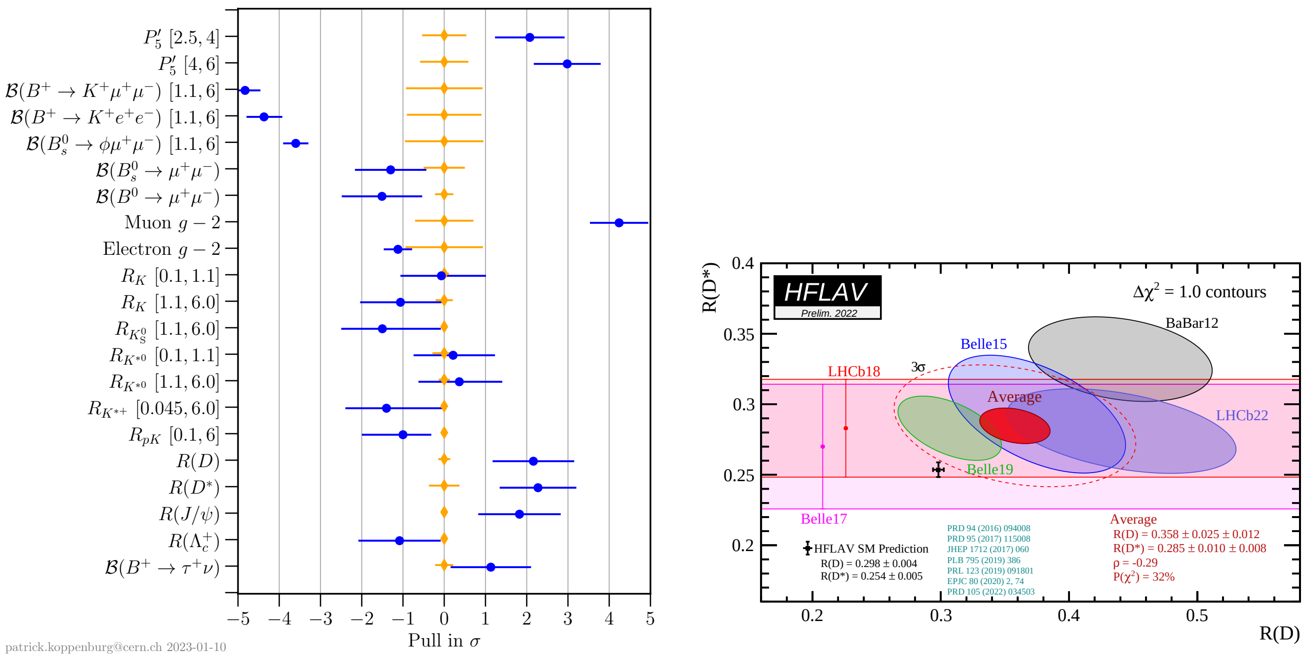

Figure 3.3: Measurements sensitive to flavor anomalies. **Left**: A selection of known observables to test LFU created by P. Koppenburg [139]. Each row shows the significance of a measurement (blue), with the SM expectation (orange) set to zero. The experimental and theoretical uncertainties are summed in quadrature and normalised to unity. The interval between the square brackets indicates the range of q^2, the squared invariant mass of the dilepton system. **Right**: Summary of $R(\mathrm{D})$ versus $R(\mathrm{D}^*)$ measurements, created by HFLAV [140]. Black point indicates the SM prediction with uncertainties and the red ellipse shows the average of all results, including preliminary 2022 results by LHCb (purple ellipse).

intermediate charmonium resonances.

This process involves an FCNC, which in the SM must proceed through a loop diagram at LO, as shown in Fig. 3.4. Because it is loop-suppressed, this variable could be sensitive to contributions from processes predicted by extensions to the SM. The ratio can be calculated to percent-level precision, due to the fact that perturbative and nonperturbative QCD contributions and their uncertainties cancel out [141]. In the SM, this ratio would be close to unity because of the relatively small mass difference between the electron and muon compared to the B meson mass [142]. Measurements made by Belle [143–145] and BaBar [146] were consistent with the SM. LHCb, on the other hand, had reported several measurements of both $R(\mathrm{K})$ [147–149] and $R(\mathrm{K}^*)$ [150, 151], with about half the uncertainty, which initially showed discrepancies with the SM of up to 3.1 and 2.6 standard deviations, respectively. These were recently resolved by new LHCb measurements, which showed no significant deviation from the SM after improving the treatment of the misidentified background in the decay channel with final-state electrons [152, 153]. Other noteworthy anomalies have appeared in the differential decay rates [150, 154–156] and angular analysis [157–160] of these type of semileptonic decays.

Secondly, one can construct a similar ratio for the $\mathrm{b} \to \mathrm{c}\ell^-\overline{\nu}_\ell$ transition,

$$R(\mathrm{D}^{(*)}) = \frac{\Gamma\left(\mathrm{B} \to \mathrm{D}^{(*)}\tau^-\overline{\nu}_\tau\right)}{\Gamma\left(\mathrm{B} \to \mathrm{D}^{(*)}\ell^-\overline{\nu}_\ell\right)}, \tag{3.3}$$

where again the B can be charged or neutral, and the inclusion of charge-conjugation is implied. This process can happen at tree level in the SM, since, as shown in Fig. 3.4, it is not suppressed, and has a large visible branching fraction. Because LFU has been confirmed in comparisons between $\mathrm{B} \to \mathrm{D}^{(*)}\mu\overline{\nu}_\mu$ and $\mathrm{B} \to \mathrm{D}^{(*)}\mathrm{e}\overline{\nu}_\mathrm{e}$ [161], and third-generation leptons could be more sensitive to new physics, it is more interesting to consider the semileptonic decays with a τ lepton.

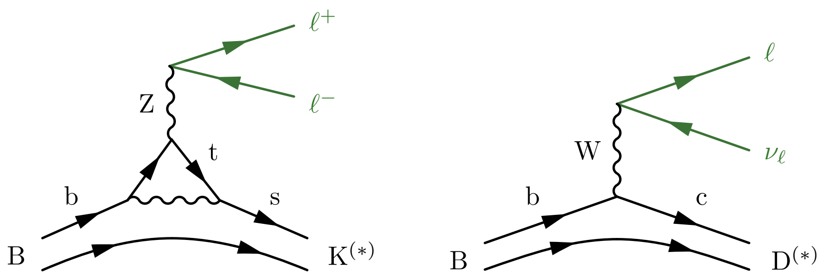

Figure 3.4: Feynman diagrams for rare semileptonic decays of B hadrons. **Left**: $B \to K^{(*)}\ell^+\ell^-$, an FCNC, which in the SM must occur through a loop diagram at LO. **Right**: $B \to D^{(*)}\ell^-\overline{\nu}_e$, which is a tree-level diagram at LO. Fig. 3.8 presents examples of new physics contributions.

The denominator of Eq. (3.3) is either the decay rate of the final state with a muon ($\ell = \mu$), or it is the average decay rate of the final states with an electron or a muon ($\ell = e, \mu$). Measurements of $R\big(D^{(*)}\big)$ reported by the BaBar [162, 163], Belle [164–170], and LHCb [171–173] Collaborations collectively deviate from the SM predictions by about four standard deviations [174]. Their results and the average are shown in Fig. 3.3. The deviations in $R(D)$ and $R\big(D^*\big)$ are on the order of 10%, which is quite large considering the SM process occurs at tree-level. If this anomaly holds, it would be evidence of τ/e and τ/μ universality violation in $b \to c\ell^-\overline{\nu}_\ell$ charged currents.

3.3 Effective field theory

In the modern view, the SM can be regarded as an EFT. The basic premise of the EFT framework is that the details of the dynamics of high energies (or equivalently, small length scales) do not affect the dynamics at lower energies (largest length scales) [175]. One can construct an effective Lagrangian with all possible local operators built from a combination of SM fields that are allowed by certain symmetries [176, 177]. The SM Lagrangian, then, is the renormalizable part of some more fundamental theory, while nonrenormalizable operators reflect the high-energy dynamics. The effective Lagrangian takes the form

$$\mathcal{L}_{\text{eff}} = \mathcal{L}_{\text{SM}} + \sum_{d>4} \sum_{n} \frac{C_d^{(n)}}{\Lambda^{d-4}} \mathcal{O}_d^{(n)}, \tag{3.4}$$

where each new term contains a nonrenormalizable operator $\mathcal{O}_d^{(n)}$ of mass-dimension d that is suppressed by the inverse powers of some energy scale Λ [56, 177]. The validity of this approximation is ensured by the Appelquist-Carazzone theorem [178]. Every term also introduces a dimensionless *Wilson coefficient* $C_d^{(n)}$, which is a new parameter that can be measured in experiment. It can be compared to the SM expectation, which is simply $C_d^{(n)} = 0$.

Conversely, one can obtain the effective operators and their Wilson coefficient in a top-down approach by integrating out the degrees of freedom from heavy fields in a given theory with tools known from Wilsonian renormalization [62, 179]. The Wilson coefficients can depend on several parameters from this theory, like coupling constants and masses. If a deviation from the SM is found in a precision measurement, one can then quantify how consistent the measurement is with the proposed theory. This information can then be used to guide subsequent measurements or direct searches.

3.3.1 Fermi four-fermion interaction

As a simple demonstration of the procedure, this section will outline how one can integrate out the W_μ^+ field of the SM, in order to get an EFT operator for the semileptonic $b \to c\tau^-\overline{\nu}_\tau$ transition. This is needed to analyze the semileptonic transitions of the flavor anomalies, which

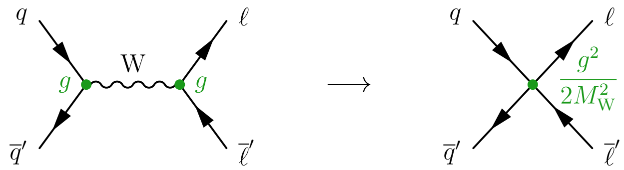

Figure 3.5: Feynman diagrams of semileptonic four-fermion interaction through a charged-current at LO in the SM (left) and in an EFT (right).

change quark flavor.

At LO, the only relevant interaction terms are those of the weak charged current in Eq. (2.10), which can be written as

$$\mathcal{L}_{\mathrm{SM}}^{\mathrm{CC}} = -\frac{g}{\sqrt{2}} J_{\mathrm{W}}^{\mu} W_{\mu}^{+} + \mathrm{h.c.}, \tag{3.5}$$

where the weak charged current is

$$J_{\mathrm{W}}^{\mu} = V_{\mathrm{CKM}}^{fg} \overline{u}_{\mathrm{L}}^{f} \gamma^{\mu} d_{\mathrm{L}}^{g} + \overline{e}_{\mathrm{L}}^{\ell} \gamma^{\mu} \nu_{\mathrm{L}}^{\ell}, \tag{3.6}$$

with an implicit summation over the generation indices f, g, and ℓ, and where the quarks are in their mass basis. In perturbative calculations, this current leads to the W_{μ}^{+} boson propagator,

$$\frac{-i(g_{\mu\nu} - q_{\mu}q_{\nu}/M_{\mathrm{W}}^{2})}{q^{2} - M_{\mathrm{W}}^{2}}, \tag{3.7}$$

with q the momentum of the virtual W boson. Because the mass of the W boson, $M_{\mathrm{W}} \approx 80.4\,\mathrm{GeV}$, is so much heavier than the momentum scale relevant for analyzing hadron decays, one can integrate out the momentum in terms of the amplitudes of four-fermion interactions after having expanded (3.7) into inverse powers of M_{W}. At LO, the effective, local Lagrangian is

$$\mathcal{L}_{\mathrm{eff,SM}}^{\mathrm{CC}(0)} = -\frac{4G_{\mathrm{F}}}{\sqrt{2}} g_{\mu\nu} J_{\mathrm{W}}^{\mu} J_{\mathrm{W}}^{\nu} + \mathrm{h.c.}, \tag{3.8}$$

which is exactly the four-fermion interaction posited by Fermi (see Section 2.1.5), and which provides a reasonable approximation for low-energy processes. The Fermi constant G_{F} can be written as

$$\frac{4G_{\mathrm{F}}}{\sqrt{2}} = \frac{g^{2}}{2M_{\mathrm{W}}^{2}} = \frac{2}{v^{2}} \approx 3.3 \times 10^{-5}\,\mathrm{GeV}^{-2}. \tag{3.9}$$

Notice that the operator in this effective Lagrangian has four fermion fields, and is therefore of mass dimension 6. For B decays, higher-order corrections will be of size $\mathcal{O}(m_{\mathrm{B}}^{2}/M_{\mathrm{W}}^{2})$, which can be taken into account by adding dimension-8 operators [56]. The new dimension-6 operators are represented by the contact interaction diagram shown in Fig. 3.5.

3.3.2 Effective Lagrangian for the flavor anomalies

For $\mathrm{b} \to \mathrm{c}\ell^{-}\overline{\nu}_{\ell}$ at LO, it is sufficient to only consider

$$\mathcal{L}_{\mathrm{eff,SM}}^{\mathrm{bc}\ell\nu(0)} = -\frac{4G_{\mathrm{F}}}{\sqrt{2}} V_{\mathrm{CKM}}^{cb} \overline{c}_{\mathrm{L}} \gamma^{\mu} b_{\mathrm{L}} \overline{\ell}_{\mathrm{L}} \gamma_{\mu} \nu_{\mathrm{L}} + \mathrm{h.c.}. \tag{3.10}$$

Taking the scale as $\Lambda = M_{\mathrm{W}}$, the corresponding Wilson coefficient is $C_{6}^{\mathrm{CC}} = g^{2} V_{\mathrm{CKM}}^{cb}/2$.

It is possible to construct a more general effective Lagrangian for $\mathrm{B} \to \mathrm{D}\ell\nu_{\ell}$ decays, in order to take into account possible new physics effects. All four-fermion operators respecting Lorentz invariance and the SM gauge symmetries are

$$\mathcal{L}_{\text{eff}}^{\text{bc}\ell\nu} = -\frac{4G_{\text{F}}}{\sqrt{2}}\Big[C_{\text{LL}}^{\text{S}}(\bar{c}_{\text{R}}b_{\text{L}})(\bar{\ell}_{\text{R}}\nu_{\text{L}}) + C_{\text{RL}}^{\text{S}}(\bar{c}_{\text{L}}b_{\text{R}})(\bar{\ell}_{\text{R}}\nu_{\text{L}})$$
$$+ \left(V_{\text{CKM}}^{cb} + C_{\text{LL}}^{\text{V}}\right)(\bar{c}_{\text{L}}\gamma^{\mu}b_{\text{L}})(\bar{\ell}_{\text{L}}\gamma_{\mu}\nu_{\text{L}}) + C_{\text{RR}}^{\text{V}}(\bar{c}_{\text{R}}\gamma^{\mu}b_{\text{R}})(\bar{\ell}_{\text{R}}\gamma_{\mu}\nu_{\text{R}})$$
$$+ C_{\text{LL}}^{\text{T}}(\bar{c}_{\text{R}}\sigma^{\mu\nu}b_{\text{L}})(\bar{\ell}_{\text{R}}\sigma_{\mu\nu}\nu_{\text{L}})\Big] + \text{h.c.}, \tag{3.11}$$

with the tensor $\sigma^{\mu\nu} = i/2[\gamma^{\mu}, \gamma^{\nu}]$, and Wilson coefficients C_{XY}^{J} for scalar (J = S), vector (J = V), and tensor currents (J = T) [180]. In the SM, all coefficients C_{XY}^{J} vanish. The next section will discuss how $\mathcal{L}_{\text{eff}}^{\text{bc}\ell\nu}$ can be simplified under certain experimental and theoretical constraints.

3.4 Phenomenology of Leptoquarks

LQs are hypothetical bosons that carry both nonzero baryon and lepton numbers. As the name suggests, LQs simultaneously couple to a lepton and a quark. For this reason, they must have fractional electric charge Q, and transform as color-triplets such that they carry color charge like quarks. In local QFTs, they can either be scalar or vector bosons. The number of the LQ multiplets under the SM gauge group is limited if one requires that they form direct couplings to a lepton and quark that are gauge and Lorentz invariant. In that case, there are in all six scalar ($\overline{S}_1$, S_1, $\widetilde{S}_1$, $\widetilde{R}_2$, R_2, S_3^i) and six vector LQ multiplets ($\overline{U}_{1\mu}$, $U_{1\mu}$, $\widetilde{U}_{1\mu}$, $\widetilde{V}_{2\mu}$, $V_{2\mu}$, $U_{3\mu}^i$) [112], which are listed in Table 3.1 with their respective properties. Their quantum numbers are also graphed in Fig. 3.6, from which the charge Q of each LQ state can be read off. Also listed in Table 3.1 are the allowed fermion couplings, which will generally have different mixes of left- and right-handed fermions, as well as up- and down type fermions, depending on the LQ charge. This includes couplings that involve right-handed neutrinos, otherwise $\overline{S}_1$ and $\overline{U}_{1\mu}$ would be excluded as in Ref. [181]. Note that eight of these LQ states can also permit diquark couplings. Furthermore, LQs have a well-defined fermion number $F = 3B + L$. LQs with $|F| = 2$ couple a quark to a lepton, while those with $F = 0$ couple an antiquark to a lepton.

These type of bosons emerge naturally from many extensions of the SM, such as grand unification theories (GUTs) [182–189], which unify matter under some larger symmetry group, or theories invoking technicolor [190–192], or compositeness [193–195]. They are furthermore found in supersymmetry models with R-parity violation [196–199], and even in some string theories [200, 201]. Interestingly, in most of these scenarios, LQs will be accompanied by other particles. For massive vector LQs, for example, one needs to have additional vector states for ultraviolet (UV) completion [202].

3.4.1 Constraints on LQs

LQs could mediate the decay of a proton or bound neutron, either through direct couplings to two first-generation quarks, or through other types of couplings. As the lower bound on the lifetime of the proton is already extreme, the lower limits on the LQ mass are very stringent, assuming diquark-couplings are not suppressed in some way [112]. Similarly, stringent bounds on first-generation couplings are set by precise measurements of atomic parity violation in cesium [203, 204]. Besides protons, LQs would contribute in any decays involving both a lepton and a quark at tree level, and so limits can be set from measuring both leptonic and semileptonic meson decays,

Table 3.1: Summary of all possible LQ fields with their representation under $\mathrm{SU}(3)_\mathrm{C} \times \mathrm{SU}(2)_\mathrm{L}$, along with hypercharge Y, fermion number $F = 3B + L$, charge $Q = T_3 + Y/2$, and the fermion current(s) they couple to (hermitian conjugate omitted). Bold numbers indicate the dimension of the representation under the respective gauge group. Charge conjugation is indicated by $\psi^C = C\overline{\psi}^\mathrm{T}$ with $C = i\gamma^2\gamma^0$. Adapted from Refs. [112] and [181].

LQ field	$\mathrm{SU}(3)_\mathrm{C}$	$\mathrm{SU}(2)_\mathrm{L}$	$Y/2$	$F = 3B + L$	$Q = T_3 + Y/2$	Fermion current
Scalar						
$\overline{S}_1$	$\overline{\mathbf{3}}$	$\mathbf{1}$	$-2/3$	-2	$\mp\frac{2}{3}$	$\overline{u}^C_\mathrm{R}\nu_\mathrm{R}$, $\overline{d}^C_\mathrm{R}d_\mathrm{R}$
S_1	$\overline{\mathbf{3}}$	$\mathbf{1}$	$1/3$	-2	$\pm\frac{1}{3}$	$\overline{Q}^C_\mathrm{L}\varepsilon L_\mathrm{L}$, $\overline{u}^C_\mathrm{R}e_\mathrm{R}$, $\overline{d}^C_\mathrm{R}\nu_\mathrm{R}$, $\overline{Q}^C_\mathrm{L}\varepsilon Q_\mathrm{L}$, $\overline{u}^C_\mathrm{R}d_\mathrm{R}$
$\widetilde{S}_1$	$\overline{\mathbf{3}}$	$\mathbf{1}$	$4/3$	-2	$\pm\frac{4}{3}$	$\overline{d}^C_\mathrm{R}e_\mathrm{R}$, $\overline{u}^C_\mathrm{R}u_\mathrm{R}$
$\widetilde{R}_2$	$\mathbf{3}$	$\mathbf{2}$	$1/6$	0	$\mp\frac{1}{3}, \pm\frac{2}{3}$	$\overline{d}_\mathrm{R}\varepsilon L_\mathrm{L}$, $\overline{Q}_\mathrm{L}\nu_\mathrm{R}$
R_2	$\mathbf{3}$	$\mathbf{2}$	$7/6$	0	$\pm\frac{2}{3}, \pm\frac{5}{3}$	$\overline{u}_\mathrm{R}\varepsilon L_\mathrm{L}$, $\overline{e}_\mathrm{R}Q_\mathrm{L}$
S_3^i	$\overline{\mathbf{3}}$	$\mathbf{3}$	$1/3$	-2	$\pm\frac{1}{3}, \mp\frac{2}{3}, \pm\frac{4}{3}$	$\overline{Q}^C_\mathrm{L}\varepsilon T_i L_\mathrm{L}$, $\overline{Q}^C_\mathrm{L}\varepsilon T_i Q_\mathrm{L}$
Vector						
$\overline{U}_{1\mu}$	$\mathbf{3}$	$\mathbf{1}$	$-1/3$	0	$\mp\frac{1}{3}$	$\overline{d}_\mathrm{R}\gamma^\mu\nu_\mathrm{R}$
$U_{1\mu}$	$\mathbf{3}$	$\mathbf{1}$	$2/3$	0	$\pm\frac{2}{3}$	$\overline{Q}_\mathrm{L}\gamma^\mu L_\mathrm{L}$, $\overline{d}_\mathrm{R}\gamma^\mu e_\mathrm{R}$, $\overline{u}_\mathrm{R}\gamma^\mu\nu_\mathrm{R}$
$\widetilde{U}_{1\mu}$	$\mathbf{3}$	$\mathbf{1}$	$5/3$	0	$\pm\frac{5}{3}$	$\overline{u}_\mathrm{R}\gamma^\mu e_\mathrm{R}$
$\widetilde{V}_{2\mu}$	$\overline{\mathbf{3}}$	$\mathbf{2}$	$-1/6$	-2	$\pm\frac{1}{3}, \mp\frac{2}{3}$	$\overline{u}^C_\mathrm{R}\gamma^\mu L_\mathrm{L}$, $\overline{Q}^C_\mathrm{L}\gamma^\mu\nu_\mathrm{R}$, $\overline{d}^C_\mathrm{R}\gamma^\mu Q_\mathrm{L}$
$V_{2\mu}$	$\overline{\mathbf{3}}$	$\mathbf{2}$	$5/6$	-2	$\pm\frac{1}{3}, \pm\frac{4}{3}$	$\overline{d}^C_\mathrm{R}\gamma^\mu\varepsilon L_\mathrm{L}$, $\overline{Q}^C_\mathrm{L}\varepsilon\gamma^\mu e_\mathrm{R}$, $\overline{Q}^C_\mathrm{L}\gamma^\mu u_\mathrm{R}$
$U^i_{3\mu}$	$\mathbf{3}$	$\mathbf{3}$	$2/3$	0	$\mp\frac{1}{3}, \pm\frac{2}{3}, \pm\frac{5}{3}$	$\overline{Q}_\mathrm{L}\gamma^\mu T_i L_\mathrm{L}$

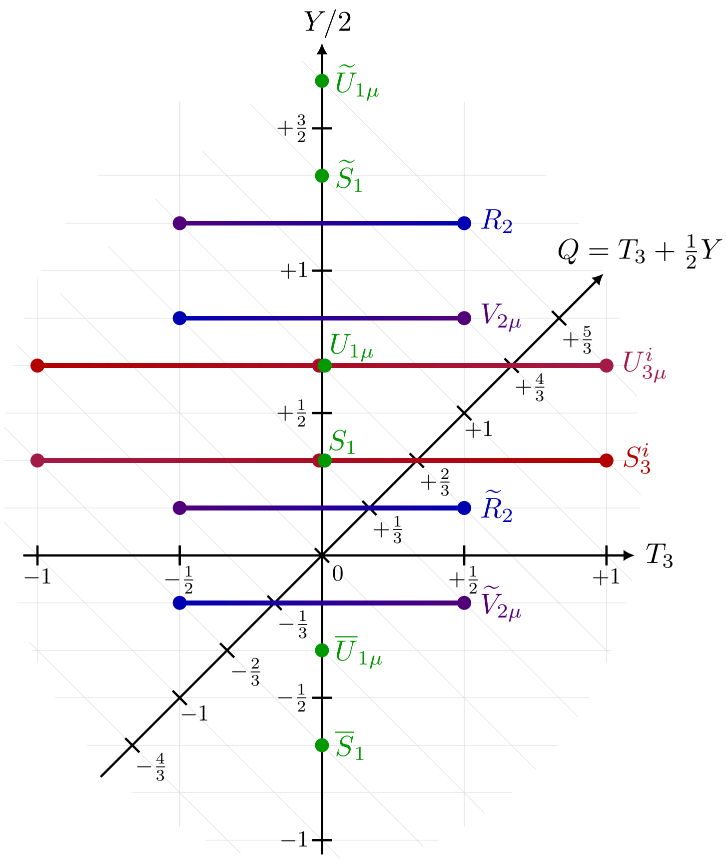

Figure 3.6: Graph of the $\mathrm{SU}(2)_\mathrm{L} \times \mathrm{U}(1)_\mathrm{Y}$ quantum numbers $(T_3, Y/2)$ of all possible LQ fields [112, 181]. The points represent mass eigenstates that also have a well-defined electric charge.

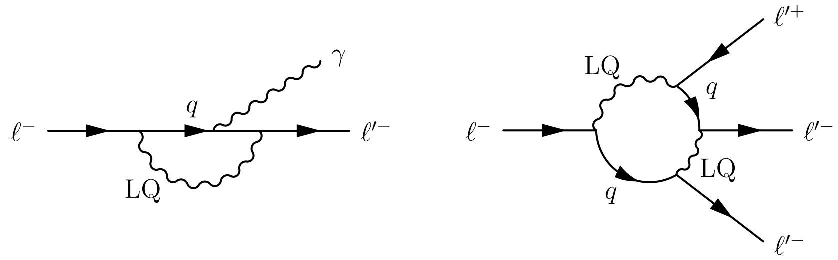

Figure 3.7: Some examples of contributions to LFV decays of $\ell^- \to \ell^-\gamma$ and $\ell^- \to \ell^-\ell^-\ell^+$. These can be compared to the SM diagrams in Fig. 2.5.

semileptonic τ decays, and $\mu \to e$ conversions in nuclei [205]. Because there is no fundamental reason LQs should respect lepton flavor symmetry, strong limits on LQs can also be set from measurements of decay rates, or from bounds on lepton-flavor violating decays like $\mu \to e\gamma$ or $\ell \to 3\ell'$ [206]. Some examples of LQ contributions are shown in Fig. 3.7. As mentioned before, FCNCs especially offer a good probe, thanks to their suppression in the SM. The implication of the B anomalies will be discussed in the next section.

Direct evidence of LQs has been extensively searched for at previous e^+e^- colliders like LEP, as well as the electron-proton collider HERA. However, these have primarily focused on LQs with couplings to the first generation. A comprehensive overview of constraints on LQs from both low-energy experiments and high-energy colliders is given by Ref. [112]. Constraints from the LHC will be discussed in Sections 3.4.3 and 13.5.

3.4.2 Explanation for the B anomalies

LQ models have recently received renewed theoretical interest as a possible explanation for the flavor anomalies. Namely, the Feynman diagrams in Fig. 3.8 show how contributions from LQs could appear at tree-level in these semileptonic transitions, while for four-quark or four-fermion contact interactions, for which no anomalies have so far been found, LQs would only contribute at the loop-level.

Furthermore, the couplings between fermions and LQs should in general have a nontrivial flavor structure that explicitly breaks the SM's flavor symmetry. More specifically, the anomalies would appear in processes involving semileptonic transitions of the bottom quark, while universality tests with lighter fermions or purely leptonic processes show no deviations, as discussed in Section 3.2. Therefore, LQs that couple most strongly to third-generation fermions and have a small, but nonnegligible mixing with the lighter generations could offer a coherent explanation for the rates observed in $B \to D^{(*)}\ell\overline{\nu}_\ell$ decay, and other B anomalies. This has been widely discussed in the literature, as in Refs. [112, 113, 174, 180, 202, 207–233].

Several studies have pointed out that the U_1 field with a mass in the TeV range is the best candidate to explain both the data of the charged- and neutral-current B anomalies with a single LQ mediator [180, 216, 226, 230]. Without deviations in measurements with currents like $R(K^{(*)})$, other scenarios involving scalar LQ are also possible [180, 230].

More can be learned from an EFT analysis of the anomalies relating to $b \to c\ell^-\overline{\nu}_\ell$. A general

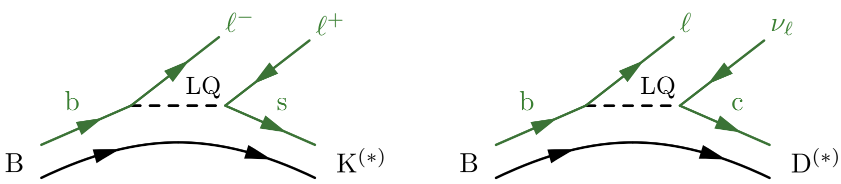

Figure 3.8: Tree-level contributions from LQs to $B \to K^{(*)}\mu^+\mu^-$ (left) and $B \to D^{(*)}\tau^-\overline{\nu}_\tau$ decay (right). SM diagrams are shown in Fig. 3.4.

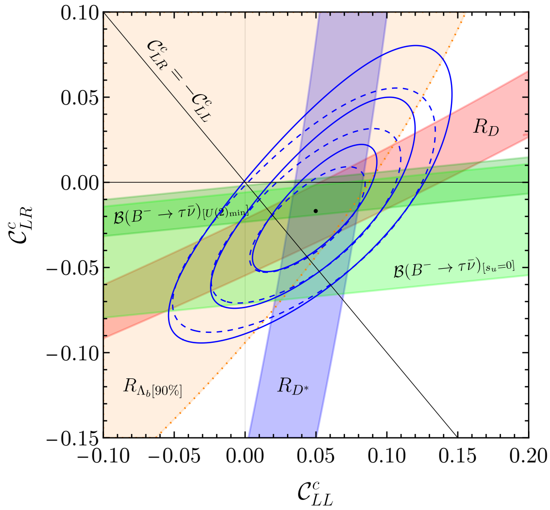

Figure 3.9: Determination of the Wilson coefficients $C^c_{\rm LL}$ & $C^c_{\rm RL}$ with χ^2-fits to several observables of B decay. The SM is at $\left(C^c_{\rm LL}, C^c_{\rm RL}\right) = (0,0)$. The black dot represents the combined fit of $\rm b \to c\ell\overline{\nu}_\ell$ observables, with contours (blue) of the confidence interval for 1, 2 and 3 standard deviations. Taken from Ref. [233].

current demonstrating which SM fermion fields that the U_1 can couple to is

$$J^\mu_{U_1} = \lambda\left[\beta^{q\ell}_{\rm L}(\overline{Q}^q_{\rm L}\gamma^\mu L^\ell_{\rm L}) + \beta^{q\ell}_{\rm R}(\overline{d}^q_{\rm R}\gamma^\mu e^\ell_{\rm R})\right], \tag{3.12}$$

with an implicit summation over the quark (q) and lepton generational indices (ℓ), where λ is the overall coupling constant, and the flavor structure is given by $\beta^{q\ell}_{\rm L}$. The effective Lagrangian given by Eq. (3.11) can be simplified when assuming a U_1 model with an approximate flavor symmetry for the lighter generation [216, 231]. In that case, it is convenient to rewrite the Lagrangian as

$$\mathcal{L}^{\rm bc\ell\nu}_{\rm eff} = -\frac{2V^{cb}_{\rm CKM}}{v^2}\left[\left(1 + C^c_{\rm LL}\right)(\bar{c}_{\rm L}\gamma^\mu b_{\rm L})(\bar{\ell}_{\rm L}\gamma_\mu\nu_{\rm L}) - 2C^c_{\rm RL}(\bar{c}_{\rm L}b_{\rm R})(\bar{\ell}_{\rm R}\nu_{\rm L})\right], \tag{3.13}$$

after having integrated out the heavy LQ state and redefined the Wilson coefficients. The Wilson coefficients can be written in terms of the U_1 model parameters:

$$C^c_{\rm LL} \propto \frac{v^2\lambda^2}{M^2_{U_1}}, \tag{3.14}$$

and

$$C^c_{\rm RL} \propto \frac{v^2\lambda^2}{M^2_{U_1}}. \tag{3.15}$$

A fit of the Wilson coefficients $C^c_{\rm LL}$ and $C^c_{\rm RL}$ to several charged-current measurements is shown in Fig. 3.9. This shows that the deviation from the SM of the $\rm b \to c\ell^-\overline{\nu}_\ell$ observables combines to about 3 standard deviations. Interestingly, the fit is compatible with the case of a pure left-handed interaction ($C^c_{\rm LR} = 0$), as well as the case with right-handed interactions of equal magnitude ($C^c_{\rm LR} = -C^c_{\rm LL}$). Both scenarios are special benchmarks that are favored by different UV completions of leptoquark models [223, 233].

If one considers a simplified U_1 model with couplings only to left-handed fermions,

$$\mathcal{L}_{U_1} \supset \lambda\beta^{q\ell}_{\rm L}(\overline{Q}^q_{\rm L}\gamma^\mu L^\ell_{\rm L})U_{1\mu}, \tag{3.16}$$

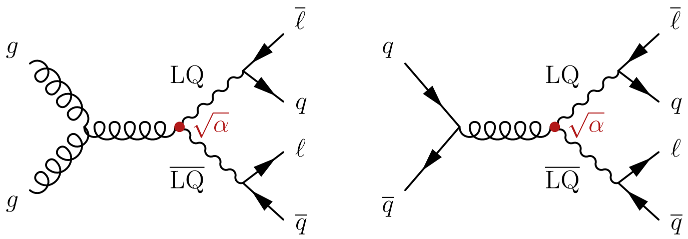

Figure 3.10: Examples of Feynman diagrams of LQ pair production in pp collisions through gluon fusion (left) and quark-antiquark annihilation (right), where ℓ can be a charged or neutral lepton.

the flavor structure that can best explain the B anomalies is roughly given by [113, 231]

$$\beta_{\mathrm{L}}^{q\ell} = \begin{pmatrix} 0 & 0 & 0 \\ 0 & \mathcal{O}(0.01) & \mathcal{O}(0.1) \\ 0 & -\mathcal{O}(0.1) & 1 \end{pmatrix}. \tag{3.17}$$

Here, the coupling strength λ is normalized such that $\beta_{\mathrm{L}}^{b\tau} = 1$. Entries that are negligible are set to zero. The main takeaway is that the flavor structure is very hierarchical, with the largest couplings to the third generation, LQ-bτ or LQ-tν_τ, while the couplings to the lighter generations are weaker by roughly an order of magnitude or more. The size of these couplings is mainly driven by the discrepancy observed in $R(\mathrm{D}^{(*)})$. This motivates searches for "third-generation" LQs at the LHC, with signatures that contain top or bottom quarks with τ leptons or neutrinos.

3.4.3 LQ signals at the LHC

There are several strategies to look directly for LQs at the LHC if they do exist. As LQs have color charge, they can be created in pp collisions via QCD processes either singly or as an LQ-LQ pair. Otherwise, they can also be exchanged through the nonresonant production of two leptons. Let us discuss each in more detail.

First, LQ pair production is very similar to the production of a top quark pair. At LO, this includes gluon fusion, shown in Fig. 3.10, or quark-antiquark annihilation. Pair production of LQs through the strong interaction tends to have the highest cross section for most LQ scenarios with masses up to a few TeV. The decay products of two heavy LQs will also have a harder energy spectrum than a singly produced LQ, making them easier to distinguish from the backgrounds. For these reasons, most searches so far have exclusively focused on pair production. Furthermore, pair production tends to be largely model independent. For example, pair production at LO is independent of the coupling strength λ, in contrast to the other production modes.

Secondly, single LQs can be produced via quark-gluon fusion, in association with an extra lepton in the final state. Two example diagrams are shown in Fig. 3.11. For masses below a few TeV and a coupling strength $\lambda \leq 2$, the cross section for this mode of production tends to be subdominant to pair production. However, the cross section scales with λ^2, as can be seen

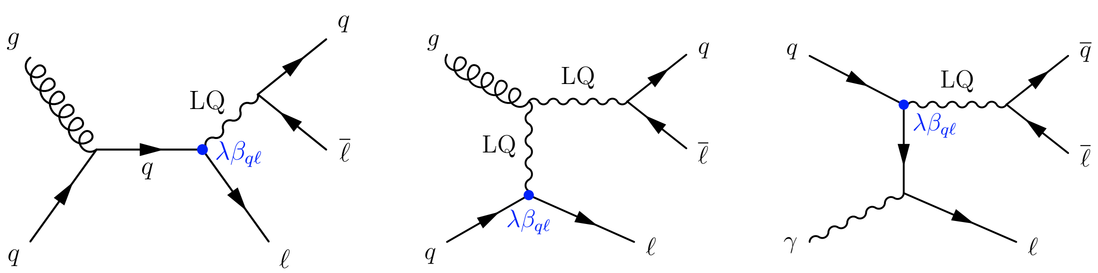

Figure 3.11: Examples of Feynman diagrams of single LQ production in pp collisions through quark-gluon fusion (left & center) or lepton-induced production (right).

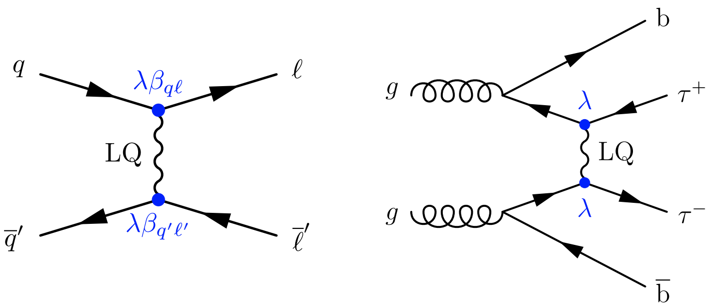

Figure 3.12: Feynman diagrams of nonresonant dilepton production in pp collisions through the t-channel exchange of an LQ. For the case of LQ $\rightarrow$ bτ couplings, there is a bottom quark is in the initial state, which can be produced in gluon splitting as shown on the right.

from the blue vertices in Fig. 3.11. As a consequence, searches can benefit from considering this mode of production at high λ. As will be discussed in more detail later, the decay width also scales with λ^2. This slightly degrades the sensitivity at high λ for single production due to the widening of the resonance. Recently, a different production mechanism for single LQ was proposed with one lepton in the initial state [234]. This is possible due to the nonzero photon PDF in the proton, which allows photon splitting into a lepton-antilepton pair [235]. Although this PDF is heavily suppressed, such a case could produce events in which a proton remains intact, yielding a search with little contaminating background.

Finally, in the last several years, increased attention has been given to the possibility of nonresonant production of two leptons through the t-channel exchange of an LQ [236, 237], shown in Fig. 3.12. The cross section of this mode scales with λ^4, adding signal sensitivity at high values of the coupling strength λ. As the name suggests, the dilepton system will be nonresonant, making it harder to separate from backgrounds. Instead of a “bump hunt” in an invariant mass, one can look for deviations in the tails of dilepton distributions. Alternatively, one can define an angular observable wherein the signal will peak compare to other backgrounds. Above LQ masses of roughly 1 TeV, nonresonant LQ production can be approximated by a four-fermion contact interaction, and an ambiguity between the LQ mass and its coupling strength would develop in an experimental search.

The typical signature of all production modes includes two energetic leptons, and for the case of single or pair production, one or two quark-initiated jets, respectively. It is difficult to distinguish the single LQ and pair production by the observed final state due to the combinatorics of correctly pairing the jets and leptons. While these modes are typically resonant, it is hard to reliably reconstruct the LQ mass. For the same reason, it can be difficult to distinguish the signatures of LQs with different types of couplings or electric charges. Most LQ searches instead take advantage of the fact that the final state objects in the signal events are very energetic, and construct a variable like the “scalar sum p_{T}”, which is introduced later.

This thesis considers a search for an LQ that exclusively decays to a bottom quark and τ lepton. In that case, both the single and nonresonant processes have at least one bottom quark in the initial state, which leads to a suppression of the crosssection due to the small bottom-quark PDF. The processes will be dominantly initiated by gluon splitting, which leads to the associated production of at least one bottom quark. As shown in the right diagram of Fig. 3.12, nonresonant production can even have two bottom quarks in the initial state. Although the jets from these bottom quarks will tend to be less energetic and more forward, the final states of single, pair and nonresonant production will be very similar: two τ leptons, and up to two bottom-flavored jets (b jets).

The results of previous LQ searches will be compared to our results in Section 13.5.

4 The CMS Experiment

In order to push the boundaries of fundamental physics and shed light on the questions raised in Chapters 2 and 3, we need to probe Nature at its smallest length scales. In turn, this means we need to collide particles at very high energies to reach these length scales. This is why we need large accelerators for controlled collisions inside large detectors. This chapter will discuss the experimental setup that enables the search presented in this thesis for indirect or direct evidence of LQs. More detail is given to the pixel detector, because this is most relevant for the accurate reconstruction and identification of bottom quarks and τ leptons, and because I have contributed to its calibration and operation.

4.1 The Large Hadron Collider

The Large Hadron Collider (LHC) is the world's largest and most powerful particle collider. It is designed to accelerate beams of hadrons at very high energies in both directions and collide them head-on at four interaction points inside four large detectors; ATLAS, CMS, ALICE, and LHCb. The accelerated hadrons are primarily protons, but heavy ions like lead or xenon are also used. The LHC machine is situated in a circular tunnel 100 meters under the ground near Geneva, Switzerland, and is part of CERN. The first particle beams were circulated in the LHC in 2008. With its 27 km circumference and record collision energy of 13.6 TeV, it surpasses the

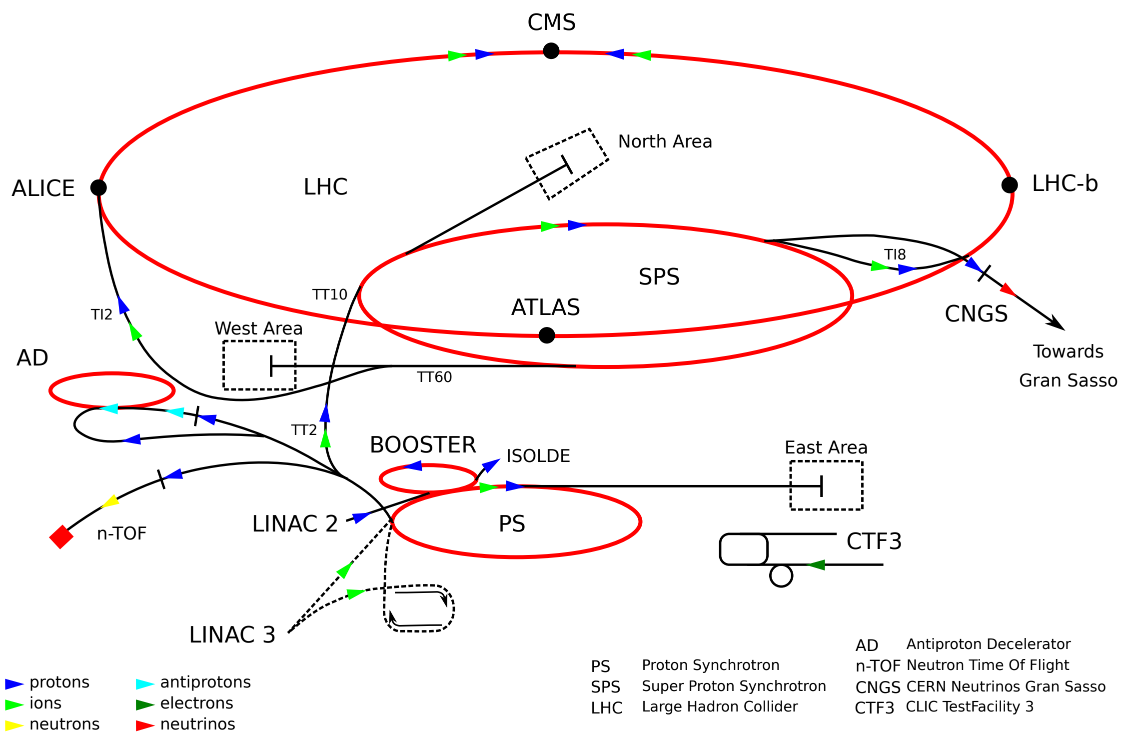

Figure 4.1: CERN's accelerator complex. Protons for the LHC start in a hydrogen tank at LINAC 2 and are accelerated through different stages until they are injected into the LHC, which speeds them up from 450 GeV up to 6.5 TeV over a period of 20 minutes. Taken from [238].

Tevatron accelerator at Fermilab in the United States [239], which was about 6.3 km and reached a center-of-mass energy of 1.96 TeV, and LEP, which was previously in the same tunnel as the LHC and reached a center-of-mass energy of 209 GeV [13, Section 32].

The LHC is a synchrotron: The particle beams are accelerated to higher energies while the magnetic field is steadily increased to maintain the particles at a fixed trajectory inside the ring. Before the proton beams reach the LHC, they go through several stages of acceleration as shown in Fig. 4.1. They start as hydrogen gas in a single bottle. After the electrons are stripped, they are first accelerated by LINAC 2, a linear accelerator. Then they pass through the Proton Synchrotron Booster to the the Proton Synchrotron (PS), followed by the Super Proton Synchrotron (SPS), where they are accelerated up to an energy of about 450 GeV. Finally, the proton beams are injected into the LHC, which ramps them up to several TeV in less than half an hour. During the data-taking period of 2015 to 2018, referred to as "Run 2", the energy of each proton beam was 6.5 TeV, which means the center-of-mass energy was $\sqrt{s} = 13\,\text{TeV}$. After a multiyear shutdown for maintenance and upgrades, the LHC reached a new collision energy of 13.6 TeV in 2022. The LHC machine is described in more technical detail in Ref. [240].

The main goals of the physics program of the LHC and its detectors are the discovery and study of the Higgs boson, tests of the SM of particle physics, and the search for new physics beyond the SM. As mentioned before, the discovery of the Higgs boson was already achieved using some of the Higgs boson decay modes in 2012.

4.1.1 Luminosity

Besides a record center-of-mass energy, the LHC has reached record beam intensities for hadron colliders [242]. An important measure of a collider's intensity is the *instantaneous luminosity* $\mathcal{L}$, which measures how many pp interactions happen per unit of time and cross section. It depends on several beam parameters. The simplified expression is [13, p. 533]:

$$\mathcal{L} = \frac{N_1 N_2 f}{A}, \tag{4.1}$$

where f is the frequency at which the beams cross, A is the cross-sectional area of the beams' overlap, and N_1, N_2 are the number of particles in each beam. The particles in the beams approximately follow Gaussian distributions in the transverse x and y directions, such that the area at the interaction point should be given by the root-mean-square (RMS) σ_x^* and σ_y^* of the beam sizes in either direction: $A = 4\pi\sigma_x^*\sigma_y^*$. The LHC is designed to reach the nominal luminosity of $\mathcal{L} = 10^{34}\,\text{cm}^{-2}\,\text{s}^{-1}$, but it had already surpassed that number by a factor of two in 2017, as can be seen in Fig. 4.2 [243]. A more exact and technical definition of LHC's instantaneous luminosity is given in Ref. [240].

Because of the way they are accelerated, proton beams are not continuous, but divided into groups of protons clumped together, called *bunches*. In 2016, the maximum number of proton bunches per beam was 2220, while in 2017 and 2018, it was 2556. [244]. Each bunch contains about 110 billion protons [240, 244]. During Run 2, the nominal time interval between two bunches crossing at each interaction point was 25 ns, which corresponds to a rate of $f = 40\,\text{MHz}$.

How many actual pp collisions are there? With the numbers introduced so far, one can roughly estimate the number of actual pp collisions per second. Taking the peak luminosity of $\mathcal{L} = 2 \times 10^{34}\,\text{cm}^{-2}\,\text{s}^{-1}$, and a total pp cross section of $\sigma_{\text{pp}}^{\text{tot}} \approx 100\,\text{mb}$, we find an *event rate* of $\mathcal{L}\sigma_{\text{pp}}^{\text{tot}} = 2$ billion collisions per second, or 50 collisions per bunch crossing. Figure 4.4 shows the distribution of the number of interactions per bunch crossing in all data-taking years of Run 2.

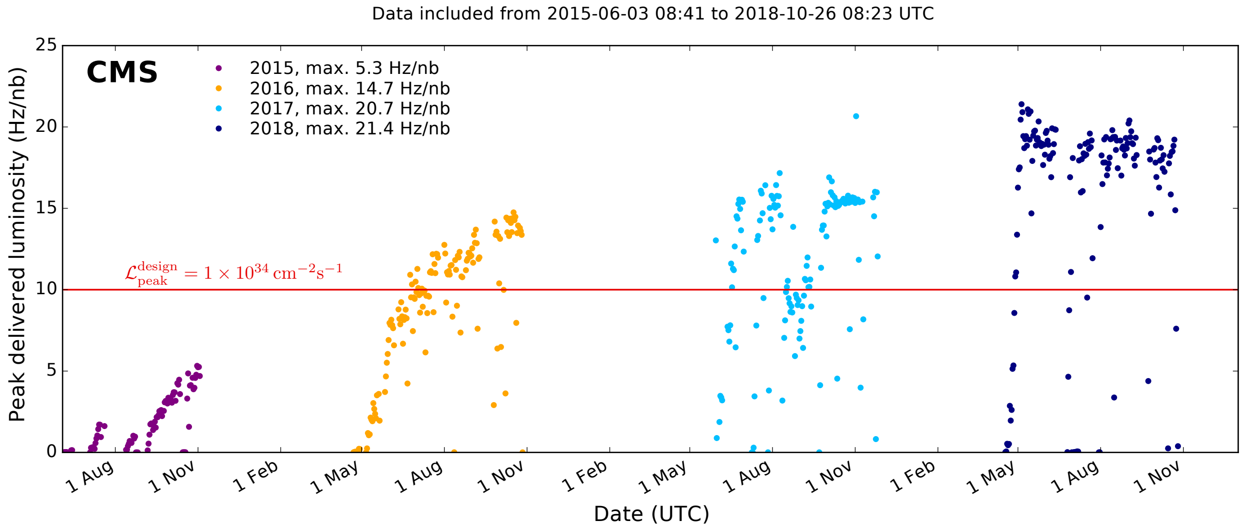

Figure 4.2: The increasing proton beam intensities at LHC in terms of peak instantaneous luminosity $\mathcal{L}$ per day, see Eq. (4.1). The LHC design luminosity of $\mathcal{L}_{\rm peak}^{\rm design} = 10^{34}\,{\rm cm}^{-2}\,{\rm s}^{-1}$ has been surpassed since 2016. The LHC was shut down between 2013 and 2015 for an upgrade before "Run 2". Note that 10 Hz/nb corresponds to $10^{34}\,{\rm cm}^{-2}\,{\rm s}^{-1}$. Adapted from [241].

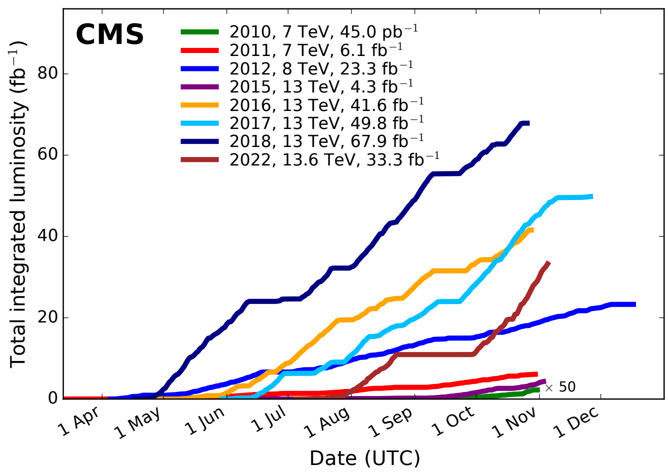

Figure 4.3: Cumulative data volume collected by CMS versus day during Run-2 data taking between 2015 and 2018 at $\sqrt{s} = 13\,\text{TeV}$ in terms of integrated luminosity. Figure taken from [241].

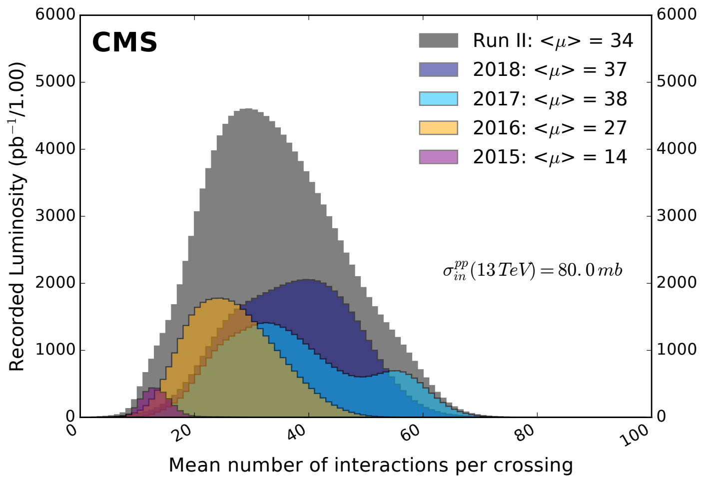

Figure 4.4: Distribution of number of pp interactions (pileup) per beam crossing in CMS during Run-2 data taking between 2015 and 2018 at $\sqrt{s} = 13\,\text{TeV}$, assuming an inelastic cross section of 80 mb. Figure taken from [241].

The average number of interactions per crossing varied between 27 and 37, which is of the same order as what was naively calculated above. As discussed in Section 2.3.2, the vast majority of pp collisions do not have a hard scattering process. The "extra" pp interactions in an event are called *pileup*, and add background noise to most measurements, we therefore mitigate it with dedicated algorithms and corrections. The pp interactions are typically spread out along the beam line within a length of 14 cm around the center of CMS.

This thesis is based on an analysis of pp collision data recorded between 2016 and 2018. Figure 4.3 shows a comparison of the data volume accumulated per day of each data-taking year up to 2022. The amount of data is expressed in terms of *integrated luminosity* L, which is simply the instantaneous luminosity $\mathcal{L}$ integrated over the time the LHC was running:

$$L := \int_{\text{data taking}} \mathcal{L}(t)\mathrm{d}t, \tag{4.2}$$

given in units of inverse area, such as the inverse barn (b^{-1}). Between 2016 and 2018, CMS collected about $138\,\mathrm{fb}^{-1}$ of pp collision data that is suitable for physics analysis, see Chapter 7.

4.2 The CMS detector

The Compact Muon Solenoid (CMS) detector is located near the French town of Cessy, and lies about 100 meters deep at one of the interaction points at the LHC (see Fig. 4.1). The LHC delivers beams which cross at the detector's very center. The detector is approximately cylindrically symmetric, with a length of 21.5 meters and diameter of 14.6 meters. An illustration is shown in Fig. 4.5. The following sections will give a broad overview. A detailed description can be found in Ref. [245].

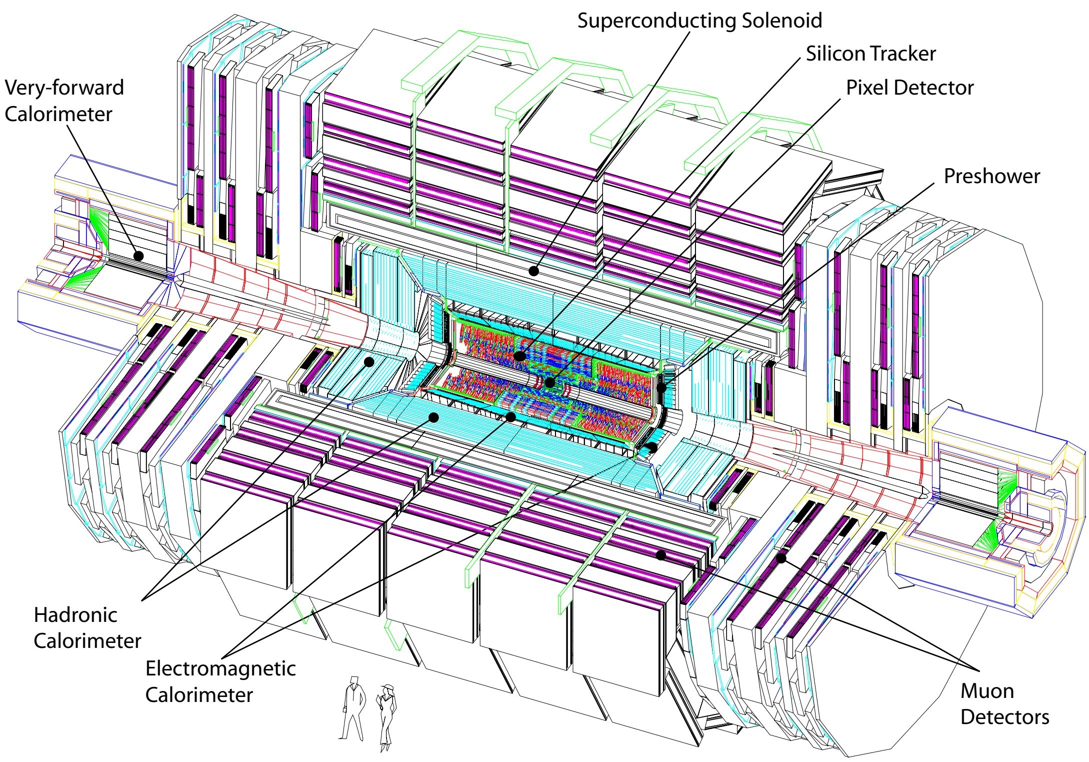

Figure 4.5: The CMS detector is made up of layers of different subdetectors, and has an approximate cylindrical symmetry. Taken from [245].

4.2.1 Coordinate system

The conventional coordinate system of CMS is defined in Fig. 4.6. With the origin in the center of the detector, the y axis points upward to the sky, the x axis points towards the center of the LHC and the z axis points tangentially along the beam line towards the Jura mountains, which lie to the west of CMS. This is also the direction of the anticlockwise beam (viewed from above). This makes the xy plane orthogonal to the beam axis the *transverse plane*, and the z axis the *longitudinal direction*. The *azimuthal angle* $\phi \in [0, 2\pi]$ is the angle with respect to the positive x axis in the xy plane, while the *polar angle* $\theta \in [0, \pi]$ is with respect to the z axis. Due to the nature of the inelastic collisions of two hadrons, it is more convenient to use the so-called *pseudorapidity* η instead of θ:

$$\eta := -\ln\left[\tan(\theta/2)\right]. \tag{4.3}$$

When referring to the direction of motion of particles produced in collisions, η can be written in terms of the total momentum $p = |\vec{p}|$ and longitudinal momentum p_z of the particle:

$$\eta = \frac{1}{2}\ln\left(\frac{p + p_z}{p - p_z}\right). \tag{4.4}$$

Several values of η are shown in Fig. 4.6. Note that η runs from 0 to positive infinity as θ goes from $\pi/2$ to 0, and runs from 0 to negative infinity when θ goes from $\pi/2$ to π. This means that the detector can be divided into two hemispheres: The forward direction with positive z values has $\eta > 0$, while negative values of z correspond to $\eta < 0$. The difference in pseudorapidity $\Delta\eta$ between two vectors is Lorentz-invariant under boosts along the longitudinal z axis. This is a convenient property in hadron colliders, because particles produced in hard scattering process will be boosted along the z axis, as explained in Section 2.3.2.

For a couple of reasons explained later, particle physicists make frequent use of the *transverse momentum* $p_\mathrm{T} = \sqrt{p_x^2 + p_y^2}$, which is simply the transverse component $\vec{p}_\mathrm{T} = p_x\hat{x} + p_y\hat{y}$ of a momentum vector $\vec{p}$. Similarly, the *transverse energy* is given by $E_\mathrm{T} = \sqrt{m^2 + p_\mathrm{T}^2}$, which is the same as p_T if the four-momentum's invariant mass is zero, $E_\mathrm{T} = p_\mathrm{T}$.

The radial distance from the beam axis in the xy plane is often denoted by $r = \sqrt{x^2 + y^2}$. Furthermore, with the above definitions, it is useful to express the *distance in the $\phi\eta$ plane*

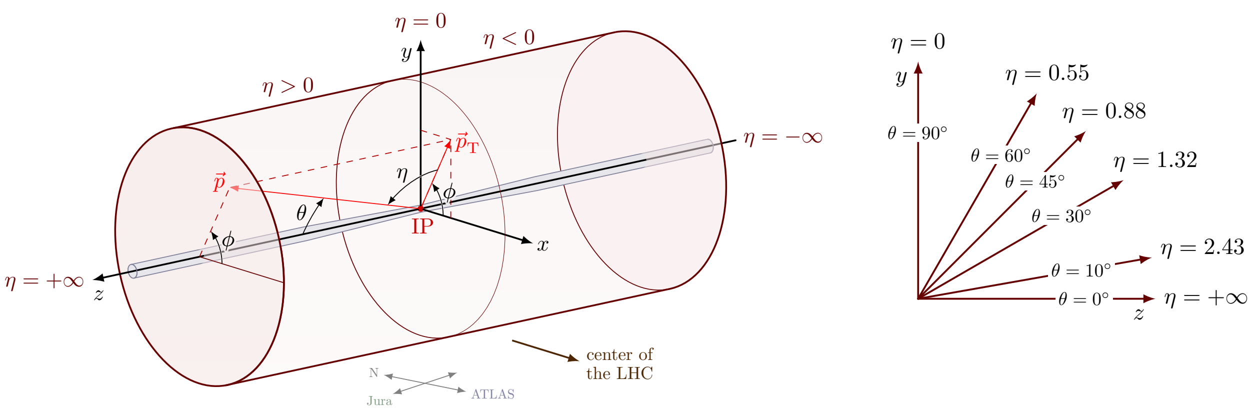

Figure 4.6: Left: The conventional coordinate system of CMS with respect to the LHC. The origin is set at the interaction point (IP). The direction of a momentum vector $\vec{p}$ is defined in terms of pseudorapidity η and azimuthal angle ϕ. The transverse momentum vector $\vec{p}_\mathrm{T}$ is defined as the projection of $\vec{p}$ onto the xy plane, which is transverse to the z axis along the beam line. **Right**: Several example values of $\eta = -\ln\left[\tan(\theta/2)\right]$ with the corresponding polar angle θ.

between two vectors with the variable

$$\Delta R = \sqrt{\Delta\phi^2 + \Delta\eta^2}, \tag{4.5}$$

where $\Delta\eta$ is the difference in pseudorapidity, and $\Delta\phi$ is the difference in azimuthal angle in radians. This is used as a Lorentz-invariant measure of the *opening angle* between particles and to define *cone size* of a group, or *jet*, of particles.

4.2.2 Geometry & layout

The CMS detector is designed to cover a solid angle as large as possible in order to capture most of the debris coming from collisions. It is therefore built out of several layers of subdetectors around the central interaction point. The subdetectors typically have a *barrel* section forming a cylindrical layer around the beam axis, and forward or *endcap* sections that cover the forward directions with disk-shaped detectors on either side. These layers are shown in Fig. 4.7 with the forward coverage measured in η. The subdetectors have the following order moving outwards from the collision point: a *tracking system* to measure the tracks of charged particles, an *electromagnetic calorimeter* to stop and measure the energy of electrons and photons, a *hadronic calorimeter* to stop and measure the energy of hadrons, and finally the *muon system*, which measures the charge and momentum of long-lived, minimum-ionizing muons by their tracks. In addition, two "very-forward" hadron calorimeters extend coverage up to $|\eta| < 5$ in either z direction.

4.2.3 The solenoid magnet & flux-return yoke

The inner tracker system and the calorimeters are enclosed by a *superconducting solenoid magnet*. The magnet is a 13 m long cylinder with an inner diameter of 6 m. It produces a very strong and uniform magnetic field of $B = 3.8$ Tesla inside the tracker volume with a field parallel with the z axis. In this way, charged particles are bent in the transverse plane so that their transverse momentum and electric sign can be measured from the curvature of their helical trajectory. The simplified relation is $p_{\mathrm{T}} = |q|BR$, where q is the charge, and R is the radius of curvature of the particle.

Outside the solenoid, the muon stations are interspersed with layers of iron which serve as a flux-return yoke to return approximately two thirds of the magnetic field inside the detector. This reduces the field outside the detector and provides added bending power in the muon detectors. The yoke also makes the field more homogenous in the tracker and even contributes about 8% of the central flux density. In addition, the yoke's steel serves as an absorber for the muon system [249].

4.2.4 The pixel tracker

The inner tracker system is comprised of two components: a *silicon pixel tracker*, and a *silicon microstrip tracker*. Figure 4.8 presents a closer look of the full tracker layout. The innermost part that is closest to the beam axis is the pixel tracker. The concentric cylindrical pixel layers are part of the so-called BPIX, while the disk layers in the two forward directions are part of the FPIX. The pixel tracker used from 2008 up to 2016 was composed of 1440 sensor modules with a total of 66 million silicon pixels that were distributed over three BPIX layers and two FPIX disks on either side [250]. During the technical shutdown between 2016 and 2017, the

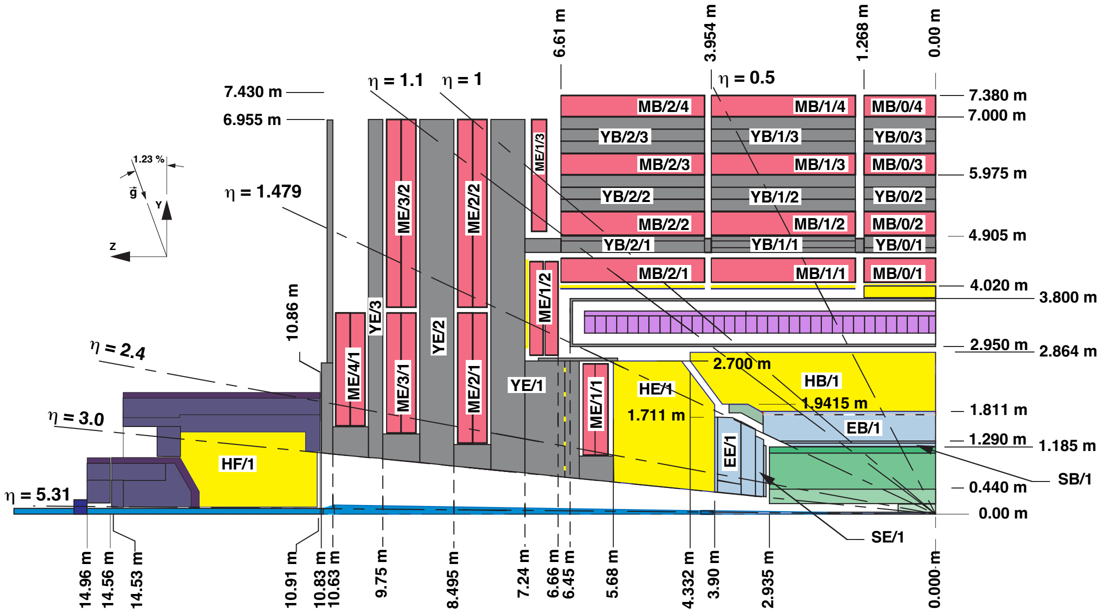

Figure 4.7: Schematic of one quadrant of the CMS detector in the positive zy-plane. Different values of pseudorapidity η are indicated. Shown are the tracker (green), the ECAL (light blue), the HCAL (yellow),the muon stations (red), the solenoid magnet (purple), and the iron flux-return yoke (dark grey). Adapted from [246].

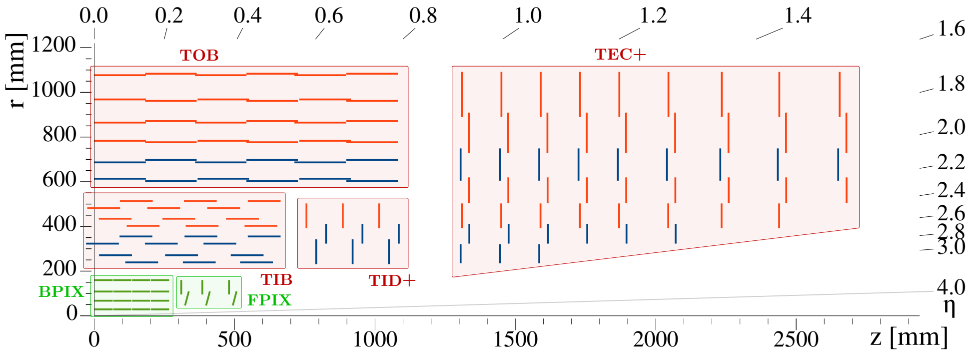

Figure 4.8: Schematic view of one quadrant of the CMS tracking system in the positive zr-plane, showing the positions of the tracking modules. The green boxes indicate the (Phase-1) pixel tracker; the red boxes the silicon strip detector. Adapted from from [247].

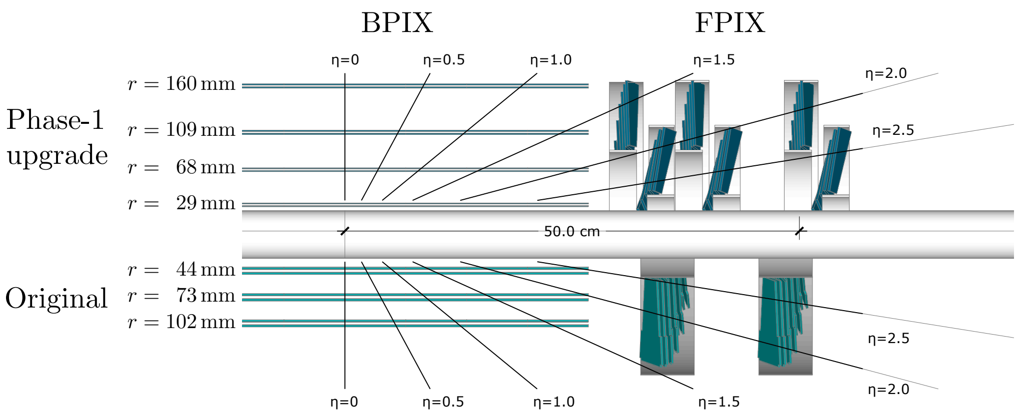

Figure 4.9: Layout of the CMS Phase-1 pixel detector (top) compared to the original detector layout used from 2008 to 2012 (bottom) in the zr-plane. Note the original beam pipe with a radius of 30 mm was replaced by one with a radius 23 mm was installed. Adapted from from [248].

system was upgraded to the "Phase-1" pixel detector with four BPIX layers and three FPIX disks on each end, and is built from 1856 modules with 124 million pixels in total [248, 251]. This was necessary because of the radiation damage the original pixel detector accumulated, and because the increased beam intensities during Run 2 required a larger buffer and readout bandwidth to ensure a good tracking efficiency. Additionally, four layers and a smaller radius for the innermost layer improve the tracking performance. Their layouts are compared in Fig. 4.9. The full longitudinal length of the barrel layers is less than 60 cm, while the disks are positioned at distances between $30 < |z| < 46.5\,\mathrm{cm}$ from the center, giving a coverage up to $|\eta| < 2.5$. The innermost layer of the original pixel tracker had a radius of 4.4 cm from the beam line, whereas the innermost layer of the Phase-1 tracker has a radius of only 2.9 cm. The pixels provides a spatial resolution of about 10 µm transversally ($r\phi$ direction) and between 20–30 µm longitudinally for the coordinates of charged particles that traverse them, depending on the pixel location, angle, and the amount of radiation they receive over time. Thanks to the good pixel resolution and the tracking and vertexing software, the three-dimensional position of collision vertices can be determined with a resolution down to about 10 µm for a vertex with more than 80 tracks, and down to 72 µm for those with around 10 tracks [250, 252]. This makes it possible to reconstruct and separate different vertices of nuclear or pp interactions by extrapolating tracks back towards the beam line. Furthermore, a precise measurement of the vertex position is needed to identify particles with a nonnegligible lifetime, like B hadrons and τ leptons, which may travel up to a few millimeters from the beam line before decaying and creating a *secondary* or *displaced vertex*. This will be discussed in more detail in Chapters 5 and 6.

4.2.5 The silicon strip tracker

The silicon strip tracker is larger, and is designed to measure the trajectory of charged particles and measure their momentum through their curvature in the magnetic field. The barrel section of the strip tracker encloses the pixel detector and has a radius of between 20 cm and 116 cm. This tracker section includes the inner and outer barrel tracker (TIB and TOB), as well as the inner disks (TID±) shown in Fig. 4.8. The endcaps (TEC±) give an additional longitudinal extension up to $|z| < 282\,\mathrm{cm}$. There are in total 15 148 modules with 9.3 million silicon strips. The hit resolution varies from 10 to 50 µm. All sections together offer coverage up to $|\eta| < 2.5$. A detailed description of the tracking and vertexing software is given in Ref. [250].

4.2.6 The electromagnetic calorimeter

The *electromagnetic calorimeter* (ECAL) is built around the tracker. It measures the energy of electrons [1] and photons by containing all their energy using a high-Z material absorber (i.e. with a large number of protons per atom). High-momentum electrons and photons interact electromagnetically with the ECAL, and create *electromagnetic showers*, a cascade of secondary photons from brehmsstrahlung, or electrons and positrons produced from photon conversion. The ECAL is built to fully capture the shower and absorb its energy. CMS uses lead tungstate crystals ($PbWO_4$) as scintillators to converted the absorbed energy to light. These crystals have been chosen because they have a short radiation length, are fast, and radiation hard. The ECAL does not need to be too thick thanks to the shower properties of its absorbing material. The whole detector (active material plus photon detectors) in the barrel region is about 512 mm

[1] Throughout the rest of this thesis "electron" also implies positron, unless specified otherwise.

thick in the radial direction, and 740 mm along the beam axis in the endcap region. This is enough to provide about 25 radiation lengths. The coverage of the barrel is up to $|\eta| < 1.48$, while the endcaps extend it up to $|\eta| < 3.0$. The crystals in the barrel region have a front area of about 22 mm × 22 mm, are 230 mm long and point almost radially outwards from the center. This corresponds to a granularity of about $\Delta\eta \times \Delta\phi = 0.0175 \times 0.0175$ rad. The crystals in the endcap region are a bit wider and shorter because of the projective geometry. *Silicon avalanche photodiodes* (APDs) at the end of the crystals collect and detect the scintillation light in the barrel region. In the endcap region this is done by *vacuum phototriodes* (VPTs). The energy resolution can be parametrized as a function of energy [245]:

$$\left(\frac{\sigma_E}{E}\right)^2 = \left(\frac{S}{\sqrt{E}}\right)^2 \oplus \left(\frac{N}{E}\right)^2 \oplus C^2, \tag{4.6}$$

with the stochastic term S, the noise N, and a constant term C. The final resolution varies from approximately 0.40 to 1%. The ECAL has been designed with the goal of precisely measuring the photon energies of the process $\mathrm{H} \to \gamma\gamma$ in order to reconstruct the Higgs boson mass. It is therefore important to have the best experimental mass resolution, which is much larger than the width of the Higgs signal. The best mass resolution achieved is about 1% for diphoton and dielectron masses around 100 GeV.

Between the tracker and ECAL endcaps sits a *preshower* detector. This is a thin lead conversion plate that causes electrons and photons to shower, with a thin layer of silicon detectors (SE) on the back that allows a measurement of the cross-sectional profile of the shower. This helps discriminate between a forward photon from the Higgs decay $\mathrm{H} \to \gamma\gamma$ and from the neutral pion decay $\pi^0 \to \gamma\gamma$ decay that are typically more collimated. [253, p. 231]. The technical design report [253] describes the ECAL in more technical detail.

4.2.7 The hadronic calorimeter

The last subdetector inside the solenoid is the *hadron calorimeter* (HCAL). Like the ECAL, it measures the energy of showers by completely absorbing them. However, the HCAL induces the shower through nuclear interactions from the incoming hadrons, while the ECAL is based on absorbing electromagnetic showers. The HCAL of CMS is a sampling calorimeter: It contains alternating layers of brass absorbers and plastic scintillators whose light is guided to *hybrid photodiode detectors* (HPDs) by fibres. The typical energy resolution of a jet of hadrons in the barrel is about 15–20% at a total transverse momentum of 30 GeV, 10% at 100 GeV, and 5% at 1 TeV [254].

The *very forward HCAL* (HF) is positioned around the beamline outside the detector, 11 m from the interaction point, and allows the measurement of very forward jets in the $3.0 < |\eta| < 4.7$ range. The HF is also a sampling detector that is designed to withstand the very high radiation environment in the forward direction. It is therefore made out of steel absorbers and radiation-hard quartz fibers for detection.

4.2.8 The muon system

Finally, there is the muon system, which is almost completely outside the solenoid magnet. This is the outermost and largest part of the detector: The barrel section covers $|z| < 6.6$ m along the beam line, and the endcaps extend the coverage to $5.7 < |z| < 10.9$ m. The muon system consists of several sections of muon detectors called *muon stations*: four *barrel wheels* and four *endcap* *disks*. The muon detectors are made out of several technologies for gaseous detectors: aluminum *drift tube chambers* (DTs) in the barrel region ($|\eta| < 1.2$) and *cathode strip chambers* (CSCs) in the endcap region ($0.9 < |\eta| < 2.4$). *Resistive plate chambers* (RPCs) complement each layer of muon stations in both regions. The CSCs are multiwire proportional chambers (MWPCs) comprised of six anode wire planes interleaved between seven cathode panels. They were chosen for the endcap because they can operate with precision in an environment with higher muon rates, higher rates of neutron induced backgrounds, and a large, nonuniform magnetic field. They offer an offline position resolution between 100 to 200 µm, depending on the station [255]. The DTs were chosen in the barrel region because the muon rate is smaller, there is a smaller neutron background, and the field is both weaker and more uniform. The position resolution is about 200 µm. The RPCs have coarser position resolution than the DTs and CSCs, but they offer fast readout and time resolution, which ensures good operation of muon triggers during high collision rates. The choice of having an excellent muon momentum resolution is what drives CMS's design and gives it its name. This includes the choice of a very strong solenoid magnet for large bending power, the large iron flux-return yoke outside, and the multiple layers of muon detectors. The latter improve the resolution significantly for muons with very large momenta ($p_{\mathrm{T}} > 200\,\mathrm{GeV}$) if combined with the inner tracker. At low momentum, the muon momentum resolution is mostly affected by multiple scattering due to the muon's Coulomb interaction with the detector material, while at large momentum, the resolution is driven by the resolution of the hit position that is needed to determine the curvature of the muon track. The final momentum resolution can be roughly parametrized as follows:

$$\left(\frac{\sigma_{p_{\mathrm{T}}}}{p_{\mathrm{T}}}\right)^2 = (A \cdot p_{\mathrm{T}})^2 \oplus C^2, \tag{4.7}$$

where A, and C are constants determined by the hit resolution and multiple scattering, respectively [256]. The resolution grows with momentum, because the track becomes more straight, which increases the uncertainty in its curvature. In total, CMS has an excellent muon reconstruction and identification efficiency of at least 95% for energies above a few GeV and a very good muon momentum resolution that varies between 1 and 6% for muons with $p_{\mathrm{T}} < 100\,\mathrm{GeV}$, and less than 10% for $p_{\mathrm{T}} < 1\,\mathrm{TeV}$ [257]. The charge sign of muons can be unambiguously determined for $p_{\mathrm{T}} < 1\,\mathrm{TeV}$. The technical design report can be found in Ref. [258].

4.2.9 The trigger system

The collision rate of 40 MHz is higher than is possible to record offline. However, most collisions are soft, and only a small fraction of events are of interest for physics analysis. Therefore, besides capturing and measuring collisions, the experiment must quickly select and accurately store only events that are potentially interesting for further analysis. This is the task of the *trigger system*. It works in two tiers. Fast readout from the calorimeters and muon detectors are first collected and analyzed by hardware processors in the *Level-1* (L1) trigger. The L1 trigger decides which events to keep at a rate of about 100 kHz, in a time interval of less than 4 µs after the collision itself. If the event is deemed interesting, it goes to the next level, the *high-level trigger* (HLT). Here, a full reconstruction of the event is carried out by a farm of processors with software that is optimized for fast processing. The HLT has more complex selection criteria to select events. Events passing the HLT are stored on disk. By then, the event rate has been reduced to an average of 400 Hz [259].

5 Object & Event Reconstruction

The lifetimes of particles like the Higgs, W, and Z bosons are extremely short ($\tau < 10^{-20}\,\mathrm{s}$) and they decay shortly after their creation in pp collisions. Even if they have a large momentum, which increases their lifetime in the lab frame due to time dilation, they will travel a negligible distance, never reaching the pixel detector. The same is true for most hypothetical scenarios with LQs. This means we have to infer their presence by analyzing pp collision events that leave a signal in the detector consistent with their decay.

In this thesis, I am interested in LQ signatures with at least two τ leptons and some number of (bottom) quarks (see Section 3.4.3). As the heaviest lepton, with a mass of $m_{\tau} = 1.776\,\mathrm{GeV}$, a τ lepton can decay not just to electrons and muons, but also to lighter hadrons. In each τ decay, there will be at least one neutrino carrying away some momentum.

Except for the weakly interacting neutrinos, each of the final state particles mentioned above interacts with the detector in some special way. This chapter is therefore devoted to describing how pp collision events and physics objects are reconstructed from data collected by the CMS detector and identified with dedicated algorithms. A separate chapter will be dedicated to τ leptons that decay to hadrons (τ_{h}), as their complex reconstruction builds on the techniques described in this chapter, and because I was involved with their reconstruction and identification in CMS.

5.1 Principles of particle identification at CMS

A pp collision event can produce many different types of particles with various masses and lifetimes. Figure 5.1 compares some prominent examples, dividing them in different regions of stability in the context of the CMS experiment. Electrons, muons, photons, and many hadrons like protons, neutrons, charged pions, and kaons have a lifetime that is long enough to travel through the detector without decaying. Each of these particles has a unique set of properties that leave a characteristic signal in one or more of the subdetector, as illustrated in Fig. 5.2. Electrically charged particles produce ionization in the silicon semiconductors and curve in the magnetic field, whereas neutral particles like neutrons and photons will pass through unbent with little to no interaction. Electrons and photons create electromagnetic showers in the ECAL. Hadrons shower in the HCAL via nuclear interactions, although a shower might already start in the ECAL. Muons are 207 times heavier than electrons, and are therefore less likely to emit bremsstrahlung and lose energy when moving through matter. This allows high-momentum muons to pass through the whole detector without decaying or being stopped. Muons are characterized by long, single tracks that are picked up by both the tracker and the muon system. Finally, neutrinos and hypothetical dark matter candidates will escape the detector without leaving any trace. Still, they carry away a large amount of momentum, a fact that can be exploited, as discussed later.

All these signatures are exploited in the reconstruction and identification of objects discussed below. However, these algorithms will never be 100% efficient, nor is there a guarantee that

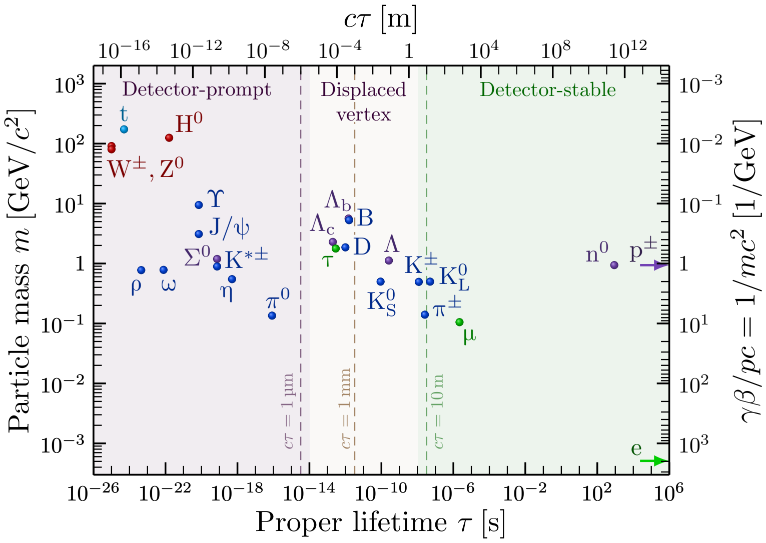

Figure 5.1: Plot of the mass versus lifetime τ of many composite and fundamental SM particles. The particles in the green-shaded region have a lifetime long enough to travel into the detector before decaying. Particles in the orange-shaded zone can travel some measurable distance, creating a decay vertex measurably displaced from the production vertex, whereas the decay length of those in the purple-shaded region are not observable. Note that relativistic particles will travel a larger distance on average due to time dilation, with the decay length given by $L = \gamma\beta c\tau$, with $\gamma\beta = p/mc$. Adapted from [260].

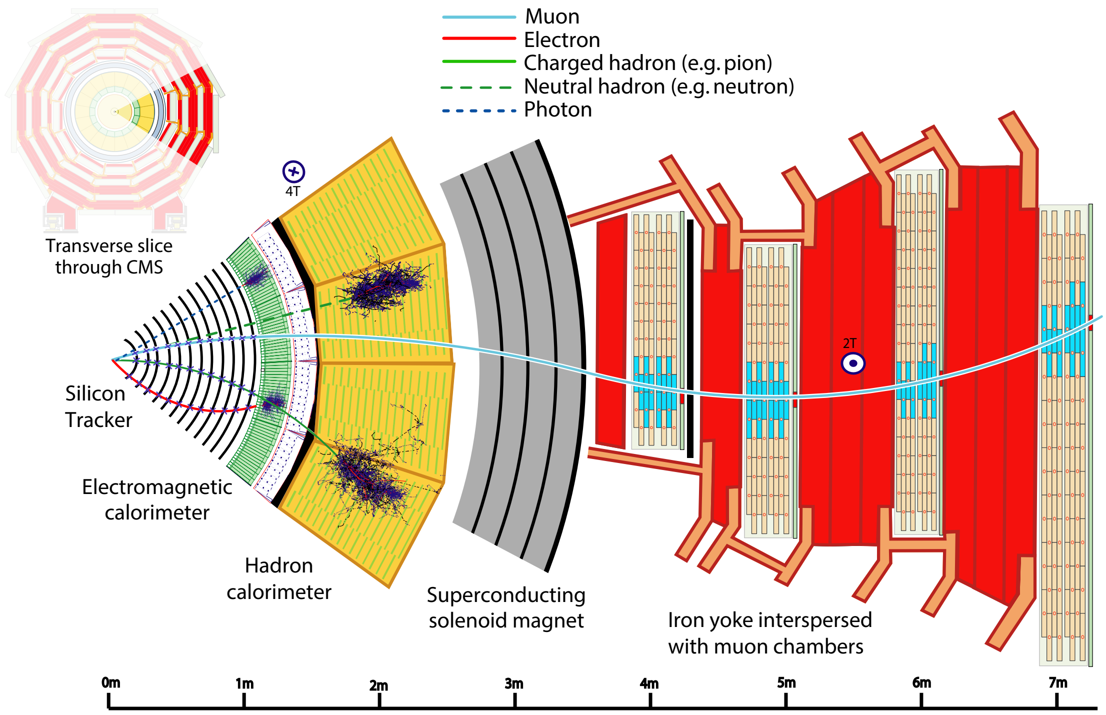

Figure 5.2: Cross-sectional segment of the CMS detector in the transverse plane illustrating how different types of particles interact with the various subdetectors and leave their signature. The straight, dashed tracks indicate electrically neutral particles that do not leave a measurable signal in the tracker. Neutrinos and hypothetical dark matter particles escape the detector without leaving a direct signal. Adapted from from [261].

the wrong particle will be rejected by an identification algorithm. Such a particle is referred to as a *fake*. Identification criteria often have several *working points* (WPs) that either have a high efficiency and a high *misidentification rate* ("loose" WP), or a lower efficiency with a lower misidentification rate ("tight" WP). The choice of WP is optimized for each analysis.

Collisions also generate high-momentum quarks and gluons, whether from proton debris, hard processes, or from the decay of some particle like the top quark or W boson. However, quarks and gluons cannot be isolated as free and stable particles as a consequence of color confinement in QCD. Instead, they hadronizes into a "jet" of hadrons as new quark and antiquarks are generated from the strong QCD fields until they form colorless bound states, i.e. hadrons. CMS reconstructs such jets by grouping particles into cones, as explained in Section 5.6. The only exception is the top quark, which decays almost exclusively into a bottom quark and a W boson instead of fragmenting into jets like the other quarks [262]. This is because the top's lifetime of $\tau \approx 5 \times 10^{-25}$ s is shorter than the time scale for fragmentation, which is around 10^{-24} s (or equivalently, a distance scale of about 1 fm) [263, 264].

Bottom quarks produced in high-energy collisions form B hadrons that have typical lifetimes of $\tau \sim 1.5$ ps. This is long enough for them to travel a measurable distance of the order of a few millimeters before decaying and creating a jet known as a *b jet*. This can therefore create a *secondary vertex* that is displaced from its production vertex, which CMS's tracking algorithm can reconstruct. As Fig. 5.1 shows, τ leptons and charmed hadrons are also capable of creating secondary vertices, although each of their decays tend to have a different topology, providing us with some efficiency for distinguishing them with identification algorithms.

Muon and electron candidates can be misidentified jets, or be a real lepton from a hadron decay inside a jet initiated by a quark or a gluon. Looking at Fig. 5.1, we see there are some particles that leave a displaced vertex, and when these are produced in a jet and then decay to a lepton, this lepton may pass standard lepton reconstruction requirements. Heavy-flavor hadrons are more likely to decay to muons or electrons inside the detector, for example $\mathrm{D}^{\pm} \to \ell^{\pm} X$ (33.7%), $\mathrm{D}^{0} \to \ell^{\pm} X$ (13.3%) [13, p. 43, 46]. B hadrons decay to these charmed hadrons, but they themselves also have a significant branching fraction of direct decay to electrons and muons: $\mathcal{B}(\mathrm{B} \to \ell^{\pm} X) \approx 21\%$ [13, p. 54, 61]. It is possible to discriminate against these cases by demanding that the lepton is relatively isolated from other particles with a cone of some ΔR size, because jets are typically associated with multiple particles.

5.2 Particle-flow algorithm

The particle-flow (PF) algorithm [265, 266] fully reconstructs the event of a pp collision with an optimized combination of all measurements of the CMS subsystems. It first combines signals from different detector components into so-called *PF elements*. These are tracks from the inner tracker, tracks from the muon system, and clusters from calorimeter cells. These elements are linked together if they are sufficiently close, and are consistent with that expected from electrons, muons, photons, charged hadrons, or neutral hadrons.

Tracks in the inner tracker or muon system are iteratively built from hits, using the *Kalman-filter* (KF) *technique* [267, 268]. Calorimeter clusters are built starting from a seed, which is a cell with the largest local energy, after which adjacent cells are iteratively combined into a cluster if their energy exceeds twice the noise level. In the HF, each cell is instead considered a separate cluster.

Photons are defined as ECAL clusters that are not linked with an extrapolated track, and their energy is obtained from the ECAL measurement. Charged particle tracks that are not identified as electrons or muons are assumed to be charged hadrons, and their momentum is determined by a combination of the measurements of the calorimeter and tracker, the latter of which is much more precise. Neutral hadrons are identified from HCAL energy clusters that cannot be linked to any track, or from an energy excess in the ECAL and HCAL that does not fit the expected energy deposit of a charged hadron. The reconstruction & identification of electrons and muons will be discussed in more detail below. The efficiency to correctly identify a track in the barrel with a p_T between 1 and 100 GeV is estimated to be better than 90% for isolated tracks from charged pions and electrons that are isolated, while for muons it is close to 100% [250]. The *objects* from PF are used to reconstruct objects composed of multiple particles like jets (Section 5.6) and hadronically decaying τ candidates (Chapter 6), and also to calculate the missing transverse energy (Section 5.8).

5.3 Primary vertex

The algorithm locates primary vertices (PVs) of pp collisions by finding tracks that emerge from them in three steps. It first selects tracks reconstructed by the PF algorithm that extrapolate back to the beam line and pass some quality requirements. Then tracks are clustered based on their z coordinate at their point of closest approach to the beam spot using the *deterministic annealing algorithm* [269]. Finally, candidate vertices with at least two associated tracks are fitted using an *adaptive vertex fitter* [270] to obtain the best vertex parameters.

The PVs in an event are ordered by the quadratic sum of the p_T of their tracks, $\sum_\mathrm{tracks} p_\mathrm{T}^2$. The one with the largest sum of squared transverse track momenta is assumed to be the vertex of the hard scattering process, while the others are considered to be pileup [250, 266, 271]. The efficiency to determine the correct vertex with three or more tracks is close to 100% [250]. The distribution of the number of PVs per beam crossing was shown in Fig. 4.4.

The PF algorithm removes the charged hadrons that are assigned to pileup PVs from the collection of objects for physics analysis. This is called *charged-hadron subtraction* (CHS). As neutral particles from PU cannot be associated with PVs, other correction techniques are needed for jets, lepton isolation, and the identification of hadronically decayed τ leptons.

5.4 Electrons

Electrons are reconstructed by associating a track in the inner tracker to clusters of energy deposits in the ECAL. One of the difficulties in reconstructing electrons is that they can emit a significant amount of bremsstrahlung before reaching the ECAL. This has two effects. Firstly, it causes significant and sudden changes in their curvature. As a consequence, the standard tracking algorithm based on the KF may not be able to collect all hits, and may make a poor estimation of the track parameters. That is why candidate tracks are refitted with the *Gaussian sum filter* (GSF) [272]. Secondly, the electron energy is also spread out over several ECAL crystals, mostly along the ϕ direction because of the bending of the electron trajectory in the magnetic field. The ECAL clusters within a certain geometrical window around a seed cluster are therefore recombined into a so-called *supercluster*.

As estimated from $\mathrm{Z} \to \mathrm{ee}$ decays, the momentum resolution for electrons with a p_T of approximately 45 GeV ranges from 1.6 to 5%. The resolution is generally better in the barrel region than in the endcaps, and depends on the amount of bremsstrahlung the electron radiates before reaching the ECAL [273, 274].

Electrons that are produced "promptly", i.e., produced at the PV, have several sources of background: photon conversion, hadrons misidentified as electrons, and secondary electrons from hadron decays. The electron identification is based on discriminating variables that can be grouped into the following three categories:

1. variables such as track-cluster matching that compare ECAL and tracker measurements;
2. ECAL measurements such as shower shapes (electromagnetic showers are typically more narrow than hadronic showers) and energy deposits in the HCAL or endcap preshower;
3. tracking measurements such as fit parameters (hadrons emit less bremsstrahlung) and separations with respect to charged hadrons.

The electron identification in this analysis is based on a multivariate analysis (MVA): A boosted decision tree (BDT) algorithm [275] is trained on these variables in bins of η and p_{T}. In addition, electrons must pass the requirement that rejects electrons from photon conversion. This analysis uses the MVA-based identification with a nominal 90% efficiency WP, based on a training without including isolation variables. The reconstruction and identification of electrons, as well as high-energy photons, are discussed in more detail in Refs. [276] and [273].

To discriminate against jets misidentified as leptons, a simple variable to quantify isolation, called the *relative isolation*, is often used. The most simple version is the sum over the p_{T} of all PF particles within a cone of some size ΔR, normalized by the lepton's own momentum, p_{T}^{ℓ}:

$$I_{\mathrm{rel}}^{\ell} := \frac{1}{p_{\mathrm{T}}^{\ell}} \sum_{\mathrm{particles}} p_{\mathrm{T}}. \tag{5.1}$$

This definition is further improved by not considering charged particles that originate from pileup, as well as subtracting the estimated contribution of neutral particles, with the so-called *rho-effective-area method* [277], quantified by the variable:

$$I_{\mathrm{rel}}^{\mathrm{e}} := \frac{\sum_{\mathrm{charged}} p_{\mathrm{T}} + \max\left(0, \sum_{\mathrm{neutral}} E_{\mathrm{T}} - \rho A_{\mathrm{eff}}\right)}{p_{\mathrm{T}}^{\mathrm{e}}}. \tag{5.2}$$

In this expression, $\sum_{\mathrm{charged}} p_{\mathrm{T}}$ is the scalar p_{T} sum of the charged hadrons originating from the PV, and located in a cone of size $\Delta R = 0.3$ centered on the electron direction. The sum $\sum_{\mathrm{neutral}} E_{\mathrm{T}}$ represents the same quantity for neutral hadrons and photons with the transverse energy calculated as $E_{\mathrm{T}} = E \sin\theta$. The neutral contribution from pileup is estimated as the event-specific ρA_{eff}, where ρ is the average pileup energy density per unit area in the $\phi\eta$ plane, and A_{eff} is the effective area in the $\phi\eta$ plane. For a given ΔR, the energy density ρ depends roughly linearly on the number of PVs in the event [276]. In the analysis presented in this thesis, $I_{\mathrm{rel}}^{\mathrm{e}} < 0.10$ is used as the isolation requirement for the electron.

5.5 Muons

Muon candidates in CMS are reconstructed as *standalone muons*, *tracker muons*, and/or *global muons* [278]. Standalone muons are tracks that are reconstructed solely from hits in the muon stations. Conversely, tracker muons are built from tracks reconstructed in the inner tracker that match at least one hit in the DT or CSC segments of the muon system. Global muons are obtained from standalone muons that match "inner" tracks. After finding such a match, a fit to the combined track with the KF is performed in order to improve the muon momentum resolution. Global muons and tracker muons are merged as a single muon candidate if they share the same inner track. Owing to the high tracking efficiency, about 99% of muons produced within the geometrical acceptance of the muon system are reconstructed as either a tracker or global muon [278]. Tracker muons that are not identified as global muons typically originate from remnant of a hadron shower in the HCAL that reaches the inner muon stations (*punch-through*). The energy and momentum of the muon candidate is determined from the curvature of the track.

A muon identification criterium is defined for three WPs: loose, medium, and tight. A loose muon is a PF muon that is either a tracker or global muon. These WPs are used to identify prompt muons originating from the PV and "secondary" muons from hadron decay, while maintaining a low rate for the misidentification of charged hadrons as muons. In the analysis for this thesis though, the medium WP is used. A medium muon is a loose muon that passes several quality criteria of the track.

Just like for electrons, the relative isolation of a muon can be defined. The contribution of neutral particles is taken into account with the so-called $\Delta\beta$*-corrections*:

$$I_{\mathrm{rel}}^{\mu} := \frac{\sum_{\mathrm{charged}} p_{\mathrm{T}} + \max\left(0, \sum_{\mathrm{neutral}} E_{\mathrm{T}} - \Delta\beta \sum_{\mathrm{charged,\ PU}} p_{\mathrm{T}}\right)}{p_{\mathrm{T}}^{\mu}}. \tag{5.3}$$

The muon isolation cone is of angular size $\Delta R = 0.4$. This expression is similar to Eq. (5.2), but in I_{rel}^{μ} the neutral contribution from pileup is estimated from the scalar p_{T} sum of charged hadrons originating from pileup vertices, $\sum_{\mathrm{charged,\ PU}} p_{\mathrm{T}}$. This sum is multiplied by a factor of $\Delta\beta = 0.5$, which corresponds approximately to the phenomenological ratio of neutral- to charged-hadron production in the hadronization process of inelastic pp collisions, as estimated from simulation. In the present thesis, $I_{\mathrm{rel}}^{\mu} < 0.15$ is used as the nominal isolation requirement for the muon.

5.6 Jets

Jets are most often reconstructed by a sequential clustering algorithm that iteratively groups particles together, based on some measure of distance d_{ij} between two reconstructed objects, and a cut d_{cut}. Such an algorithm starts by recombining all particle pairs (i, j) that are closest together in d_{ij}, as long as $d_{ij} < d_{\mathrm{cut}}$. After every step, the recombined pairs are removed from the list and replaced with a "proto-jet" that has their summed four-momenta. The algorithm stops when there are no pairs left that pass the cut.

A good jet algorithm must have two criteria. Firstly, the jet properties must be invariant under the radiation of a soft gluon (*infrared safe*). Secondly, the reconstruction must be insensitive to the collinear splitting of a particle (*collinear safe*), i.e., if a particle is replaced by two collinear particles who in sum have the same four-momentum.

There are several infrared and collinear-safe algorithms for jets in CMS. In this thesis, we use the *anti-*k_T (AK) *algorithm*, which utilizes the following metric:

$$d_{ij} := \min\left(p_{\mathrm{T,i}}^{-2}, p_{\mathrm{T,j}}^{-2}\right) \frac{\Delta R_{ij}^2}{\Delta R_y^2}, \tag{5.4}$$

where ΔR_y is a cone size parameter and $\Delta R_y = \sqrt{\Delta y^2 + \Delta\phi^2}$ is the distance in (y, ϕ)-space with the *rapidity*

$$y := \frac{1}{2} \ln\left(\frac{E + p_z}{E - p_z}\right), \tag{5.5}$$

not to be confused with Eq. (4.5), where $y \approx \eta$ if $p \gg m$, leading to Eq. (4.4). The ΔR_{ij} is the ΔR_y distance between particles i and j. If a cluster i of combined objects satisfies

$$d_{ij} > d_{i\mathrm{B}} = p_{\mathrm{T,i}}^{-2}, \tag{5.6}$$

the algorithm defines it to be a jet and removes its PF candidates from consideration in clustering subsequent jets. Here, d_{iB} is called i's distance to the beam [266, 279]. The PF jets are clustered with the standard cone-size parameter $\Delta R_y = 0.4$, and are therefore sometimes referred to as "AK4 jets". In CMS, the AK algorithm is implemented in the FastJet library [280, 281], and CHS is used to remove charged PF candidates not associated with the PV of the hard interaction.

The jet momentum is defined as the vectorial sum of all momenta of the jet constituents. In order to reconstruct the original quark or gluon accurately and precisely, the energy of jets needs to be calibrated to take into account detector noise and contributions from additional pp interactions within the same or nearby bunch crossings. The CMS Collaboration determines *jet energy corrections* (JECs) in several steps, which are explained in detail in Ref. [282]. Additionally, the jet energy and *jet energy resolution* (JER) of jets in simulation are corrected to obtain better agreement between simulation and data.

In the analysis presented in this thesis, two identification requirements are applied in order to distinguish genuine jets from those arising from pileup [283], as well as to remove spurious jet-like features that originate from isolated noise patterns in certain HCAL regions [284]. The latter is achieved with additional selection criteria on the energy fractions and multiplicity of charged and neutral particles, which corresponds to the "tight" jet identification in CMS. It has an almost 100% efficiency for jets with $p_{\mathrm{T}} > 30\,\mathrm{GeV}$ and $|\eta| < 0.5$, but degrades down to 97% in the forward region [284]. If candidate jets fall within a $\Delta R < 0.5$ from one of the selected τ lepton candidates (i.e., an electron, muon, or τ_{h} object), they are assumed to be the same object, and are removed from the jet collection.

5.7 Bottom quark identification

As mentioned in Section 5.1, the relatively long lifetime of B hadrons produced by bottom quarks can be exploited to identify bottom-quark intitiated jets. Besides lifetime, one can exploit the relatively large mass of the B hadron, and the pattern of fragmentation and decay. This is referred to as *b tagging*. Most b tagging algorithms use a combination of information about the secondary vertex and track parameters, like the impact parameter (distance of closest approach of the track to the PV), but also exploit information about the jet topology and other properties.

The LQ $\to$ bτ analysis employs the DeepCSV algorithm [285, 286] for b tagging jets. DeepCSV is a deep neural network (DNN) with four hidden layers that is an extension of the combined secondary vertex (CSV) algorithm [285, 286]. The loose and medium working points (WPs) of DeepCSV are used, which are respectively defined by a 10 and 1% misidentification rate of jets originating from light quarks or gluons. The η of tagged jets is required to have $|\eta| < 2.4$ (2.5) in 2016 (2017 and 2018). Figure 5.4 shows the efficiency and mistag rate

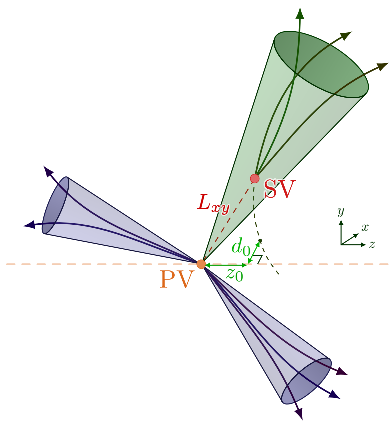

Figure 5.3: Because of its relatively long lifetime, a B hadron travels some distance on the order of 1 mm from the primary vertex (PV) where it was produced, before decaying and creating a secondary vertex (SV) with displaced tracks. Illustrated are the transverse and longitudinal impact parameters, d_0 and z_0, respectively, as well as the flight distance in the transverse plane, L_{xy}.

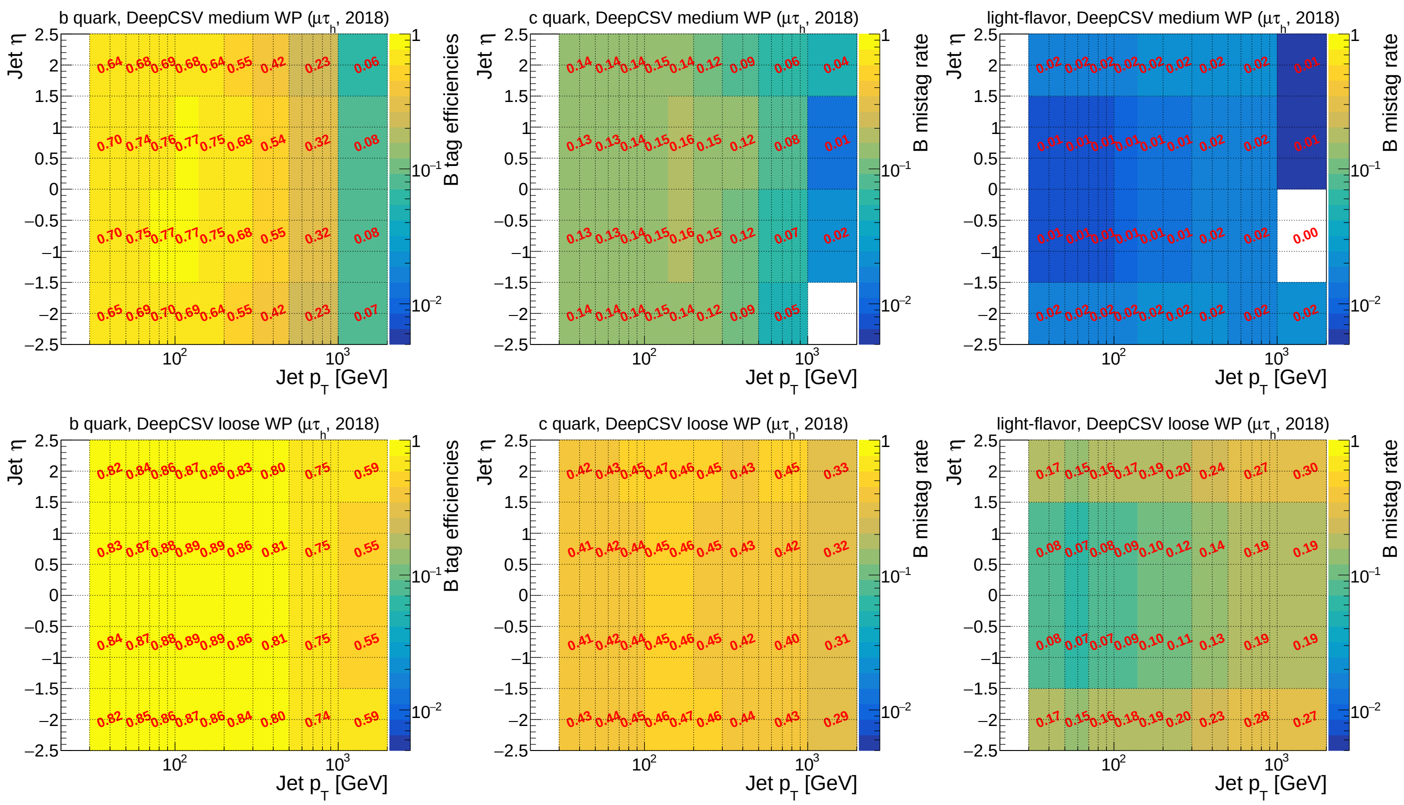

Figure 5.4: B tagging efficiencies (left column) and the mistag rate of jets originating from a c quark (center column), and originating from a light-flavor quark or gluon (right column) of the DeepCSV tagger in simulated events. The efficiencies and mistag rates are shown for the medium (top row) and loose WPs (bottom row) in $\mu\tau_\mathrm{h}$ events.

for jets in simulated events that pass the selections of the $\mu\tau_\mathrm{h}$ channel (see Chapter 10) and do not match the selected muon and τ_h candidates within $\Delta R < 0.5$. The efficiency and mistag rates are very similar between the different $\tau\tau$ decay channels. The medium WP has a typical efficiency of about 75%, while the loose WP efficiency can reach up to 90%, depending on the jet p_T and η. Nevertheless, the b tagging significantly degrades at $p_\mathrm{T} \gtrsim 500\,\mathrm{GeV}$, and more so for the medium than the loose WP.

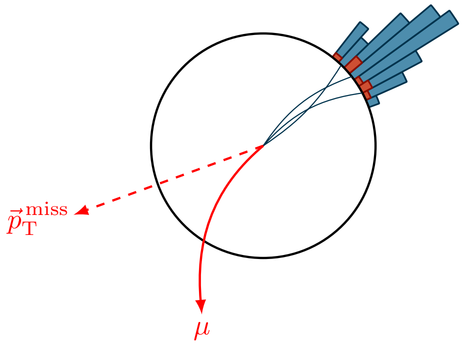

Figure 5.5: Simple illustration of missing transverse energy (MET), which is defined as the negative vectorial sum of the transverse momentum of all objects in the event. The red solid line represents a muon track, while the polar bars represent energy deposits in the ECAL (dark red) and HCAL (blue).

5.8 Missing transverse energy

As mentioned in Section 2.3, the longitudinal boost of the hard scattering is unknown, but the total transverse momentum is assumed to be exactly zero and conserved. This is useful to infer invisible particles that have carried away a significant amount of momentum, like neutrinos or hypothetical dark matter particles. After the PF algorithm has reconstructed all particles in the event and removed charged particles not coming from the PV, it vectorially sums the remaining objects to determine the total transverse momentum that is missing:

$$\vec{p}_{\mathrm{T}}^{\mathrm{miss}} := -\sum_{\mathrm{i}} \vec{p}_{\mathrm{T}}^{\,i}. \tag{5.7}$$

This vector, or its length, is often referred to as the *missing transverse momentum*, or *missing transverse energy* (MET). The accuracy of the MET relies on a good calibration of all PF objects. Therefore, the calibration of the jet energy scale has to be propagated correctly. Several other corrections are applied, for example, in case the computed MET is very large, the PF algorithm checks for cosmic muons, badly reconstructed muon tracks, and fake muons [266]. More details can be found in Refs. [287] and [288].

6 Reconstruction & Identification of Hadronically Decayed τ Leptons

A significant fraction of τ leptons decay to hadrons and such decays are denoted as τ_h. It is therefore an important decay mode in physics analyses that target final states including τ leptons, and accurately and precisely reconstructing such decays becomes crucial. A dedicated identification algorithm is needed to reduce the large backgrounds mimicking this type of decay, while maintaining a good efficiency for genuine τ decays.

During my PhD, I have been involved with several projects of the *Tau Physics Object Group* (TauPOG) in the CMS Collaboration. This included the measurement of the τ_h reconstruction and identification efficiency, as well as the τ_h energy scale. A new τ_h identification algorithm, called DeepTau [289], was developed during my work on the search for an LQ coupling to bτ. I contributed to the first validation of DeepTau in comparisons between Run-2 data and simulation, before applying it in our own LQ analysis to attain a significant gain in signal sensitivity.

This chapter will discuss the reconstruction and identification of τ_h objects in CMS used during Run 2. The measurement of its performance and corrections to simulation will be discussed in Chapter 9.

6.1 τ lepton decay

With a mass of $m_\tau = 1.776\,\mathrm{GeV}$, the τ lepton is the heaviest lepton. It can not only decay to electrons and muons, but also to the lighter pions ($m_\pi \approx 0.14\,\mathrm{GeV}$) and kaons ($m_K \approx 0.50\,\mathrm{GeV}$) through the weak interaction. Figure 6.1 shows two examples of Feynman diagrams at tree level. As the left pie chart in Fig. 6.2 shows, τ leptons decay leptonically about 35.2% of the time, while the hadronic final state has the largest branching ratio, 64.8%. As a consequence, one pair of τ leptons has hadrons in its final state about 88% of time. Specifically, the branching fraction of the semileptonic final state ($e\tau_h$, $\mu\tau_h$) is 46%, while that of the fully hadronic state ($\tau_h\tau_h$) is 42%. Fully leptonic decays of a τ pair not only have a small branching fraction of 12%, but they also tend to have a larger background from Drell-Yan ($Z/\gamma^* \to \ell^+\ell^-$), top quark pair

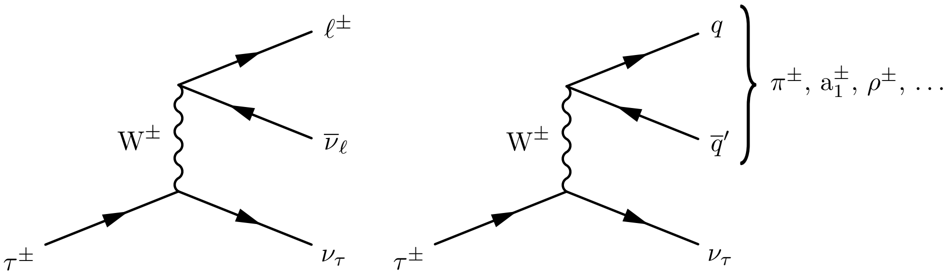

Figure 6.1: Tree-level Feynman diagrams of τ lepton decay through the weak interaction [290, 291]. **Left**: Leptonic decay $\tau^\pm \to \ell^\pm\overline{\nu}_\ell\nu_\tau$ with $\ell = e, \mu$. **Right**: Hadronic decay $\tau^\pm \to q\overline{q}'\nu_\tau$. These quarks can form intermediate resonances like $\pi^\pm$, $a_1^\pm$, and $\rho^\pm$. The latter two will further decay mostly into pions: $\rho^\pm \to \pi^\pm\pi^0$, and $a_1^\pm \to \rho^\pm\pi^0 \to \pi^\pm\pi^0\pi^0$ or $a_1^\pm \to \rho^0\pi^\pm \to \pi^\pm\pi^\mp\pi^\pm$ [13].

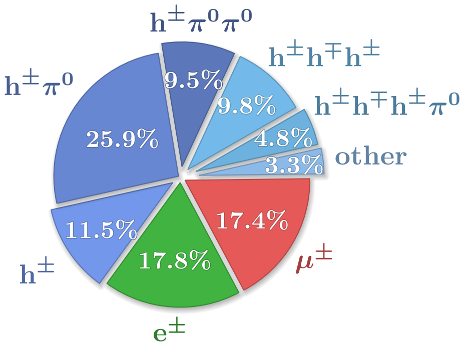

Figure 6.2: Pie charts of branching fractions of a single τ lepton and a pair of τ leptons. **Left**: τ lepton decay. For leptonic decay there are two neutrinos, and for hadronic decay only one. (τ_h stands for the hadronic decay.) **Right**: Decay channels of a pair of τ leptons. Numbers from PDG [13, p. 28].

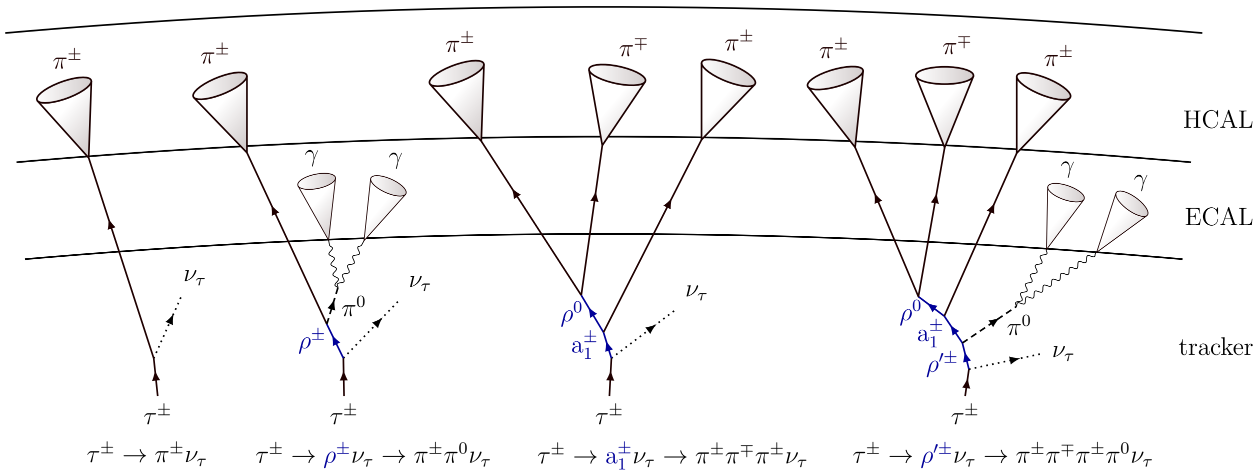

Figure 6.3: An illustration of the detector signatures of several common hadronic decay modes of the τ lepton. Charged pions typically leave a track in the tracker and energy deposits in the HCAL. Neutral pions π^0 promptly decay to photons that create ECAL showers, reconstructed as strips by the HPS algorithm. Also shown are examples of intermediate resonances (blue) corresponding to bound states of quarks such as the vector ρ meson and pseudovector a_1 meson. Not to scale. Inspired by Ref. [292, p. 37].

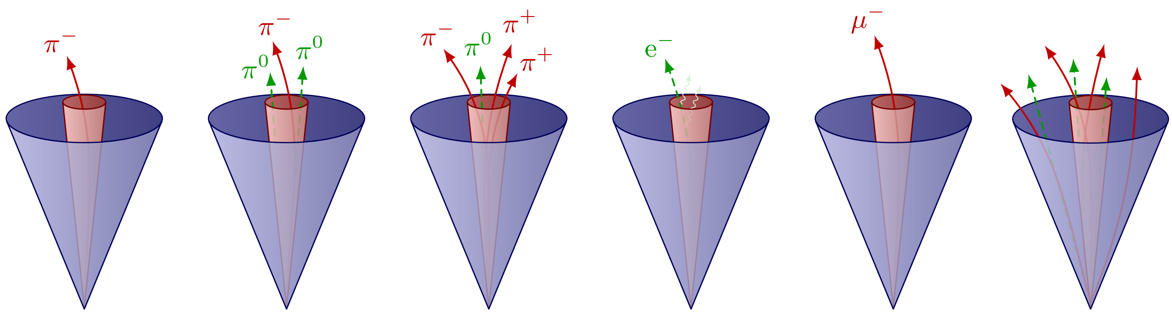

(a) Genuine π^-. **(b)** Genuine $\pi^-\pi^0\pi^0$. **(c)** Genuine $\pi^+\pi^-\pi^+\pi^0$. **(d)** Isolated electron. **(e)** Isolated muon. **(f)** Quark or gluon jet.

Figure 6.4: Illustration of several hadronic decay modes of the τ leptons (a-c) and their backgrounds (d-f). With $p_T \gtrsim 15\,\text{GeV}$, genuine hadronic τ decays form very collimated jets of some number of light hadrons that fall in a signal cone with an opening angle $0.05 \leq \Delta R \leq 0.1$ (red). This can easily be mimicked by quark-/gluon-initiated jets, although they tend to have more activity in the isolation cone of $\Delta R = 0.4$ (blue). Furthermore, electrons and muons can form well-isolated single-track jets like the $h^{\pm}$ decay mode, and electrons can be misidentified as the $h^{\pm}\pi^0$ mode as well due to their ECAL clusters.

($\mathrm{t\bar{t}}$), or diboson production. The semileptonic and fully hadronic decay channels are therefore essential for physics analyses with two τ lepton in the final state.

As discussed in Section 5.1, the τ lepton has a very short mean lifetime of $\tau = 2.90 \times 10^{-13}\,\mathrm{s}$, or $0.290\,\mathrm{ps}$ [13, p. 28]. The decay length is given by $L = \gamma\beta c\tau \approx pc \times 49.0\,\mathrm{\mu m/GeV}$, so a τ lepton with a momentum $p = 20\,\mathrm{GeV}$ travels on average about 1 mm before decaying. The direct observation of a τ lepton track was first reported by the CHORUS experiment in 1998 [293, 294], and later by the DONUT experiment in 2001 [30]. They both used nuclear emulsions to capture the short track and look for a "kink" indicating its decay. In the context of the CMS detector, τ leptons produced at the beam line will not reach the pixel tracker, and have to be inferred from their decay signature. And although the decay length is shorter than that of heavy-flavored hadrons, the excellent vertex and impact parameter resolution of the pixel tracker provide us a good handle on the secondary vertex for efficient identification.

Figure 6.3 showcases several detector signatures characteristic of common hadronic decay modes. Most of the charged hadrons in τ decays are pions or kaons, which typically create a track and leave energy deposits in the HCAL before decaying. About 65% of hadronic τ decays involve neutral pions, which decay promptly ($\tau = 8.4 \times 10^{-17}\,\mathrm{s}$) to two photons 98.8% of the time [13, p. 33]. Furthermore, for τ leptons with momenta typical for physics analyses ($p_\mathrm{T} \gtrsim 15\,\mathrm{GeV}$), the decay products will be sufficiently boosted to form a collimated jet with a size of about $\Delta R < 0.10$, as shown in Fig. 6.4. Therefore, a narrow jet with one or three charged hadrons (*prongs*) with perhaps some ECAL deposits is a helpful signature to identify most hadronic τ decays.

One other interesting feature of hadronic decays is that several decay modes have an intermediate resonance as shown in Fig. 6.3. In particular, $\tau^\pm \to h^\pm\pi^0\nu_\tau$ has a $\rho(770)$ intermediate resonance, while $\tau^\pm \to h^\pm\pi^0\pi^0\nu_\tau$ and $\tau^\pm \to h^\pm h^\mp h^\pm\nu_\tau$ predominantly go through $\mathrm{a}_1(1260)$ [294, p. 85]. Both these meson decays promptly in one or more steps to pions and kaons. These intermediate resonances shape the measured distribution of the invariant mass of the visible decay products, that we can use to define efficient mass ranges per decay mode. The resonant structure of four-pion decays, like $\tau^\pm \to h^\pm h^\mp h^\pm\pi^0\nu_\tau$, is much more complicated due to a multitude of intermediate decay products, of which $\rho' = \rho(1450)$ is one [295–297].

6.2 The HPS reconstruction algorithm

Hadronic decays of τ leptons are reconstructed with the *hadron-plus-strips* (HPS) *algorithm* [289, 298–300]. First, the algorithm starts from PF jets that were reconstructed by the anti-k_T algorithm with a distance parameter of $\Delta R = 0.4$ (see Section 5.6). These jets serve as seeds for τ_h candidates. All PF particles within $\Delta R \leq 0.5$ around the jet axis are considered in the following steps. Charged particles used to construct the τ_h object must have $p_\mathrm{T} > 0.5\,\mathrm{GeV}$, and a transverse impact parameter $d_{xy} < 0.1\,\mathrm{cm}$ from the PV, while electrons and photons must have $p_\mathrm{T} > 1\,\mathrm{GeV}$.

Secondly, the algorithm reconstructs π^0 candidates as so-called *strips* from the jet constituents. Because photons are frequently converted into an $\mathrm{e}^+\mathrm{e}^-$ pair, both electron and photon constituents in the jet are clustered into rectangular windows in the $\eta\phi$ plane, called strips. The strips are narrow in η, but extended in the ϕ direction due to the spreading out of $\mathrm{e}^+\mathrm{e}^-$ conversion pairs in the magnetic field. They are seeded by the most energetic electron and photon (e/γ) candidate. Other candidates that fall inside some $\Delta\eta \times \Delta\phi$ window around the strip center are iteratively added to the strip until no new candidates are found in the window. Each time the strip momentum is recomputed as the vectorial sum of all strip constituents. This process is repeated until all e/γ objects in the jet are clustered in a strip. The strip size and position is discussed separately in Section 6.2.1.

Thirdly, from the set of highest-energy charged hadrons and strips (up to six each) within the seed region, τ_h candidates are reconstructed by making all possible combinations of charged hadrons and strips that are compatible with one of seven "reconstructed decay modes" listed in Table 6.1:

Table 6.1: Reconstructed τ_h decay modes

DM	Decay mode	Target τ decay
0	$h^\pm$	$\tau^\pm \to h^\pm \nu_\tau$
1	$h^\pm \pi^0$	$\tau^\pm \to h^\pm \pi^0 \nu_\tau$
2	$h^\pm \pi^0 \pi^0$	$\tau^\pm \to h^\pm \pi^0 \pi^0 \nu_\tau$
5	$h^\pm h^{\pm/\mp}$	$\tau^\pm \to h^\pm h^\mp h^\pm \nu_\tau$
6	$h^\pm h^{\pm/\mp} \pi^0$	$\tau^\pm \to h^\pm h^\mp h^\pm \pi^0 \nu_\tau$
10	$h^\pm h^\mp h^\pm$	$\tau^\pm \to h^\pm h^\mp h^\pm \nu_\tau$
11	$h^\pm h^\mp h^\pm \pi^0$	$\tau^\pm \to h^\pm h^\mp h^\pm \pi^0 \nu_\tau$

Within CMS, the hadronic decay modes are uniquely numbered by

$$\mathrm{DM} = 5 \times (N_\mathrm{prongs} - 1) + N_\mathrm{strips}. \tag{6.1}$$

which is indicated by the first column of Table 6.1. The decay modes with two charged hadrons are included to recover τ decays with three hadrons where one hadron is not reconstructed as a hadron or a track. The (visible) four-momentum of the τ_h candidate is simply the vectorial sum of its charged hadron and strip constituents, from which the invariant mass m_{τ_h} is computed. For the $h^\pm$ decay mode the pion mass is assumed. The τ_h charge is the sum of the charged hadrons, except for the decay modes with only two hadrons, for which the charge is set to the charge of the hadron with the larger p_T.

Fourth, a single τ_h candidates is chosen among the candidates that satisfy the following constraints:

- The invariant mass of the candidate must fall within a *mass window* of some assumed intermediate resonance. This is discussed in more detail in Section 6.2.2.
- The τ_h charge must be ± 1.
- The charged hadrons and strips used in the τ_h reconstruction must fall within a *signal cone* of size $\Delta R = 3\,\mathrm{GeV}/p_\mathrm{T}$ (limited to the range 0.05–0.1) around the τ_h momentum.

The candidate with the highest p_T is chosen. Besides a signal cone, an *isolation cone* of $\Delta R = 0.5$ around the τ_h axis is defined to measure the activity around a τ_h candidate that is not used for the construction of the final τ_h object.

6.2.1 Dynamic strip reconstruction

During Run 1, the window size was fixed to $\Delta\eta \times \Delta\phi = 0.05 \times 0.20$ [298]. However, this size is not always large enough to contain all (secondary) particles from hadronic τ decay, like low-p_T particles from nuclear interaction between charged hadrons and the detector, or secondary electrons and photons from π^0 decays that undergo multiple scattering and bremsstrahlung. This can lead to a worse τ_h reconstruction, but also a reduced identification efficiency because

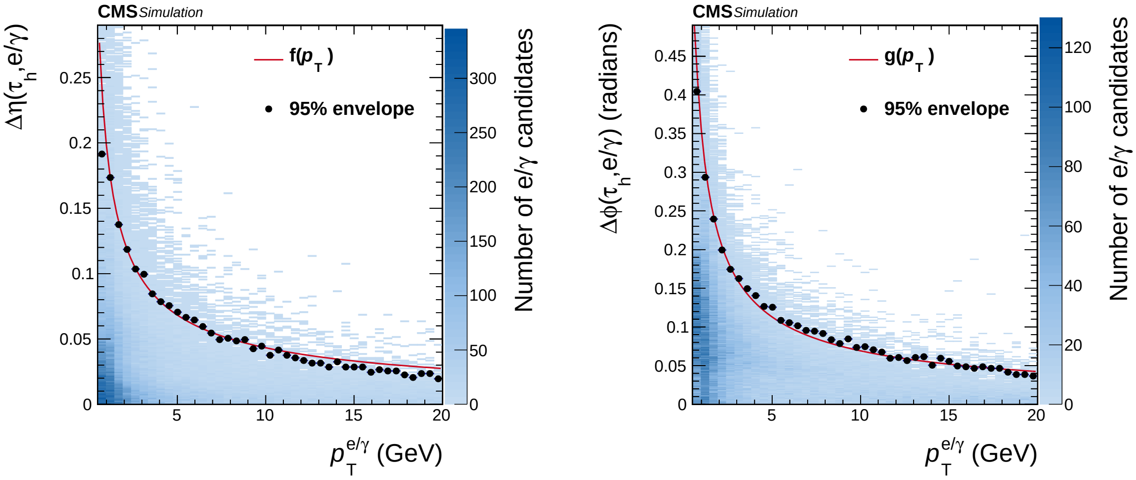

Figure 6.5: $\Delta\eta$ (left) and $\Delta\phi$ between the τ_h and e/γ candidate for strip reconstruction as a function of $p_T^{e/\gamma}$ of the e/γ candidate. A sample of simulated events with a single τ that has a uniform p_T in the range 20–400 GeV and $|\eta| < 2.3$ is used. The black points indicate the 95% envelope for a given $p_T^{e/\gamma}$ bin, and the red solid line represents the fitted function f and g given by Eqs. 6.2 and 6.3. Figures taken from [300].

particles that fall outside the strip window can contribute to worse isolation. Conversely, smaller windows reduce background contributions to strips of genuine τ_h decays with high p_T, which have more collimated decay products, while simultaneously allowing for better rejection of the less isolated jets initiated by a quark or a gluon ("quark or gluon jets"). This is why the *dynamic strip reconstruction* was introduced to dynamically determine the strip size and position during Run 2 [299, 300].

The $\eta\phi$ dimensions of the strip are determined as simple functions of p_T, such that the strip contains about 95% of all e/γ candidates from τ_h decay as determined from a study on simulated events with a single τ_h object that has a uniform p_T distribution in the range 20–400 GeV and $|\eta| < 2.3$. Analytic functions of the form $a/(p_T/\text{GeV})^b$ are obtained separately for $\Delta\eta(\tau_h, e/\gamma)$ and $\Delta\phi(\tau_h, e/\gamma)$ between the τ_h and e/γ candidate by fitting all 95% envelope points in each $p_T^{e/\gamma}$ bin as shown in Fig. 6.5. The results are

$$f(p_T) = 0.20 \cdot (p_T/\text{GeV})^{-0.66}, \tag{6.2}$$
$$g(p_T) = 0.35 \cdot (p_T/\text{GeV})^{-0.71}, \tag{6.3}$$

for $\Delta\eta(\tau_h, e/\gamma)$ and $\Delta\phi(\tau_h, e/\gamma)$, respectively.

The HPS algorithm with dynamic strip reconstruction proceeds as follows [300]:

1. A seed is obtained from the highest-p_T e/γ candidate not yet included in a strip. The initial η_{strip} and ϕ_{strip} position of the strip's center is set to the η and ϕ of the seed.
2. The e/γ candidate that has the next highest p_T and falls within

$$\Delta\eta = \min\left[f(p_T^{\gamma}) + f(p_T^{\text{strip}}), 0.15\right], \tag{6.4}$$
$$\Delta\phi = \min\left[g(p_T^{\gamma}) + g(p_T^{\text{strip}}), 0.30\right], \tag{6.5}$$

from the strip center, is added to the strip. The $\Delta\eta$ is limited to the range 0.05–0.15, while $\Delta\phi$ is limited to 0.05–0.30.

3. The strip position is recomputed as a p_T-weighted average of all e/γ constituents:

$$\eta_\text{strip} = \frac{1}{{S_\mathrm{T}}^\text{strip}} \sum_c p_\mathrm{T}^c \eta_c, \tag{6.6}$$

$$\phi_\text{strip} = \frac{1}{{S_\mathrm{T}}^\text{strip}} \sum_c p_\mathrm{T}^c \eta_c, \tag{6.7}$$

where ${S_\mathrm{T}}^\text{strip} = \sum_c p_\mathrm{T}^c$ is the total scalar sum p_T.

4. Steps 2 and 3 are repeated until no further e/γ candidates are found within the $\Delta\eta \times \Delta\phi$ window.

6.2.2 Mass constraints

The invariant mass of each τ_h candidate must fall in a certain range to ensure compatibility with the respective τ_h decay mode the candidate was reconstructed in. This window is optimized for each decay mode to maximize the ratio of the τ_h reconstruction efficiency to the probability of misidentifying a jet. Furthermore, for decay modes with strips and $p_\mathrm{T}^{\tau_\mathrm{h}} > 100\,\mathrm{GeV}$, the upper mass limit is enlarged as a function of $\sqrt{p_\mathrm{T}^{\tau_\mathrm{h}}}$ to account for the resolution at high p_T. The limits for decay modes with strips are also enlarged as a function of the strip size because the energy of a strip depends on its size. As an estimation of the change in m_{τ_h} brought about by the addition of e/γ candidates to the strip, the quantity $\Delta m_{\tau_\mathrm{h}}$ is constructed as

$$\Delta m_{\tau_\mathrm{h}} = \sqrt{\left(\frac{\partial m_{\tau_\mathrm{h}}}{\partial \eta_\text{strip}} f\left(p_\mathrm{T}^\text{strip}\right)\right)^2 + \left(\frac{\partial m_{\tau_\mathrm{h}}}{\partial \phi_\text{strip}} g\left(p_\mathrm{T}^\text{strip}\right)\right)^2}, \tag{6.8}$$

with the partial derivatives

$$\frac{\partial m_{\tau_\mathrm{h}}}{\partial \eta_\text{strip}} = \frac{p_z^\text{strip} E_{\tau_\mathrm{h}} - E_\text{strip} p_z^{\tau_\mathrm{h}}}{m_{\tau_\mathrm{h}}}, \tag{6.9}$$

$$\frac{\partial m_{\tau_\mathrm{h}}}{\partial \phi_\text{strip}} = \frac{\left(p_x^{\tau_\mathrm{h}} - p_x^\text{strip}\right) p_y^\text{strip} - \left(p_y^{\tau_\mathrm{h}} - p_y^\text{strip}\right) p_x^\text{strip}}{m_{\tau_\mathrm{h}}}, \tag{6.10}$$

where $p^\mu_{\tau_\mathrm{h}} = (E_{\tau_\mathrm{h}}, p_x^{\tau_\mathrm{h}}, p_y^{\tau_\mathrm{h}}, p_z^{\tau_\mathrm{h}})$ and $p^\mu_\text{strip} = (E_\text{strip}, p_x^\text{strip}, p_y^\text{strip}, p_z^\text{strip})$ are the four-momenta of the τ_h candidate and strip, respectively. The mass windows are defined as follows [300, 301]:

- For $\boldsymbol{h}^\pm$, $0 < m_{\tau_\mathrm{h}} < 1\,\mathrm{GeV}$ to allow for kaons. After a τ_h candidate with this decay mode is chosen, the mass is fixed to the pion mass, $m_{\tau_\mathrm{h}} = 0.140\,\mathrm{GeV}$ because in about 94% of one-prong decays, the hadron is a charged pion [13, p. 28].
- For $\boldsymbol{h}^\pm\boldsymbol{\pi}^\mathbf{0}$, $0.3\,\mathrm{GeV} - \Delta m_{\tau_\mathrm{h}} < m_{\tau_\mathrm{h}} < 1.3\sqrt{p_\mathrm{T}^{\tau_\mathrm{h}}\,\mathrm{GeV}/100} + \Delta m_{\tau_\mathrm{h}}$, with the upper limit constrained between 1.3 and 4.2 GeV.
- For $\boldsymbol{h}^\pm\boldsymbol{\pi}^\mathbf{0}\boldsymbol{\pi}^\mathbf{0}$, $0.4\,\mathrm{GeV} - \Delta m_{\tau_\mathrm{h}} < m_{\tau_\mathrm{h}} < 1.4\sqrt{p_\mathrm{T}^{\tau_\mathrm{h}}\,\mathrm{GeV}/100} + \Delta m_{\tau_\mathrm{h}}$, with the upper limit constrained between 1.2 and 4.0 GeV.
- For $\boldsymbol{h}^\pm\boldsymbol{h}^{\pm/\mp}$, $0.4\,\mathrm{GeV} < m_{\tau_\mathrm{h}} < 1.2\,\mathrm{GeV}$.
- For $\boldsymbol{h}^\pm\boldsymbol{h}^{\pm/\mp}\boldsymbol{\pi}^\mathbf{0}$, $0 < m_{\tau_\mathrm{h}} < 1.2\sqrt{p_\mathrm{T}^{\tau_\mathrm{h}}\,\mathrm{GeV}/100} + \Delta m_{\tau_\mathrm{h}}$, with the upper limit constrained between 1.2 and 4.0 GeV.
- For $\boldsymbol{h}^\pm\boldsymbol{h}^\mp\boldsymbol{h}^\pm$, $0.8\,\mathrm{GeV} < m_{\tau_\mathrm{h}} < 1.5\,\mathrm{GeV}$.
- For $\boldsymbol{h}^\pm\boldsymbol{h}^\mp\boldsymbol{h}^\pm\boldsymbol{\pi}^\mathbf{0}$, $0.9\,\mathrm{GeV} - \Delta m_{\tau_\mathrm{h}} < m_{\tau_\mathrm{h}} < 1.6 + \Delta m_{\tau_\mathrm{h}}$.

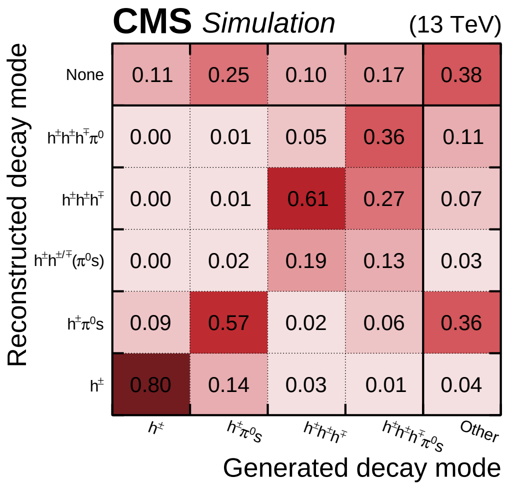

Figure 6.6: Confusion matrix of τ_h decay mode reconstruction. For each generated τ_h decay mode (column), the fractions of decay mode it is reconstructed as are shown. A sample of $Z \to \tau^+\tau^-$ events with $m_{\tau\tau} > 50\,\text{GeV}$ is used. Both generated and reconstructed τ_h fulfill $p_T > 20\,\text{GeV}$ and $|\eta| < 2.3$. Taken from [289].

6.2.3 Reconstruction performance

Figure 6.6 show how τ_h decays with $p_T > 20\,\text{GeV}$ and $|\eta| < 2.3$ from a sample of $Z \to \tau^+\tau^-$ events are reconstructed. For example, the $h^\pm$ decay mode is correctly reconstructed 80% of the time, while $h^\pm h^\mp h^\pm$ is correctly reconstructed with a probability 61%, and is recovered by the two-prong decay modes with a rate of 19%. The fraction of τ_h decays not reconstructed at all ranges from 10% for $h^\pm h^\mp h^\pm$ to 25% for $h^\pm\pi^0$. The reconstruction efficiency of genuine τ_h decays is limited by the reconstruction of charged hadrons, which in the barrel has an efficiency of around 90% for pions with $1 < p_T < 100\,\text{GeV}$ [250]. The correct charge assignment for decay modes without missing hadrons varies from about 99% for $p_T < 200\,\text{GeV}$ to 92% for $p_T \sim 1\,\text{TeV}$, while the charge assignment for two-prong decay modes is correct in only 70% of the cases [289].

The two-prong decay modes are mostly useful for analyses that are not limited by backgrounds, and the decay mode $h^\pm\pi^0\pi^0$ has an extremely low branching fraction times efficiency. Therefore, I will only consider the reconstructed $h^\pm$, $h^\pm\pi^0$, $h^\pm h^\mp h^\pm$, and $h^\pm h^\mp h^\pm\pi^0$ decay modes in this thesis.

6.3 The DeepTau identification algorithm

When searching for hadronically decaying tau leptons, there is a huge background of quark and gluon jets because τ_h decays are effectively collimated jets of hadrons, as illustrated in Fig. 6.4. Additionally, electrons and muons can form well-isolated single-track jets as the $h^\pm$ decay mode, and electrons can be misidentified as the $h^\pm\pi^0$ mode as well due to its ECAL clusters. Jets initiated by a quark or gluon tend to have a larger cone size with more activity than τ_h decays. Therefore, requiring some type of isolation helps to reduce the background from quark and gluon jets that are misidentified as τ_h decays. One can use simple cut-based variables like relative isolation as in Eq. (5.3), but most physics analyses with τ_h decays use multivariate analysis (MVA) identification for maximum background rejection power. In the rest of the present thesis, the misidentified leptons will be denoted by "$\ell \to \tau_h$ fakes", while "$j \to \tau_h$ fakes" will refer to misidentified quark and gluon jets.

This section describes the DeepTau identification algorithm, which is based on a convolutional deep neural network (DNN). It is designed with the following three premises in mind:

1. **Multiclass**: The final goal is to efficiently discriminate against electrons, muons, and quark and gluon jets that are misidentified as τ_h decays. The DNN is therefore designed & trained to classify reconstructed τ_h as either real τ_h decays, or misidentified electrons, muons, or quark and gluon jets with a predicted probability, from which discriminators are constructed. Previously, separate dedicated algorithms were used to reject these backgrounds. A multiclass approach that produces the three discriminators improves the overall performance, and reduces the overhead.
2. **Usage of lower-level information**: While previous MVA-based discriminators in CMS mainly used higher-level input variables from τ_h reconstruction, DeepTau also processes lower-level observables of individual particles around the τ_h object with convolutional layers to exploit complex patterns of detector interactions and jet fragmentation. These techniques makes use of convolutional architectures of the sort used in image recognition based on the premise that a fragment of an image can be processed independently of its position, relying on translational invariance.
3. **Domain knowledge**: DeepTau still processes **high-level input variables** that have proven helpful to identify τ_h and rejects backgrounds like quark or gluon jets in previous MVA classifiers. Given large enough training samples, a dedicated DNN should in principle achieve the same performance without higher-level information, but including this information may reduce the amount of training events necessary, and aid the convergence of the training, as shown by previous studies of jet flavor identification algorithms that use convolutional layers [302].

Various neural network architectures that satisfy the premises above have been considered under the constraints of the above premises and the available resources. Two main advantages of convolutional layers to others like graph-based networks is that they have smaller computational complexity, and are efficiently implemented in available deep learning software. This is described in more detail in Ref. [289].

6.3.1 Inputs

The low-level input variables are basic observables of different types of particle objects around the τ_h object. The particle objects are different kinds of reconstructions of charged and neutral hadrons, electrons, photons, and muons. In addition to their reconstruction from PF, electron and muon objects from standalone reconstruction algorithms are used to take advantage of more specific information that is useful to distinguish them from other particles. The observables include basic kinematic quantities (p_T, η, ϕ), tracking & vertexing parameters, cluster shape & energy measurements from the calorimeter, and pileup probability from the *pileup identification* (PUPPI) *algorithm* [303].

To capture complex patterns in $\eta\phi$ space, the low-level information is partitioned by two overlapping grids in $\eta\phi$ space that are centered around the reconstructed τ_h axis, as shown in Fig. 6.7. The grids have a different number of cells and cell granularity. The "inner" grid has 11×11 cells with size 0.02×0.02, such that it fully covers the signal cone with a radius of $\Delta R = 0.1$. The "outer" grid has 22×22 cells with 0.05×0.05 each, and covers the isolation cone of $\Delta R = 0.5$. The finer granularity of the inner grid permits a better resolution of the collimated τ_h decays in the signal cone, as well as the dense core of high-p_T quark and gluon jets, while the outer cone is used to capture the extra activity typical of jets initiated by a quark or a gluon.

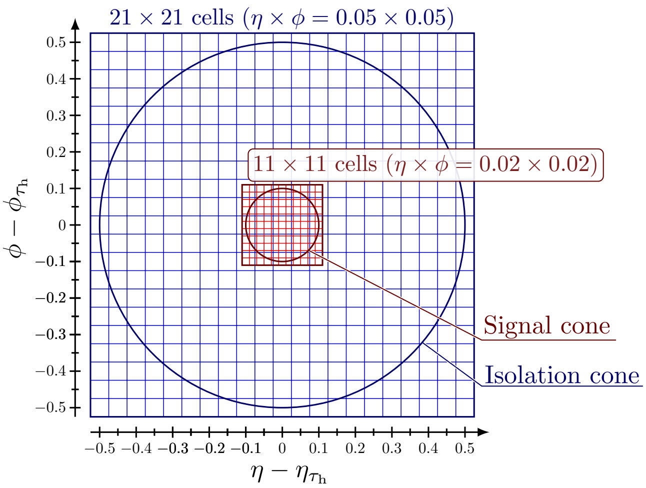

Figure 6.7: Layout of the two grids in $\eta\phi$ space and centered around the reconstructed τ_h axis (η, ϕ), which are used to process particle-level information as input to the convolutional layers of DeepTau. The inner grid (red) is comprised of 11×11 cells of size 0.02×0.02 each, while the outer grid (blue) has 21×21 cells of size 0.05×0.05. The inner and outer grids overlap. Also shown are the signal cone of radius $\Delta R = 3\,\mathrm{GeV}/p_\mathrm{T}$, limited by 0.05–0.1, and the isolation cone of $\Delta R = 0.5$ to define higher-level observables. Adapted from [289].

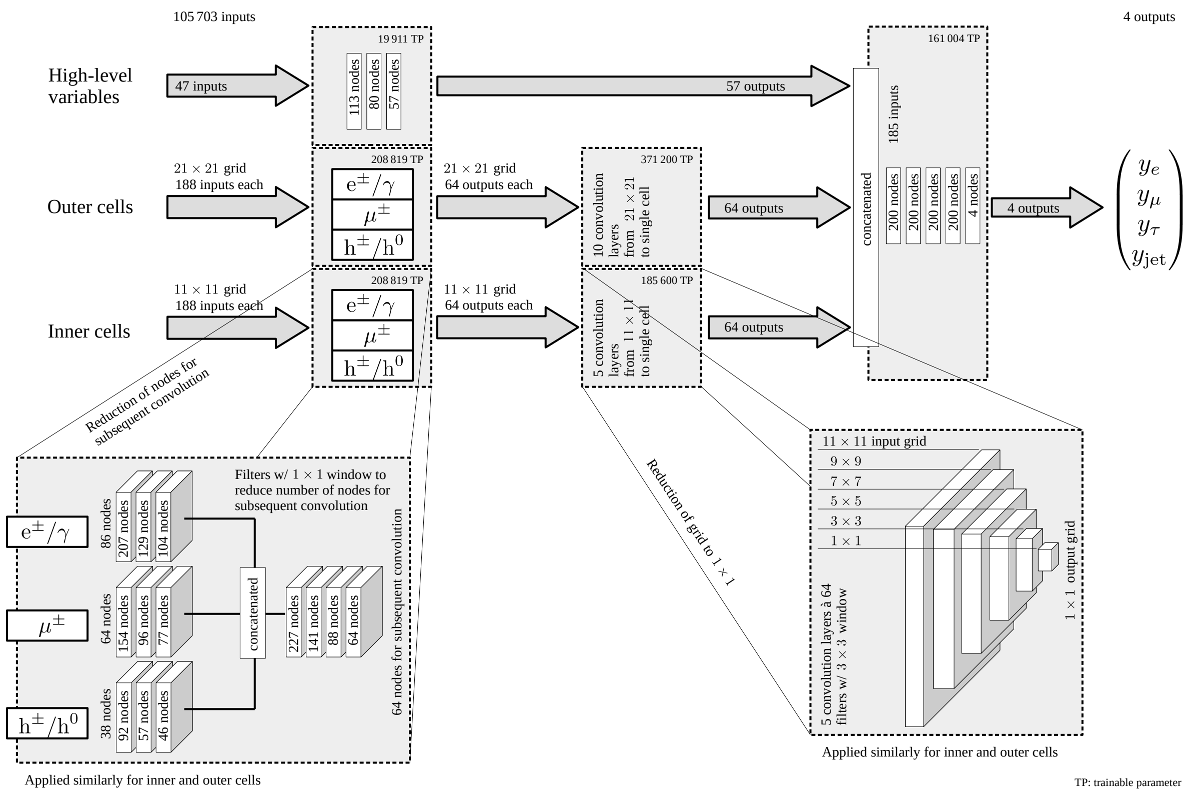

Figure 6.8: Overview of the DNN architecture of the DeepTau algorithm. The network consists of three subnetworks, which are finally concatenated and are passed through four fully connected layers, ending in the final output layer yielding four output parameters x_α that each target one of the four classes, $\alpha \in \{\tau_\mathrm{h}, \mathrm{jet}, \mu, \mathrm{e}\}$. The low-level input variables are reduced to 64 variables per cell by several fully connected layers, before they are processed by the convolution layers that contracts each of the two grids to a single cell with 64 output variables. See text for more explanation. Figure taken from [289].

On average, 1.7% (7.1%) of the inner (outer) grid cells are occupied. If more than one particle of a given type is found in a cell, the one with the highest p_T is used as input. This occurs in about 10% of the occupied cells.

The list of high-level input variables is similar to that of previous MVA classifiers. There are in total 47 of such variables, which include the reconstructed four-momentum, charge of the τ_h candidate, but also the number of charged and neutral constituents, quantities related to its lifetime (vertex parameters), isolation, strip energy, compatibility with being an electron, and estimated pileup.

Linear transformations are applied to rescale or standardize inputs within a limited range before passing them to the DNN.

6.3.2 Architecture

Figure 6.8 shows a schematic of the DeepTau architecture. It has three main subnetworks:

1. The 47 high-level input variables are processed by three fully connected layers, which have 57 output nodes.
2. The low-level input variables from the outer grid are first processed through a set of fully connected layers to reduce the dimensionality from 188 inputs to 64 outputs per cell. Then they are passed through 10 convolutional layers to contract the 22×22 input grid to a single output cell with 64 final outputs.
3. The low-level input variables from the inner grid are processed by a subnetwork that has a similar structure as the one for the outer grid, but contains five convolutional layers instead to reduce the 11×11 grid to one cell with again 64 outputs.

The convolutional layers each have 64 filters of size 3×3 with no padding with empty cells around the input grid in order to reduce with each step the dimension of the grids by two cells in either direction.

The output parameters of these three subnetworks, 185 in total, are then concatenated before being passed through four fully connected layers with 200 nodes each, ending in the final output layer yielding four output parameters x_α that each target one of the four classes, $\alpha \in \{\tau_h, \mathrm{jet}, \mu, \mathrm{e}\}$. A *softmax activation function* [304, p. 79, 180–184] is applied to normalize the outputs to

$$y_\alpha = \frac{\exp(x_\alpha)}{\sum_\beta \exp(x_\beta)}. \tag{6.11}$$

The value of y_α measures the probability between 0 and 1 that a given τ_h candidate belongs to the class α.

6.3.3 Loss function & training

The loss function is constructed as the sum of three different terms that guide the training to aim for a high efficiency of genuine τ_h decays with maximal rejection power against the background in the regions most interesting for physics analyses, which typically operate at a 50–80% efficiency [289]. The three terms are:

1. a regular *cross-entropy term* [304, p. 73, 129, 130] to target the genuine τ_h class;

2. a *focal loss term* [305] for the binary classification of genuine τ_h against all background classes combined, that optimizes rejection at the highest τ_h efficiencies;
3. another focal loss term with a smoothened step function that is nonzero for τ_h candidates with $y_{\tau_h} \gtrsim 0.10$ in order to ignore background separation at low τ_h efficiencies.

The parameters of the terms are chosen to make them more numerically equal, while prioritizing discrimination against quark and gluon jets. The full details of the loss function is given in Appendix A of Ref. [289].

The training is performed on a sample of 140 million τ_h candidates from various simulated processes in the CMS detector with conditions of the 2017 data-taking period. For the τ_h objects from generated τ_h decays, electrons, and muons, samples from simulated events with $Z \to \ell^+\ell^-$ (NLO), $Z' \to \ell^+\ell^-$, $W + \text{jets}$, and top pair production are used, with $m_{Z'}$ ranging between 1 to 5 GeV. For quark and gluon jets misidentified as τ_h decays, samples of QCD multijet and top pair production are used. For testing and validation, 10 million τ_h candidates from independent $H(125) \to \tau^+\tau^-$ and $Z \to \ell^+\ell^-$ (LO) samples are used. The training of the final classifier was run for 10 epochs, with an average of about 69 hours per epoch.

6.3.4 Discriminators & expected performance

From the four DNN outputs y_α, the three DeepTau discriminators are constructed,

$$D_\alpha(\mathbf{y}) = \frac{y_{\tau_h}}{y_{\tau_h} + y_\alpha}, \tag{6.12}$$

which efficiently reject misidentified electrons (D_e), muons (D_μ), and jets (D_{jet}). Within CMS, these are available under the names `DeepTau2017v2p1VSe`, `-VSmu`, and `-VSjet`, respectively, where `2017` refers to the training data set with conditions of 2017 data taking, and `v2p1` indicates the version, 2.1. The discriminators take on values between 0 and 1, where a lower "cut" on a given discriminator reduces the associated background, while increasing the purity of real τ_h decays.

For the convenience of physics analyses, WPs are defined that target fixed identification efficiencies of genuine τ_h decays. The (expected) efficiencies are defined with a sample of reconstructed τ_h candidates with $30 < p_T < 70$ GeV from $H(125) \to \tau^+\tau^-$ events. Table 6.2 lists the WP efficiencies, which show that the expected efficiency of D_{jet} varies between 40 and 98%, while the efficiencies of D_μ ranges from 99.5 to 99.95% thanks to its great discrimination power.

The reconstruction and identification efficiency of genuine τ_h decays before and after requiring a Loose, Medium, or Tight WP of the D_{jet} discriminator is evaluated as a function of p_T of the generated τ_h decays. This is shown in Fig. 6.9. A sample of τ_h candidates from simulated $Z \to \tau^+\tau^-$ events, and reconstructed with $p_T > 20$ GeV and $|\eta| < 2.3$ are used. Without including the two-prong decay modes, the reconstruction efficiency is between 75 and 82% above $p_T > 30$ GeV. For τ_h decays with $p_T \sim 20$ GeV, the efficiency goes down to approximately 40%.

Table 6.2: The τ_h identification efficiencies for the different WPs of the three DeepTau discriminators. The target efficiencies are evaluated with the $H \to \tau^+\tau^-$ event sample for τ_h with $30 < p_T < 70$ GeV [289]. Each letter 'V' stands for "Very".

	VVTight	VTight	Tight	Medium	Loose	VLoose	VVLoose	VVVLoose
D_e	60%	70%	80%	90%	95%	98%	99%	99.5%
D_μ	—	—	99.5%	99.8%	99.9%	99.95%	—	—
D_{jet}	40%	50%	60%	70%	80%	90%	95%	98%

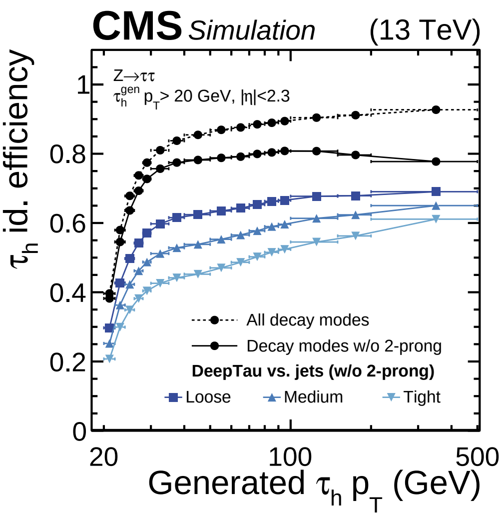

Figure 6.9: Reconstruction & identification efficiency of genuine τ_h decays as a function of generated τ_h p_T for candidate τ_h, as determined from a simulated $Z \to \tau^+\tau^-$ sample with $p_T > 20\,\text{GeV}$ and $|\eta| < 2.3$ for the generated τ_h decays. The black points shows the efficiencies to be reconstructed by the HPS algorithm before identification with DeepTau. The blue points show the efficiencies after several requirements of different WPs of the D_{jet} discriminator against quark and gluon jets. Figure taken from [289].

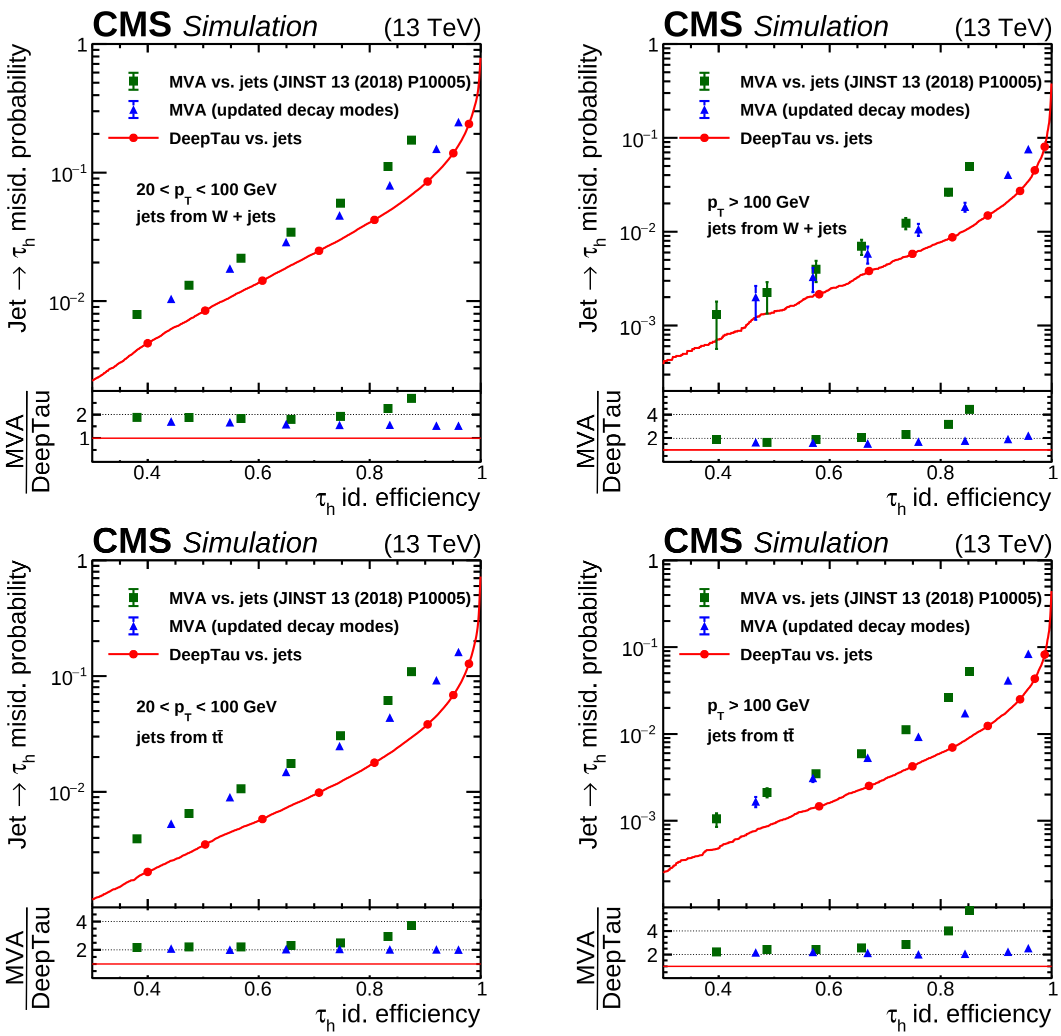

Figure 6.10: Misidentification rate of quark and gluon jets versus genuine τ_h efficiency when applying a lower cut on anti-jet discriminators. Misidentified quark and gluon jets are taken from a simulated W + jets (top row) and $t\bar{t}$ (bottom row) sample. **Left**: For τ_h candidates with $20 < p_T < 100\,\text{GeV}$. **Right**: For τ_h candidates with $p_T > 100\,\text{GeV}$. Figures taken from [289].

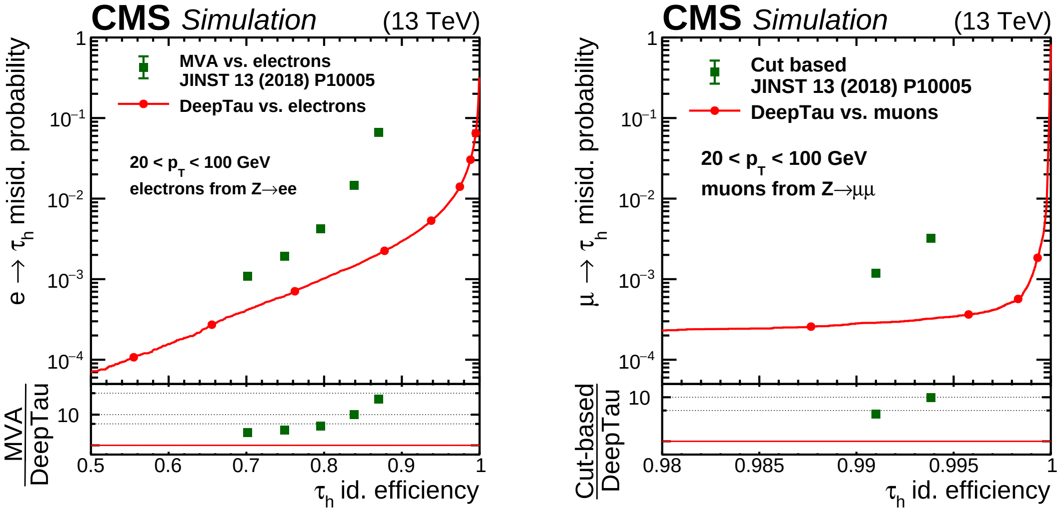

Figure 6.11: Probability for electron (left) or muons (right) versus to be identified as a τ_h decay versus genuine τ_h efficiency for τ_h objects satisfying a particular selection on the discriminator value. Misidentified leptons have $20 < p_\mathrm{T} < 100\,\mathrm{GeV}$, and are taken from a simulated $\mathrm{Z} \to \ell^+\ell^-$ sample. **Left**: Electrons with D_e. **Right**: Muons with D_μ. Figures taken from [289].

The efficiency of applying the DeepTau discriminator against quark and gluon jets is in line with what is reported in Table 6.2.

The expected performance of each DeepTau classifier is evaluated and compared to previous discriminators of the same type. Figures 6.10 and 6.11 show the *receiver operating characteristic* (ROC) *curves* of the discriminators, which graph the misidentification rate of a given background versus the identification efficiency for genuine τ_h decays for objects satisfying a particular selection on the discriminator value. The ROC curves have been produced using various samples of τ_h candidates with $20 < p_\mathrm{T} < 100\,\mathrm{GeV}$, as well as $p_\mathrm{T} > 100\,\mathrm{GeV}$. To calculate the misidentification rate of quark and gluon jets for the D_jet discriminators, a sample of simulated $\mathrm{W}+\mathrm{jets}$ events was used, as well as a sample of simulated $\mathrm{t\bar{t}}$ events, which have a larger fraction of bottom quarks and gluon jets, and tend to have more activity. The DeepTau discriminators show a large overall improvement in signal efficiency for a given misidentification rate. The rejection of the quark and gluon jet background with D_jet compared to the previous MVA discriminator is about 50% better overall for the $\mathrm{W}+\mathrm{jets}$ sample, and about two times better for the $\mathrm{t\bar{t}}$ sample. Conversely, the signal efficiency increases by more than 30% for the tightest D_jet WPs, and more than 10% for the loosest ones. The misidentification rate of quark and gluon jets with D_jet is almost a factor two lower for the $\mathrm{t\bar{t}}$ sample than for the $\mathrm{W}+\mathrm{jets}$ sample below $p_\mathrm{T} < 100\,\mathrm{GeV}$, but they are more similar above $p_\mathrm{T} > 100\,\mathrm{GeV}$. Overall, D_jet has a lower misidentification rate at high p_T than the MVA algorithm.

The DeepTau discriminators against leptons improve the electron or muon rejection by a factor of three for the tightest WP, and up to a factor 40 (10) for the loosest D_e (D_μ) WP with respect to the previous MVA algorithm. Their performance is similar between the two p_T regions studied [289].

The comparison between observed data and simulation will be discussed in Chapter 9.

6.4 Validation

To validate the performance of the DeepTau identification algorithm, I have studied distributions of several observables in a sample with relatively pure τ_h events coming from the $\mathrm{Z} \to \tau^+\tau^-$ resonance in the $\mu\tau_\mathrm{h}$ final state. As a representative illustration, the observed and expected dis-

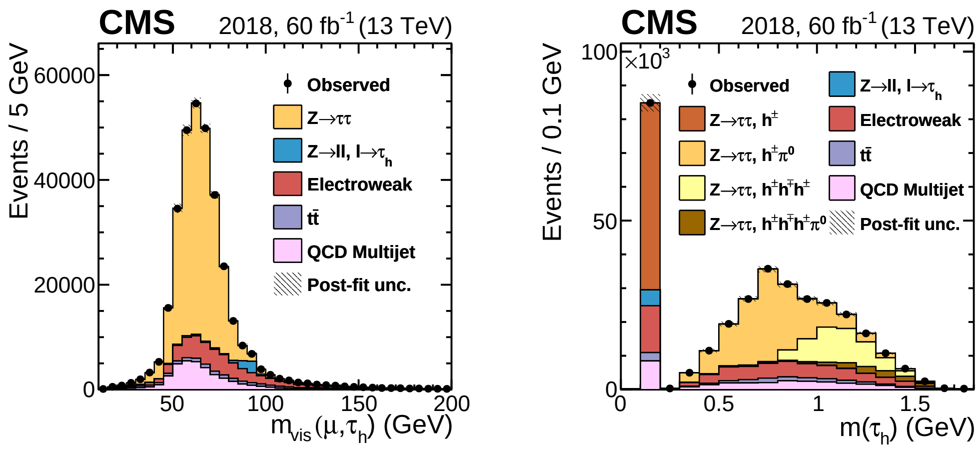

Figure 6.12: Observed and expected distributions in $\mu\tau_\mathrm{h}$ events of the 2018 data set. Corrections discussed in Chapters 8 and 9 are applied. The electroweak background includes W + jets, diboson, single top production, as well as Z + jets events where a quark or gluon jet is misidentified as a τ_h candidate. **Left**: Invariant mass of the $\mu\tau_\mathrm{h}$ system, m_vis. **Right**: Reconstructed τ_h mass. Figures taken from [289].

tributions of the invariant mass of the $\mu\tau_\mathrm{h}$ system, m_vis, and the reconstructed τ_h mass are shown in Fig. 6.12. These distributions already incorporate the corrections to simulated τ_h candidates that are discussed in Chapter 9, and are obtained from a maximum likelihood fit [306] with the full set of systematic uncertainties discussed. The selections of $\mu\tau_\mathrm{h}$ events are purified in $\mathrm{Z} \to \tau^+\tau^-$ events with selection criteria. The event selections and systematic uncertainties are discussed in Section 9.1. The Tight WP of the `DeepTau2017v2p1VSjet` discriminator is used. In the left panel of Fig. 6.12, the main $\mathrm{Z} \to \tau^+\tau^-$ signal is shown in orange. Because part of the four-momentum is carried away by three neutrinos in the $\tau\tau$ decay, the resonance is located around $m_\mathrm{vis} \approx 60\,\mathrm{GeV}$. The main backgrounds are W + jets and QCD multijet production. Due to the high rejection power of the Tight WP of the `DeepTau2017v2p1VSmu` discriminator, the $\mathrm{Z} \to \mu^+\mu^-$ peak around $m_\mathrm{vis} \approx 91\,\mathrm{GeV}$ (blue) is significantly suppressed, with little loss of genuine τ_h events. In the m_{τ_h} distribution shown in the right panel of Fig. 6.12, the $\mathrm{Z} \to \tau^+\tau^-$ events are further subdivided into different reconstructed decay modes. Per construction, the one-prong decay, $h^\pm$, is set to the charged pion mass, $m_{\tau_\mathrm{h}} = 0.140\,\mathrm{GeV}$. The other decay modes are distributed around the mass of their respective intermediate resonance: $\rho(770)$ for $h^\pm\pi^0$, $\mathrm{a}_1(1260)$ for $h^\pm h^\mp h^\pm$, and $\rho(1450)$ for $h^\pm h^\mp h^\pm \pi^0$.

Within the post-fit uncertainties, the predicted distributions agree well with the observed data. This indicates that with the corrections, CMS can obtain a good description of a data sample enriched in τ_h objects, thus validating the HPS reconstruction algorithm and the DeepTau identification algorithm.

7 Data sets & Simulated Samples

The LQ search in this thesis is performed with pp collision data collected by the CMS detector in the data-taking periods between 2016 and 2018 with a center-of-mass energy $\sqrt{s} = 13\,\mathrm{TeV}$. There are several common SM background processes that have similar signatures to the LQ $\rightarrow$ bτ signal discussed in Section 3.4.3. By simulating these SM processes, we can better understand the underlying background composition of observed data, and with the simulated LQ signal, we can study and optimize the selections in order to maximize discovery potential.

This chapter will discuss in more detail the data sets of pp collision events used, as well as the samples of simulated background and LQ signal events.

7.1 Data sets

The total data set recorded between 2016 and 2018 corresponds to an integrated luminosity of approximately $138\,\mathrm{fb}^{-1}$ at $\sqrt{s} = 13\,\mathrm{TeV}$. Only data events that are fully certified for physics analysis by the CMS *Data Quality Monitoring* team are selected for use in this analysis. The data sets provided by the CMS *Data Aggregation System* with their respective LHC run-number ranges and integrated luminosity for physics analysis are listed per year in Table 7.1.

Table 7.1: LHC run number ranges and corresponding integrated luminosity L recorded by CMS and certified for physics analysis.

Run number range	L [fb^{-1}]
272007–284044	36.3
297020–306462	41.5
315252–325175	59.7

The LQ search in this thesis targets five out of six $\tau\tau$ decay channels: $\tau_h\tau_h$, $e\tau_h$, $\mu\tau_h$, $e\mu$, and $\mu\mu$. This analysis makes use of data that was collected with three different types of triggers depending on the channel, as listed in Table 7.2:

Table 7.2: Triggers used to target the various $\tau\tau$ decay channels.

Trigger type	Online p_T thresholds [GeV]	$\tau\tau$ decay channel
Single electron	25 or 27 in 2016 36 in 2017 33 or 36 in 2018	$e\tau_h$
Single isolated muon	25 in 2016 25 or 28 in 2017 & 2017	$\mu\tau_h$, $e\mu$, $\mu\mu$
Double τ_h objects (PF or HPS)	35 in 2016 35 or 40 in 2017 & 2018	$\tau_h\tau_h$

In most years, multiple triggers of the same type are combined inclusively for complementarity and optimal efficiency. Because it is difficult to model the trigger efficiency as a function of p_T around the online p_T threshold (*turn on*), the offline minimum-p_T requirement for physics analysis is increased with respect to the online p_{T} threshold of the fired trigger by 1 GeV for muons and electrons, and 5 GeV for τ_{h} objects. As the p_{T} threshold varied between triggers of the same type, the offline p_{T} requirement is decided based on the trigger with the lowest p_{T} threshold that also fired. Some single-electron or double-τ_{h} triggers were limited to $|\eta| < 2.1$, and if in an event only a trigger with this restriction was satisfied, then the $|\eta|$ of the corresponding object is required to be below 2.1.

7.2 Event simulation

Event generators use the so-called *Monte Carlo* (MC) *method* that mimics the probabilistic nature of these processes with (pseudo-)random generators [308]. With this practical method, pp collision data are generated event by event, from the pp collisions themselves up to the resulting signals that would be produced in the detector.

The simulation of pp collision data involves several steps. First, the main, hard scattering process is generated. Short-lived particles such as the W and Z boson are decayed according to their branching ratios. This hard process corresponds to a process at high energy, or equivalently at a short length scale. At these scales, interactions are well above the QCD confinement scale, and perturbation theory can be used.

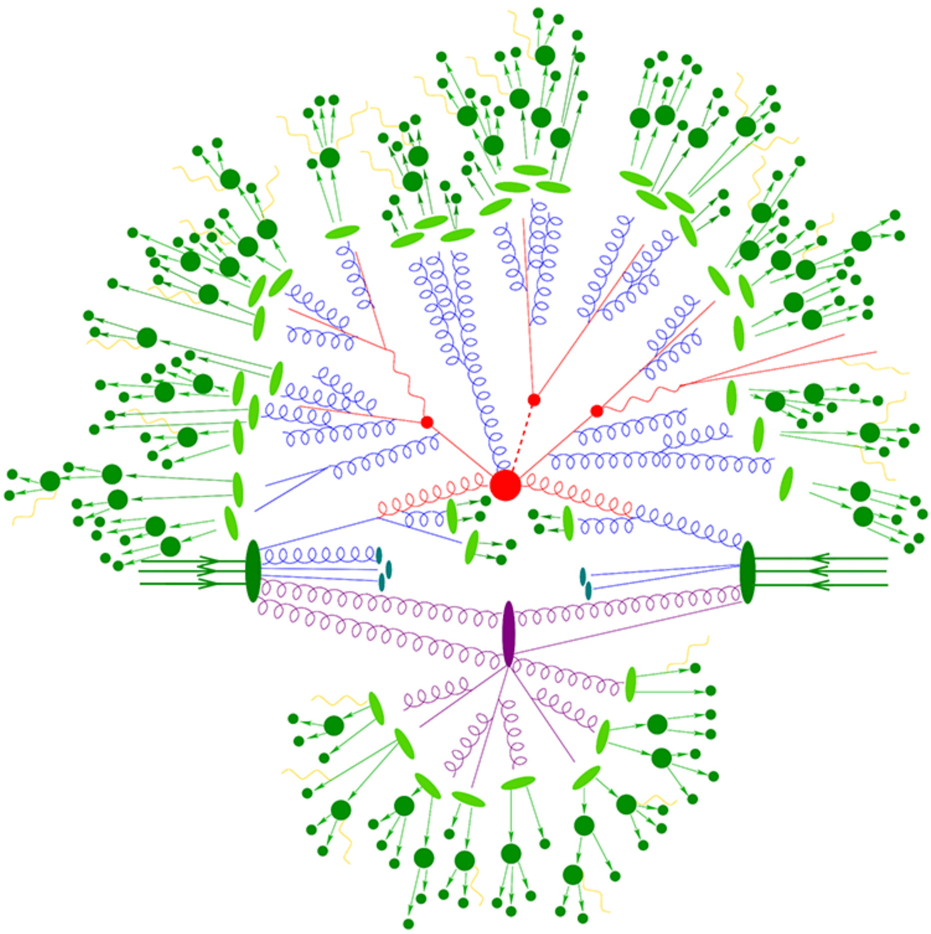

Figure 7.1: Schematic diagram explaining event generation of two colliding protons, coming in from the sides, with a hard process in red and the proton remnants in purple undergoing *multiple particle interactions*. Initial- and final-state radiation (ISR, FSR) is added to the whole event, shown in blue and red, respectively. The partons are then hadronized (light green) and undergo further decay (dark green). Retrieved from [307].

Then *parton showering* is performed: *Initial-* and *final-state radiation* (ISR, FSR) are simulated. These are the emissions of lighter particles like photons, gluons, or quarks that can happen before or after the hard scattering process. Some generator programs will already generate ISR before the parton showering algorithm, and special matching and merging algorithms are needed to prevent overcounting of these types of partons.

The third step is *hadronization*, or *fragmentation*, wherein the partons (quarks and gluons) form colorless hadrons, which may decay further. Jet production can be safely separated from the hard process during simulation, since it happens at a much longer distance scale ($> 1\,\text{fm}$). It cannot, however, be understood from first principles with perturbative QCD, so phenomenological models are used. The previous steps are considered to be simulation at *generator level* and are shown in Fig. 7.1. The parton showering, fragmentation, underlying event, as well as τ decays are modeled by PYTHIA for most simulated event samples in the CMS Collaboration. The PYTHIA parameters affecting the description of the underlying event are set to the CUETP8M1 (CP5) tune for all 2016 (2017 and 2018) samples [309, 310], except for the 2016 $\mathrm{t\bar{t}}$ sample, for which CUETP8M2T4 [311] is used. These tunes model the observed particle production in LHC collisions.

The next steps are to simulate the interactions of the resulting particles with the detector material and the subsequent detector response. The interaction with the CMS detector is simulated by GEANT4 [316] for the main samples of physics analyses. Also, additional pp interactions are added as pileup, which is generated with PYTHIA.

Finally, the simulated detector response is processed by the same reconstruction software as data. The final output is simulated pp collision data that can be compared to observed data to understand its composition, compare to SM expectation, make measurements, etc. *A priori*, the modeling of the detector is not perfect, so corrections need to be derived from measurements in independent subsets of the collected data. Furthermore, some processes are approximated with a subset (a “lower order”) of the possible Feynman diagrams for practical reasons, and need corrections to their kinematic distributions, which are derived from high-order predictions, or measured in observed data. This will be discussed in more detail in Chapters 8 & 9.

Event generation is described in more detail in Refs. [13, p. 717], [317] and [308].

7.3 Backgrounds

There are several backgrounds for analyses that target final states with two τ leptons, and perhaps a (bottom) jet. The dominant backgrounds are Drell-Yan, $\mathrm{t\bar{t}}$, and the quark or gluon jets misidentified as τ_h decays, which include mainly $\mathrm{W}+\text{jets}$ and QCD-induced multi-jet production.

The Drell-Yan process $\mathrm{Z}/\gamma^* \to \ell^+\ell^-$ produces a pair of τ leptons one third of the time, and has a large peak with a mass around that of the Z boson. In addition to the production of a real

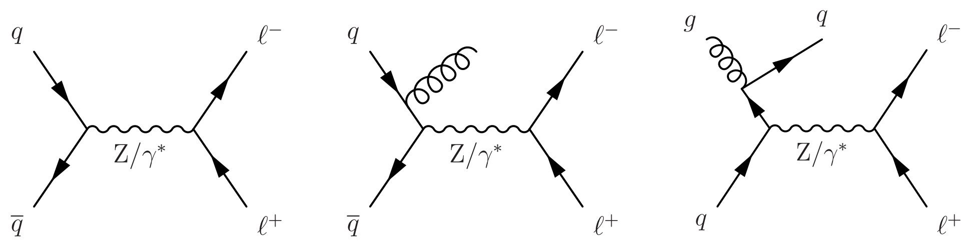

Figure 7.2: Examples of Feynman diagrams for Drell-Yan without partons (left) and plus one parton origination from an initial state radiation (ISR), which can be a gluon or quark (middle and right) [312, 313].

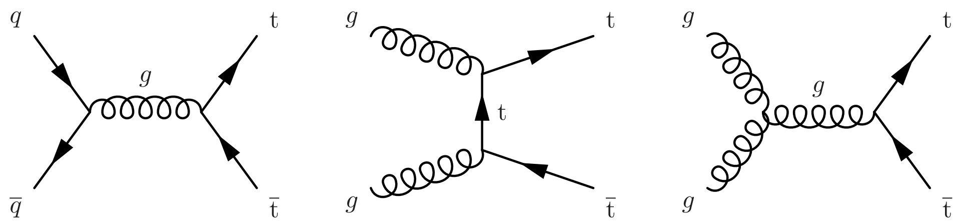

Figure 7.3: LO Feynman diagrams $t\bar{t}$ production [314, 315].

pair of τ leptons, one of the electrons (muons) from $Z/\gamma^* \to e^+e^-$ ($\mu^+\mu^-$) can be misidentified as a τ_h candidate, although this background is efficiently suppressed with the DeepTau lepton discriminators. Extra high-p_T jets that are produced by ISR or FSR in Drell-Yan (Figs. 2.8 & 7.2) can be misidentified as τ_h objects. Besides the application of the DeepTau anti-jet discriminator, this background can be suppressed by vetoing events with "extra" electrons or muons that were not selected as candidates consistent with τ decay. Therefore, we will refer to "Z + jets" as Drell-Yan for short.

Top quark pairs are copiously produced at the LHC (Fig. 7.3), and primarily decay via $t\bar{t} \to b\bar{b}W^+W^-$. Their final state therefore can also contain real τ leptons, or lighter leptons and jets that fake τ_h decays. Furthermore, especially event selections that require high-p_T b jets will create a sample with a large fraction of $t\bar{t}$ events.

A large amount of $j \to \tau_h$ fake background originates from W + jets and QCD-induced multijet production. Due to its lepton plus jet(s) final state, W + jets is prevalent in $e\tau_h$ and $\mu\tau_h$. QCD events may also contain real leptons from hadron decays in addition to quark and gluon jets. On the other hand, QCD is an almost negligible background in the dileptonic channels like $\mu\mu$ and $e\mu$. Often, *data-driven methods* are used to estimate the QCD multijet or $j \to \tau_h$ background in analyses with τ leptons because the misidentification rate and all its dependencies are hard to model from simulation. Simulated QCD samples also have larger uncertainties, and are less practical to use. The two methods used by this thesis are discussed in Chapter 11.

7.3.1 Simulated backgrounds

All the simulated background samples used in this thesis are listed in Table 7.3. The W + jets samples are used for several studies, but in the main LQ analysis, it is included via the data-driven method to model the total $j \to \tau_h$ fake background. The data-driven methods are described in Chapter 11.

The W + jets and Z + jets processes are generated with MadGraph [318] at LO precision. The MLM jet matching and merging scheme [319] is used to match partons between MadGraph and pythia and prevent overcounting. To increase the number of simulated Drell-Yan and W + jets events with high jet multiplicity, samples that are generated with a fixed number of partons in the hard process at MadGraph level are included. The Z + jets samples generated at NLO by MadGraph5_aMC@NLO [320] are used for one part of the LQ analysis to gain a higher number of events at high invariant mass. The production of $t\bar{t}$ and singly produced top quarks is simulated with the powheg [321–323] 2.0 and 1.0 generators, respectively, at NLO precision [324–327]. Diboson production is generated at LO with pythia 8 [328, 329]. The NNPDF3.0 PDF sets [330] are used with all generators for 2016 samples, and the order of the set is matched to that of the matrix element calculations. For 2017 and 2018 samples, the NNPDF3.1 [69] sets were used.

Table 7.3: Summary of simulated SM backgrounds, including generator(s) and cross sections (for 2017 & 2018 samples with the CP5 tune). Drell-Yan and W + jets samples with "+ n jets" refer to a fixed number of partons, n, at the level of the hard process in MadGraph.

Process	Generators	Cross section σ [pb]
Drell-Yan, $Z/\gamma^* \to \ell^+\ell^-$, LO		
+ jets, $10 < m_{\ell\ell} < 50\,\mathrm{GeV}$	MadGraph, pythia	15810.0 (LO), 18610.0 (NLO)
+ jets, $m_{\ell\ell} > 50\,\mathrm{GeV}$	MadGraph, pythia	5343.0 (LO), 6077.2 (NNLO)
+ 1 jets, $m_{\ell\ell} > 50\,\mathrm{GeV}$	MadGraph, pythia	877.8 (LO)
+ 2 jets, $m_{\ell\ell} > 50\,\mathrm{GeV}$	MadGraph, pythia	304.4 (LO)
+ 3 jets, $m_{\ell\ell} > 50\,\mathrm{GeV}$	MadGraph, pythia	111.5 (LO)
+ 4 jets, $m_{\ell\ell} > 50\,\mathrm{GeV}$	MadGraph, pythia	44.05 (LO)
Drell-Yan, $Z/\gamma^* \to \ell^+\ell^-$, NLO		
+ jets, $m_{\ell\ell} \in [100, 200[\,\mathrm{GeV}$	aMC@NLO, pythia	247.8 (NLO)
+ jets, $m_{\ell\ell} \in [200, 400[\,\mathrm{GeV}$	aMC@NLO, pythia	8.502 (NLO)
+ jets, $m_{\ell\ell} \in [400, 500[\,\mathrm{GeV}$	aMC@NLO, pythia	0.4514 (NLO)
+ jets, $m_{\ell\ell} \in [500, 700[\,\mathrm{GeV}$	aMC@NLO, pythia	0.2558 (NLO)
+ jets, $m_{\ell\ell} \in [700, 800[\,\mathrm{GeV}$	aMC@NLO, pythia	0.04023 (NLO)
+ jets, $m_{\ell\ell} \in [800, 1000[\,\mathrm{GeV}$	aMC@NLO, pythia	0.03406 (NLO)
+ jets, $m_{\ell\ell} \in [1000, 1500[\,\mathrm{GeV}$	aMC@NLO, pythia	0.01828 (NLO)
+ jets, $m_{\ell\ell} \in [1500, 2000[\,\mathrm{GeV}$	aMC@NLO, pythia	0.002367 (NLO)
+ jets, $m_{\ell\ell} \in [2000, 3000[\,\mathrm{GeV}$	aMC@NLO, pythia	5.409×10^{-4} (NLO)
+ jets, $m_{\ell\ell} \in [3000, \infty[\,\mathrm{GeV}$	aMC@NLO, pythia	3.048×10^{-5} (NLO)
W + jets, $W \to \ell\nu$		
+ jets	MadGraph, pythia	52940.0 (LO), 61526.7 (NLO)
+ 1 jets	MadGraph, pythia	8104.0 (LO)
+ 2 jets	MadGraph, pythia	2793.0 (LO)
+ 3 jets	MadGraph, pythia	992.5 (LO)
+ 4 jets	MadGraph, pythia	544.3 (LO)
$t\bar{t}$ + jets		833.9 (NNLO)
Fully leptonic	powheg, pythia	88.29 (NNLO), $\mathcal{B} = 10.6\%$
Semi-leptonic	powheg, pythia	365.35 (NNLO), $\mathcal{B} = 43.9\%$
Fully Hadronic	powheg, pythia	377.96 (NNLO), $\mathcal{B} = 45.4\%$
Single top		
$t + W^-$	powheg, pythia	35.85 (NNLO)
$\bar{t} + W^+$	powheg, pythia	35.85 (NNLO)
Single t, t channel	powheg, pythia	136.02 (NNLO)
Single $\bar{t}$, t channel	powheg, pythia	80.95 (NNLO)
Diboson		
WW	pythia	75.88 (LO)
WZ	pythia	27.60 (LO)
ZZ	pythia	12.14 (LO)

7.3.2 Cross sections

Table 7.3 also lists the theoretical cross sections σ for each sample. In order to obtain the expected yield for a given integrated luminosity L, the events of each sample are weighted by a normalized factor

$$Z = \frac{L\sigma}{N_{\text{tot}}}, \tag{7.1}$$

where N_{tot} is the total number of simulated events. If a sample is generated at a high order, events typically have a nonconstant generator weight w_{gen}. Formula (7.1) then, will be slightly rewritten to

$$Z = \frac{L\sigma}{\sum w_{\text{gen}}} w_{\text{gen}}. \tag{7.2}$$

The LO cross sections of the Z + jets and W + jets samples in Table 7.3 are computed with MadGraph and the CP5 tune for the 2017 and 2018 samples. The 2016 samples with the CUETP8M1 tune have slightly different cross sections at LO. I used the fewz [331] program to compute the Z + jets cross section at NNLO in perturbative QCD, and with NLO electroweak corrections. The $\mathrm{t\bar{t}}$+jets cross section was computed with the Top++v2.0 program [332, 333] at NNLO and at next-to-next-to-leading logarithmic (NNLL) accuracy. The W + jets production is normalized with cross sections computed at NLO accuracy.

7.4 Simulated LQ signals

To search for LQs coupling to b quarks and τ leptons ("LQ $\to$ bτ signal"), this thesis targets the different modes of production introduced in Section 3.4.3: the single and pair production of such an LQ, as well as the nonresonant production of a τ pair through the t-channel exchange of an LQ mediator. For brevity, the latter will be referred to simply as "nonresonant production" in this thesis. The Feynman diagrams of these processes are shown in Fig. 7.4. Furthermore, this analysis considers both scalar and vector models, each with one mass parameter and one coupling strength between the LQ and a pair of fermions. For the vector model, one additional QCD coupling parameter is taken into account.

Direct LQ searches at the LHC frequently use a parameter β to quantify the branching fraction for an LQ decays to a charged leptons (rather than a neutrino). For a purely third-generation LQ, with sufficient mass to decay to either bτ or tν_τ, β is defined such that

$$\beta = \mathcal{B}(\mathrm{LQ} \to \mathrm{b}\tau) = 1 - \mathcal{B}(\mathrm{LQ} \to \mathrm{t}\nu_\tau). \tag{7.3}$$

If $m_{\mathrm{LQ}} \gg m_{\mathrm{t}}$, β is approximately the relative coupling strength of the LQ to bτ or tν_τ. The

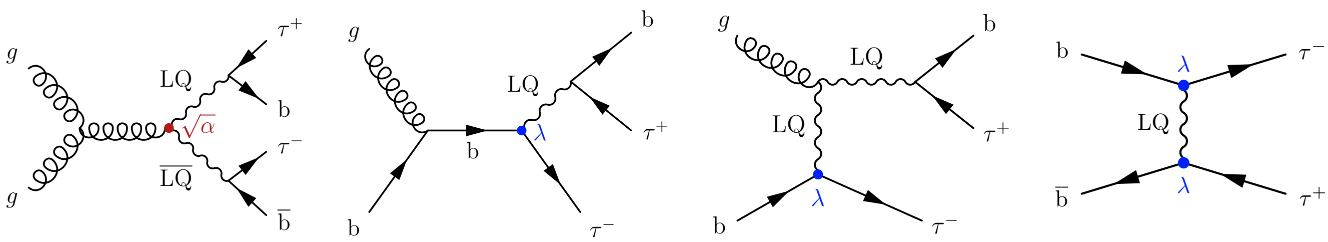

Figure 7.4: Examples of LO Feynman diagrams of the LQ $\to$ bτ signal: LQ pair production (left), single LQ production (center two), as well as nonresonant production of two τ-leptons with the LQ in the t channel (right).

LQ $\to$ bτ search can therefore be classified as the case with $\beta = 1$.

The simulated signal events are generated at LO precision using the MadGraph 2.6.1 [318] event generator with Universal FeynRules Output (UFO) models provided by theorists, which are explained in more detail below. The events are generated with the LO NNPDF3.1 PDF set `NNPDF31_lo_as_0130`, and the *five-flavor scheme* (5FS), wherein the PDF of the b quark is included. As with the backgrounds, PYTHIA 8 is used for the parton showering, hadronization, τ lepton decay, and modeling of the underlying event. The factorization and renormalization scales are fixed to the LQ mass for the resonant signals, as per convention, while for the nonresonant production, they are allowed to run dynamically.

7.4.1 Scalar LQ models & samples

The UFO model for the simulation of the scalar-LQ signal is based on a simplified version of the $\widetilde{R}_2$ model, which is available from Ref. [334]. As shown in Table 3.1 in Section 3.4, the $\widetilde{R}_2$ model consists of two scalar LQs that form a doublet under $\mathrm{SU}(2)_\mathrm{L}$: one with charge $Q = \pm 2/3$ and one with charge $Q = \mp 1/3$. The UFO model only considers the LQ with $Q = \pm 2/3$, and assumes this LQ can only decay to SM particles of the same generation, thus excluding right-handed neutrinos and cross-generational couplings. This leaves couplings $\lambda_{q\ell}$ to one down-type quark q and one charged lepton ℓ, namely to de, sμ, or bτ. There are four model-dependent parameters that are set as follows for event generation.

- The Yukawa coupling of the LQ to the b quark and τ lepton is set to $\lambda_{\mathrm{b}\tau} = 1$, while the Yukawa couplings to first and second generation fermions are set to $\lambda_{\mathrm{de}} = 0 = \lambda_{\mathrm{s}\mu}$, respectively. Therefore, the LQ becomes a purely third-generation LQ, and we write $\lambda := \lambda_{\mathrm{b}\tau}$ from now on as the only LQ-fermion coupling. This is the convention also used in the previous CMS analysis searching for LQ production [335].
- The following set of LQ mass values are chosen: $m_\mathrm{LQ} = 600$, 800, 1000, 1200, 1400, 1600, 2000 GeV. For the nonresonant process, the set of mass points are further extended with 2500, 3000, 4000, 5000, 7000, 10000 GeV.

The decay width Γ of the LQ is generated automatically by the UFO model for each mass point based on the above parameters, following the LO equation, which for a single Yukawa coupling λ, and negligible fermion masses is

$$\Gamma = \frac{\lambda^2 m_\mathrm{LQ}}{16\pi}. \tag{7.4}$$

The only LQ-fermion interaction term left in the Lagrangian then, is

$$\mathcal{L} \supset \lambda \bar{b}_\mathrm{R} \tau_\mathrm{L} S + \mathrm{h.c.}, \tag{7.5}$$

where S is the scalar LQ. The model properties and parameters are summarized in Table 7.4.

The decay of the LQ is prompt, i.e., there is no need to consider long-lived LQs. Below $\lambda \lesssim 1.5$, the direct production of an LQ can be considered a narrow resonance. Above that, the width of the LQ becomes so wide as to smear out the resonance and degrade the overall sensitivity. Therefore, extra samples of single LQ production with $\lambda = 1.5$, 2.0 and 2.5 are generated to take into account the wider mass distribution of the LQ $\to$ bτ resonance, $M_{\mathrm{b}\tau}$. However, when $\lambda > 1$ a pole appears at $M_{\mathrm{b}\tau} = 0$, which roughly grows with λ^4. Most of these events produce low-momentum particles and do not pass the signal selection, or appear in the

Table 7.4: Summary of properties and parameter settings in the UFO models used for event generation of single and pair LQ production. See Section 3.4 for a general discussion of LQ models.

Property / Parameter	`LQ_UFO` [334]	`VectorLQ_UFO` [336, 337]
Model	Scalar $\tilde{R}_2$	Vector U_1
$\mathrm{SU(3)_C \times SU(2)_L \times U(1)_Y}$	$(\mathbf{3}, \mathbf{2}, 1/6)$	$(\mathbf{3}, \mathbf{1}, 2/3)$
Charge	$\pm 2/3$	$\pm 2/3$
Decays	$\mathrm{LQ} \to \mathrm{de}, \mathrm{s\mu}, \mathrm{b\tau}$	$\mathrm{LQ} \to \mathrm{b\tau}, \mathrm{t\nu_\tau}$
Mass	$m_{\mathrm{LQ}} = 600, 800, 1000, 1200, 1400, 1600, 2000\,\mathrm{GeV}$	$m_{\mathrm{LQ}} = 500, 800, 1100, 1400, 1700, 2000, 2300\,\mathrm{GeV}$
LQ-fermion coupling strengths	$\lambda_{\mathrm{de}} = 0 = \lambda_{\mathrm{s\mu}},\ \lambda_{\mathrm{b\tau}} = 1$	$g_{\mathrm{bL}} = 0.1 = g_{\mathrm{tL}}$
Nonmininal coupling strength	—	$\kappa = 1$
Width	$\Gamma \approx \dfrac{\lambda^2_{\mathrm{b\tau}} m_{\mathrm{LQ}}}{16\pi}$	$\Gamma \approx \dfrac{({g_{\mathrm{bL}}}^2 + {g_{\mathrm{tL}}}^2) m_{\mathrm{LQ}}}{24\pi}$

region (high-$S_{\mathrm{T}}^{\mathrm{MET}}$) where the LQ $\to$ bτ analysis is most sensitive. Still, due to the size of the pole, enough events do pass the selections to increase the final yield, competing with the effect of decreased sensitivity due to the broader width. This is shown in Fig. 7.5. Note that MadGraph has a mass window around the generator mass, called the *Breit-Wigner* (BW) *cutoff*. By default, this cutoff is set to 15 times the LQ width, such that each generated event is forced to have

$$m_{\mathrm{LQ}} - 15\Gamma < M_{\mathrm{b\tau}} < m_{\mathrm{LQ}} + 15\Gamma \tag{7.6}$$

In the event generation of single single scalar-LQ production with $\lambda = 2.0$ and 2.5, this is set to 30 times the LQ width to capture the pole at $M_{\mathrm{b\tau}} = 0$.

The samples are produced with about 250 000 events per mass point.

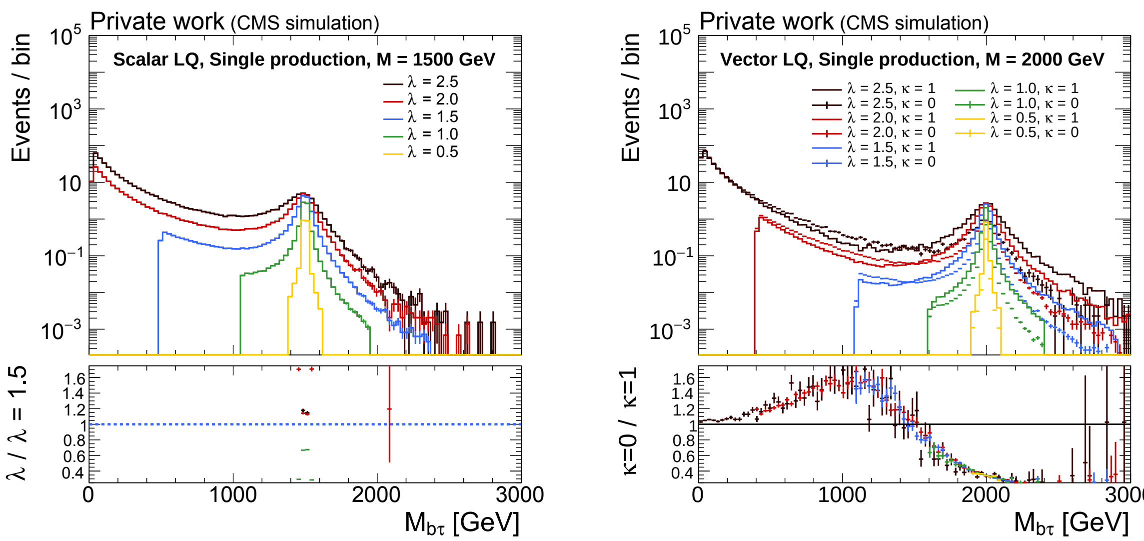

Figure 7.5: Generator-level distributions of $M_{\mathrm{b\tau}}$ spectrum in single LQ production for different values of λ. A pole appears at $M_{\mathrm{b\tau}} = 0$. By default, the BW cutoff in MadGraph is set to 15 times the LQ width, like in the generator-level study used to produce these plots. In the event generation of single scalar production at high λ this cutoff is set to 30 instead.

7.4.2 Vector LQ models & samples

To generate the vector-LQ signal, the UFO model presented in Ref. [336] is used. It is available from Refs. [337], or Ref. [338]. It is based on the U_1 model, wherein the LQ is a $\mathrm{SU(2)_L}$ singlet. The UFO model has simplified couplings to fermions: The LQ couples only to a b quark and τ lepton (top quark and ν_τ) with a coupling strength g_{bL} (g_{tL}). The Lagrangian contains only left-handed couplings:

$$\mathcal{L} \supset g_{\mathrm{bL}}\bar{b}_{\mathrm{L}}\gamma_\mu\tau_{\mathrm{L}}U_1^\mu + g_{\mathrm{tL}}\bar{t}_{\mathrm{L}}\gamma_\mu\nu_{\tau\mathrm{L}}U_1^\mu + \mathrm{h.c.} \tag{7.7}$$

with only left-handed fermions. (Note that some papers use a different normalization, $\lambda = g/\sqrt{2}$.) As explained above, we adopt the benchmark where the coupling $\lambda \equiv g_{\mathrm{bL}} = 1$, and $\beta = 1$, such that $g_{\mathrm{tL}} = 0$. There remains only one LQ-fermion interaction term in the Lagrangian:

$$\mathcal{L} \supset \lambda\bar{\mathrm{b}}_L\gamma_\mu\tau_L U_1^\mu + \mathrm{h.c.} \tag{7.8}$$

The width at LO then simply becomes

$$\Gamma = \frac{\lambda^2 m_{\mathrm{LQ}}}{24\pi}. \tag{7.9}$$

The model has an additional parameter κ, which is the nonminimal coupling [336], which is not present in the scalar model. It is defined as

$$\mathcal{L} \supset -ig_{\mathrm{s}}\kappa U_{1\mu}^\dagger T^a U_{1\mu} G_a^{\mu\nu}. \tag{7.10}$$

The κ parameter captures some of the dependence on specific models with UV completion. This analysis considers the scenarios of $\kappa = 1$, which corresponds to the Yang-Mills case, and $\kappa = 0$, which is the case of minimal coupling. The kinematics of pair and nonresonant production do not depend on κ. For the case of single production, there is a difference for $\lambda > 1$ that is discussed below. Therefore, separate samples are produced.

The cards with the settings for MadGraph generation are available on GitHub [339, 340]. Each sample has about 1 million events. For practical reasons, these samples were shared with the analysis in Ref. [341], which uses the $\beta = 0.5$ benchmark. Therefore, the settings $g_{\mathrm{bL}} = g_{\mathrm{tL}}$ were used, and the vector-LQ is allow to decay to $\mathrm{t}\nu_\tau$ roughly 50% of the time. To get a pure $\beta = 1$ sample for this analysis, each signal event is required to have zero top quarks at generator level. The samples have vector-LQ mass values 500, 800, 1100, 1400, 1700, 2000, 2300 GeV. As was done for the scalar samples, the samples of nonresonant production are further extended up to 10000 GeV, and extra samples of single vector-LQ production with $\lambda = 1.5$, 2.0 and 2.5 are generated to take into account of wider LQ mass distribution and low-$M_{\mathrm{b}\tau}$ pole.

The event generation of nonresonant production in the vector model is done with $\beta = 1$, with about 250 000 events per mass point. The above-mentioned UFO model is slightly modified to allow for nonresonant $\tau\tau$ production. The modified version is available in Ref. [342]. The same mass points are produced, with β set to 1. Events are generated assuming no interference with the SM Drell-Yan process, as the reduction of the signal yield in sensitive regions of the analysis is less than 5% for $\lambda > 1$ [237].

Table 7.4 again summarizes the model parameters, while Table 7.5 lists the UFO models used for event generation. Figure 7.6 summarizes which for points in the λ-mass phase space samples are produced.

Table 7.5: Summary of UFO models used to generate events of different LQ production modes, and compute their respective cross sections. Everything is generated with LO accuracy, except for the case indicated with (*), which is computed at NLO.

Production mode	Event generation	Cross section computation
Scalar		
Single	`LQ_UFO` [334]	`LQ_UFO` [334]
Pair	`LQ_UFO` [334]	`Leptokvark_NLO`* [336, 338]
Nonres.	`LQ_UFO` [334]	`LQ_UFO` [334]
Vector		
Single	`VectorLQ_UFO` [336, 337]	`VectorLQ_UFO` [336, 337]
Pair	`VectorLQ_UFO` [336, 337]	`VectorLQ_UFO` [336, 337]
Nonres.	`VectorLQ_UFO_tchannel` [336, 342]	`VectorLQ_UFO_tchannel` [336, 342]

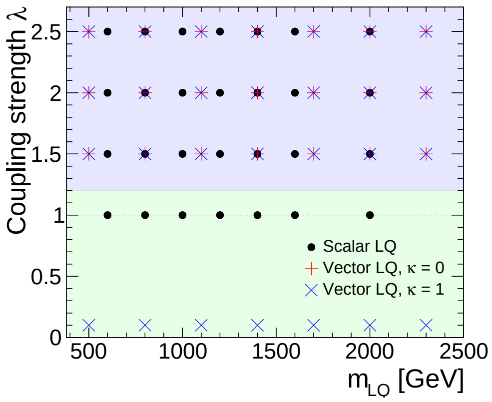

Figure 7.6: Summary of generated single LQ production samples in this analysis. Note that $\lambda > 1$ and/or $\kappa = 0$ samples are only generated for single LQ production, and all nonresonant samples have $\lambda = 1$. Below $\lambda < 1.5$ (green), the width in single production can be safely ignored.

For the vector-LQ scenario, the B anomalies imply a coupling of roughly

$$\lambda = (0.59 \pm 0.20) \times \frac{m_{\mathrm{LQ}}}{\mathrm{TeV}}. \tag{7.11}$$

This relationship was determined by the authors of Refs. [113] and [231] with the method explained in Section 3.4.2.

7.4.3 Study of the LQ $\to$ bτ signal

To better understand the LQ $\to$ bτ signal, we have performed several studies of the generator-level distributions. These are shown in Figs 7.7–7.9 for single production, Figs 7.10 and 7.11 for pair production, and Figs. 7.12 and 7.13 for nonresonant production. The vector and scalar scenarios with $m_{\mathrm{LQ}} = 600$, 1000 and 2000 GeV are compared.

Most noteworthy for an LQ $\to$ bτ search is the fact that the τ leptons in each production mode have a hard p_{T} distribution (see Figs 7.8, 7.10, and 7.12). This includes τ leptons that are produced in association with a single LQ. For resonant production modes, the p_{T} distributions of the τ lepton from LQ decay strongly depend on the LQ mass, with the bulk above $p_{\mathrm{T}} > 100$ GeV. The same is true for the b quark from LQ decay (Figs. 7.7 and 7.10), and the leading jet in the events of single and pair production (Figs. 7.9 and 7.11). For nonresonant production on the other hand, the distributions depend little on the LQ mass: The biggest difference is that the distributions of the τ lepton p_{T} and the invariant mass between the two τ leptons are slightly shifted towards higher values for higher masses, as can be seen in Fig 7.12. Above roughly $m_{\mathrm{LQ}} \gtrsim 2500$ GeV, the kinematic distributions become almost identical, as the t-channel process

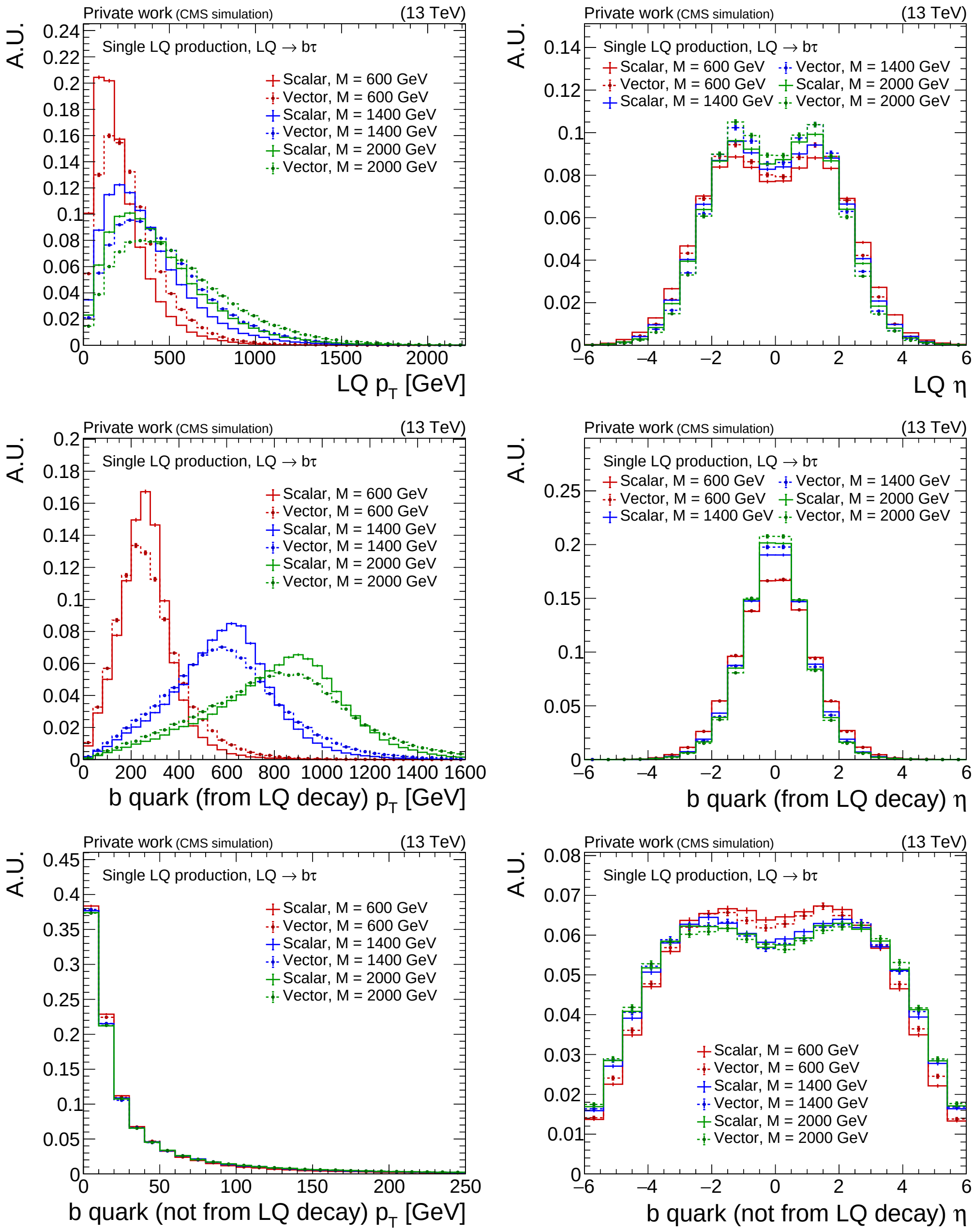

Figure 7.7: Generator-level distributions of single LQ production in the scalar- (solid line) and vector-LQ model (dashed line). **Top**: p_T (left) and η (right) of the LQ. **Middle**: p_T (left) and η (right) of the b quark from LQ decay. **Bottom**: p_T (left) and η (right) of the b quark produced in association (i.e., not from LQ decay).

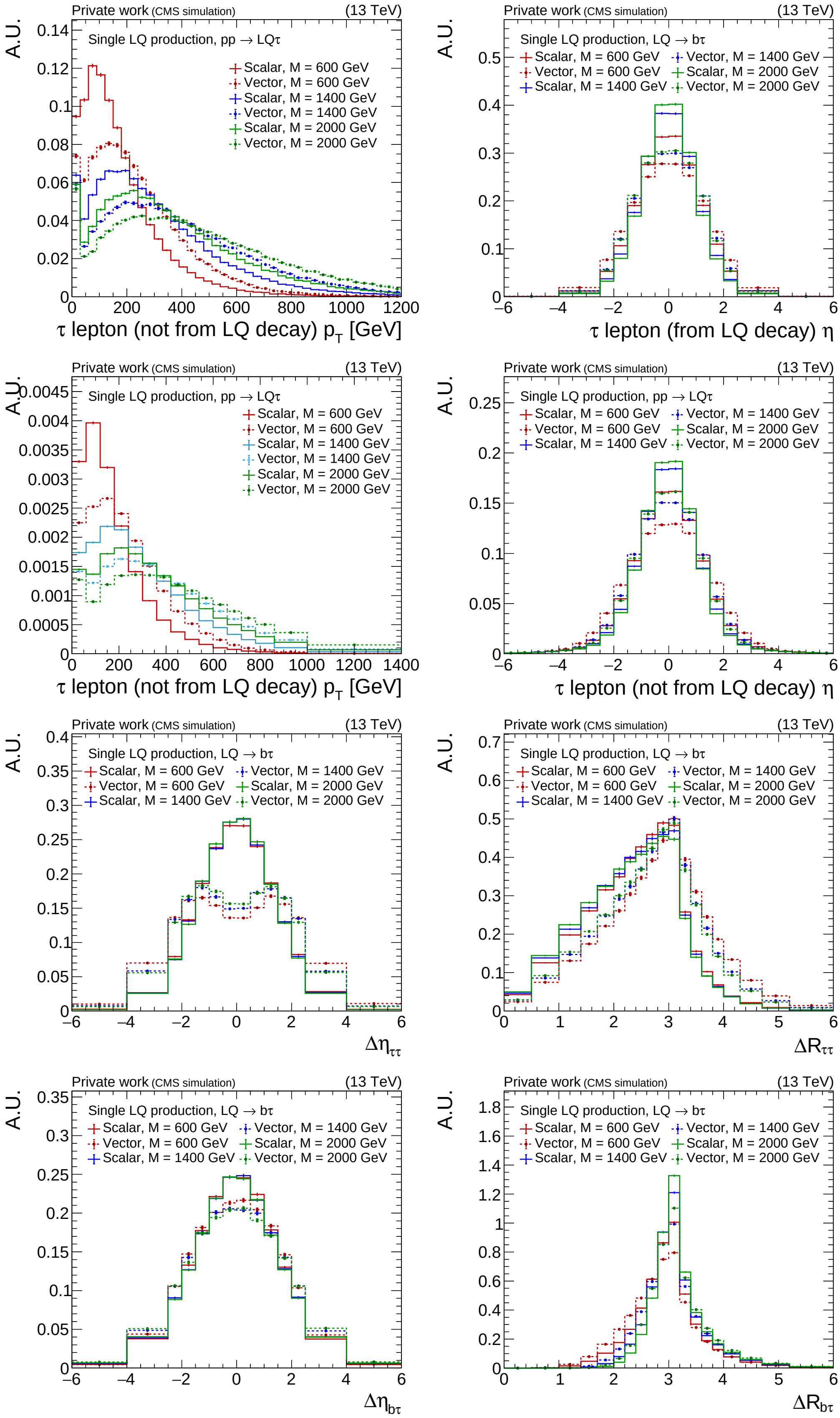

Figure 7.8: Generator-level distributions of the τ leptons from single LQ production in the scalar- (solid line) and vector-LQ model (dashed line). **Top row**: p_{T} (left) and η (right) of the τ leptons from LQ decay. **Second row**: p_{T} (left) and η (right) of the τ leptons produced in association. **Third row**: Opening angles $\Delta\eta$ (left) and ΔR (right) between the two τ leptons. **Bottom row**: Opening angles $\Delta\eta$ (left) and ΔR (right) of LQ $\rightarrow$ bτ decay.

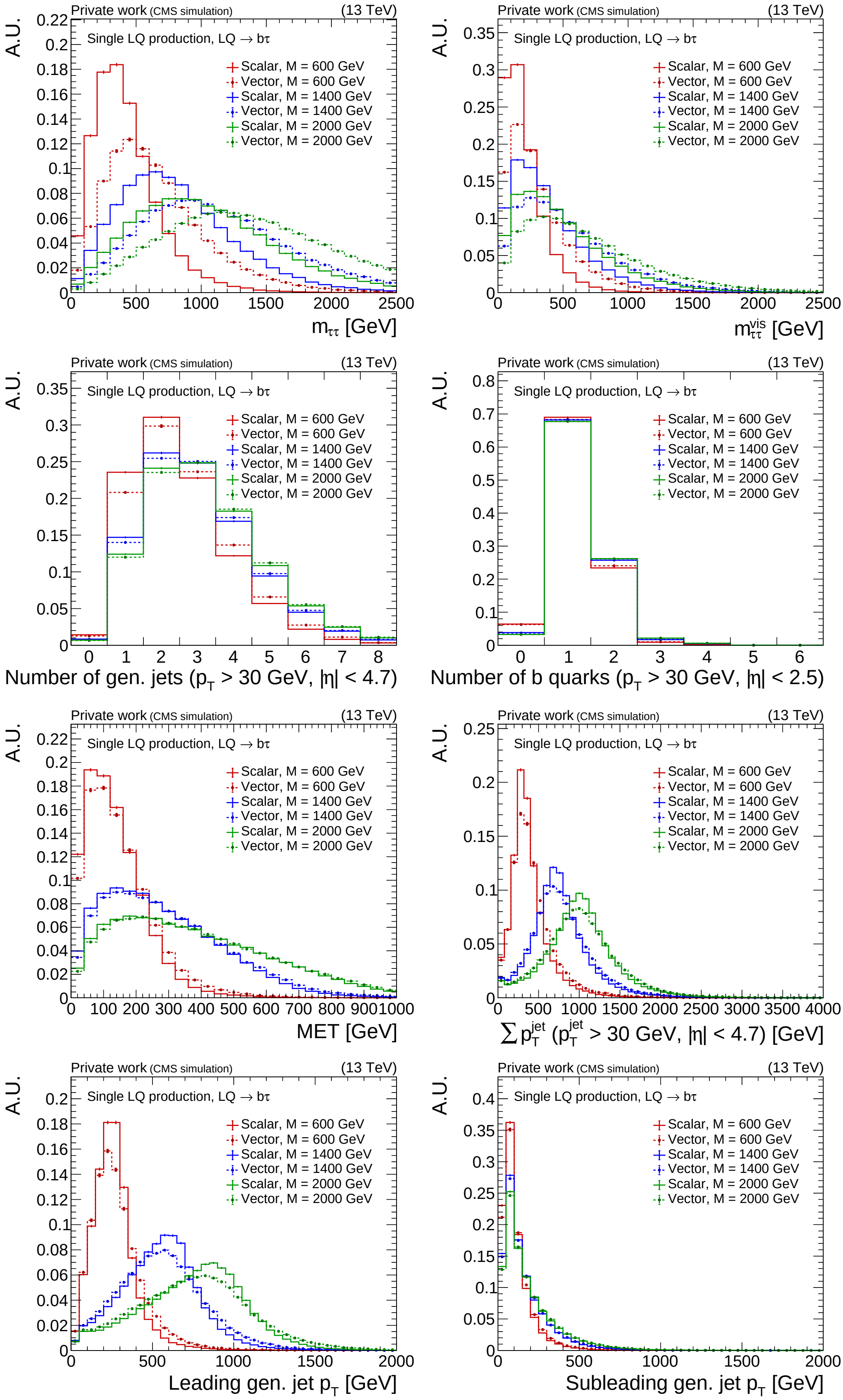

Figure 7.9: Generator-level distributions of single LQ production in the scalar- (solid line) and vector-LQ model (dashed line). **Top row**: Invariant mass between the two τ leptons (left) and the visible τ decay products (right). **Second row**: Multiplicity of jets with $p_{\mathrm{T}} > 30\,\mathrm{GeV}$ and $|\eta| < 4.7$ (left) and b quarks with $p_{\mathrm{T}} > 30\,\mathrm{GeV}$ and $|\eta| < 2.5$ (right). **Third row**: $p_{\mathrm{T}}^{\mathrm{miss}}$ (left) and scalar sum of jet p_{T} (right). **Bottom row**: Leading (left) and subleading jet p_{T} (right) with $|\eta| < 4.7$.

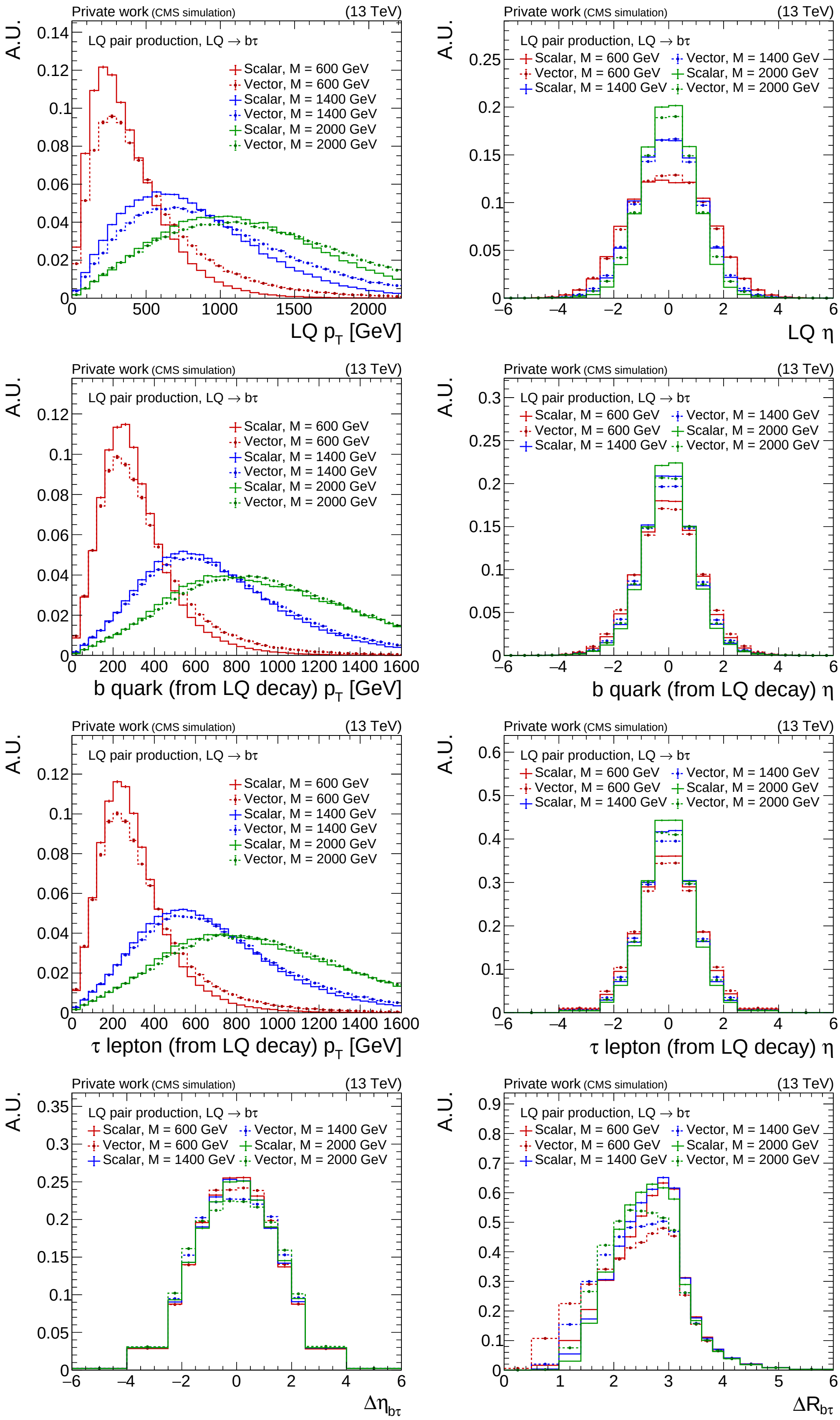

Figure 7.10: Generator-level distributions of LQ pair production for the scalar- (solid line) and vector-LQ model. **Top row**: p_{T} (left) and η (right) of the LQ. **Second row**: p_{T} (left) and η (right) of the b quark from LQ decay. **Third row**: p_{T} (left) and η (right) of the τ lepton from LQ decay. **Bottom row**: Opening angles $\Delta\eta$ (left) and ΔR (right) of LQ $\rightarrow$ bτ decay.

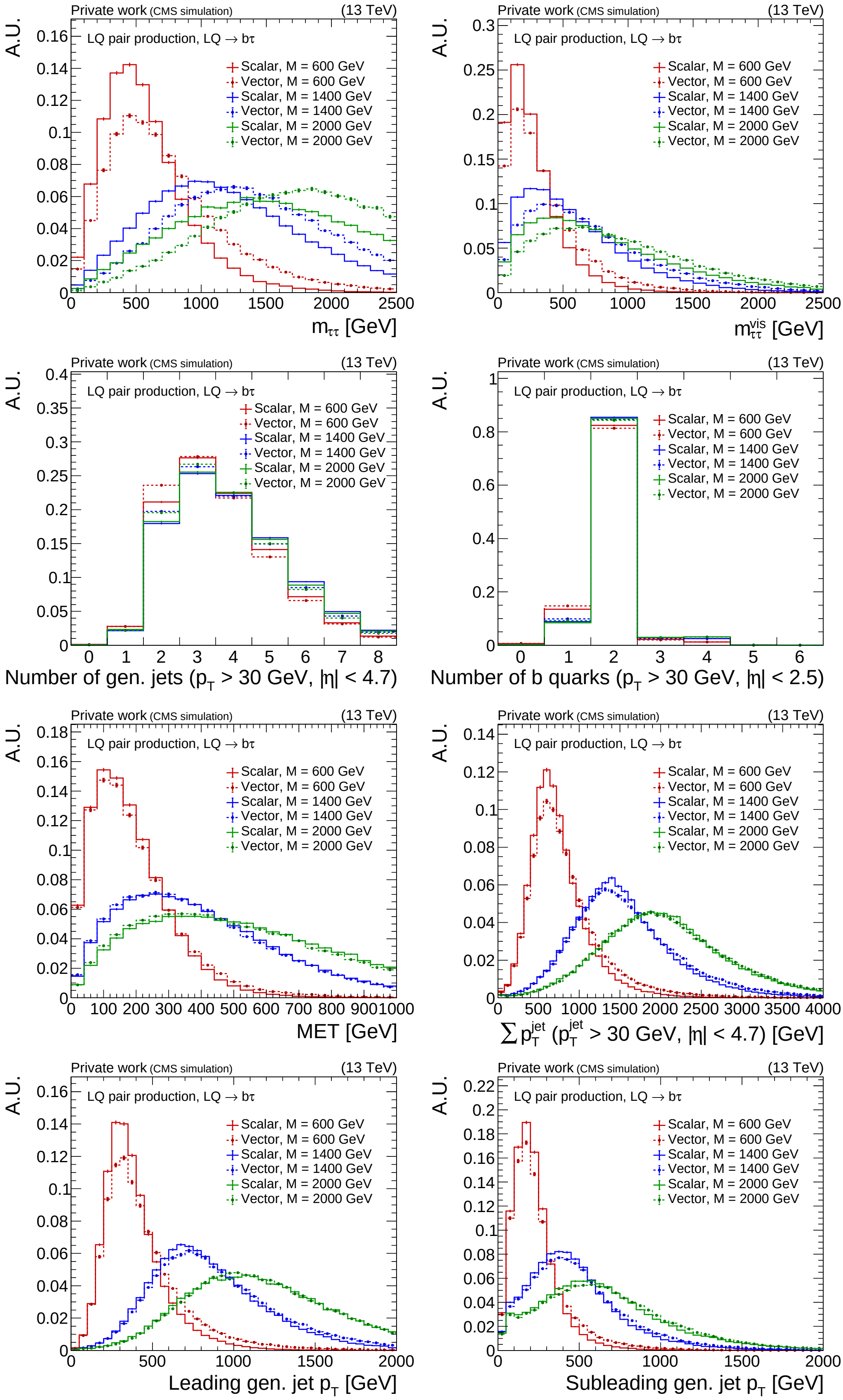

Figure 7.11: Generator-level distributions of LQ pair production in the scalar- (solid line) and vector-LQ model (dashed line). **Top row**: Invariant mass between the two τ leptons (left) and the visible τ decay products (right). **Second row**: Multiplicity of jets with $p_{\mathrm{T}} > 30\,\mathrm{GeV}$ and $|\eta| < 4.7$ (left) and b quarks with $p_{\mathrm{T}} > 30\,\mathrm{GeV}$ and $|\eta| < 2.5$ (right). **Third row**: $p_{\mathrm{T}}^{\mathrm{miss}}$ (left) and scalar sum of jet p_{T} (right). **Bottom row**: Leading (left) and subleading jet p_{T} (right) with $|\eta| < 4.7$.

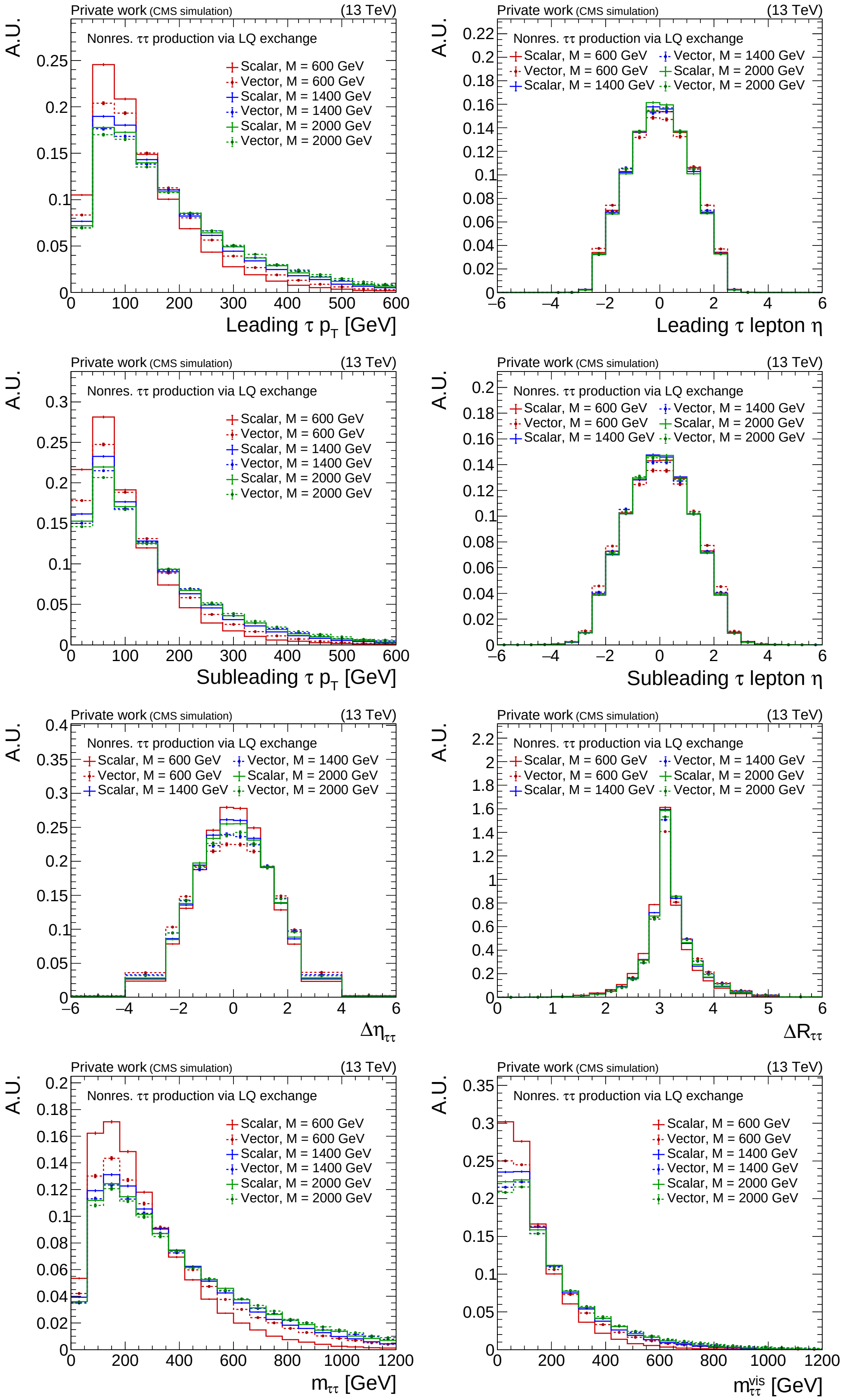

Figure 7.12: Generator-level distributions of the τ leptons in nonresonant $\tau\tau$ production through the t-channel exchange of an LQ in the scalar- (solid line) and vector-LQ model (dashed line). **Top row**: p_T (left) and η (right) of the leading τ lepton. **Second row**: p_T (left) and η (right) of the subleading τ lepton. **Third row**: $\Delta\eta$ (left) and ΔR between the two τ leptons (right). **Bottom row**: Invariant mass between the two τ leptons (left) and the visible τ decay products (right).

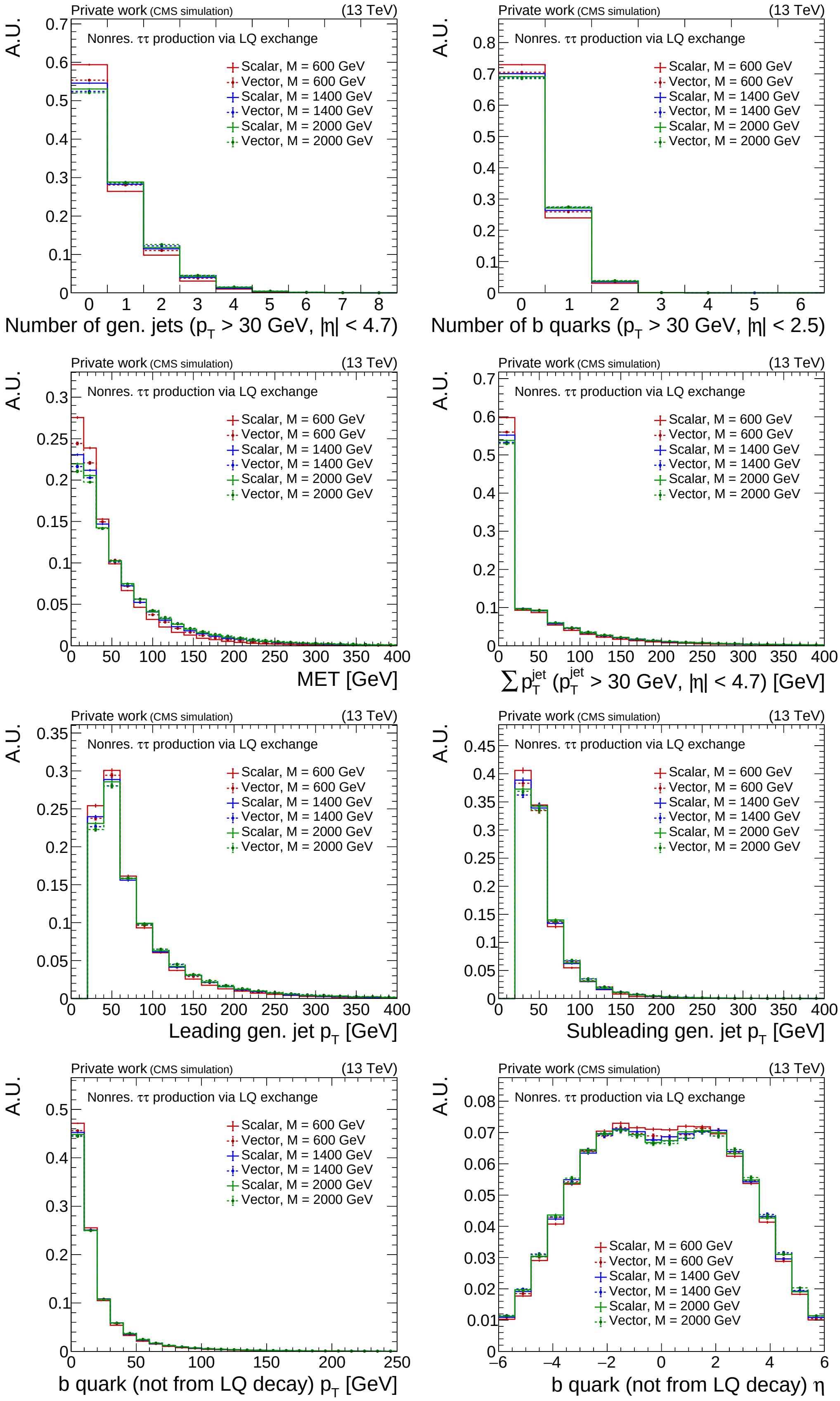

Figure 7.13: Generator-level distributions of nonresonant $\tau\tau$ production through the t-channel exchange of an LQ in the scalar- (solid line) and vector-LQ model (dashed line). **Top row**: Multiplicity of jets with $p_\mathrm{T} > 30\,\mathrm{GeV}$ and $|\eta| < 4.7$ (left) and b quarks with $p_\mathrm{T} > 30\,\mathrm{GeV}$ and $|\eta| < 2.5$ (right). **Second row**: $p_\mathrm{T}^\mathrm{miss}$ (left) and scalar sum of jet p_T (right). **Third row**: Leading (left) and subleading jet p_T (right) with $|\eta| < 4.7$. **Bottom row**: p_T (left) and η (right) of a b quark produced in association (e.g., from gluon splitting).

becomes effectively a four-fermion contact interaction. The only difference between them is the theoretical cross section, which naively scales with $\sigma \propto (\lambda/m_{\mathrm{LQ}})^4$, in analogue to Fermi's interaction discussed in Section 3.3.1.

Another interesting difference between the resonant (i.e., single and pair) and nonresonant production modes is the number of high-p_{T} jets: Events from single and pair production typically have two or more jets with a $p_{\mathrm{T}} > 30\,\mathrm{GeV}$ and $|\eta| < 5$, mostly from the b quarks and hadronic radiation, while those of nonresonant production mostly have fewer than two. Furthermore, the resonant production modes have two or more b quarks in the final state, as is apparent from Figs 7.9, 7.11 and 7.13. In pair production, both b quarks originate from LQs, whereas in the case of single production, a second b quark is often produced from gluon splitting. Meanwhile, a large fraction of nonresonant production has two b quarks in the final state from gluon splitting. although these b quarks tend to be very soft and not traverse the barrel detector where b tagging is possible (Fig. 7.13). This fact and the big difference in number of high-p_{T} jets makes it possible to define orthogonal categories which can efficiently separate the resonant and nonresonant signal with negligible cross contamination of the different signals.

Lastly, in all production modes, the τ-lepton pairs tend to be produced back-to-back in terms of $\Delta\phi$ and ΔR.

7.4.4 Cross sections of LQ production

All cross sections are computed by MadGraph at LO according to the UFO model used for event generation, with the only except being scalar pair production, which is computed by MadGraph5_aMC@NLO at NLO [336]. For single scalar production, the `Leptokvark_NLO` UFO model [336, 338] offers NLO cross sections as well, but these cannot take into account the above-mentioned pole that appears at low $M_{\mathrm{b}\tau}$ values. The models used for cross section computation are summarized in Table 7.5. In the case of the vector model, $g_{\mathrm{bL}} = 1$ and $g_{\mathrm{tL}} = 0$ are set. In all cases, the PDF set `NNPDF31_lo_as_0130` is used. The cross sections of each production mode and their sum as a function of LQ mass for $\lambda = 1$ and 2.5 are shown in Fig. 7.14.

In the case of single and nonresonant production, the cross sections depend on λ, while pair production does not. The cross sections of pair and single vector LQ production depend on the nonminimal coupling κ, and so are calculated for $\kappa = 0$ and 1. The cross section for nonresonant production does not depend on κ.

We use the following notation for single, pair, and nonresonant production:

$$\sigma^{\mathrm{single}} = \sigma(\mathrm{pp} \to \tau\mathrm{LQ}), \tag{7.12}$$

$$\sigma^{\mathrm{pair}} = \sigma(\mathrm{pp} \to \mathrm{LQ}\overline{\mathrm{LQ}}), \tag{7.13}$$

$$\sigma^{\mathrm{nonres}} = \sigma(\mathrm{pp} \to \tau\tau), \tag{7.14}$$

respectively. For maximal sensitivity, these three production modes are treated as one signal. Therefore, this analysis derives an upper limit on the sum of their cross sections:

$$\sigma^{\mathrm{tot}} = \sigma^{\mathrm{single}} + \sigma^{\mathrm{pair}} + \sigma^{\mathrm{nonres}} \tag{7.15}$$

As single and pair production share very similar final states, the optimization for the final signal selections targeting their combination in Section 10.2, is based on the expected upper limit on

Table 7.6: Summary of the cross section (σ) and kinematic (kin.) dependence on coupling strength λ (scalar and vector) and nonminimal coupling κ (vector only).

Parameter	Pair	Single	Nonresonant
λ	σ^{pair} independent Kin. independent	$\sigma^{\text{single}} \propto \lambda^2$ (on BW peak, or $\lambda \leq 1$) Width and low-$M_{\text{b}\tau}$ pole (negl. for $\lambda < 1.5$)	$\sigma^{\text{nonres}} \propto \lambda^4$ Independent
κ	σ^{pair} dependent Kin. independent	σ^{single} dependent Kin. dependent (negl. for $\lambda < 1.5$)	σ^{nonres} independent Kin. independent

the sum of their cross sections in the absence of a signal:

$$\sigma^{\text{res}} = \sigma^{\text{single}} + \sigma^{\text{pair}}, \tag{7.16}$$

where "res" stands for "resonant production".

As discussed in Section 3.4.3, cross sections have different dependencies on λ: The single production of an on-shell LQ will depend on λ as $\sigma^{\text{single}} \propto \lambda^2$, while the nonresonant production scales with $\sigma^{\text{nonres}} \sim \lambda^4$. We can therefore derive the upper limits as function of both m_{LQ} and λ, by using the fact that

$$\sigma^{\text{single}} = \lambda^2 \sigma^{\text{single}}_{\lambda=1} \tag{7.17}$$

$$\sigma^{\text{pair}} = \sigma^{\text{pair}}_{\lambda=1} \tag{7.18}$$

$$\sigma^{\text{nonres}} = \lambda^4 \sigma^{\text{nonres}}_{\lambda=1} \tag{7.19}$$

$$\sigma^{\text{tot}} = \lambda^2 \sigma^{\text{single}}_{\lambda=1} + \sigma^{\text{pair}}_{\lambda=1} + \lambda^4 \sigma^{\text{nonres}}_{\lambda=1} \tag{7.20}$$

However, for $\lambda > 1.0$, a large pole appears at values in the $M_{\text{b}\tau}$ spectrum of the single LQ production, as was shown in Fig. 7.5. To take into account the extra events of this pole, the cross sections for single production are recomputed for $\lambda = 1.5$, 2.0, and 2.5. At high $\lambda > 1$, the BW peak of the on-shell LQ still grows with λ^2, but the $M_{\text{b}\tau} = 0$ pole scales with roughly λ^4. In the computation of the single production cross section, the same BW cut is used as is in event generation. Table 7.6 summarizes how the kinematic behavior and cross section of each production mode depends on the λ and κ parameters.

The exact method of extracting the signal and deriving upper limits on the cross section and Yukawa coupling λ will be discussed in Section 12.

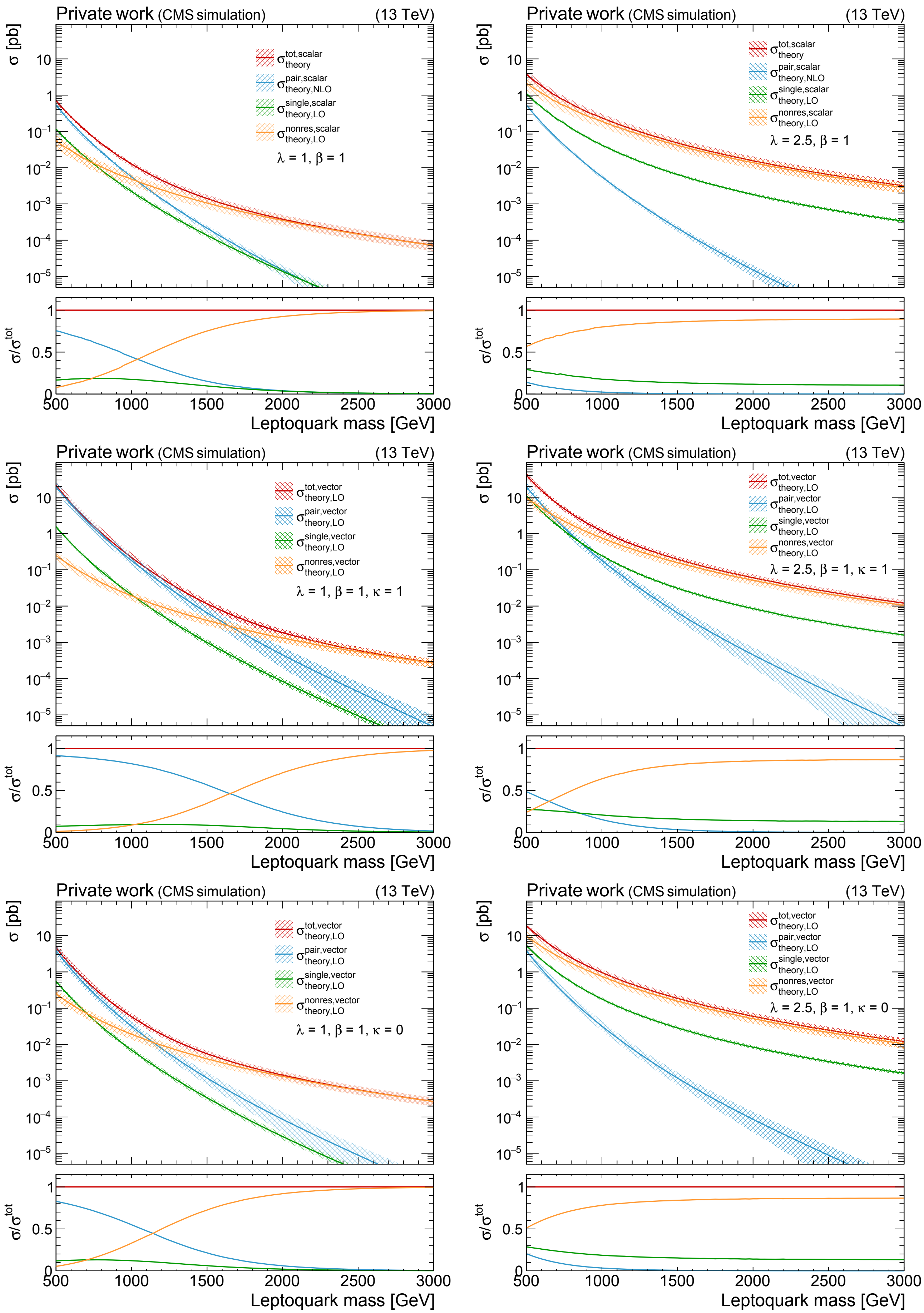

Figure 7.14: Cross section of LQ production in pp collisions at 13 TeV, through single, pair and nonresonant production, for the scalar (top) and vector model with $\kappa = 1$ (middle) and 0 (bottom), and assuming $\lambda = 1$ (right) or 2.5 (left). The nonresonant cross section scales with λ^4.

8 Corrections to Simulated Events

Simulated data has various mismodelings, which include imperfect reconstruction and identification of particles, unsimulated effects of detector noise, and the inaccurate modeling of the effects of pileup. Differences between observed and simulated data can also be due to the limited accuracy of MC generation. This section describes several methods to derive and apply corrections to simulated events in order to improve the agreement between the background expectation and the observed data. I have derived a number of these myself, such as the Z p_{T} corrections. Others were derived by the designated *Physics Object Groups* (POGs) within CMS. Corrections to τ_{h} objects will be discussed in Chapter 9.

8.1 Pileup reweighting

Pileup reweighting is applied to simulated events so that simulated events have the same distribution of the number of PVs per event as the data they are representing. In doing this, the multiplicity of particles and the energy deposited in the various sub-detectors in simulated events is expected to better match the data. This is done with the "true pileup reweighting method". The "true pileup" is the mean of the Poisson distribution from which the number of interactions per bunch crossing has been sampled. This variable is reweighted in 100 bins between 0 to 100 such that it matches the estimated number of PVs during data taking. The mean pileup in "real" data is estimated from dedicated instantaneous luminosity measurements and assuming a total pp inelastic cross section of $\sigma_{\mathrm{pp}}^{\mathrm{inel}} = 69.2\,\mathrm{mb}$ with an uncertainty of 4.6%. The total inelastic cross section is often referred to as the *minimum bias cross section* in this context.

The pileup profiles and the resulting weight (i.e., data/simulation ratio) are shown in Fig. 8.1, for different assumptions of the minimum bias cross section. While pileup reweighting improves the agreement between the observed and simulated number of PVs, discrepancies are still present, as this method is mostly correlated with the estimation of the median p_{T} density, ρ, which shows better improvement. Furthermore, this method does not take into account the efficiency of PV reconstruction. The residual discrepancy in number of PVs should, however, not affect the LQ search, because the variables under study are more strongly correlated with ρ, rather than the number of PVs.

8.2 Triggers efficiencies

Trigger efficiencies are measured in both real and simulated data. Scale factors (SFs) are derived from their ratio that are used to reweight simulated events for improving agreement with observed efficiencies.

The efficiencies for the single-electron and single-muon trigger are measured with the *tag-and-probe method* [257, 278, 343, 344], which aims to collect an unbiased sample of "probe objects" by tagging events with a "tag object" which is assumed to be constructed well and identified with a minimal background.

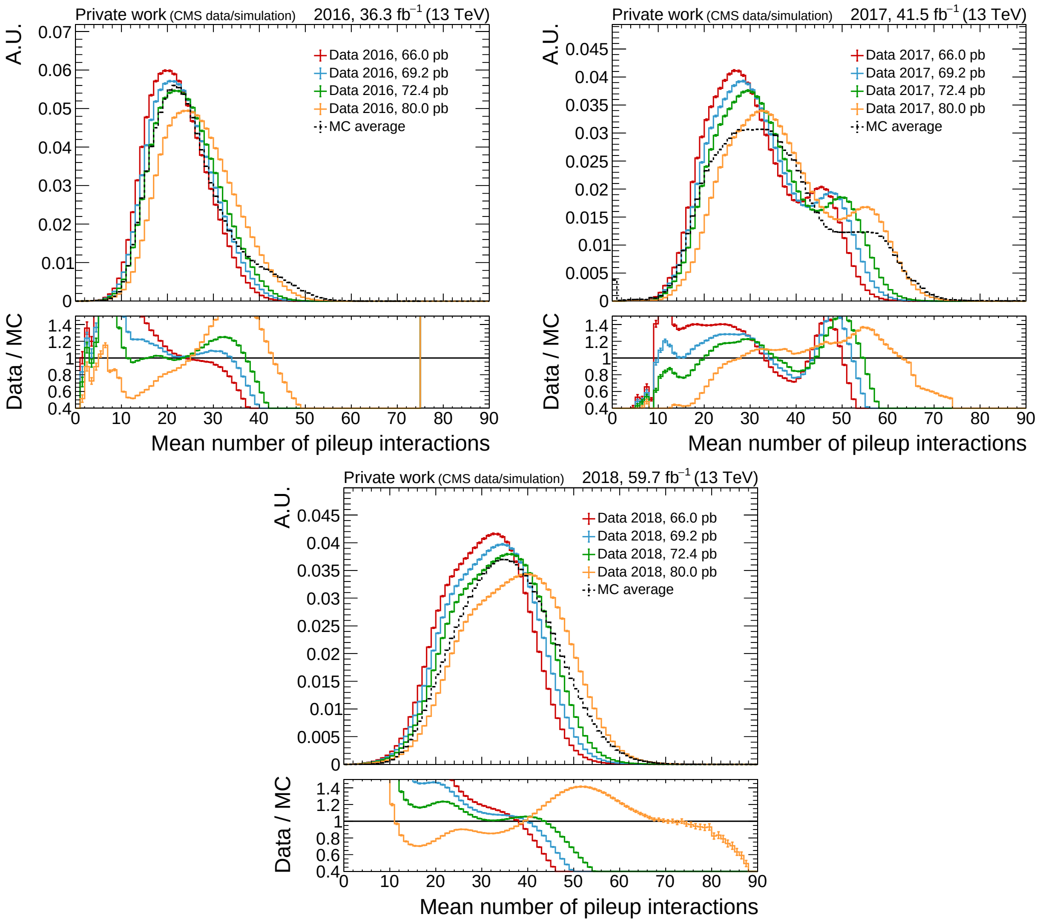

Figure 8.1: Distribution of the mean number of pp interactions per bunch crossing ("true pileup") in 2016 (left), 2017 (center) and 2018 (right). Compared are the estimated pileup profiles in simulated and real data for different total pp inelastic (minimum-bias) cross section. The recommended value for PU estimation within CMS is $\sigma_{\mathrm{pp}}^{\mathrm{inel}} = 69.2\,\mathrm{mb}$ with a 4.6% uncertainty, while 80.0 mb is used for public comparisons with ATLAS.

Given the kinematic regime of the single-lepton triggers used in this analysis, the $\mathrm{Z} \to \ell^+\ell^-$ events are targeted by selecting events with two leptons that have the same flavor, opposite charge, and an invariant mass of $m_{\ell\ell} > 50\,\mathrm{GeV}$. Furthermore, they must each pass tight identification and isolation requirements and be separated by $\Delta R > 0.5$. The "tag" lepton must also match the requirement of the corresponding trigger and match a "trigger object" that caused the trigger selection to be fulfilled. The other lepton is considered the "probe", and is divided into a "Fail" or "Pass" group, based on whether it caused the trigger selection to be satisfied. Efficiencies ε_i are measured as a function of p_{T} and η of the reconstructed probe lepton in data and simulation, and the resulting SF is simply the ratio $\varepsilon_{\mathrm{obs}}/\varepsilon_{\mathrm{sim}}$.

The SFs for the double-τ_{h} trigger are obtained with a similar technique by the TauPOG. The efficiencies in data and simulated events are fitted as a function of τ_{h} p_{T} and decay mode for different WPs of the `DeepTau2017v2p1VSjet` discriminator.

8.3 Electron & muon efficiencies

Lepton identification and isolation efficiencies are also measured in data and simulation with a tag-and-probe method using $\mathrm{Z} \to \mathrm{e}^+\mathrm{e}^-$ and $\mathrm{Z} \to \mu^+\mu^-$ events [257, 278]. The tag lepton must pass the kinematic requirements (i.e., p_{T} and η), identification, and isolation criteria, and match the trigger object as before, while the probe lepton has to pass at least the kinematical requirements. The lepton identification and isolation efficiency is then defined as the number of probes passing the identification and isolation requirements, divided by the total number of probes by fitting the invariant mass $m_{\ell\ell}$ in a window around the Z peak. The SFs are again defined as the ratio $\varepsilon_{\mathrm{obs}}/\varepsilon_{\mathrm{sim}}$ binned in p_{T} and η.

8.4 B tagging reweighting

The difference in b tagging efficiency between observed and simulated data has been taken into account by applying a weight that is calculated on an event-by-event basis. The probability of finding an observed or simulated event with a given collection $\{b\}$ of b-tagged jets and a collection $\{j\}$ of untagged jets, is determined by the tagging efficiencies:

$$P(\text{data with } \{j\},\, \{b\}) = \prod_{\{b\}} \varepsilon_b \prod_{\{j\}} (1-\varepsilon_j) \tag{8.1}$$

$$P(\text{simulation with } \{j\},\, \{b\}) = \prod_{\{b\}} \varepsilon_b^{\mathrm{sim}} \prod_{\{j\}} (1-\varepsilon_j^{\mathrm{sim}}) \tag{8.2}$$

where the efficiencies, or the mistag rate for jets not originating from b jets, ε_i and $\varepsilon_i^{\mathrm{sim}}$ are measured in observed and simulated data, respectively. They are parametrized according to the jet flavor, p_{T}, and η. The b tagging SFs have been measured by the *B-tagging and Vertexing* (BTV) POG in CMS, and are defined such that $\varepsilon_i = \mathrm{SF}_i \varepsilon_i^{\mathrm{sim}}$ per jet flavor i. The measurement of the SFs are documented in Ref. [286]. The ratio of Eqs. 8.1 and 8.2 provides the total event weight to the simulated events,

$$w = \frac{P(\text{data with } \{j\},\, \{b\})}{P(\text{simulation with } \{j\},\, \{b\})} = \prod_{\{b\}} w_b \prod_{\{j\}} w_j, \tag{8.3}$$

where each jet in the event will contribute a factor term

$$w_b = \mathrm{SF}_b \qquad \text{(b tagged)}, \tag{8.4}$$

$$w_j = \frac{1-\mathrm{SF}_j \varepsilon_j^{\mathrm{sim}}}{1-\varepsilon_j^{\mathrm{sim}}} \qquad \text{(untagged)}. \tag{8.5}$$

The efficiencies and mistag rates may also depend on the selections, as removing the overlap between jets and selected objects may bias the efficiencies. The efficiency and mistag rate of b tagging of jets in simulation have therefore been measured for each of the $\tau\tau$ decay channels of the LQ $\to$ bτ analysis, after removing from the jet collection jets that are within $\Delta R < 0.5$ of electron, muon, and τ_{h} candidates that have been preselected with loose isolation criteria. The b-tagging efficiencies in simulation are shown in Fig. 5.4 for the $\mu\tau_{\mathrm{h}}$ channel as an example. They are very similar across the different channels.

8.5 Z p_{T} corrections

The dimuon p_{T} distributions of Drell-Yan events generated by MadGraph at LO show significant disagreement with observed data as recoil of the Z boson is not well modeled without higher-order corrections. Therefore, weights are measured from data, and are applied to events of this sample. The corrections are measured separately for each data-taking year from a dimuon region in data that is enriched in Z $\to$ $\mu^+\mu^-$ events. The dimuon region is defined as the set of events that have two opposite-charge muons, where each muon is consistent with the PV of

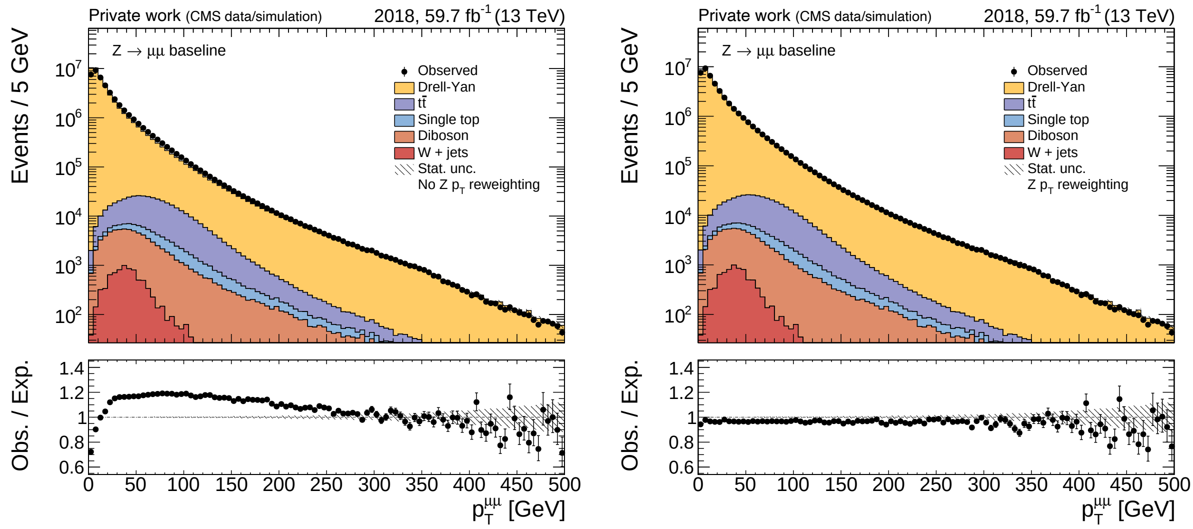

Figure 8.2: The dimuon p_T distributions in 2018 data, before (left) and after (right) applying the Z p_T reweighting to the Drell-Yan sample generated by MadGraph with LO accuracy (orange). Note the Drell-Yan events are reweighted such that only the shape of the distribution is corrected, and not the overall normalization.

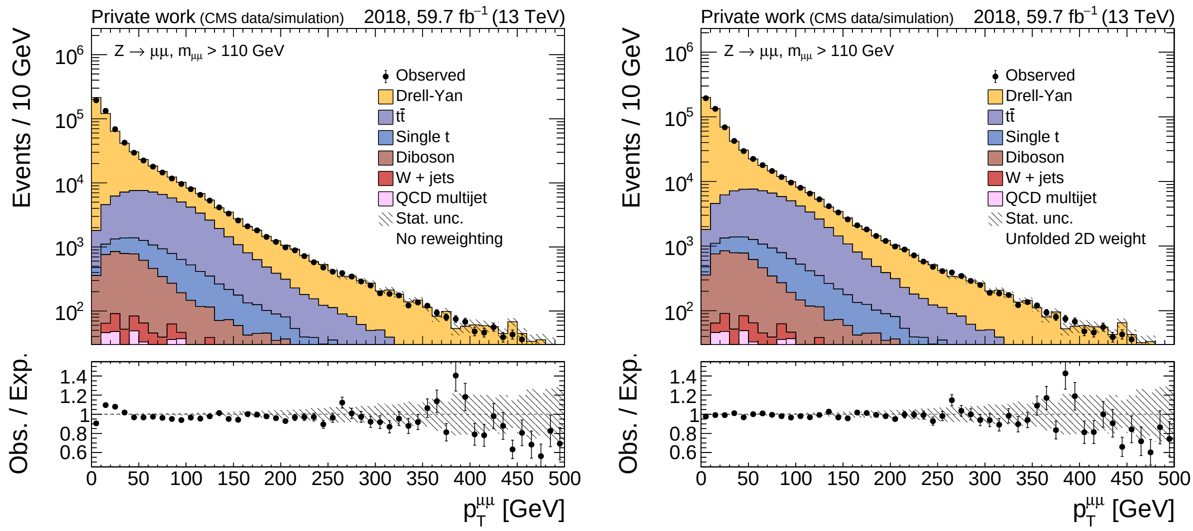

Figure 8.3: The dimuon p_T distributions in 2018 data, before (left) and after (right) applying the Z p_T reweighting to the Drell-Yan sample generated by MadGraph5_aMC@NLO with NLO accuracy and $M_{\ell\ell} > 100\,\text{GeV}$ (orange).

the hard process, passes the medium ID, and has a relative isolation less than $I^{\mu}_{\text{rel}} < 0.15$. The leading muon is required to pass a minimum p_T cut that is 1 GeV higher than the online p_T threshold of the fired single-muon trigger (see Table 7.2), while the subleading muon is required to have $p_T > 15\,\text{GeV}$. Events with additional identified and isolated electrons and muons are discarded.

The weights are computed in bins of generator-level $p_T^{\mu\mu}$ and $m_{\mu\mu}$ such that the observed and expected event yields match in the two-dimensional histogram of the reconstructed dimuon $p_T^{\mu\mu}$ versus invariant mass $m_{\mu\mu}$. In this procedure, the expected backgrounds are minor, and are subtracted from observed data. The resulting weights are normalized in order to have a shape-only effect, leaving the total expected Drell-Yan yield unaffected. The distributions of the reconstructed dimuon p_T before and after reweighting are shown in Fig. 8.2.

The initial agreement with the observed dimuon p_T spectrum is much better for the Drell-Yan sample generated with MadGraph5_aMC@NLO, except for below 50 GeV. Using a similar technique, weights are derived for this sample in the dimuon region, but with a $m_{\mu\mu} > 110\,\mathrm{GeV}$ cut because of the minimum generator cut of this sample (see Table 7.3). The reconstructed dimuon p_T before and after reweighting are shown in Fig. 8.3. To validate the measurement method and ensure that the results are consistent, a *closure test* has been performed between the distributions predicted by the LO and NLO samples, and found good agreement after applying their respective Z p_T corrections.

8.6 Top-quark p_T corrections

It has been found that the p_T distribution of top quarks in $\mathrm{t\bar{t}}$ events is softer in data than in simulation. The weights computed by comparing the p_T spectrum of the top quark generated by NNLO and NLO generators do not improve the agreement of the kinematic distributions between observed and expected events in the final LQ signal selections described in Chapter 10 for final states with an electron and a muon. Based on measurements of the $\mathrm{t\bar{t}}$ cross section in pp collisions at 13 TeV [345, 346], corrections have been derived for simulated $\mathrm{t\bar{t}}$ events. By fitting the difference between data and the prediction by the POWHEG + PYTHIA generator, a SF for each top quark was found to be

$$\mathrm{SF}\left(p_\mathrm{T}\right) = \sqrt{\exp\left(0.0615 - 0.0005 \cdot \min\left[p_\mathrm{T}/\mathrm{GeV}, 500\right]\right)}, \tag{8.6}$$

where the SF is a function of the top-quark p_T, and is taken as constant beyond $p_\mathrm{T} = 500\,\mathrm{GeV}$. Because $\mathrm{t\bar{t}}$ events are a major background in the LQ search, the top-quark p_T reweighting is not applied nominally in the final signal selections, and needs to be determined from a dedicated $\mathrm{t\bar{t}}$ control region. For the case of the LQ analysis, this is the $\mathrm{e}\mu$ channel, which is very pure in $\mathrm{t\bar{t}}$ and is expected to have a negligible amount of LQ signal. The above SF is used to produce a reasonable shape variation of the final discriminant. The reweighting is fully constrained by the control region in $\mathrm{e}\mu$. This is fitted simultaneously with the signal regions, taking into account all the common theoretical and experimental uncertainties.

8.7 ECAL L1 prefiring

In 2016 and 2017, an increasing offset in the timing calibration of ECAL pulses was observed. This was not properly propagated to L1 trigger primitives (TP). As a result, a significant fraction of TPs in the forward $2 < \eta < 3$ region were mistakenly associated to the previous bunch crossing [347]. This prefiring effect is not taken into account in MC and has a small but nonnegligible effect on the signal. It is therefore taken into account with an event weight that is computed by looping over all offline photons and jets in the event and assigning to them a prefiring probability with some uncertainty.

8.8 HEM 15/16

Due to power interruptions, HCAL endcaps HEM15 and HEM16 could no longer be operated from Run 319077 until the end of the 2018 run. The affected region is in $-3.0 < \eta < -1.3$ and $-1.57 < \phi < -0.87$. It was checked that the failure in this region has no impact on the observed data and simulation of the LQ $\rightarrow \mathrm{b}\tau$ search.

9 Measurement of the τ_h Identification Efficiency & Energy Scale

As argued in Chapter 6, the reconstruction and identification of τ_h decays are indispensable in analyses involving τ leptons. Besides having a set of dedicated algorithms that perform well, it is important to have a good description of data with simulation. Therefore, I have been closely involved in several measurements of the reconstruction and identification efficiency, as well as the τ_h energy scale in the TauPOG, which are used in most CMS analyses that employ τ_h objects. This chapter will discuss these and other measurements.

9.1 Reconstruction & identification efficiency

There is an overestimation of up to roughly 10% of the τ_h efficiency of the `DeepTau2017v2p1VSjet` discriminator at values close to 1, where the purity of genuine τ_h decay is the highest. Efficiency SFs are therefore measured for physics analyses, and are applied to simulated τ_h objects that match a hadronic decay of a τ lepton at generator level. Similar to the measurements of lepton SFs in Sections 8.2 and 8.3, the `DeepTau2017v2p1VSjet` efficiency SF measurement is based on a tag-and-probe method, using $\mu\tau_h$ event selections that target the $Z \to \tau^+\tau^-$ resonance.

9.1.1 Object & event selections

The object and event selection follows closely that of the common preselection for the $\mu\tau_h$ channel described in more detail in Section 10.1. Events are required to have been recorded with a single-muon trigger (see Section 7.1), and contain an identified and isolated muon that has a p_T of at least 1 GeV higher than the p_T threshold of the trigger. The τ_h candidate must pass the VVLoose WP of the `DeepTau2017v2p1VSe` discriminator, and the Tight WP of the `DeepTau2017v2p1VSmu` discriminator. A tigher WP is chosen for the muon discriminator to significantly reduce the $Z \to \mu^+\mu^-$ background. Only the following reconstructed decay modes are considered: $h^\pm$, $h^\pm\pi^0$, $h^\pm h^\mp h^\pm$, and $h^\pm h^\mp h^\pm \pi^0$.

To further reduce the background with little loss of $Z \to \tau^+\tau^-$ events, further purification selections are applied. First, the transverse mass of the muon and $\vec{p}_T^{\,miss}$,

$$m_T = \sqrt{2 p_T^{\mu} p_T^{miss} (1 - \cos\Delta\phi)}, \tag{9.1}$$

must be below $m_T < 60$ GeV, where $\Delta\phi$ is the angle between the muon momentum and $\vec{p}_T^{\,miss}$ in the transverse plane. In addition, events are required to satisfy $p_\zeta^{miss} - 0.85 p_\zeta^{vis} > -25$ GeV, where p_ζ^{miss} is the component of the $\vec{p}_T^{\,miss}$ along the bisector axis $\vec{\zeta}$ of the $\vec{p}_T$ of the lepton and τ_h, while p_ζ^{vis} is the vector sum of the lepton and τ_h candidate momenta, also projected on the $\vec{\zeta}$ axis [348]. This variable quantifies the compatibility of events with the topology wherein the direction of neutrinos from the τ-lepton decays are aligned with the direction of the visible τ-lepton decay products. This requirement is optimized to remove a substantial amount of $t\bar{t}$

as well as W + jets events. It is defined in more detail in Section 10.1.4. Finally, the maximum separation in pseudarapidity between the muon and τ_h candidate is required to be $|\Delta\eta| < 1.5$.

A $Z \to \mu^+\mu^-$ event sample complementary to the $\mu\tau_\mathrm{h}$ sample is created to control the theoretical cross section in the final fit. This sample is obtained from $\mu\mu$ events requiring the same trigger and muon selection criteria as for the $\mu\tau_\mathrm{h}$ event sample. The invariant mass of the two muons must be in a window around the Z boson mass: $60 < m_{\mu\mu} < 120\,\mathrm{GeV}$.

In addition to the $Z \to \ell^+\ell^-$ samples, a separate event sample of $W^* \to \tau\nu_\tau$ is created to measure the efficiency SFs at τ_h $p_\mathrm{T} > 100\,\mathrm{GeV}$, as the number of $Z \to \tau^+\tau^-$ events at high τ_h p_T is limited. The sample is created by selecting events with a τ_h object, plus large $p_\mathrm{T}^\mathrm{miss}$, and no other hadronic jets. A $W^* \to \mu\nu_\mu$ control region is also included to constrain the fiducial cross section of W^* production. The procedure is documented in Ref. [299].

9.1.2 Measurement

As an observable, the invariant mass m_vis of the muon and τ_h candidates in the 50–150 GeV range is used to fully capture the $Z \to \tau^+\tau^-$ resonance while keeping part of the sideband, which helps to constrain the backgrounds. The SF is obtained as the parameter of interest in a binned maximum likelihood fit [306] of the SM expectation to the observed m_vis distribution in the $\mu\tau_\mathrm{h}$ events, and the expected to observed yield in the $\mu\mu$ events. The SF represents the ratio of the observed and expected efficiency for a genuine τ_h object to be reconstructed and pass the identification. Several systematic uncertainties of known sources are incorporated in the fit as nuisance parameters. These include uncertainties in the normalization of various SM processes, muon efficiencies, integrated luminosity, as well as uncertainties due to the limited number of simulated events in each histogram bin. The $Z \to \ell^+\ell^-$ normalization is left freely floating while correlating relevant systematic uncertainties like muon efficiencies and luminosity such that they partially cancel.

Previous τ_h efficiency SF measurements in Run 2 instead performed a simultaneous fit with a "Fail" region of $\mu\tau_\mathrm{h}$ events wherein the τ_h candidate failed a given WP of the identification. The expected number of events with genuine τ_h candidates in the Fail region was properly anti-correlated with the events in the "Pass" region in order to constrain the SF. This did not improve the overall fit, and was dropped for simplicity.

The fit is performed separately for each year and `DeepTau2017v2p1VSjet` WP, and in bins of τ_h p_T. The resulting p_T-dependent SFs for several WPs and for 2018 data are shown in Fig. 9.1. For the measurement in $Z \to \tau^+\tau^-$ events, the edges of the p_T bins are 20, 25, 30, 35, 40, 50, 70 GeV, where the last bin includes all events with $p_\mathrm{T} > 70\,\mathrm{GeV}$. The SFs above $p_\mathrm{T} > 40\,\mathrm{GeV}$ have negligible p_T dependency within the uncertainties, and are therefore fitted with a single constant (shown as the red line). The uncertainties in this fit are linearly enlarged up to double the uncertainty from 500 to 1000 GeV, after which, it is taken as constant. Overall, the dominant source of uncertainty is statistical in nature due to the limited number of events per bin.

The efficiency SFs are therefore also measured for the four main decay modes instead of p_T, namely $h^\pm$, $h^\pm\pi^0$, $h^\pm h^\mp h^\pm$, and $h^\pm h^\mp h^\pm\pi^0$. This is done because the trigger efficiency of τ_h objects differs between reconstructed decay modes, and as a consequence, the double-τ_h trigger algorithm introduces a bias in the relative distribution of the τ_h decay mode. Because of the trigger thresholds of these triggers, the measurement is performed with $p_\mathrm{T} > 40\,\mathrm{GeV}$. The results are shown in Fig. 9.1.

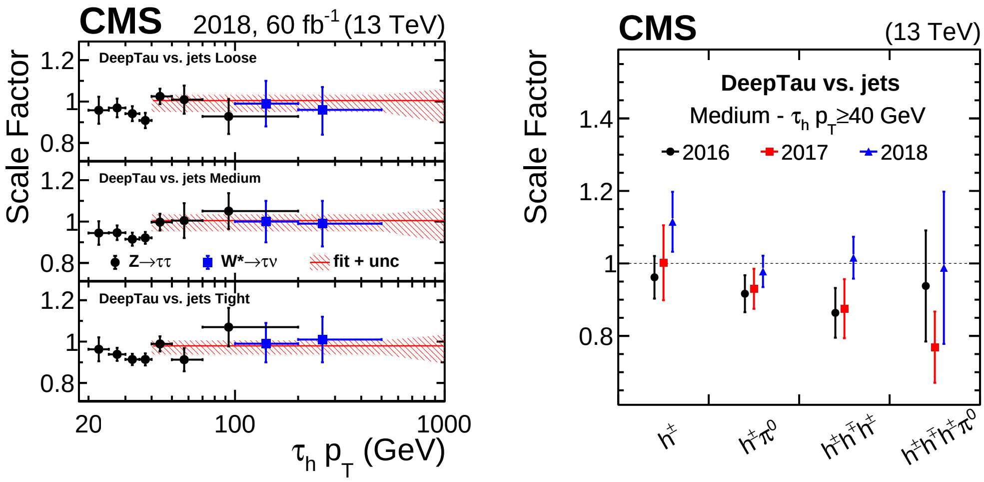

Figure 9.1: Data-to-simulation scale factors (SFs) for the τ_h reconstruction and identification efficiency with `DeepTau2017v2p1VSjet`. **Left**: p_T-dependent SFs for the Loose, Medium, and Tight WPs in the 2018 data-taking period, as measured in the $Z \to \ell^+\ell^-$ (black) and $W^* \to \ell\nu_\ell$ (blue) samples. **Right**: SFs per τ_h decay mode for the Medium WP of `DeepTau2017v2p1VSjet`, and the data taken in 2016, 2017, and 2018. Figures taken from [289].

9.2 Lepton misidentification rate

The probabilities of an electron or a muon to be misreconstructed and misidentified by the DeepTau algorithm are measured in data and simulation with a similar tag-and-probe method around the $Z \to \ell^+\ell^-$ resonance, where $\ell^\pm = e^\pm$, $\mu^\pm$. A sample of $\ell\tau_h$ events is created, where one electron or muon, the probe, is misreconstructed as a τ_h object. The probabilities are extracted from a pass and fail region, where the electron (muon) passes or fails a given WP of `DeepTau2017v2p1VSe` (`DeepTau2017v2p1VSmu`). To reflect the segmentation of the relevant subdetector systems, the measurements are done as a function of η^{τ_h}. SFs are then obtained from the data-to-simulation ratio of the misidentification probability for each WP of the respective lepton discriminator.

The methods are described in more detail in Refs. [289], [299], and [301]. Several representative SFs are shown in Fig. 9.2.

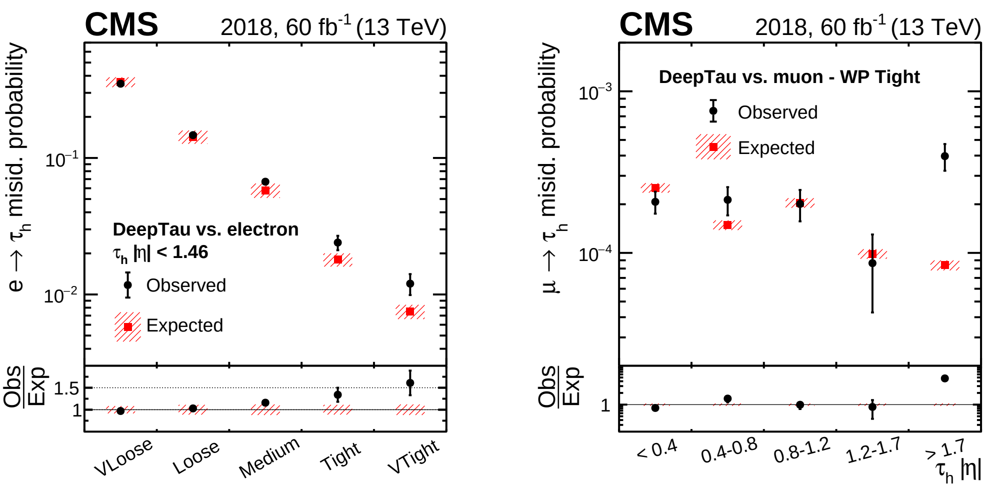

Figure 9.2: Observed and expected probabilities of leptons to be misreconstructed and misidentified as a τ_h object with the DeepTau discriminators in 2018 data. The ratio shows the data-to-simulation scale factors. **Left**: Electrons in the ECAL barrel region ($|\eta| < 1.46$) for several WPs of `DeepTau2017v2p1VSe`. **Right**: Muons in several η^{τ_h} regions for the Tight WP of `DeepTau2017v2p1VSmu`. Figures taken from [289].

9.3 Energy scale

τ_h objects in CMS are reconstructed by combining PF objects, which are already very well calibrated. The reconstructed momentum and energy of τ_h decays are therefore already very accurate and have a resolution of about 10% [299]. The energy scale (ES) of simulated τ_h candidates varies between decay modes by an offset of less than 2%. In this section, I will detail the measurement of the τ_h ES I have performed during Run 2. This measurement has been published in Ref. [289], and previous measurements are also documented in Ref. [299].

9.3.1 Object & event selection

The ES measurements are based on the same $\mu\tau_h$ event sample as the efficiency SF measurement, and closely follows the object and event selections in Section 9.1.1. The τ_h candidates are required to pass the Tight WP of `DeepTau2017v2p1VSjet`, and the VVLoose (Tight) WP of `DeepTau2017v2p1VSe` (`DeepTau2017v2p1VSmu`). To reduce statistical fluctuations in the final fit, the only purification criterion used, with respect to Section 9.1.1, is $m_T < 50\,\text{GeV}$.

9.3.2 Measurement

Two alternative observables are used to extract the τ_h ES: m_{τ_h} and m_{vis}. As m_{τ_h} is constant for the one prong decay $h^\pm$, the ES of τ_h decay reconstructed in this decay mode is measured exclusively in m_{vis}. The ES is measured separately for each observable decay mode, and data-taking period. As the measurement is performed per decay mode of τ_h candidates with $p_T > 20\,\text{GeV}$, dedicated efficiency SFs are measured as a function of the decay mode with $p_T > 20\,\text{GeV}$ (see Section 9.1.2).

The main procedure is to vary the ES in a range, and perform for each value a maximum likelihood fit of the expected to the observed distribution. The ES is varied in the $Z/\gamma^* \to \tau^+\tau^-$ events by scaling the reconstructed τ_h four-momentum by a given value of ES if the reconstructed τ_h object matches a τ_h decay at generator-level. The variation of the τ_h four-momentum is propagated to all affected variables, which include the p_T, m_{τ_h}, and m_{vis}. The difference is also vectorially subtracted from $\vec{p}_T^{\text{miss}}$.

For each ES variation, a new shape template of the m_{vis} or m_{τ_h} distribution is created. Note that m_{τ_h} scales proportionally to the ES, while m_{vis} scales approximately as $\sqrt{\text{ES}}$. The τ_h ES is varied discretely between -3 and $+3\%$ in steps of 0.2%. This range is sufficient to contain for each decay mode the measured τ_h ES value and its uncertainty interval of one standard deviation. The step size of 0.2% is small compared to the precision that needs to be achieved with the τ_h ES measurement. This yields a total of 121 shape templates per τ_h ES measurement.

During the HPS reconstruction, τ_h candidates with a reconstructed mass that fall outside the mass window of the respective reconstructed decay mode are discarded, as detailed in Section 6.2.2. Because the ES is varied after HPS reconstruction, the mass window needs to be narrow to avoid boundary effects when creating the m_{τ_h} templates for the final fit to the observed distribution. The m_{τ_h} ranges are restricted to the following:

- $0.35 < m_{\tau_h} < 1.20\,\text{GeV}$ for $h^\pm\pi^0$.
- $0.83 < m_{\tau_h} < 1.43\,\text{GeV}$ for $h^\pm h^\mp h^\pm$.
- $0.93 < m_{\tau_h} < 1.53\,\text{GeV}$ for $h^\pm h^\mp h^\pm \pi^0$.

These ranges are chosen such that they contain the largest ES variations from the boundaries.

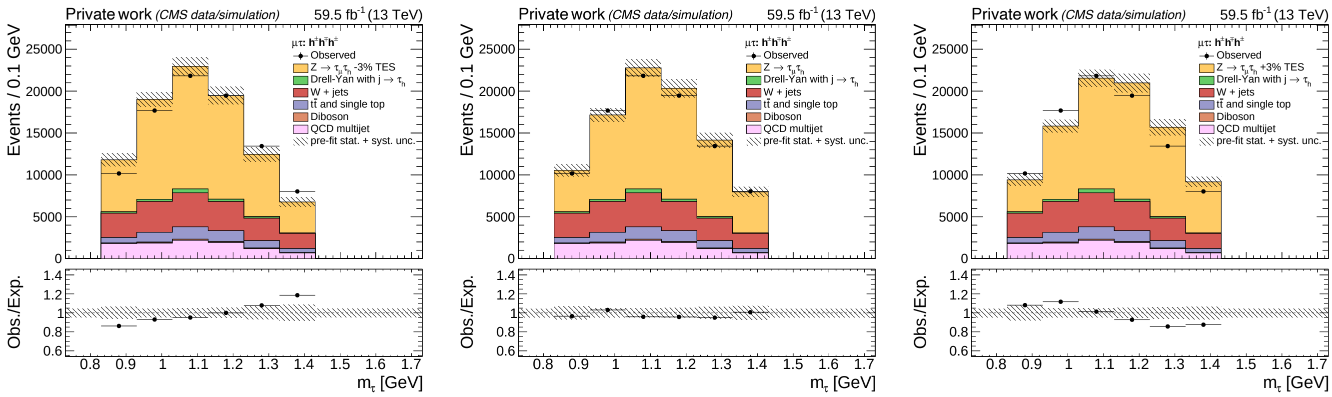

Figure 9.3: Pre-fit distributions of reconstructed m_{τ_h} of a τ_h candidate reconstructed in the $h^{\pm}h^{\mp}h^{\pm}$ decay mode in $\mu\tau_\mathrm{h}$ events of the data-taking period 2018. Shown are variations of the τ_h energy scale (TES) in simulated $\mathrm{Z}/\gamma^* \to \tau^+\tau^-$ events (orange): -3% (left), 0% (center) and $+3\%$ (right).

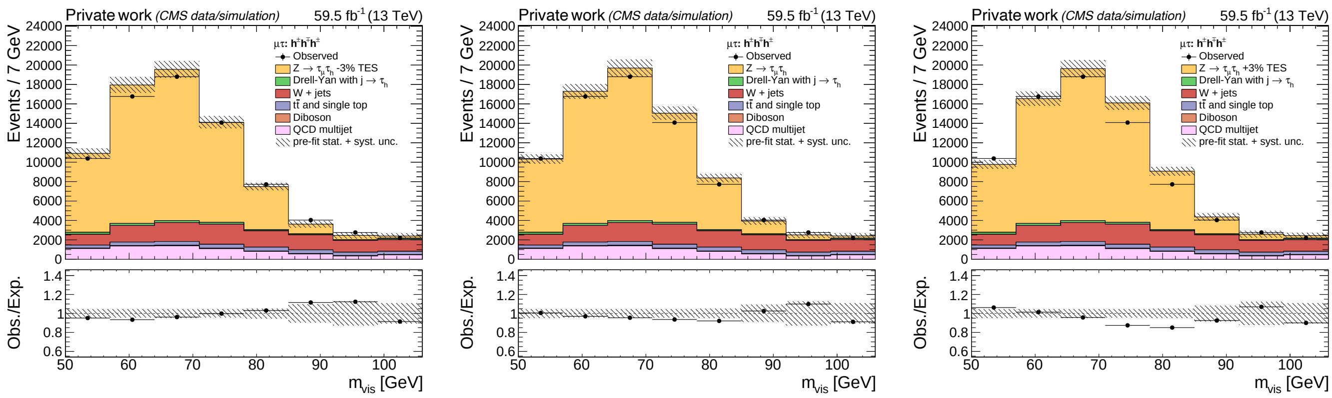

Figure 9.4: Pre-fit distributions of the invariant mass m_vis of the muon and a τ_h candidate reconstructed in the $h^{\pm}h^{\mp}h^{\pm}$ decay mode in $\mu\tau_\mathrm{h}$ events of the data-taking period 2018. Shown are variations of the τ_h energy scale (TES) in simulated $\mathrm{Z}/\gamma^* \to \tau^+\tau^-$ events (orange): -3% (left), 0% (center) and $+3\%$ (right).

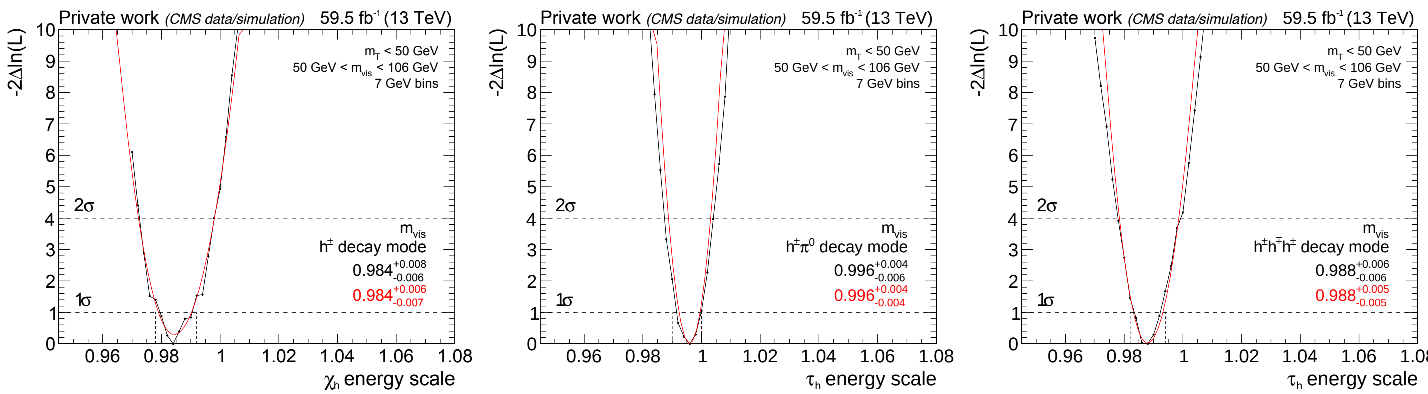

Figure 9.5: Negative log-likelihood $-2\Delta\ln\mathcal{L}$ profiled as a function of τ_h energy scale, as measured from the m_vis observable in the 2018 data-taking period. Shown are the $h^{\pm}$ (left), $h^{\pm}h^{\mp}h^{\pm}$ (center), and $h^{\pm}h^{\mp}h^{\pm}\pi^0$ (right) decay modes. Asymmetric parabolae (red) are fitted to the values below $-2\Delta\ln\mathcal{L} < 5$.

As representative examples, the pre-fit m_{τ_h} (m_{vis}) distributions for the $h^\pm h^\mp h^\pm$ decay mode are shown in Fig. 9.3 (9.4), where the τ_h ES is shifted to -3%, 0, and $+3\%$ in the $Z/\gamma^* \to \tau^+\tau^-$ template. As expected, the ES shifts introduce a visible trend with a positive and negative excess in the data-to-expectation ratio, as shown in the lower panel of each figure. The effect of ES variation is stronger in m_{τ_h}, as argued above, but the downside of the m_{τ_h} observable is that the shape of the $Z/\gamma^* \to \tau^+\tau^-$ signal and background distributions are not that different, while in the m_{vis} observable, one can exploit the sideband above the $Z \to \tau^+\tau^-$ resonance to constrain the background.

To extract the τ_h ES from a given observable, we profile the likelihood $\mathcal{L}(t)$ as a function of the τ_h ES t by performing a maximum likelihood fit for each ES variation [349]. If the ES variation $\hat{t}$ has the largest likelihood ratio $\mathcal{L}(\hat{t})$, the negative logarithm of the likelihood ratio is

$$-2\Delta\ln\mathcal{L} = -2\ln\frac{\mathcal{L}(t)}{\mathcal{L}(\hat{t})}. \tag{9.2}$$

The likelihood profiles obtained from the fits of m_{vis} in 2018 data are presented in Fig. 9.5.

We fit the profiles to the $-2\Delta\ln\mathcal{L}$ values below 5, to smooth out statistical fluctuations due to the limited number of simulated events. The shape of the $-2\Delta\ln\mathcal{L}$ profile can be approximated by a parabola, as the likelihood ratio typically approaches a gaussian distribution [306]. Furthermore, the profiles are found to be asymmetric. I have therefore constructed the "asymmetric-parabola" fit function

$$f(t) = \begin{cases} a_L(t-t_o)^2 + c & \text{for } t < t_0 \\ a_R(t-t_o)^2 + c & \text{for } t \geq t_0 \end{cases} \tag{9.3}$$

with four fit parameters: left width $a_L > 0$, right width $a_R > 0$, $t = t_0$ at the minimum, and vertical offset c. The parameter c is introduced to allow the parabola to be offset with respect to the measured profile, and is constrained to small values. We extract the final τ_h ES as the one where the parabola reaches its minimum t_0. The upper and lower uncertainties in the measurement are taken from where the parabola intersects $-2\Delta\ln\mathcal{L} = 1 + c$, which represent one standard deviation ("1σ").

During my studies of the τ_h ES, I considered different selections and choices of binning. One of the biggest challenges was the fit stability due to limit statistics per bin and migration effects. I converged on a relatively wide binning of the observables to ensure smooth profiles, at the cost of a slightly larger uncertainty because of the widening of the profile. As the ES showed some

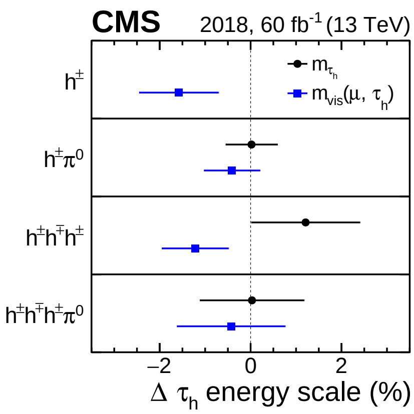

Figure 9.6: Energy scales of the reconstructed τ_h decays in simulation for 2018 data. Shown are the measurements in the m_{τ_h} (black) and m_{vis} (blue) observables. Figures taken from [289].

dependency on the binning and selections, an additional 0.5% uncertainty is added in quadrature to take into account this dependence on choice.

The final results for 2018 data are shown in Fig. 9.6. The values obtained for the two different observables overall agree within one standard deviation, with the largest deviation being 1.5 standard deviations observed for the $h^{\pm}h^{\mp}h^{\pm}$ decay mode. The overall uncertainty in the ES is less than 1%, ranging from 0.6% for $h^{\pm}\pi^{0}$ and $h^{\pm}h^{\mp}h^{\pm}$ decay modes, up to 0.8% for $h^{\pm}$.

The ES has also been measured for τ_{h} $p_{\mathrm{T}} > 100\,\mathrm{GeV}$ with a $\mathrm{W} + \mathrm{jets}$ event sample, and shows consistent results within uncertainties.

10 Object & Event Selections

The third-generation LQ search considers three types of LQ signals which have been introduced earlier in Section 3.4.3: single, pair, and nonresonant production. The properties of their final states were discussed in more detail in Section 7.4.

Here we consider the signature of events with high-p_T τ leptons and b quarks in the final state. This section discusses the event selection of this analysis to target that final state. First, Section 10.1 introduces a common preselection which requires events to be consistent with either the $e\tau_h$, $\mu\tau_h$, $\tau_h\tau_h$, $e\mu$, or $\mu\mu$ decay channel, where the electron, muon, and τ_h objects are assumed to be the visible products of τ lepton decays. This preselection is used for studies to validate background estimations, and optimize the final event selection that targets the LQ signal. As mentioned in Section 6.1, the semileptonic and fully hadronic channels have the largest branching fractions. They also offer more sensitivity to $\tau^+\tau^-$ signals, due to the smaller background relative to the fully leptonic channels. Still, the $e\mu$ and $\mu\mu$ decay channels are included in the search because they provide good control regions for the $Z+\text{jets}$ and $t\bar{t}$ backgrounds, and help constrain systematic uncertainties. The only channel not used in the present search is the ee channel since it has a very similar background composition as the $\mu\mu$ channel, and does not significantly improve the analysis.

After the preselection, event categories are defined that target the LQ signal. The resonant LQ search categories with at least one high-p_T jet are defined in Section 10.2. The nonresonant search category is based on events with no high-p_T jets and is defined in Section 10.3. The flow chart in Fig. 10.1 gives a quick overview of the final signal selection after the optimization discussed below.

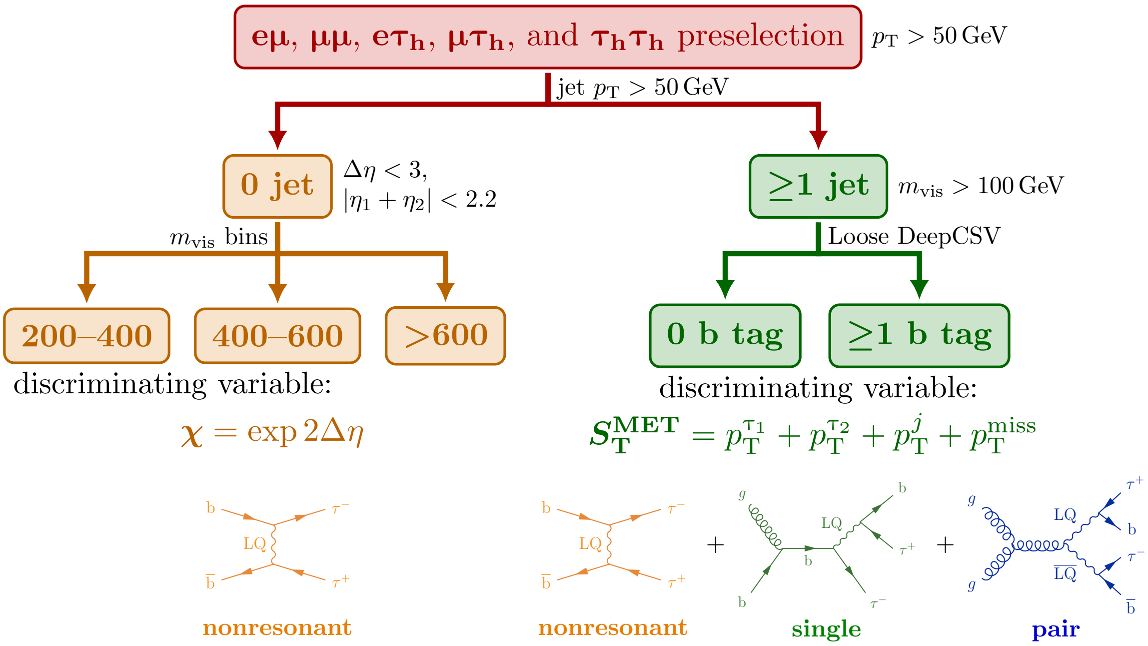

Figure 10.1: Flow chart of signal selection. The 0j category is split into bins of m_vis, while the ≥1j category is split into the 0b and ≥1b categories using the Loose WP of the DeepCSV b-tagging algorithm. A more detailed summary is given in Tables 10.1 and 10.3.

Throughout the rest of the thesis, "lepton" will refer to an electron or muon, unless specified otherwise. The electron, muon, and τ_h candidates in each $\tau\tau$ decay channel will collectively be referred to as the "visible τ candidates".

10.1 Common preselection

The single-lepton and double-τ_h triggers used to collect events have already been discussed in Section 7.1. The minimum p_T requirement of the visible τ candidates in the physics analysis is based on the online p_T threshold of the trigger(s) that selected the event. It is increased by 1 GeV for electrons and muons, and by 5 GeV for τ_h objects to avoid turn-on effects, where the efficiency is quickly changing as a function of p_T. However, in the final signal selection, the electrons, muons, and τ_h objects must have $p_T > 50$ GeV.

10.1.1 Baseline $e\tau_h$ and $\mu\tau_h$ selections

Events in the $e\tau_h$ channel must contain one electron candidate that geometrically matches the object that caused the firing of the single-electron trigger, has $|\eta| < 2.5$, and a relative isolation of $I^e_{rel} < 0.15$ (Eq. (5.2)). The electron trajectory extrapolated to the z axis should have a distance of $d_z < 0.2$ cm from the PV, and a radial distance of $d_{xy} < 0.045$ cm. Additionally, the electron candidate is required to be inconsistent with a conversion, have one or no missing hits in the inner tracker, and pass the 90% WP of the MVA-based discriminator without isolation (see Section 5.4).

Similarly, $\mu\tau_h$ events are selected by requiring one muon candidate with relative isolation $I^\mu_{rel} < 0.15$ (Eq. (5.3)) and $|\eta| < 2.4$. The same d_z and d_{xy} requirements as those imposed on electron candidates are applied to muons.

In addition to a lepton, each channel must contain a τ_h candidate with $p_T > 20$ GeV and $|\eta| < 2.3$, and pass the Medium WP of the `DeepTau2017v2p1VSjet` discriminator, as detailed in Section 6. The selected lepton and τ_h should have an opening angle of $\Delta R > 0.5$ and have opposite-sign (OS) electric charges. If multiple τ_h candidates passing these criteria are found, the one with the largest p_T is selected.

Furthermore, the anti-lepton DeepTau discriminators are applied in both channels. In the $e\tau_h$ ($\mu\tau_h$) channel, the Tight (VVLoose) WP of the anti-electron discriminator and the VLoose (Tight) WP of the anti-muon discriminator are required. These WPs are chosen to reject background events mainly from the $Z \to e^+e^-$ and $Z \to \mu^+\mu^-$ processes.

Lastly, for both the $e\tau_h$ and $\mu\tau_h$ channels, "lepton vetoes" are applied in order to reduce Z + jets, $t\bar{t}$, and diboson backgrounds, and to keep orthogonality between the $\tau\tau$ decay channels: Events with additional isolated electrons or muons that pass looser identification criteria are discarded. The lepton vetoes also include a veto on events that contain a dielectron or dimuon pair of opposite sign and $\Delta R > 0.15$. The criteria are summarized in Table 10.2. The extra lepton is still allowed to match with a selected τ_h candidate. This is needed to ensure orthogonality, and the loss of signal events is found to be relatively small, around 1%, due to the effectiveness of the DeepTau anti-lepton discriminators.

The baseline selection for the "signal" electron, muon, and τ_h candidates are summarized in Table 10.1.

Table 10.1: Summary of the preselection of electron, muon, and τ_h candidates in the various $\tau\tau$ decay channels. The `DeepTau2017v2p1VSjet`, `-VSe`, and `-VSmu` discriminators are used for the τ_h object. Requirements indicated with (*) are trigger-dependent, see Table 7.2.

Criteria	Electron	Muon	τ_h object
p_T/GeV	$> 26, 28, 33, 36$* for $e\tau_h$ > 15 for $e\mu$	$> 23, 25, 28$* for $\mu\tau_h$ > 15 for $\mu\mu$	> 20 for $\ell\tau_h$ > 40 for $\tau_h\tau_h$
$\lvert\eta\rvert$	$< 2.3, 2.1$*	$< 2.4, 2.1$*	< 2.3 (2.1) for $\ell\tau_h$ ($\tau_h\tau_h$)
$\lvert d_{xy}\rvert$/cm	< 0.045	< 0.045	—
$\lvert d_z\rvert$/cm	< 0.2	< 0.2	< 0.2
Isolation	$I^e_{rel} < 0.10$ (ρ-corr.)	$I^\mu_{rel} < 0.15$ ($\Delta\beta$-corr.)	—
Identification	MVA w/o isolation (90% WP)	Medium ID	`-VSjet` Medium WP
Other	Conversion veto ≤ 1 missing inner hits		`-VSe` Tight ($e\tau_h$), VVLoose ($\mu\tau_h$,$\tau_h\tau_h$) `-VSmu` VLoose ($e\tau_h$, $\tau_h\tau_h$), Tight ($\mu\tau_h$)

Table 10.2: Summary of selection criteria for extra-lepton vetoes to remove $Z/\gamma^* \to \ell^+\ell^-$, $t\bar{t}$, and diboson backgrounds. Dielectron and dimuon refer to the lepton veto criteria for events with two leptons of the same flavor.

Criteria	Extra electron	Dielectron	Extra muon	Dimuon
p_T	$> 10\,GeV$	$> 15\,GeV$	$> 10\,GeV$	$> 15\,GeV$
η	< 2.5		< 2.4	
$\lvert d_{xy}\rvert$	$< 0.045\,cm$		$< 0.045\,cm$	
$\lvert d_z\rvert$	$< 0.2\,cm$		$< 0.2\,cm$	
Isolation	$I^e_{rel} < 0.10$		$I^\mu_{rel} < 0.15$	
Identification	MVA w/o isolation 90% WP	Cut-based ID	Medium ID	Global, tracker and PF muon
Other	Conversion veto ≥ 1 missing inner hits	Opposite-sign $\Delta R(e^+e^-) > 0.15$	—	Opposite-sign $\Delta R(\mu^+\mu^-) > 0.15$

Table 10.3: Summary of signal selection for a resonant (single and pair) and nonresonant LQ signal. The Loose WP of the DeepCSV algorithm is used for b tagging jets. The selected muon, electron, and τ_h objects are indicated by ℓ and ℓ'.

Criteria	Resonant		Nonresonant
	0b	≥1b	0j
Number of jets, $p_T > 50\,GeV$	≥ 1	≥ 1	0
Number of b tags, $p_T > 50\,GeV$	0	≥ 1	0
`DeepTau2017v2p1VSjet`	Medium		
`DeepTau2017v2p1VSe`	Loose ($e\tau_h$)/ VVLoose ($\mu\tau_h$, $\tau_h\tau_h$)		
`DeepTau2017v2p1VSmu`	VLoose		
Extra lepton vetoes	Yes		
Opposite charge	Yes		
p^ℓ_T/GeV	> 50		
m_{vis}/GeV	> 100		Binned in $[200, 400, 600, +\infty[$
$\lvert\eta_\ell + \eta_{\ell'}\rvert/2$	—		< 1.1
$\Delta\eta_{\ell\ell'}$	—		< 3
Discriminating variable	S^{MET}_T		χ

10.1.2 Baseline $\tau_h\tau_h$ selection

Events in the $\tau_h\tau_h$ channel are required to have two τ_h candidates with $p_T > 40\,\text{GeV}$, $|\eta| < 2.1$, and $d_z < 0.2\,\text{cm}$ that both pass the Medium WP of the `DeepTau2017v2p1VSjet` discriminator. The τ_h pair should have an opening angle of $\Delta R > 0.5$, and have opposite-sign (OS) electric charges. If more than two τ_h candidates are found, the two with the largest p_T are selected.

As in the case for the semileptonic channels, anti-lepton DeepTau discriminators and lepton vetoes are applied. As there is little background from electrons or muons faking τ_h candidates, the VVLoose and VLoose WPs of the anti-electron and anti-muon discriminators, respectively, are used. Events with an extra electron or muon passing looser selections are rejected.

10.1.3 Baseline $e\mu$ & $\mu\mu$ selections

Events in the $e\mu$ and $\mu\mu$ channels are selected with single-muon triggers, therefore, the selection criteria for the muon candidate is the same as that of the $\mu\tau_h$ channel. The electron selection is also similar to that of the $e\tau_h$ channel, except that the p_T requirement is lowered to $p_T > 15\,\text{GeV}$. Similarly, the p_T requirement of the subleading muon in the $\mu\mu$ channel is lowered to $p_T > 15\,\text{GeV}$.

10.1.4 D_ζ variable

To suppress the $t\bar{t}$ and W + jets backgrounds from $X \to \tau^+\tau^-$ decays for some particle X, the discriminating variable called D_ζ is defined. This observable was introduced in a $H \to \tau^+\tau^-$ analysis at CDF [348, 350]. In this thesis, it is only used in the measurement of the τ_h identification SFs in $Z \to \tau^+\tau^-$ events. The D_ζ variable is constructed as follows: An axis ζ is defined as the bisector of the visible transverse momenta of the two τ decay products. The sum of $\vec{p}_{T,1}^{\,\text{vis}}$ and $\vec{p}_{T,2}^{\,\text{vis}}$ is projected on the ζ-axis with and without the missing transverse momentum $\vec{p}_T^{\,\text{miss}}$:

$$\vec{p}_\zeta^{\,\text{vis}} := \left(\vec{p}_{T,1}^{\,\text{vis}} + \vec{p}_{T,2}^{\,\text{vis}}\right)\frac{\vec{\zeta}}{|\vec{\zeta}|}, \tag{10.1}$$

$$\vec{p}_\zeta := \left(\vec{p}_{T,1}^{\,\text{vis}} + \vec{p}_{T,2}^{\,\text{vis}} + \vec{p}_T^{\,\text{miss}}\right)\frac{\vec{\zeta}}{|\vec{\zeta}|}. \tag{10.2}$$

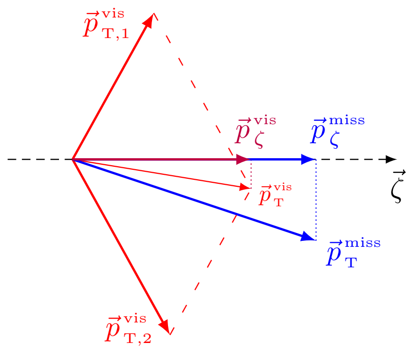

Figure 10.2: Construction of $\vec{p}_\zeta^{\,\text{vis}}$, $\vec{p}_\zeta^{\,\text{miss}}$, and $\vec{p}_\zeta$ by projecting the missing transverse momenta $\vec{p}_T^{\,\text{miss}}$ and the visible transverse momenta of each τ decay product, $\vec{p}_{T,1}^{\,\text{vis}}$ and $\vec{p}_{T,2}^{\,\text{vis}}$ onto the bisector $\vec{\zeta}$. With these definitions, $\vec{p}_\zeta = \vec{p}_\zeta^{\,\text{vis}} + \vec{p}_\zeta^{\,\text{miss}}$.

The construction of $\vec{p}_\zeta$, $\vec{p}_\zeta^{\text{vis}}$ and $\vec{p}_\zeta^{\text{miss}}$ is illustrated in Fig. 10.2. D_ζ is now defined as the magnitude of the difference of these projections:

$$D_\zeta := p_\zeta - 1.85 p_\zeta^{\text{vis}}, \tag{10.3}$$

or equivalently,

$$D_\zeta = p_\zeta^{\text{miss}} - 0.85 p_\zeta^{\text{vis}}. \tag{10.4}$$

The factor in the definitions of D_ζ is optimized for maximal background rejection with negligible loss of signal. This variable quantifies the compatibility of events with the topology wherein the direction of missing neutrinos from τ decays are aligned with the direction of the visible τ decay products. In the $\mu\tau_\text{h}$ channel the quantities $\vec{p}_{\text{T},1}^{\text{vis}}$ and $\vec{p}_{\text{T},2}^{\text{vis}}$ correspond to the transverse momenta of the muon and τ_h object.

10.2 Search for resonant LQ production

The final states from the single and pair production of LQs are characterized by two high-p_T τ leptons and at least one high-p_T b quark. At the reconstructed level, the large majority of those events have at least one or two jets with $p_\text{T} > 50\,\text{GeV}$. Furthermore, as one expects a b quark in the final state, one can use b tagging to target those jets.

The event selections and categorization targeting the LQ $\to$ bτ signal have been sequentially optimized to gain the best sensitivity. The optimization study has considered different events categorizations according to the number of (b-tagged) jets, several discriminating variables for signal extraction, b tagging WPs, minimum p_T requirements on the visible τ candidates, and a requirement on p_T^{miss}. As a measure of sensitivity, the expected significance of the vector LQ $\to$ bτ signal was chosen. The signal extraction that is used to compute the sensitivity will be described in more detail in Chapter 12. For simplicity, the shape uncertainties discussed in Section 12.4.2 are not applied, except for the statistical uncertainties that are due to the limited number of simulated events [351, 352]. To take advantage of the full data set, all three years of data are combined and analyzed, as well as the eτ_h, $\mu\tau_\text{h}$ and $\tau_\text{h}\tau_\text{h}$ channels when appropriate. The eμ and $\mu\mu$ channels are omitted from the optimization, as they have a negligible sensitivity, and are only used to constrain systematic uncertainties when fitted to data.

The optimization of signal event selection starts from the common preselection described in the previous section. An additional cut on the invariant mass between the visible τ-decay products of $m_\text{vis} > 100\,\text{GeV}$ is applied to remove Drell-Yan events, with negligible loss of signal, and at least one jet of $p_\text{T} > 50\,\text{GeV}$ and $|\eta| < 4.7$ is required.

10.2.1 Discriminating variable

Several discriminating variables have been considered as observables to extract the LQ signal. Studies of previous LQ searches have considered variables like the invariant mass, the collinear mass, and the scalar p_T sum of different combinations of the visible τ decay candidate, jet, and $\vec{p}_\text{T}^{\text{miss}}$. In most cases, the most sensitive variable turns out to be the "scalar sum-p_T"

$$S_\text{T} := p_\text{T}^{\tau_1} + p_\text{T}^{\tau_2} + p_\text{T}^{j_1}, \tag{10.5}$$

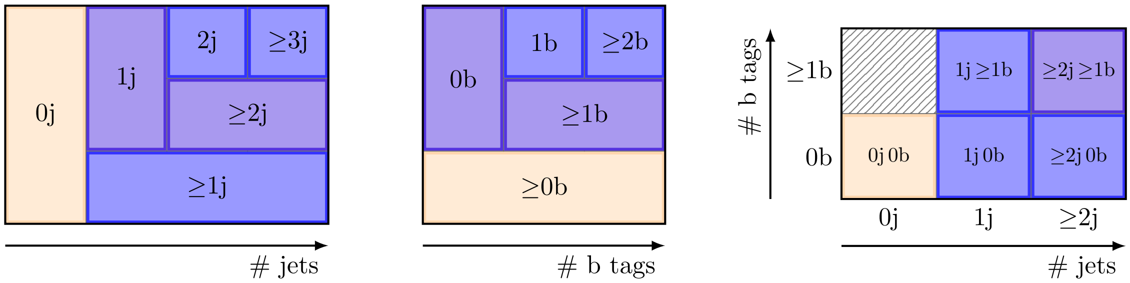

Figure 10.3: Labeling of different event categories considered in the optimization study in terms of the number of b tags and/or number of jets with $p_{\mathrm{T}} > 50\,\mathrm{GeV}$. Each rectangle is orthogonal from the other ones. Each row in the two figures on the left represents a different way of partitioning the events.

or

$$S_{\mathrm{T}}^{\mathrm{MET}} := p_{\mathrm{T}}^{\tau_1} + p_{\mathrm{T}}^{\tau_2} + p_{\mathrm{T}}^{j_1} + p_{\mathrm{T}}^{\mathrm{miss}}, \tag{10.6}$$

where $p_{\mathrm{T}}^{\tau_{1,2}}$ are the transverse momenta of the τ decay candidates, and $p_{\mathrm{T}}^{j_1}$ is the transverse momentum of the leading jet. This variable has good discriminating power because the resonant LQ signal is expected to peak at extreme high values, while most background processes have a steeply falling S_{T} spectrum. It has been used in several previous analyses, including Refs. [335, 353, 354]. Invariant masses generally do not perform as well, because of the ambiguity of how the final state objects should be combined to reconstruct the LQ $\to q\ell$ decay.

Based on the optimization studies of a lower cut on $p_{\mathrm{T}}^{\mathrm{miss}}$ in combination with either S_{T} or $S_{\mathrm{T}}^{\mathrm{MET}}$, the final choice was made to employ $S_{\mathrm{T}}^{\mathrm{MET}}$ without a cut on $p_{\mathrm{T}}^{\mathrm{miss}}$.

10.2.2 Event categorization

Different event categorizations have been constructed for optimizing the signal sensitivity according to the number of jets, the number of b-tagged jets, and a combination thereof. Only jets of $p_{\mathrm{T}} > 50\,\mathrm{GeV}$ are considered, and the S_{T} observable is used during this optimization.

As shown in the left panel of Fig. 10.4, the most sensitive case among the different ways of partitioning events by the number of b-tagged jets was found to be the combination of the 0b and ≥1b categories with the loose WP of the DeepCSV, where

- "0b" contains at least one jet with $p_{\mathrm{T}} > 50\,\mathrm{GeV}$, but no jet with $p_{\mathrm{T}} > 50\,\mathrm{GeV}$ that is b tagged,
- "≥1b" contains at least one jet with $p_{\mathrm{T}} > 50\,\mathrm{GeV}$ that is b tagged.

The 0b + ≥1b categorization has also been compared to other (b) jet categorizations such as ≥1j or 1j + ≥2j, as shown in the right panel of Fig. 10.4, but 0b + ≥1b was chosen as the final event categorization for the resonant LQ $\to \mathrm{b}\tau$ signal.

10.2.2.1 Minimum p_{T} requirement

Most of the sensitivity to the resonant signal originates from the tail of the $S_{\mathrm{T}}^{\mathrm{MET}}$ distribution at high values. The largest fraction of large $S_{\mathrm{T}}^{\mathrm{MET}}$ values in signal events tends to come from the leading jet p_{T}, so there is no need to optimize the lower bound on the jet p_{T} selection criterion. The p_{T} of the visible τ decay candidates is distributed at relatively lower values, and therefore several choices of lower bounds have been studied. Based on these results, a minimum requirement of $p_{\mathrm{T}} > 50\,\mathrm{GeV}$ on both τ decay candidates has been chosen.

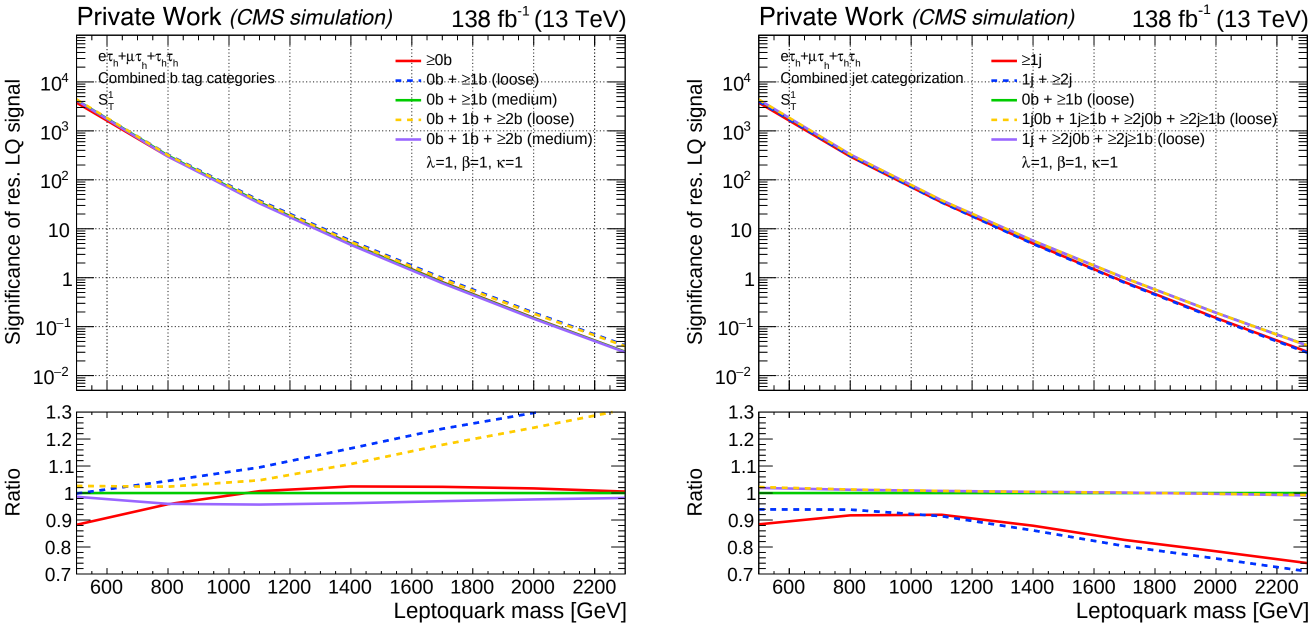

Figure 10.4: Optimization study of event categorization based on the number of jets and b-tagged jets, using the expected significance of a resonant vector LQ signal as a measure of sensitivity. The significance is computed using $S_{\mathrm{T}} = p_{\mathrm{T}}^{1} + p_{\mathrm{T}}^{2} + p_{\mathrm{T}}^{j_1}$ distributions of the $\mathrm{e}\tau_{\mathrm{h}}$, $\mu\tau_{\mathrm{h}}$ and $\tau_{\mathrm{h}}\tau_{\mathrm{h}}$ channels, as well as the 2016, 2017, and 2018 data.

10.2.3 Anti-lepton τ_{h} discriminators

Different combinations of WPs of the `DeepTau2017v2p1VSe` and `-VSmu` discriminators have been tested per $\tau\tau$ decay channel. At high p_{T}, the signal-to-background ratio can be improved by loosening these requirements because the background with leptons misidentified as τ_{h} candidates remains small, while the signal efficiency can be increased. In all channels, the looser WPs of the DeepTau anti-lepton discriminators have the highest sensitivity. There is a negligible difference in sensitivity between applying the lepton vetoes or not. However, these are needed to ensure orthogonality. We choose the following WPs for the event categories: Loose (VLoose) for the anti-electron (anti-muon) discriminator in the $\mathrm{e}\tau_{\mathrm{h}}$ channel, and VVLoose (VLoose) for the anti-electron (anti-muon) discriminator in both the $\mu\tau_{\mathrm{h}}$ and $\tau_{\mathrm{h}}\tau_{\mathrm{h}}$ channels.

10.2.4 Charge requirement

It was considered to drop the the opposite-charge requirement between the τ decay candidates since charge assignment degrades at high p_{T}. The significance can be improved by up to 5% across the full m_{LQ} range. However, the $j \to \tau_{\mathrm{h}}$ background estimation introduced in Chapter 11 relies on a same-charge region to extrapolate the QCD multijet background to the opposite sign region. Therefore, this analysis will proceed with the opposite-charge requirement.

10.2.5 Summary

Figure 10.1 and Table 10.3 summarize the event selections and categorization for the search for a resonant LQ $\to$ bτ signal after optimization. The final event categories are the "0b" and "$\geq$1b" categories with the Loose WP of DeepCSV and $p_{\mathrm{T}} > 50\,\mathrm{GeV}$ jets. The τ decay candidates must have $p_{\mathrm{T}} > 50\,\mathrm{GeV}$ in all channels and categories. The observable for the signal extraction is $S_{\mathrm{T}}^{\mathrm{MET}}$.

Figure 10.5 shows a comparison of the $S_{\mathrm{T}}^{\mathrm{MET}}$ distributions in the 0b and $\geq$1b categories for the three different production modes. The overflow events ($S_{\mathrm{T}}^{\mathrm{MET}} > 2500\,\mathrm{GeV}$) are included in

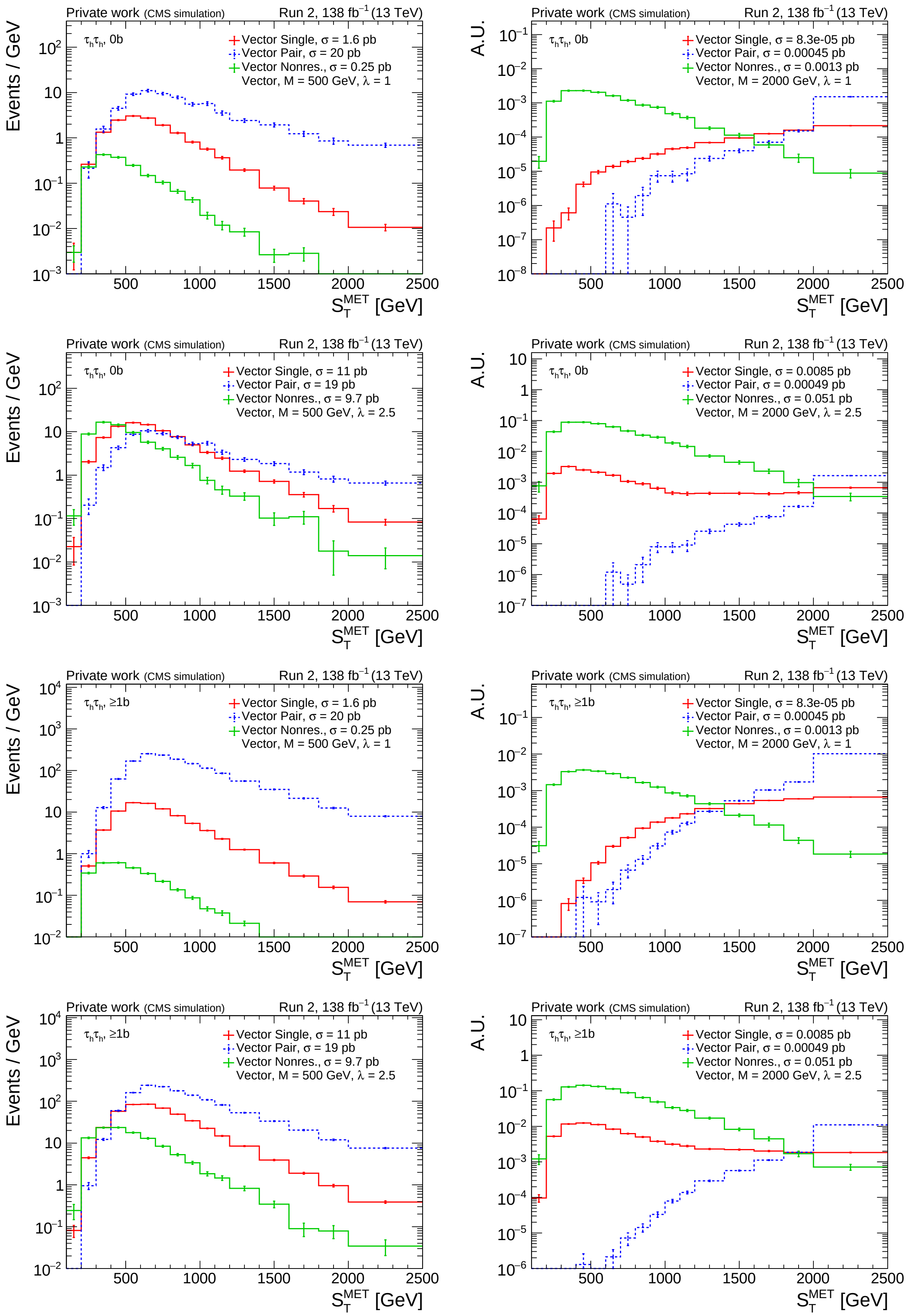

Figure 10.5: Comparison of the $S_{\mathrm{T}}^{\mathrm{MET}}$ distribution for different vector LQ production modes, masses, and coupling strengths λ. From left to right: $m_{\mathrm{LQ}} = 500$, 2000 GeV. Shown in each plot are the pair (blue dashed), single (red solid), and nonresonant LQ $\rightarrow$ bτ signal (green solid). From top to bottom: 0b with $\lambda = 1$, 0b with $\lambda = 2.5$, $\geq$1b with $\lambda = 1$, $\geq$1b with $\lambda = 2.5$. Note that the shapes are normalized to their respective theoretical cross section, as indicated in the legend. The lower panel shows the ratio with respect to the single production.

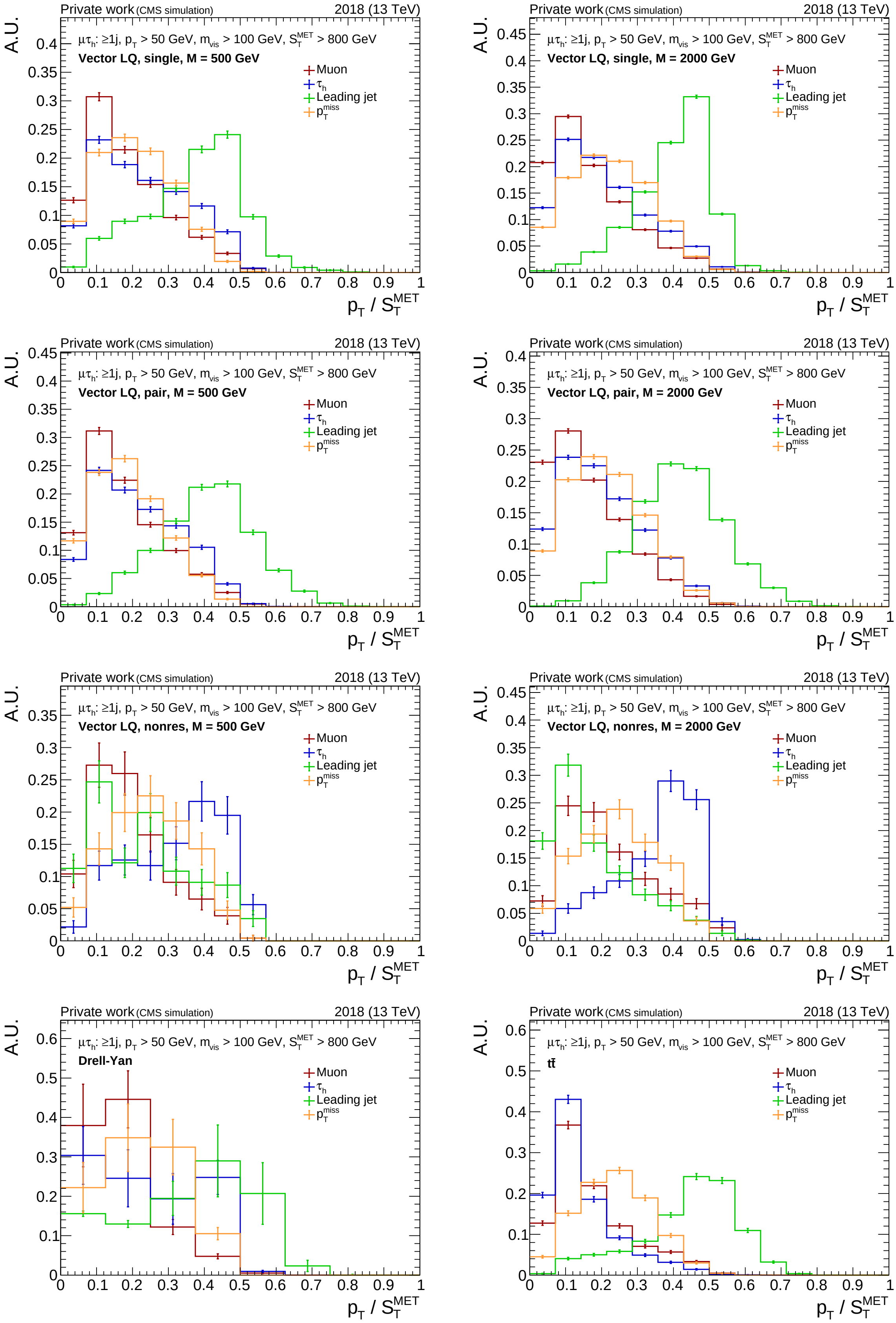

Figure 10.6: Breakdown of $S_{\mathrm{T}}^{\mathrm{MET}}$ into fractions of each p_{T} component for events in the $\mu\tau_{\mathrm{h}}$ channel and $\geq$1j category with $S_{\mathrm{T}}^{\mathrm{MET}} > 800\,\mathrm{GeV}$. The top three rows show the single (top), pair (second row), and nonresonant (third row) production of a vector LQ for $m_{\mathrm{LQ}} = 500$ (left) and 2000 GeV (right) with $\lambda = 1$. The bottom row shows the $\mathrm{Z}+\mathrm{jets}$ (left) and $\mathrm{t\bar{t}}$ backgrounds (right). Shown in each plot are the fractions of the muon p_{T} (red), τ_{h} p_{T} (blue), leading jet p_{T} (green), and $p_{\mathrm{T}}^{\mathrm{miss}}$ (orange). The error bars indicate statistical uncertainty in the bin yield.

the last bin. Pair production (blue dashed line) tends to peak at extreme values for larger m_{LQ} masses. The same is true for single production (red solid line), although a nonnegligible contribution from the pole at $M_{\mathrm{b}\tau} = 0$ appears at lower $S_{\mathrm{T}}^{\mathrm{MET}}$ values for $\lambda \gtrsim 1.5$ (see Section 7.4.1), even after the final event selections. Also shown is the nonresonant $\tau^+\tau^-$ production through t-channel LQ exchange (green solid line). The $S_{\mathrm{T}}^{\mathrm{MET}}$ observable also offers sensitivity to the nonresonant signal because the signal-to-background ratio increases toward higher values in the tail. At high coupling strength λ and high mass m_{LQ}, the nonresonant production cross sections is sufficiently large compared to the resonant production modes to contribute to the total sensitivity. This nonresonant contribution is therefore included in the total LQ signal.

Figure 10.6 shows how $S_{\mathrm{T}}^{\mathrm{MET}}$ breaks down into fractions of its four p_{T} components for events in the $\mu\tau_{\mathrm{h}}$ channel of the ≥1j category with $S_{\mathrm{T}}^{\mathrm{MET}} > 800\,\mathrm{GeV}$. For the majority of events from single and pair LQ production, as well as the Z + jets and $\mathrm{t\bar{t}}$ backgrounds, by far the largest fraction of $S_{\mathrm{T}}^{\mathrm{MET}}$ is due to the leading jet p_{T}. At the largest values of $S_{\mathrm{T}}^{\mathrm{MET}}$, the bulk of the p_{T} distribution of τ decay candidates in these events still tends to be well below 500 GeV. For nonresonant production, however, the largest fraction is from the τ_{h} candidate, as the central jets produced in association are considerably softer (see Fig. 7.13).

10.3 Search for nonresonant LQ production

If the LQ exclusively couples to b quark and the τ lepton, the nonresonant production happens through $\mathrm{b\bar{b}} \to \tau^+\tau^-$ with the t-channel exchange of the LQ, and where the b quarks are typically produced through gluon splitting.

10.3.1 Discriminating variable

Unlike pair and single LQ production, this process does not generate an on-shell resonance. Therefore, discriminating variables such as the invariant mass between the τ leptons cannot be used for the signal extraction. Instead, this analysis looks for the angular separation between two τ decay candidates, defined as

$$\chi \coloneqq \exp\left(2y^*\right), \tag{10.7}$$

where the "separation" $y^* = \frac{1}{2}|y_1 - y_2| = \frac{1}{2}\Delta y$ is the point between the rapidities y_1 and y_2 of the two τ leptons,

$$y \coloneqq \frac{1}{2}\ln\frac{E + p_z}{E - p_z}, \tag{10.8}$$

and p_z is the projection of the τ leptons' momenta on the beam axis. In $2 \to 2$ scattering processes of massless particles ($E = p$),

$$y = \frac{1}{2}\ln\frac{1 + |\cos\theta^*|}{1 - |\cos\theta^*|}, \tag{10.9}$$

where $\theta^\star$ is the scattering angle in the $\tau\tau$ center-of-mass frame w.r.t. the z axis, which is along the beam, and $p_z = p|\cos\theta^\star|$ in this frame. Because differences in rapidities are by construction invariant under Lorentz boosts along z, the rapidities of the two τ leptons are $\pm y^*$ in this frame. In the massless approximation, the angular variable χ can be written as

$$\chi = \frac{1 + |\cos\theta^\star|}{1 - |\cos\theta^\star|}. \tag{10.10}$$

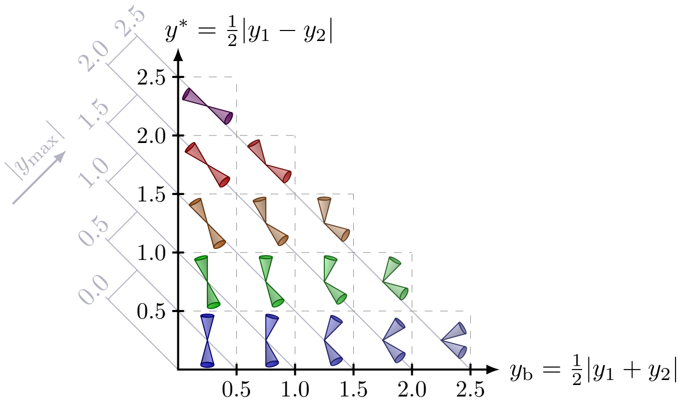

Figure 10.7: Displays of dijet events in y^*-y_b space, with $y_b = |y_{boost}|$ and separation $y^* = \frac{1}{2}|y_1 - y_2|$. Note the events displays are shown with $\Delta\phi = \pi$ for illustration purposes. Inspired by Ref. [367].

The "boost",

$$y_{boost} = \frac{1}{2}(y_1 + y_2), \tag{10.11}$$

denotes the average rapidity of the two τ leptons. In massless $2 \to 2$ scattering processes, y_{boost} specifies the longitudinal boost by which the $\tau\tau$ center-of-mass frame is boosted with respect to the detector frame. An illustration of the event topology as a function of y^* and y_{boost} is given in Fig. 10.7.

The choice of this variable is motivated by the fact that the χ distribution in Rutherford scattering is flat. It also allows signatures of new physics that might have a more isotropic angular distribution than QCD (e.g., quark compositeness) to be more easily examined as they would produce an excess at low values of χ, where $y_1 \sim y_2$. The same quantities have been examined in dijet signatures at the Tevatron by the D0 [355, 356] and CDF [357] Collaborations, and at the LHC by the ATLAS [358–362] and CMS [363–366] Collaborations.

In this analysis, instead of with two jets, χ is defined with the two respective τ-lepton decay candidates in each channel. The χ distribution is then measured over the range $1 < \chi < 21$, which implies a maximum value of $y^* < 1.52$. The maximum of the separation and boost are determined by the maximum of the τ candidate rapidities, $y_{boost} < y_{max}$ and $y^* < y_{max}$. Furthermore, they are not linearly independent, and satisfy the inequality

$$|y_{boost}| + y^* < |y_{max}|, \tag{10.12}$$

as illustrated in Fig. 10.7. Without loss of precision, pseudorapidity η instead of rapidity y is used in this analysis, so $\chi = \exp \Delta\eta$.

10.3.2 Event categorization

To select events that are like the nonresonant signal, the selected electrons, muons and τ_h-objects are required to have $p_T > 50\,\text{GeV}$ on top of the baseline selection described in Section 10.1. Furthermore, to increase the purity further, we require $|\eta_\ell + \eta_{\ell'}|/2 < 1.1$ and $\Delta\eta_{\ell\ell'} < 3$ between the two visible τ decay candidates ℓ and ℓ'.

To make this category for the nonresonant signal orthogonal from the resonant signal described in Section 10.2, selected events are required to have no jets with $p_T > 50\,\text{GeV}$. We therefore denote this category simply as the "0j" category. After these selections, the $\tau\tau$ angular distributions are measured in three bins of the visible mass m_{vis}: 200 to 400 GeV, 400 to 600 GeV, and larger than 600 GeV. Each bin with higher m_{vis} has a higher signal purity. Other

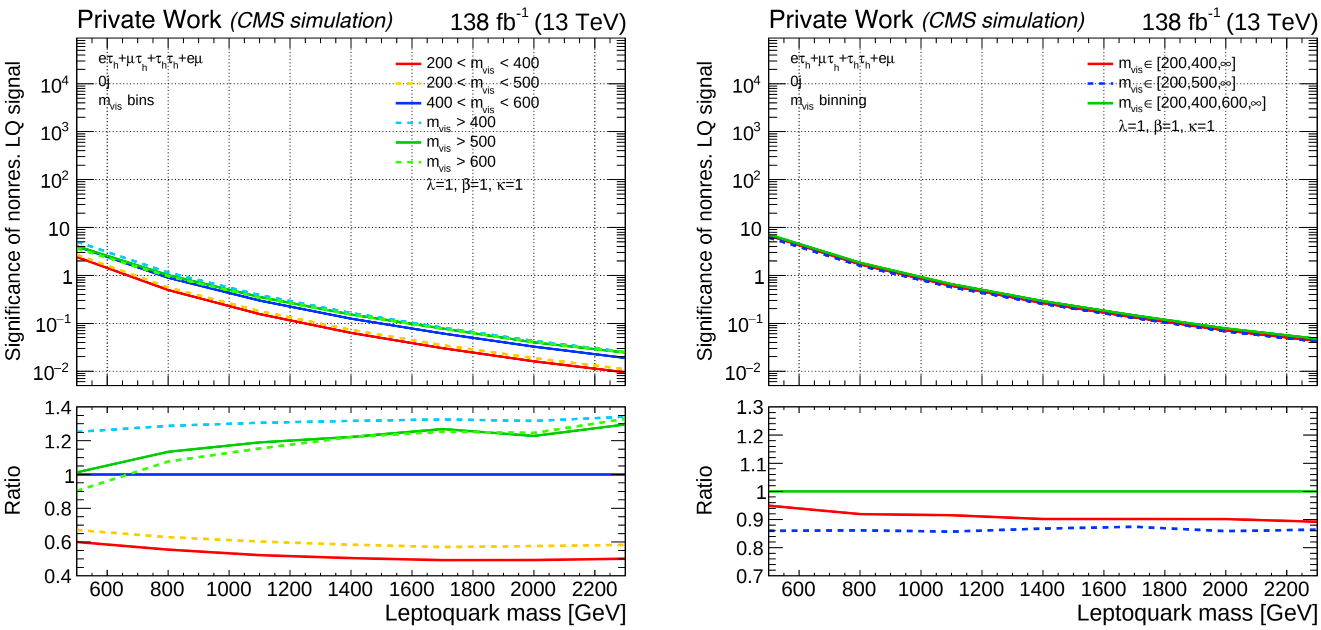

Figure 10.8: Optimization study of m_{vis} bins in the 0j category. **Left**: Comparison of each individual m_{vis} bin. **Right**: Combination of orthogonal m_{vis} bins.

binning choices of m_{vis} have been checked, as shown in Fig. 10.8. However, the combination $[200, 400, 600, \infty]$ is found to have the highest sensitivity.

As mentioned in Section 10.2.5, the nonresonant signal is also included in the signal extraction from $S_{\text{T}}^{\text{MET}}$ in the 0b and $\geq$1b categories, which adds significant sensitivity to the 0j category.

Table 10.3 summarizes the selections of the nonresonant signal category. This category will be referred to as the "0j" category.

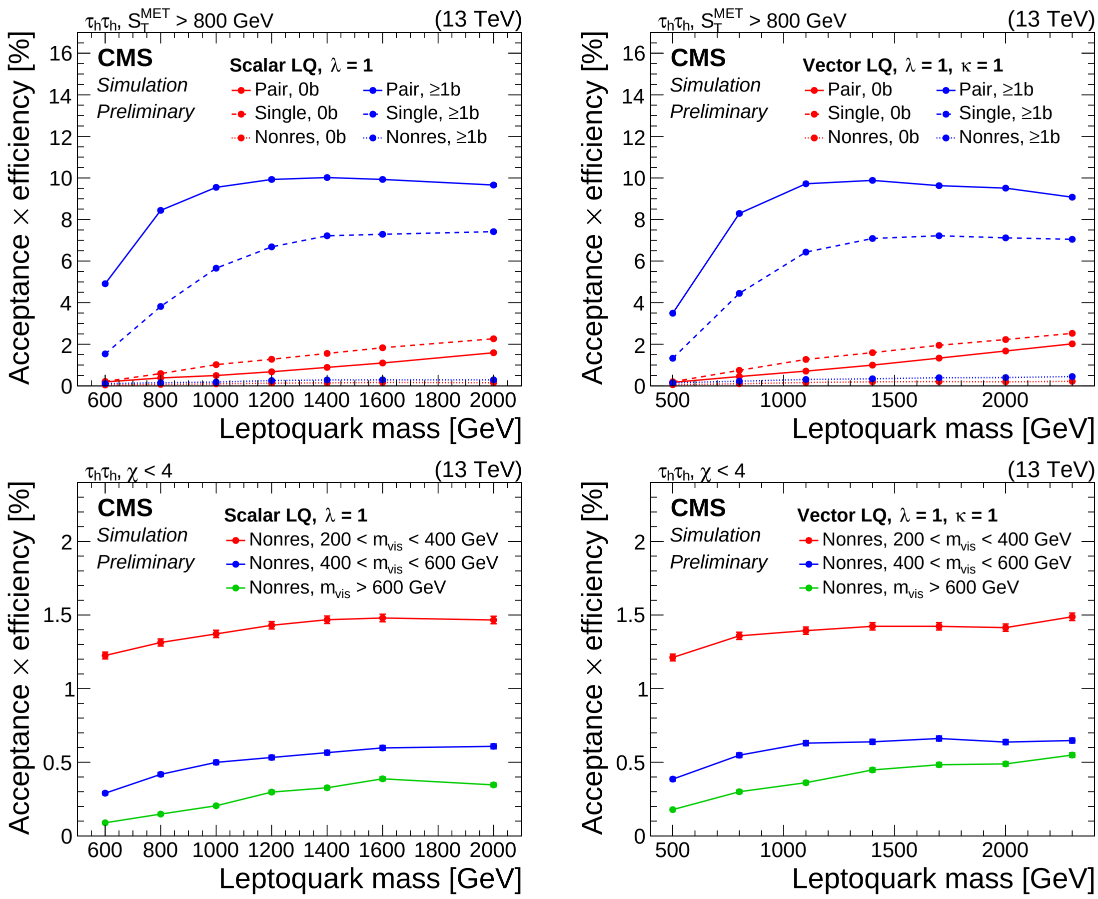

Figure 10.9: The product of acceptance and efficiency for a vector LQ signal in the $\tau_h\tau_h$ (left) and $\mu\tau_h$ (right) channels of the 0b and $\geq$1b (top), and the 0j categories (bottom) are shown. Vertical bars indicate the statistical uncertainty in the efficiency. Published in Ref. [368].

10.4 Signal acceptance times efficiency

The product of acceptance and efficiency for the vector-LQ signal in the various signal categories is shown in Fig. 10.9 as a function of m_{LQ}. The scalar-LQ signal has a very similar efficiency in all cases. The efficiencies are restricted to the sensitive region of the respective final discriminator. In the $\tau_{\mathrm{h}}\tau_{\mathrm{h}}$ channel of the $\geq$1b category, the selection efficiency for events from LQ pair production varies with mass from approximately 3.5 to 10%, while the efficiency for events from single LQ production varies between 1.0 and 7.5%. The efficiency for resonant production in $\geq$1b is smaller at lower m_{LQ} due to a softer p_{T} spectrum.

11 Data-Driven Background Estimations

In the search for a resonant LQ $\to$ bτ signal with the defined b-tag categories, the dominant background stems from $\mathrm{t\bar{t}}$ production because of the presence of genuine electrons, muons, τ leptons, and b-quark jets from top quark decays, which all tend to have a hard p_T spectrum. Meanwhile, in the search for a nonresonant signal, the main background in the sensitive region tends to be Drell-Yan, whose events also tend to peak more at lower χ values compared to the other backgrounds. The third largest background arises from jets misidentified as τ_h candidates ($j \to \tau_\mathrm{h}$ fakes), which primarily consists of QCD multijet and W + jets events, but also those from $\mathrm{t\bar{t}}$.

As mentioned in Section 7.3, *data-driven methods* are used to estimate some backgrounds like the $j \to \tau_\mathrm{h}$ background. These methods typically exploit data in certain control regions (CRs) to estimate the size and distribution in the signal region (SR). This often offers a better description of data than MC simulation because the processes of QCD multijet production and the misidentification of quark and gluon jets as τ_h decays are harder to simulate accurately. Additionally, detector conditions including pileup are *ipso facto* correctly described in the real data events used for background estimation. This can therefore lower the systematic uncertainty in a robust way. Frequently, the statistical uncertainty can be reduced compared to that achieved with MC samples if the CRs provide a larger number of events.

For the case of the dileptonic $\tau\tau$ decay channels, eμ and $\mu\mu$, of the LQ $\to$ bτ search, the QCD multijet production is estimated from a simple OS/SS method explained in Section 11.1. In the channels with a τ_h, the $j \to \tau_\mathrm{h}$ fakes are estimated in a data-driven way from CRs in data, using the so-called *fake-factor* (FF) *method*, explained in Section 11.2.

11.1 The OS/SS method

In the eμ and $\mu\mu$ channels, all backgrounds other than QCD multijet are fully estimated from simulation and normalized according to their respective cross sections, as detailed in Section 7.3.2. The dominant contribution to the eμ channel is $\mathrm{t\bar{t}}$, while in $\mu\mu$ it is Drell-Yan. In both channels, the QCD multijet background is minor and is estimated with the OS/SS method. The method utilizes events in a same-sign (SS) CR, which has all the same object and event selections as the SR, except both leptons are required to have the same sign of electric charge. The SS region is orthogonal to the SR, which has the opposite-sign (OS) requirement imposed. The SS CR is very pure in QCD and the estimated QCD multijet yield is obtained from the observed data after subtracting the total contribution of other SM background processes as determined from simulation. The expected QCD multijet contribution in the SR with the OS requirement is obtained by rescaling the distribution in the SS region with a simple "OS/SS" extrapolating factor, which is about 2.4. This was measured in a high-purity QCD multijet sample obtained by inverting the lepton isolation requirement, and comparing the QCD yield in the OS and SS regions. To create a histogram of the QCD multijet kinematics in any given variable, this procedure can be repeated on a bin-by-bin basis.

11.2 The fake factor method

The basic idea of the FF method is to define a CR that only differs from the SR by relaxing the τ_h identication requirement for the selected τ_h candidate. For the case of the LQ $\to$ bτ analysis, this entails changing the Medium WP of `DeepTau2017v2p1VSjet` to VLoose. This new region is referred to as the "application region" (AR), and is expected to be primarily populated by events with jets misidentified as τ_h and with typical impurities from genuine τ_h at the level of a few percent or below. It is kept orthogonal from the SR by excluding events that pass the tighter WP in question, i.e., τ_h candidates that pass the VLoose WP, but fail the Medium one. Finally, the $j \to \tau_h$ fake background in the SR is estimated from the observed data in the AR after applying the extrapolation factors known as "fake factors" (FFs). The FFs ensure the correct $j \to \tau_h$ fake rate is obtained in the SR. The AR is not completely pure in $j \to \tau_h$ fakes, so the contamination of backgrounds with genuine τ_h or $\ell \to \tau_h$ fakes is estimated from simulated events and is subtracted.

The FFs are parametrized in a number of different variables like τ_h p_T and number of jets, which will be discussed below per channel. Furthermore, they are measured separately for three different components of the $j \to \tau_h$ fake background: QCD multijet, electroweak (EW), and $\mathrm{t\bar{t}}$ production. The EW component mainly consists of W + jets, but also includes small amounts of Drell-Yan, diboson, and single top-quark production. In this way, the different flavor, multiplicities, and correlation with other kinematics of jets stemming from these backgrounds can be measured, and the relative background composition can be taken into account per event category. Jets in QCD multijet events are mostly initiated by gluons, while W + jets events primarily contain light-flavored jets, and $\mathrm{t\bar{t}}$ is rich in heavy-flavored jets.

The FFs are measured for each of the three types of $j \to \tau_h$ backgrounds in dedicated CRs that are enriched with the background in question, and which are called the "determination regions" (DRs). Very roughly speaking, the "raw" FFs are then the ratios of the number of observed data events in the SR-like "`Medium`" region over the AR-like "`VLoose && !Medium`" region,

$$\mathrm{FF}_b = \frac{N_b^{\mathrm{DR}}(\texttt{Medium})}{N_b^{\mathrm{DR}}(\texttt{VLoose \&\& !Medium})}, \tag{11.1}$$

in the DR of a given background, where b = QCD, EW and $\mathrm{t\bar{t}}$. $N_b(\texttt{Medium})_{\mathrm{DR}}$ denotes the number of events with a τ_h object that fulfill the Medium `DeepTauVSjet` WP in DR_b of background b, and $N_b(\texttt{VLoose \&\& !Medium})_{\mathrm{DR}}$ is the number of events in DR with a τ_h that pass the VLoose but fail the Medium WP. The choice of the looser WP depends on the following trade-off: Looser WPs increase the number of events in the denominator, reducing the statistical uncertainty, while increasing the systematic uncertainty because the τ_h candidates in these events are less similar to the τ_h candidates in the SR, which have a high `DeepTau2017v2p1VSjet` score and pass the Medium WP. With the choice of the VLoose WP, the denominator has on the order of 2.5 more events than the denominator, i.e., the FF is very roughly $\mathrm{FF}_b \approx 0.4$.

This method is therefore a so-called *ABDC method* [369, Section 8.1], which relies on the basic assumption of *universality*, meaning that the FFs measured in the DR also apply between the AR and SR:

$$\frac{N_b^{\mathrm{DR}}(\texttt{Medium})}{N_b^{\mathrm{DR}}(\texttt{VLoose \&\& !Medium})} = \frac{N_b^{\mathrm{SR}}}{N_b^{\mathrm{AR}}}, \tag{11.2}$$

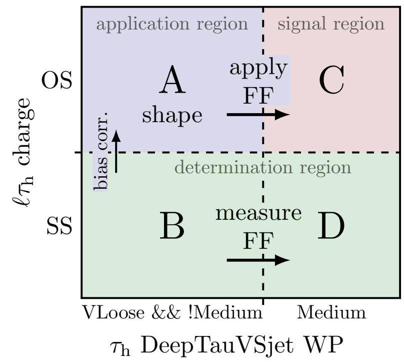

Figure 11.1: Simple schematic of the ABDC method in the fake factor (FF) method. FFs are measured as the ratio between the B to D region. Universality assumes that the number of events in the regions satisfy $N_C/N_A = N_D/N_B$. To ensure universality, bias correction are measured between the OS and SS regions. Shown are the regions to measure the FFs for QCD multijet in the $e\tau_h$ and $\mu\tau_h$ channels, by using the OS (A, C) and SS regions (B, D).

where N_b^{SR} and N_b^{AR} are the number of $j \to \tau_h$ events in the SR and AR, respectively. The ABCD method is illustrated by Fig. 11.1, using the DR for QCD as an example. The universality assumption does not always hold in fact, and some *bias corrections* are needed to restore universality to ensure the accuracy of this method. Furthermore, the closure of the FFs are tested in several variables in the DR, and small *nonclosure corrections* are applied if needed, as the main parametrization does not capture all the dependencies.

The factorization of the $j \to \tau_h$ background components makes it possible to take into account the relative background composition in different SRs, like the different jet categories in the LQ $\to$ bτ search. The relative fractions f_b of the three considered backgrounds are therefore measured in the ARs. The $j \to \tau_h$ fake components of the EW and $t\bar{t}$ backgrounds, respectively, are estimated by simulation. The remaining events from simulated event samples are considered to be "real" τ_h candidates including the small component of $\ell \to \tau_h$ fakes. The QCD multijet background, on the other hand, is estimated by subtracting all simulated background processes from the observed data in the AR:

$$N_{QCD} = \max \left[0, N_{obs} - N_{real} - N_{EW} - N_{t\bar{t}}\right]_{AR}. \tag{11.3}$$

The fractions of the three $j \to \tau_h$ fake backgrounds b = QCD, EW, and $t\bar{t}$ then, are simply

$$f_b^{AR} = \left[\frac{N_b}{N_{QCD} + N_{EW} + N_{t\bar{t}}}\right]_{AR}. \tag{11.4}$$

These fractions are normalized such that their sum adds up to 1. Additionally, they are measured as a function of one or more variables that are physically motivated. For the 0b and ≥1b categories, separate fractions from an AR with corresponding selections are computed as a function of S_T^{MET}. Similarly, the fractions in the 0j category are measured as a function of χ. Putting everything together, it means that the following "total" FF is applied to the observed events in the AR:

$$FF = \sum_b f_b^{AR} \times FF_b \times \mathrm{corr}_b, \tag{11.5}$$

where corr_b are a product of bias and nonclosure corrections discussed in the following sections. For a given variable, the predicted $j \to \tau_h$ background in a histogram bin is then estimated by

$$N(j \to \tau_h)_{SR} = \left(\sum_b f_b^{AR} \times FF_b \times \mathrm{corr}_b\right) \times \left[N_{obs} - N_{real}\right]_{AR}, \tag{11.6}$$

where the total FF in parenthesis is applied on an event-by-event basis in both observed and simulated events in the AR due to the parametrization of the background fractions, FFs, and corrections.

The FF method was fully implemented and validated by several MSSM $\mathrm{H} \to \tau^+\tau^-$ analyses such as Refs. [370] and [371], but also a $\mathrm{Z}/\gamma^* \to \tau^+\tau^-$ cross section measurement in CMS [372]. The measurement procedure and validation of the FF method for the DeepTau algorithm in Run 2 is documented in detail by Ref. [369]. Some small modifications were made for the $\mathrm{LQ} \to \mathrm{b}\tau$ analysis, mainly the choice of parametrization and the choice of `DeepTau2017v2p1VSjet` WPs. The following sections describes the method separately for the semileptonic and fully hadronic channel.

11.2.1 $\mathrm{e}\tau_\mathrm{h}$, $\mu\tau_\mathrm{h}$ channels

For the $\mathrm{e}\tau_\mathrm{h}$ and $\mu\tau_\mathrm{h}$ channels, all SM background processes except for the QCD multijet and W + jets processes are estimated by simulation. The component of jets misidentified as τ_h ("$j \to \tau_\mathrm{h}$ fakes") of each SM process is estimated with the FF method. Simulated events with a selected τ_h object that does not originate from either a lepton or genuine τ_h decay at generator-level are discarded to avoid overcounting.

Similar to the OS/SS method, the DR for the QCD component is defined as events with a SS $\ell\tau_\mathrm{h}$ pair, as shown in Fig. 11.1. The DR is binned in number of jets. The FFs are then fitted to the ratio between the `Medium` and `VLoose && !Medium` regions as a function of τ_h p_T with the sum of a Landau function and a polynomial. The DR for the W + jets component is defined by $m_\mathrm{T} \geq 70\,\mathrm{GeV}$ with no b-tagged jets. It is further binned by $\Delta R(\ell, \tau_\mathrm{h})$ and number of jets, and fitted as a function of p_T in the same way. Figure 11.3 shows the τ_h p_T distribution in the QCD and W + jets DRs. The FFs for $\mathrm{t\bar{t}}$ are instead estimated directly from simulation, as it is very hard to construct a DR enriched in $\mathrm{t\bar{t}}$ in a phase space similar to the SR, while maintaining orthogonality with the AR and SR, and preserving a sufficient number of events. They are also fitted as a function of τ_h p_T without binning in number of jets.

Figure 11.4 shows some representative examples of the FF measured in the $\mu\tau_\mathrm{h}$ channel of the 2018 data set. The black line represents the final FF values used in the analysis, and is obtained by fitting the black points from observed data (minus simulated backgrounds). The yellow uncertainty band is used in the analysis, and is created with a resampling technique by randomly fluctuating each measurement point according to its uncertainty 200 times and repeating the fit as described in [369, p. 125–127]. At large p_T values the FF is taken to be constant, and the uncertainty band is inflated.

Bias corrections for the W + jets FFs are derived by comparing the FF measured from observed data in the DR to FFs measured in purely simulated W + jets events between the AR and SR. The corrections are measured as a function of m_vis, as some dependency was found with a variation of up to 15%. Similarly, nonclosure corrections between the `Medium` and `VLoose && !Medium` regions are derived as a function of lepton p_T. For QCD, several bias corrections are obtained using lepton p_T, relative lepton isolation I^ℓ_rel, and m_vis as parametrization. Most of these corrections are close to unity. For the $\mathrm{t\bar{t}}$ FFs, nonclosure corrections are also derived from MC as a function of m_vis.

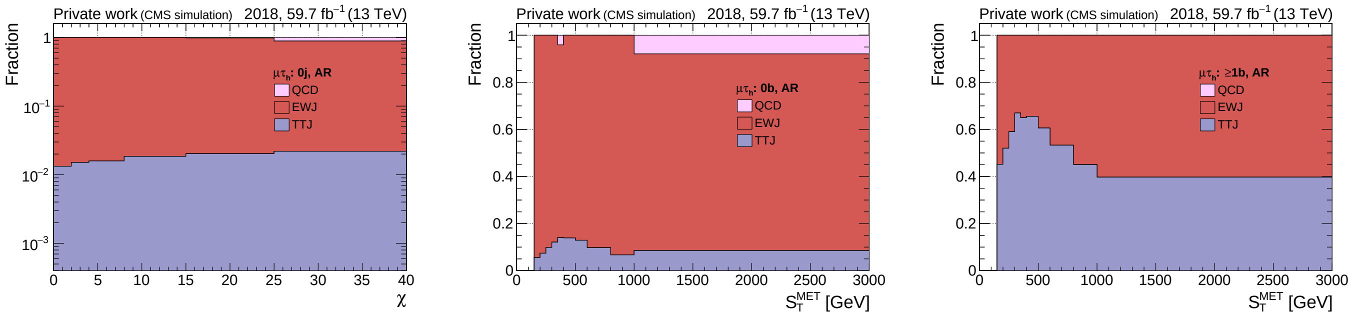

Figure 11.2: Relative fractions of the $j \to \tau_h$ backgrounds in the application region (AR) of the $\mu\tau_h$ channel in the 2018 data set. It is shown a function of χ in the 0j category (left), and as a function of S_T^{MET} in the 0b (center) and ≥1b (right) categories.

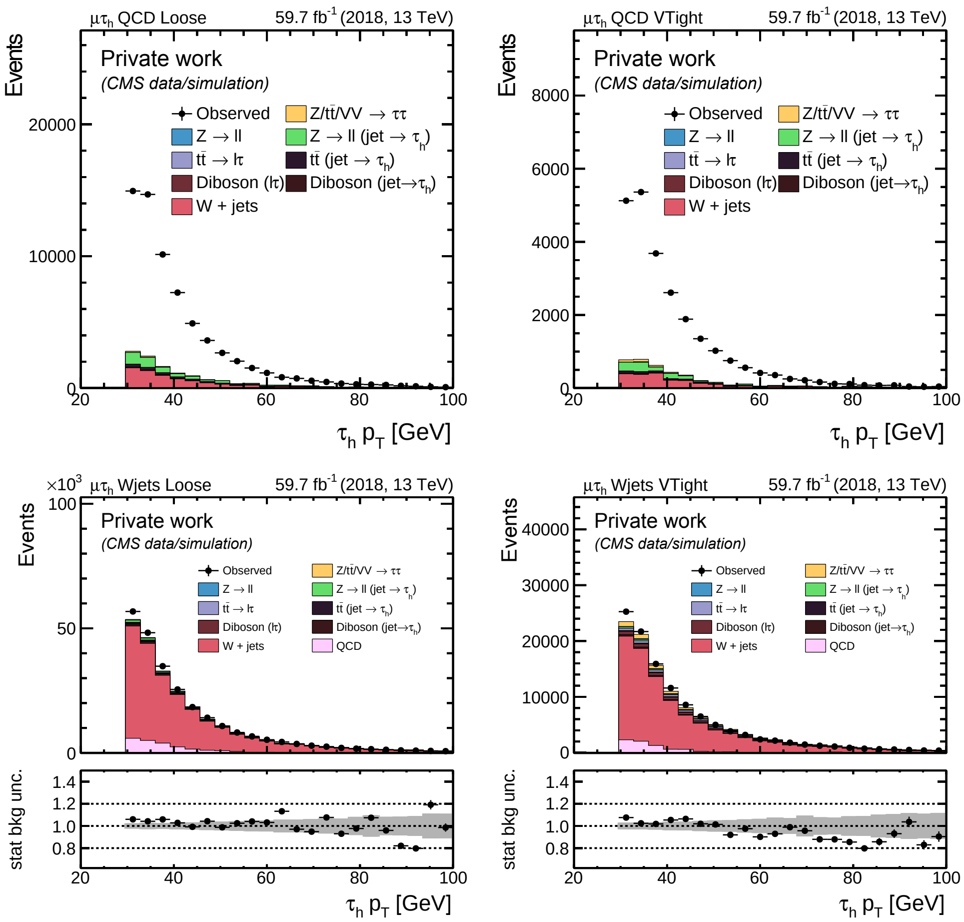

Figure 11.3: Examples of the τ_h p_T in the determination regions (DRs) of the $\mu\tau_h$ channel of the 2018 data set, from which the “raw” FF is measured for the QCD (top) and W + jets background component (bottom) (before applying any bias or nonclosure corrections). **Left**: Events where the τ_h candidate passes the VLoose, but fails the Medium WP of `DeepTau2017v2p1VSjet`. **Right**: Events where the τ_h candidate passes the Medium WP. Work by Janik Andrejkovič [369].

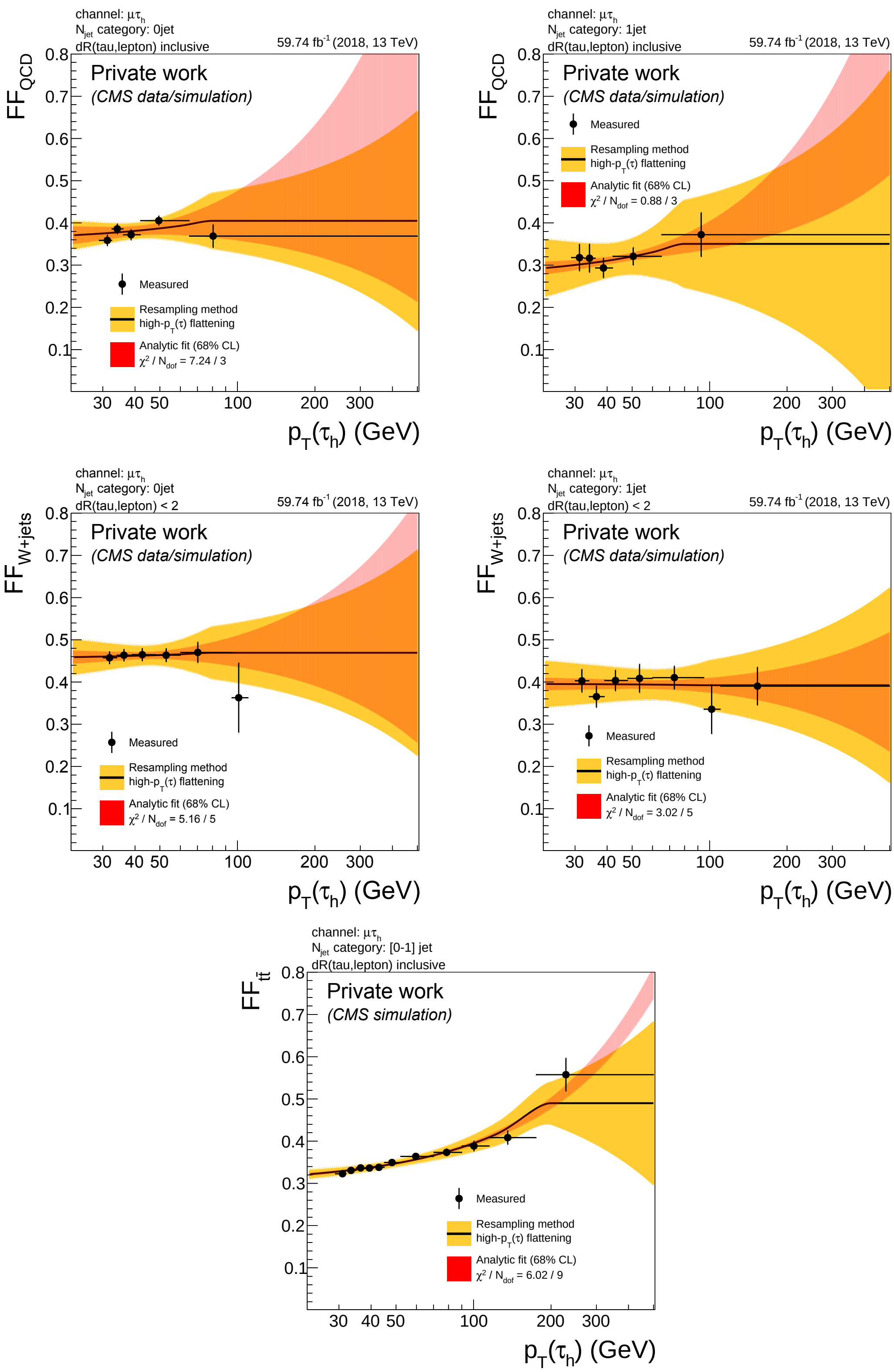

Figure 11.4: Fake factors for the different $j \to \tau_{\mathrm{h}}$ background components in the $\mu\tau_{\mathrm{h}}$ channel of the 2018 data set: QCD (top), $\mathrm{W}+\mathrm{jets}$ (middle), $\mathrm{t\bar{t}}$ (bottom). The measurement in data is shown as black points and the parametrization as a solid line. The red bands represent the fit results and are shown for comparison reasons only. In the analysis the solid black line is used. The yellow band is its associated uncertainty band, which is obtained using a resampling technique. The QCD and $\mathrm{W}+\mathrm{jets}$ FFs are shown for $N^{\mu}_{\mathrm{jets}} = 0$ (left), and for $N^{\mu}_{\mathrm{jets}} \geq 1$ (right). The $\mathrm{t\bar{t}}$ FFs are measured inclusively in N^{μ}_{jets}. The $\mathrm{W}+\mathrm{jets}$ FFs are only shown for the $\Delta R(\mu, \tau_{\mathrm{h}}) < 2$ bin. Work by Janik Andrejkovič [369].

11.3 $\tau_h\tau_h$ channel

All SM background processes in the $\tau_h\tau_h$ channels are predicted by simulation, with the exception of the $j \to \tau_h$ fake background, which is estimated with the FF method. The FF measurement for the $\tau_h\tau_h$ is very similar to the one used in the semileptonic channels, with a couple of small differences. The $j \to \tau_h$ fake backgrounds mainly consist of QCD multijets: more than 90% compared to less than 40% in the semileptonic channels [369]. The FFs are therefore only measured for QCD multijet production, and the QCD FFs are applied to the EW and $t\bar{t}$ component with increased uncertainty. Because there are two τ_h candidates, the AR is defined as the region where only one of the τ_h candidates passes the VLoose and not the Medium WP of `DeepTau2017v2p1VSjet`, while the remaining τ_h candidate must pass the Medium WP. In most QCD multijet events, both τ_h candidates are $j \to \tau_h$ fakes, and therefore the FF is applied with a factor of 0.5 to avoid double counting.

The QCD DR is again defined using a SS requirement, and it is binned according to the number of jets. The FF is extracted from a fit of a third-order polynomial to data in the DR, and as a function of p_T of the τ_h candidate that fails the Medium WP. The bias and nonclosure corrections are measured as a function of m_{vis}. Additional nonclosure corrections are measured as a function of the p_T of the τ_h candidate that passes the Medium WP.

12 Signal Extraction & Systematic Uncertainties

For maximum exclusion power, I combine the three LQ production modes (single, pair, and nonresonant) into a "total" LQ signal, which is simply the sum of the three. As discussed in Section 7.4, each production mode has a unique signature in terms of cross section and kinematic properties. I therefore also fit each production mode separately to study where the sensitivity comes from, and how it depends on different model assumptions. This would furthermore allow phenomenologists to reinterpret the final results with different LQ models or with different new physics models that have similar signals.

This chapter will cover how these LQ $\rightarrow$ bτ signals are fitted to the χ and $S_\mathrm{T}^\mathrm{MET}$ distributions to fit the observed data for a possible signal, set upper limits on the cross section and coupling strength λ, and to perform other studies, as well as an explanation of the systematic uncertainties used in the fit. The next chapter will discuss the preliminary results using the fit introduced in this chapter.

12.1 Maximum likelihood fit

A binned maximum likelihood fit [306] to the observed χ and $S_\mathrm{T}^\mathrm{MET}$ distributions is used to search for a possible signal over the expected background. As explained in Section 10.2.5, a resonant LQ $\rightarrow$ bτ signal would mostly contribute events at the highest values of $S_\mathrm{T}^\mathrm{MET}$, which has the best signal-to-background ratio, while a nonresonant signal would contribute to low values of χ, as explained in Section 10.3.1.

There are five $\tau\tau$ decay channels ($\mu\mu$, eμ, eτ_h, $\mu\tau_\mathrm{h}$, and $\tau_\mathrm{h}\tau_\mathrm{h}$) and five event categories (0b, $\geq$1b, and 0j split into three m_vis bins) for three data-taking periods (2016, 2017, 2018). This adds up to a total of 75 distributions (30 for $S_\mathrm{T}^\mathrm{MET}$, 45 for χ) that are fitted simultaneously for a total LQ $\rightarrow$ bτ signal, as explained in Section 12.2.

The $S_\mathrm{T}^\mathrm{MET}$ is plotted from 0 to 2500 GeV for visibility, but the events with $S_\mathrm{T}^\mathrm{MET} > 2500\,\mathrm{GeV}$ ("overflow") are added to the last bin. This is necessary to keep sensitivity to the signals with the largest mass values. The yield in each bin of the histograms is divided by the bin width, unless specified otherwise. The last bin of the $S_\mathrm{T}^\mathrm{MET}$ histograms also contains the overflow. Finally, the binning of all χ and $S_\mathrm{T}^\mathrm{MET}$ histograms are adjusted such that the total statistical uncertainty resulting from finite sample sizes in the SM background expectation of a given bin does not exceed 20%. To achieve this, the bin-merging algorithm of the CombineHarvester tool has been used [373], which iteratively merges bins of a given histogram. The choice of the 20% threshold is motivated by the bias study reported on in Section 12.3.

12.2 Upper limit & signal normalization

We set expected and observed upper limits on the cross section of the single, pair, nonresonant, and total signal, with the asymptotic $\mathrm{CL_s}$ modified-frequentist criterion [306, 374–376]. To get the upper limit in units of picobarns (pb), the signal in question is normalized assuming a cross section of $\sigma = 1\,\text{pb}$. To obtain the upper limit on the sum of the three signals, each signal is first weighted by its respective cross section, and normalized to the total cross section given by Eq. (7.15):

$$w_s(m_{\text{LQ}}, \lambda, \kappa) = \frac{\sigma^s(m_{\text{LQ}}, \lambda, \kappa)}{\sigma^{\text{tot}}(m_{\text{LQ}}, \lambda, \kappa)}, \tag{12.1}$$

where $s =$ single, pair, or nonres, such that the sum of the signals is normalized to 1 pb. Note that this relative weight depends on m_{LQ} and λ, and for the case of the vector-LQ model, it also depend on κ. Similarly, for the sum of the resonant signals only, i.e., single plus pair LQ production, each signal is reweighted by

$$w_s(m_{\text{LQ}}, \lambda, \kappa) = \frac{\sigma^s(m_{\text{LQ}}, \lambda, \kappa)}{\sigma^{\text{res}}(m_{\text{LQ}}, \lambda, \kappa)}, \tag{12.2}$$

where $s =$ single or pair, and σ^{res} is the resonant cross section defined by Eq. 7.16.

The upper limits on the cross sections are set as a function of m_{LQ}. We can therefore find the largest value of m_{LQ} excluded at 95% confidence level (CL) by numerically computing the intersection between the theoretical cross section and the upper limit.

As explained in Section 7.4.4, the cross sections for single and nonresonant LQ signals varies with the coupling strength λ. Consequently, an upper limit on the cross section can be derived for different values of λ. This also allows us to convert the upper limit on the cross section to an upper limit on λ at 95% CL as a function of m_{LQ}. By finding the excluded mass for a range of λ values, we exclude regions of the λ-m_{LQ} phase space for each production mode separately, and then for their combination.

Because the pair production cross section and the upper limit r_{pair} on the cross section is independent of λ, so is the lower limit on m_{LQ}. It is a single value given by the intersection between r_{pair} and the theoretical cross section. The cross section does depend on κ in the vector model, so a separate upper limit on λ is set for the two benchmarks used in this analysis, $\kappa = 0$ and 1.

For single LQ production only, both the upper limit r_{single} on the cross section and the theoretical cross section depend on the value of λ. For the vector model, there is also a dependency on the κ value. The chosen values of λ are 0.1, 0.2, 0.5, 1.0, 1.5, 2.0, and 2.5. For $\lambda > 1$, dedicated event samples and cross sections are used to take into account the increased width and the presence of soft events at low $M_{\text{b}\tau}$ (see Sections 7.4.1 and 7.4.2). For $\lambda \leq 1$, the effect of the width can be safely neglected, and therefore the simulated event sample of single LQ production with $\lambda = 1$ is used.

Because the nonresonant cross section is simply proportional to λ^4, the following formula is used to compute the upper limit on λ for a given value of m_{LQ}:

$$\lambda_{\text{min}}^{\text{nonres}} = \sqrt[4]{\frac{r_{\text{nonres}}}{\sigma^{\text{nonres}}}}, \tag{12.3}$$

where r_{nonres} is the expected upper limit on the cross section of a nonresonant signal.

For the total signal, the lower limit on m_{LQ} is found per λ with the intersection method. For $\lambda = 0$, there is no single or nonresonant production, and the excluded mass values are manually set to those of the pair LQ search. Conversely, at high values of λ, the limit on the total signal in λ-m_{LQ} phase space converges to the limit on the nonresonant signal.

For systematic studies, we typically consider two benchmarks: $m_{\text{LQ}} = 1400\,\text{GeV}$ with $\lambda = 1$, which is more sensitive to pair production, and $m_{\mathrm{LQ}} = 2000\,\mathrm{GeV}$ with $\lambda = 2.5$, which is more sensitive to the nonresonant signal.

12.3 Bias study

The 20% bin-merging threshold has been chosen with the goal of minimizing the expected bias in the signal strength extracted by the maximum likelihood fit while retaining enough sensitivity. A higher threshold, and thus finer binning, can result in a larger bias. The bias test is performed by generating toy data sets from the expected background plus signal, and performing a binned maximum likelihood fit of the signal strength μ to toy data sets. The signal is normalized to the respective expected 95% CL upper limit on the cross section to test the analysis at the threshold of its sensitivity. Furthermore, the bin-by-bin uncertainties are not included during toy generation, since these would not exist for real data. A comparison of different binning thresholds is shown in Fig. 12.2, assuming different signal strengths. The toy distribution of the signal strength with the current bin-merging threshold of 20% is shown in Fig. 12.1. Overall, the bias for an injected signal strength of $\mu_{\mathrm{inj}} = 1$ varies between -36 and -8%, depending on the LQ model (scalar or vector) and LQ mass. The same test has been done for $\mu_{\mathrm{inj}} = 2$ (twice the expected upper limit) with similar results. A 20% bias (in units of σ) corresponds to a coverage error of approximately 1.0% [377] and an uncertainty of approximately $\sqrt{1^2 + 0.2^2} - 1 = 2.0\%$.

12.4 Systematic uncertainties

This section will discuss the statistical and systematical uncertainties that are taken into account in the fit. Some uncertainties, like the one in luminosity, only introduce an overall normalization effect, while others may affect the normalization or the shape of the $S_{\mathrm{T}}^{\mathrm{MET}}$ or χ distribution of the signal and background processes. Both types are included in the fit as nuisance parameters.

12.4.1 Uncertainties in normalization

The uncertainty in the integrated luminosity varies between 1.2 and 2.5%, depending on the year [378–380], and affects the normalization of the signal and background processes that are based on simulation. Uncertainties in the electron or muon identification and trigger efficiency amount to 2% each [381]. For events where electrons or muons are misidentified as τ_{h} candidates, predominantly $\mathrm{Z} \to \mathrm{e}^+\mathrm{e}^-$ events in the $\mathrm{e}\tau_{\mathrm{h}}$ channel and $\mathrm{Z} \to \mu^+\mu^-$ events in the $\mu\tau_{\mathrm{h}}$ channel, rate uncertainties of 12 and 25% [300], respectively, are applied, as determined by a tag-and-probe method.

The QCD multijet background estimation in $\mathrm{e}\mu$ and $\mu\mu$ is found to have rate uncertainties of up to 20%. The uncertainty in the $\mathrm{Z}+\mathrm{jets}$ cross-section is estimated using a dedicated CR in events with two τ_{h} candidates and at least one b-tagged jet. A 30% uncertainty is assigned to the $\mathrm{Z}+\mathrm{jets}$ cross section in the $\geq$1b category on the basis of the expected fluctuations in the total number of data events in this CR. In the other signal categories, the uncertainty in the NNLO computation is given as 3%. The uncertainties in the cross section for the $\mathrm{t\bar{t}}$, diboson, and single top quark processes are 5.5, 6, and 5.5%, respectively. These uncertainties in the cross sections are treated as correlated between the years, but uncorrelated between the 0j and the other signal categories.

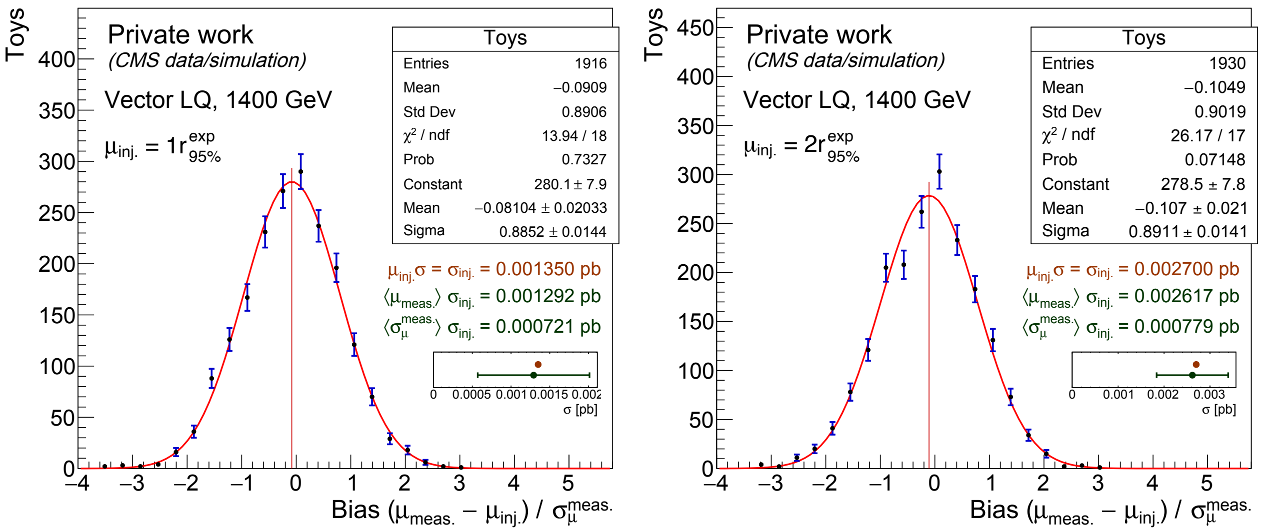

Figure 12.1: Bias test when fitting for the total vector LQ signal in all categories with the complete data set, estimated with toys using an injected signal $\mu_{\text{inj}} = 1$ (left) and 2 (right). LQ masses 500 (top), 1400 (middle), and 2000 (bottom) are shown with a coupling strength of $\lambda = 1$. The signal templates are normalized to the expected 95% CL upper limit on the cross section. Bins are merged with a 20% uncertainty threshold. The extra panel also visualizes the comparison of the injected cross section $\sigma_{\text{inj.}} = \mu_{\text{inj.}}\sigma$ to the expected cross section measurement $\langle\mu_{\text{meas.}}\rangle\,\sigma_{\text{inj.}}$, and its expected uncertainty $\langle\sigma_{\mu}^{\text{meas.}}\rangle\,\sigma_{\text{inj.}}$.

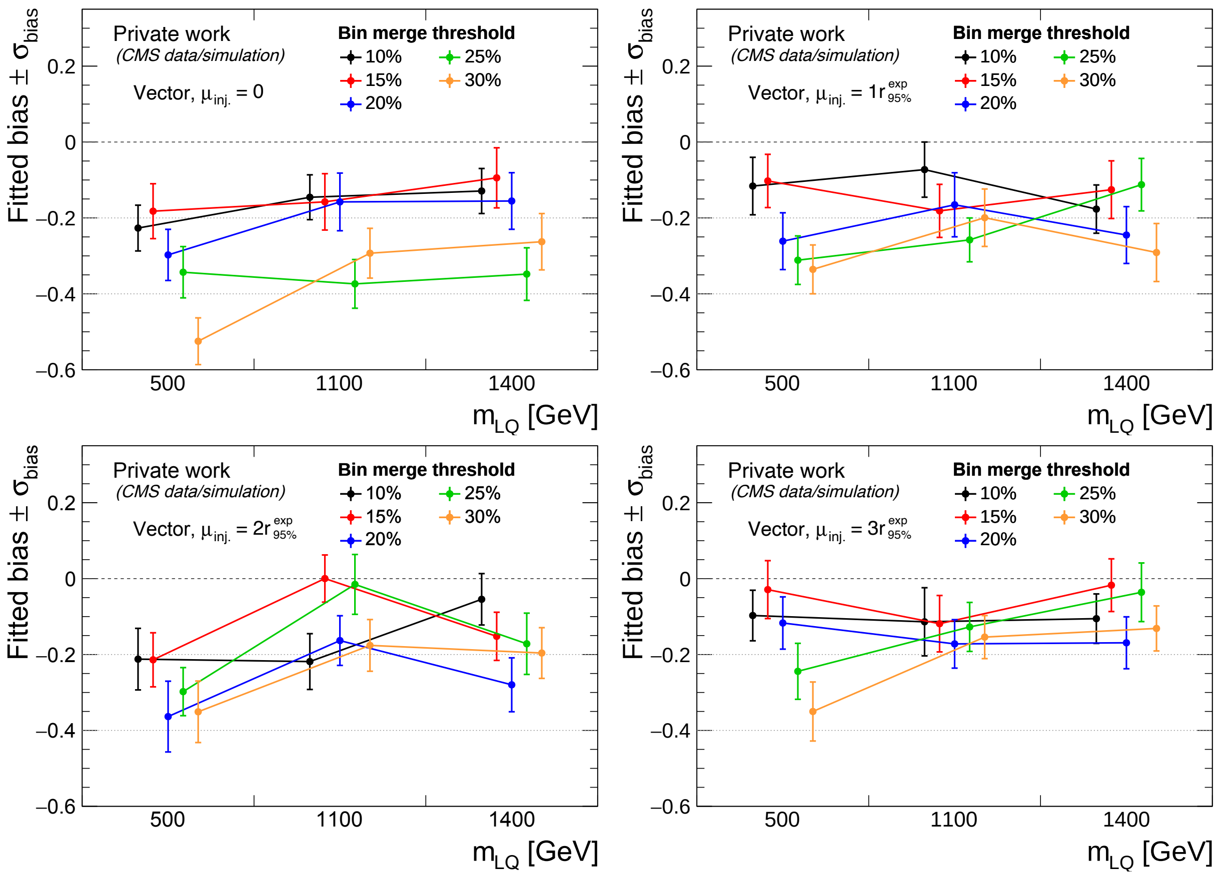

Figure 12.2: Biases versus m_{LQ} when fitting for the total vector-LQ signal using different bin-merging threshold (30% is finest, 10% is coarsest). The signal templates are normalized to the expected 95% CL upper limit on the cross section, and the bias is estimated with toys with an injected signal $\mu_{\text{inj}} = 0$ (top), 1 (second from top), 2 (second from bottom), and 3 (bottom). Different LQ masses between are shown with a coupling strength of $\lambda = 1$. The central value is the mean of the fitted gaussian (e.g. see Fig. 12.1), and the error bar is the uncertainty in the fitted mean. Note: These plots were produced before unblinding to decide on the final binning threshold of 20%.

12.4.2 Uncertainties in shape

The τ_h identification efficiency SFs are applied as a function of p_T for the semileptonic channels ($\mu\tau_h$ and $e\tau_h$), and are decay-mode dependent for the $\tau_h\tau_h$ channel because of the use of the double-τ_h trigger. The uncertainty in the τ_h identification efficiency is taken as the total uncertainty in the measurement discussed in Section 9.1.2, and is fully uncorrelated between the years.

The uncertainty in the τ_h energy scale depends on the τ_h decay mode and p_T, and varies between 0.6 and 1.4% for $p_T < 34\,\mathrm{GeV}$, and between 1 and 4% for $p_T > 170\,\mathrm{GeV}$, with a simple linear interpolation between the respective uncertainties for $34 < p_T < 170\,\mathrm{GeV}$. It is only applied to the background components with genuine τ_h, namely those in simulated Z + jets, $t\bar{t}$, and LQ events. It is uncorrelated between the years and signal categories, but correlated between the different channels. Similarly, for events where a muon or electron is misidentified as a τ_h candidate, a shape uncertainty is derived by varying the τ_h energy scale by 3%. The τ_h trigger efficiency has been measured using the "tag-and-probe" technique [299] and the shape uncertainty in the measurement is obtained with the uncertainty in the measured SFs.

The uncertainties in the jet energy scale are up to 4%, depending on the jet p_T and η [282]. The uncertainties in the jet energy scale and resolution are taken into account as shape uncertainties by taking the one-standard deviation variations of the corrections, and propagating them to all the affected variables in the analysis (including jet p_T, jet multiplicity, b tag multiplicity, p_T^{miss} and S_T^{MET}). They are uncorrelated between the years, but correlated between the different decay channels of each signal category. For the case of the 0j categories, the uncertainties in JER and unclustered energy can be neglected, while instead an overall uncertainty in acceptance of 5% is observed for the jet energy scale, which is anti-correlated to the same uncertainty in the b tag categories.

The uncertainties in the b tagging efficiency of heavy flavors (b and c quark) and the misidentification rate of light flavors (u, d and s quark, or gluon) are propagated from the uncertainties in the b tagging SFs. The efficiencies for b and c quarks are treated as correlated, as are the misidentification rate for light flavors. Furthermore, the uncertainties are correlated between the 0b and ≥1b categories. By the nature of the b tagging SFs, the overall yield of the resulting up and down shape variations are automatically anti-correlated between 0b and ≥1b, which is clear from Fig. 12.3. Most of the shape variations have little dependence on S_T^{MET}, with about a 1% change in overall yield in the ≥1b category, and less than 3% in 0b. The uncertainties are only partially correlated between the years.

The uncertainties in the FF method include the total systematic uncertainties in the measurement of the FFs and its corrections in each of the W + jets, $t\bar{t}$ and QCD CRs, as well as the statistical uncertainty in the fit of the FFs. The statistical uncertainty is split into the different N_{jets}^{μ} and $\Delta R(\ell, \tau_h)$ bins of the FF parametrization. They are treated as uncorrelated between the years and signal categories, as the dominant background process can differ. The shape uncertainties in the FFs are normalized to the nominal $j \to \tau_h$ event yield, and their total variation in event yield is combined into one normalization nuisance parameter, which is summarized in Table 12.1.

The uncertainty in the Z p_T reweighting is applied by varying the weight 50% up and down. The top p_T reweighting is not applied nominally, but a large shape variation of the $t\bar{t}$ template is chosen so that it is effectively treated as a flat prior, as discussed in Section 8.6. The shape variations are correlated across channels, but decorrelated between the 0j, 0b, and ≥1b cate-

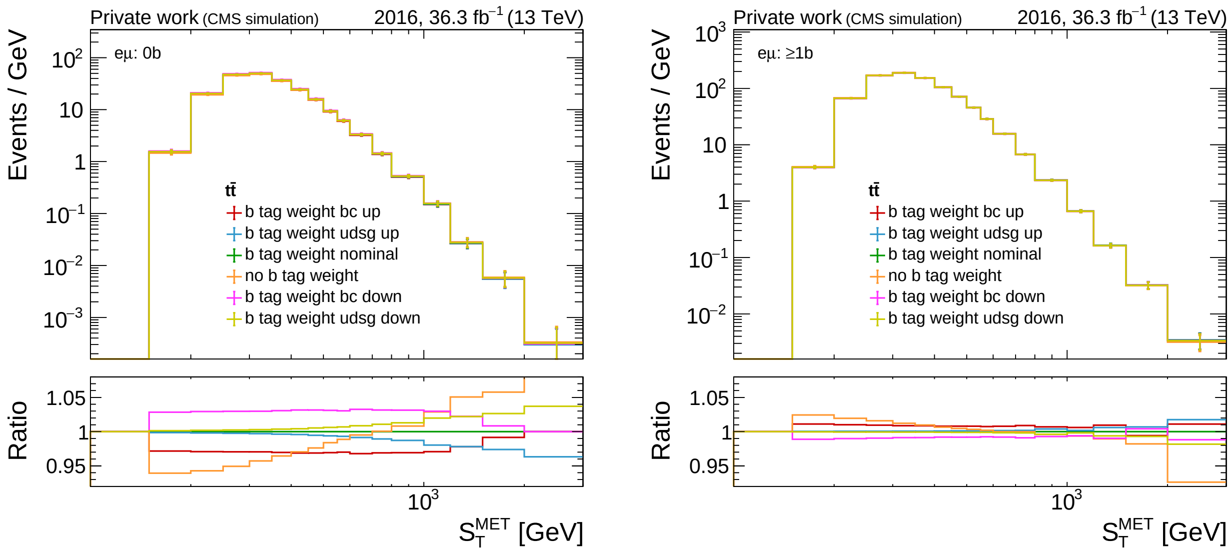

Figure 12.3: Comparison of the $S_{\mathrm{T}}^{\mathrm{MET}}$ shapes with different variations of the b tagging efficiency SFs, using simulated $\mathrm{t\bar{t}}$ events in the eμ channel. **Left**: 0b category. **Right**: ≥1b category. Note: The variations are automatically anti-correlated between these two categories, as would be expected.

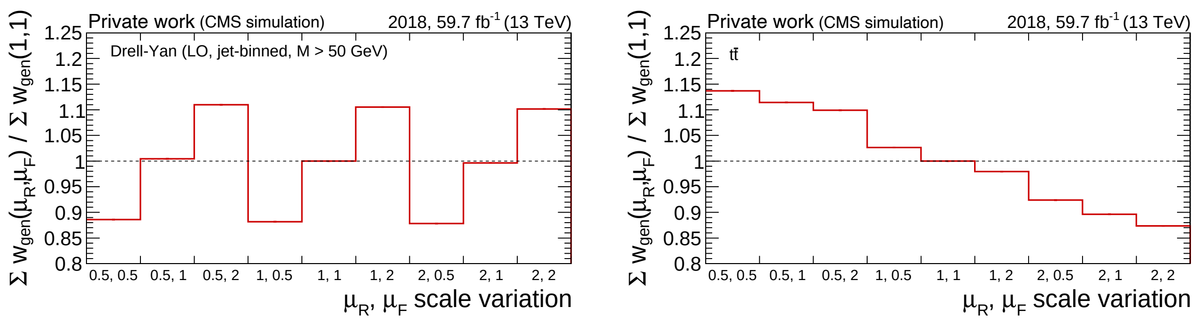

Figure 12.4: Comparison of the sum of weights for different variations of the renormalization and factorization scales, μ_{R} and μ_{F}, normalized to the nominal scale, $(\mu_{\mathrm{R}}, \mu_{\mathrm{F}}) = (1, 1)$. **Left**: Drell-Yan sample generated at LO by MadGraph with $M_{\ell\ell} > 50\,\mathrm{GeV}$. **Right**: $\mathrm{t\bar{t}}$ sample generated at NLO by powheg.

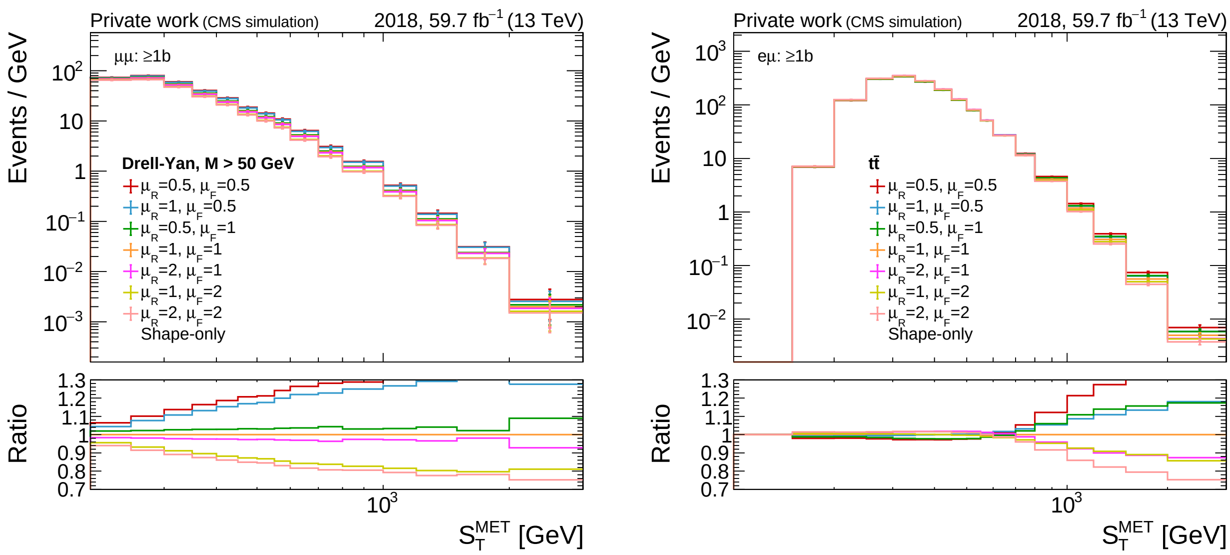

Figure 12.5: Comparison of the $S_{\mathrm{T}}^{\mathrm{MET}}$ shapes in the ≥1b category with different variations of the renormalization and factorization scales μ_{R} & μ_{F}, after renormalizing to the nominal yield. **Left**: Drell-Yan sample in the μμ channel generated at LO by MadGraph with $M_{\ell\ell} > 50\,\mathrm{GeV}$. **Right**: $\mathrm{t\bar{t}}$ sample in the eμ channel generated at NLO by powheg.

gories, as well as between years. It has been checked that this uncertainty is well-constrained by just the eμ channel, which has a large and pure $t\bar{t}$ yield compared to the other channels, and a negligible amount of signal contamination. The shape is created by taking the top-quark p_T reweighting measured with data (see Eq. (8.6)), and inflated by taking the weight to the power 5 for up, and -5 for down.

The shape uncertainties in the renormalization and factorization scales μ_R and μ_F are computed by taking the envelope of all variations generated by changing each scale simultaneously by the same or a different factor (0.5, 1 or 2) while keeping the total yield constant to the nominal one. Extreme combinations $(\mu_R, \mu_F) = (0.5, 2)$ or $(2, 0.5)$ are excluded. To renormalize each shape variation to the nominal yield, the sum of weights shown in Fig. 12.4 are used. Figure 12.5 shows examples of the shape variations of S_T^{MET} in the ≥1b category after renormalizing. Similarly, the systematic uncertainties in the PDFs are taken into account by determining in each bin the symmetric uncertainty in the cross section due to the PDF. For Hessian PDF sets, we use

$$\Delta\sigma = \sqrt{\sum_{m=1}^{N_{\rm mem}} (\sigma_m - \sigma_0)^2}, \tag{12.4}$$

where $N_{\rm mem}$ is the total number of members in a given PDF set, and σ_0 is the central value of the PDF set. For MC sets, we use the standard deviation

$$\Delta\sigma = \sqrt{\frac{1}{N_{\rm mem}-1}\sum_{m=1}^{N_{\rm mem}} (\sigma_m - \langle\sigma\rangle)^2}, \tag{12.5}$$

where $\langle\sigma\rangle$ is simply the average

$$\langle\sigma\rangle = \frac{1}{N_{\rm mem}}\sum_{m=1}^{N_{\rm mem}} \sigma_m. \tag{12.6}$$

This procedure is described in Ref. [382].

The uncertainty in the prefire corrections to 2016 and 2017 simulated events is simply taken by varying the event weight up and down by the prefire correction uncertainty.

Finally, uncertainties related to the limited number of simulated events are taken into account with the Barlow-Beeston-lite approach [351, 352]. They are considered for all bins of the distributions that are used to extract the results. They are kept uncorrelated across the different samples and across the bins of a single distribution.

All systematic uncertainties are summarized in Table 12.1.

Table 12.1: The sources of uncertainty considered, categorized as to whether they affect the normalization or shape of the distributions. "s.d." refers to the standard deviation on the uncertainty of the source.

Systematic source	Channel				
	$e\tau_h$	$\mu\tau_h$	$\tau_h\tau_h$	$e\mu$	$\mu\mu$
Integrated luminosity	1.2–2.5%				
Electron ident.	2%	—	—	2%	—
Electron trigger	2%	—	—	—	—
Muon ident.	—	2%	—	2%	2%
Muon trigger	—	2%	—	2%	2%
e misident. as τ_h rate	12%	—	12%	—	—
μ misident. as τ_h rate	—	25%	25%	—	—
p_T^{miss} scale	Up to 4%				
QCD multijet normalization	—	—	—	20%	20%
Z + jets cross section	20% in ≥1b, 3% otherwise				
$t\bar{t}$ cross section	5.5%				
W + jets cross section	—	—	—	6%	6%
Diboson cross section	6%				
Single top quark cross section	5.5%				
FF norm., 0b	3.0%	2.5%	2.2%	—	—
FF norm., ≥1b	2.5%	1.8%	1.7%	—	—
FF norm., 0j, $200 < m_{vis} < 400$ GeV	1.4%	1.1%	0.3%	—	—
FF norm., 0j, $400 < m_{vis} < 600$ GeV	3.9%	3.1%	3.0%	—	—
FF norm., 0j, $m_{vis} > 600$ GeV	4.0%	3.6%	3.0%	—	—
Jet energy scale	5% in 0j				
τ_h ident. efficiency	±1 s.d. in SF			—	—
τ_h energy scale	±1 s.d. on the energy scale			—	—
μ misident. as τ_h energy scale	±1% on the energy scale			—	—
e misident. as τ_h energy scale	±1 s.d. on the energy scale			—	—
FF shape variations	Syst. shape variations			—	—
τ_h trigger	—	—	±1 s.d. in the SF	—	—
b tagging efficiency	±1 s.d. in b tagging SFs				
b tagging mistag rate	±1 s.d. in b tagging SFs				
Jet energy scale	±1 s.d. in SF in 0b, ≥1b				
Jet energy resolution	±1 s.d. in SF in 0b, ≥1b				
PDF variations	Envelope of PDF variations				
μ_R & μ_F variations	Envelope of scale variations				
Z p_T reweighting	Weight applied ±50%				
Top p_T reweighting	(top p_T weight)^p with $p = 5$ or -5				

13 Results

This chapter will discuss the preliminary results of the LQ $\rightarrow$ bτ search that have already been made public in Ref. [368].

13.1 Fit results

As explained in Chapter 12, a binned maximum likelihood fit [376] of the observed $S_{\mathrm{T}}^{\mathrm{MET}}$ and χ distributions in all channels, event categories, and data-taking periods is performed to search for a possible signal over the expected background.

Figure 13.1 shows the postfit distributions of $S_{\mathrm{T}}^{\mathrm{MET}}$ in the $\tau_{\mathrm{h}}\tau_{\mathrm{h}}$ and eμ channels in the 0b category and $\geq$1b categories, while Fig. 13.2 shows the postfit distributions of χ in the bins of the 0j category with $400 < m_{\mathrm{vis}} < 600\,\mathrm{GeV}$ and $m_{\mathrm{vis}} > 600\,\mathrm{GeV}$. These distributions are obtained by adding up distributions from different data-taking periods. To achieve this, distributions with common binning are created, to which the fit results are applied. This is needed because the automatic rebinning described in Section 12.1 may vary between the years in the main fit. The uncertainty bands include the statistical uncertainties and all postfit uncertainties on the background expectation. The total LQ signal for the benchmark $m_{\mathrm{LQ}} = 2000\,\mathrm{GeV}$ with $\lambda = 2.5$ and $\kappa = 1$ is overlaid. The signal is normalized to the fitted cross section.

Table 13.1 shows the best-fit signal cross section with the corresponding significance for different LQ production modes. For lower masses and coupling strengths λ, the observed data agree with the standard model expectation within one standard deviation. At higher masses and coupling strengths, however, an excess with a significance of up to 3.4 standard deviations above the SM background expectation is found. This excess is observed across several channels, as well as in both the χ and $S_{\mathrm{T}}^{\mathrm{MET}}$ distributions in the different jet categories. The excess is most prominent for the nonresonant signal in the analysis, which contributes to the combined excess increasingly as larger LQ masses and couplings are considered. The significance of the nonresonant signal by itself has no strong dependence on m_{LQ} or λ, hence the trial factor is negligible. When combined with the pair and single production contributions to the total LQ signal, the excess at lower LQ masses and couplings is reduced.

To better illustrate where the excess is localized, we reorder and stack the χ and $S_{\mathrm{T}}^{\mathrm{MET}}$ bins by $S/(S+B)$, where S (B) is the total fitted signal (background) yield in a given bin. The resulting histograms are shown in Fig. 13.3 for a vector-LQ model with $m_{\mathrm{LQ}} = 1400$ (2000) GeV and $\lambda = 1$ (2.5). The excess becomes more evident at high λ, where more bins from the 0j category appear at high $S/(S+B)$ due to the increased sensitivity to a nonresonant signal. In the next section, this will be shown by a breakdown of the upper limits.

13.2 Upper limits on the cross sections

Although we find an excess in a small part of the phase space, we set upper limits on the cross section of single, pair, and nonresonant production, as well as their sum, with the asymptotic

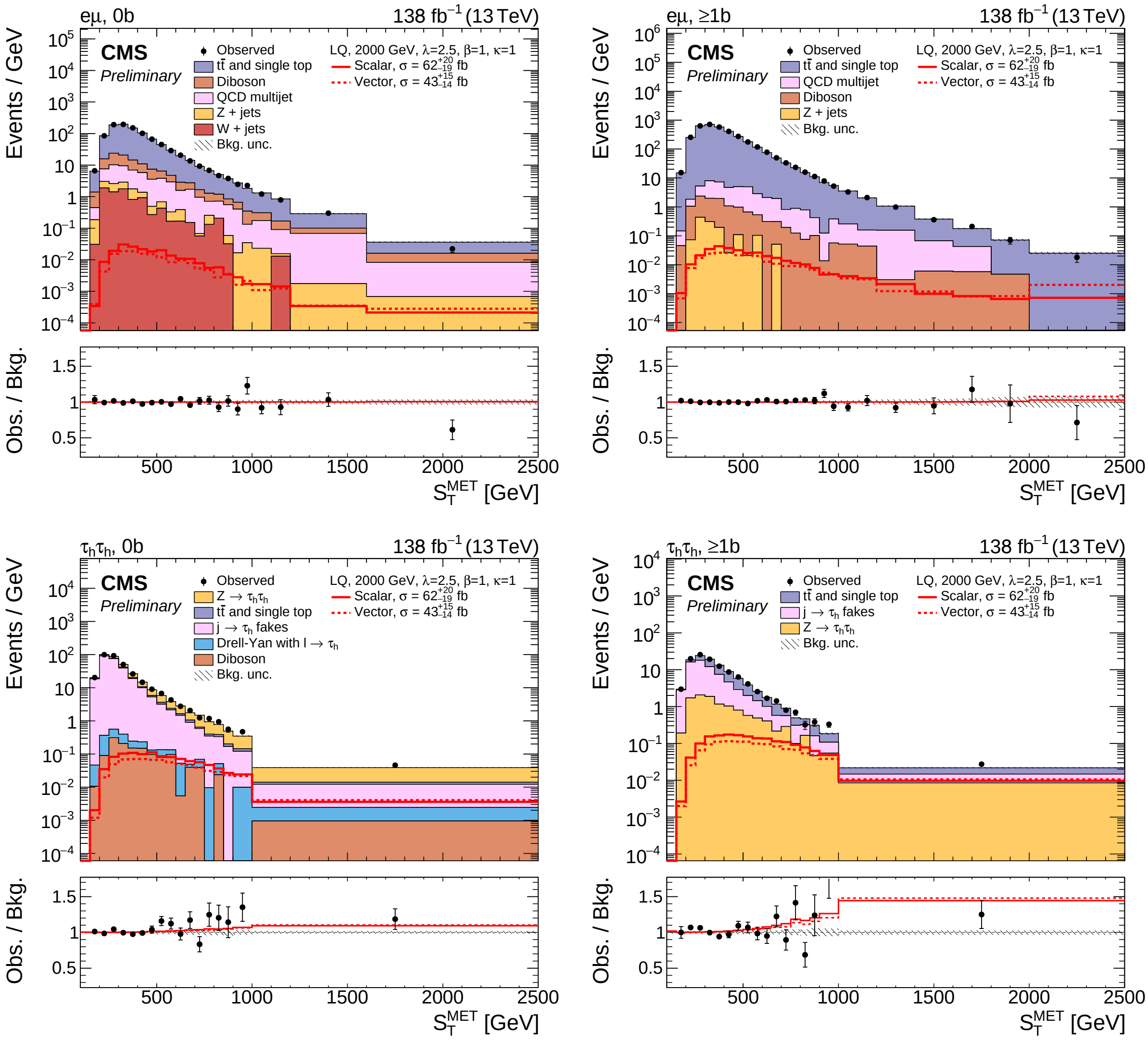

Figure 13.1: Postfit distributions of $S_{\mathrm{T}}^{\mathrm{MET}}$ for the combined 2016–2018 data set after a simultaneous fit of the scalar-LQ signal to the data in each data-taking period. The last bin includes the overflow. The eμ (top) and $\tau_{\mathrm{h}}\tau_{\mathrm{h}}$ (bottom) channels in the 0b (left) and ≥1b (right) category are shown. The fitted signal distributions for the total scalar- (solid red) and vector-LQ model (dashed red) with a mass of 2000 GeV and a coupling strength of $\lambda = 2.5$ are overlaid to illustrate the sensitivity. They include the single and pair LQ production, as well as the nonresonant production of a τ lepton pair through t-channel LQ exchange. The lower panel shows the ratio between the observed data and background from the fit (black). The hatched uncertainty bands include the total postfit uncertainties in the background.

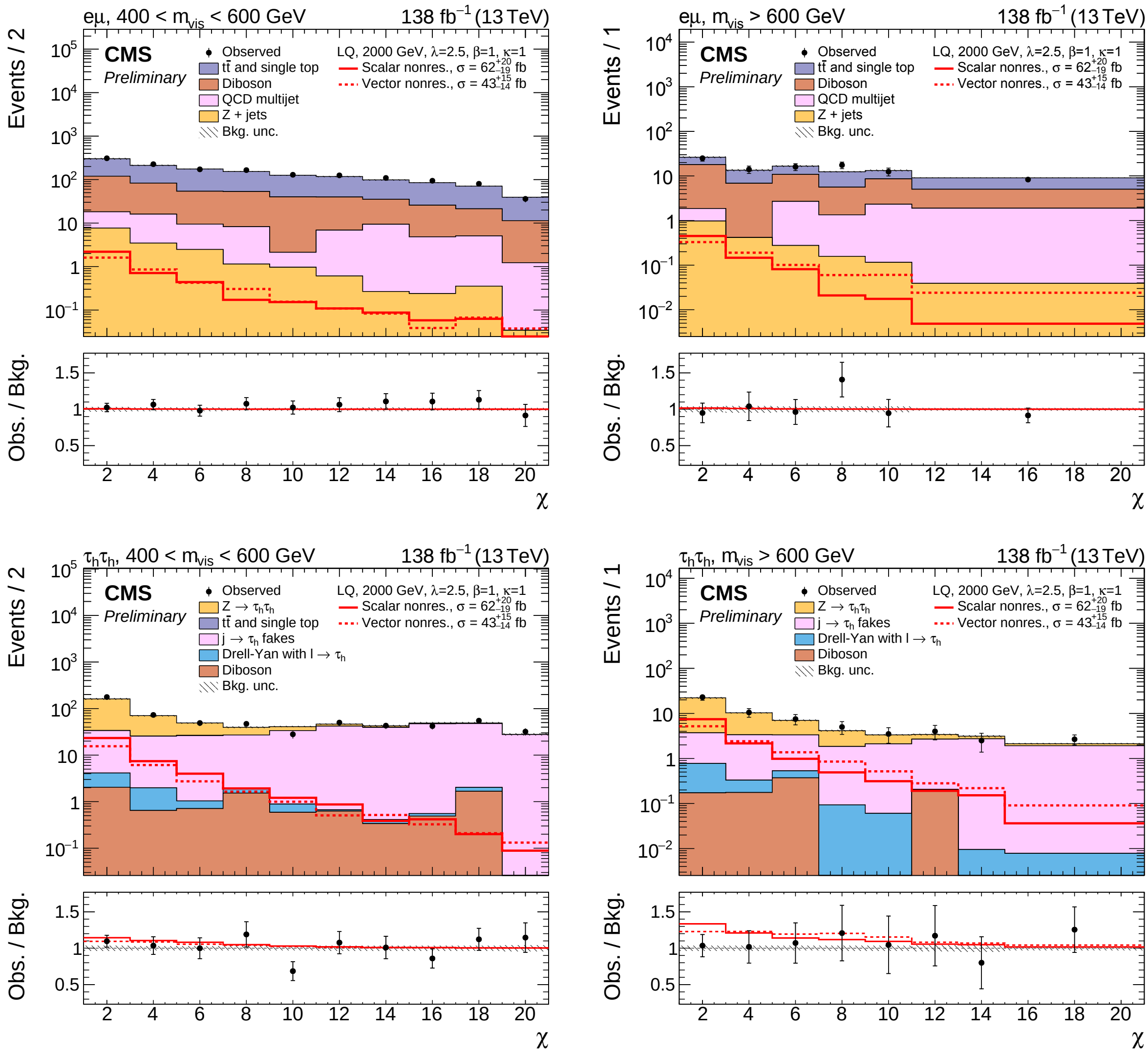

Figure 13.2: Postfit distributions of χ for the combined 2016–2018 data set after a simultaneous fit of the scalar-LQ signal to the data in each data-taking period. The $\mathrm{e}\mu$ (top) and $\tau_\mathrm{h}\tau_\mathrm{h}$ (bottom) channels in the $400 < m_\mathrm{vis} < 600\,\mathrm{GeV}$ (left) and $m_\mathrm{vis} > 600\,\mathrm{GeV}$ (right) category are shown. The fitted nonresonant signal for the scalar- (solid red) and vector-LQ model (dashed red) with a mass of 2000 GeV and a coupling strength of $\lambda = 2.5$ are overlaid to illustrate the sensitivity. The lower panel shows the ratio between the observed data and background from the fit (black). The hatched uncertainty bands include the total postfit uncertainties in the background.

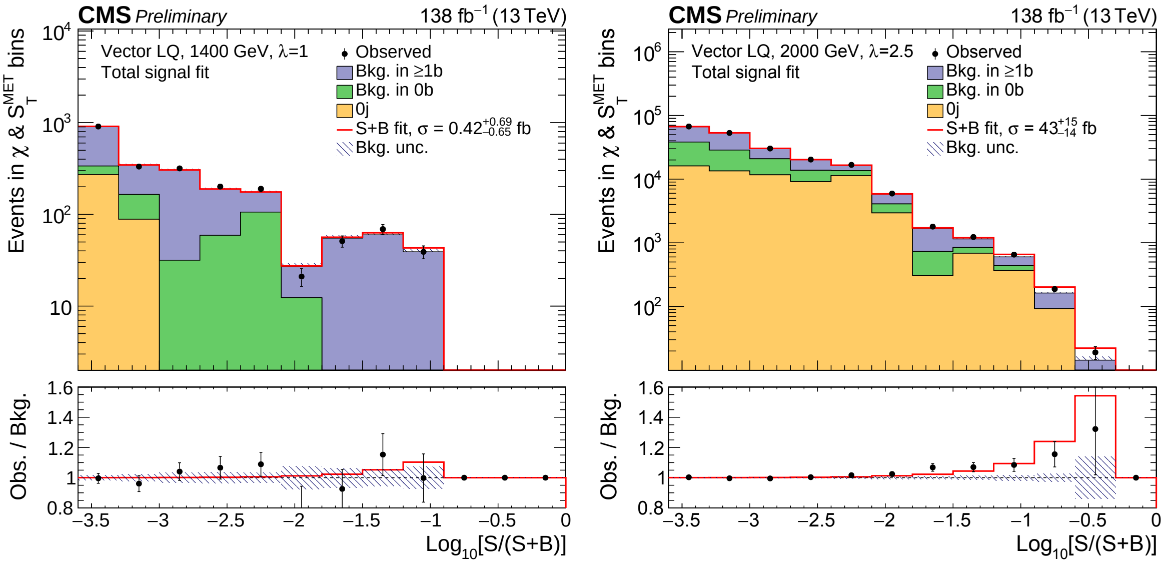

Figure 13.3: Histograms of $\log_{10}\left[S/(S+B)\right]$ counting events in all bins, assuming a vector LQ with $m_{\mathrm{LQ}} = 1400\,\mathrm{GeV}$ and $\lambda = 1.0$ (left), or $m_{\mathrm{LQ}} = 2000\,\mathrm{GeV}$ and $\lambda = 2.5$ (right). The $\log_{10}\left[S/(S+B)\right]$ is computed per bin of the postfit χ and $S_{\mathrm{T}}^{\mathrm{MET}}$ distributions after the signal fit. The total LQ signal strength (single, pair & nonresonant) is fitted simultaneously. The expected background is grouped by jet categories in stacked histograms, and the red line is the fitted signal on top of the total backgrounds. The lower panel shows the ratio of the observed data to the expected background from the fit.

Table 13.1: Best-fit LQ cross sections σ_{fit} for various masses and coupling strengths λ, and the corresponding significance z (given in standard deviations) for different production modes individually, as well as their combination.

Signal	$m_{\mathrm{LQ}} = 1400\,\mathrm{GeV}$		$m_{\mathrm{LQ}} = 2000\,\mathrm{GeV}$	
	σ_{fit} [fb]	z	σ_{fit} [fb]	z
Pair	$0.24^{+0.47}_{-0.45}$	0.5	$0.22^{+0.41}_{-0.39}$	0.0
Single, $\lambda = 1$	$1.15^{+0.95}_{-0.92}$	1.3	$0.64^{+0.68}_{-0.65}$	1.0
Single, $\lambda = 2.5$	$9.1^{+5.6}_{-5.3}$	1.7	18^{+11}_{-11}	1.7
Nonres.	70^{+23}_{-22}	3.4	63^{+20}_{-19}	3.5
Total, $\lambda = 1$	$1.7^{+1.9}_{-1.8}$	0.9	$9.6^{+6.2}_{-5.9}$	1.7
Total, $\lambda = 2.5$	43^{+16}_{-15}	2.9	62^{+20}_{-19}	3.4
Pair	$0.24^{+0.46}_{-0.44}$	0.0	$0.24^{+0.41}_{-0.39}$	0.0
Single, $\lambda = 1$	$1.00^{+0.89}_{-0.85}$	1.2	$0.60^{+0.66}_{-0.63}$	1.0
Single, $\lambda = 2.5$	$9.1^{+6.5}_{-6.2}$	1.5	25^{+18}_{-17}	1.4
Nonres.	58^{+18}_{-17}	3.5	51^{+16}_{-15}	3.5
Total, $\lambda = 1$	$1.2^{+1.5}_{-1.4}$	0.8	$7.7^{+5.1}_{-4.8}$	1.7
Total, $\lambda = 2.5$	$12.2^{+7.1}_{-6.8}$	1.8	43^{+15}_{-14}	3.1
Pair	$0.24^{+0.46}_{-0.44}$	0.0	$0.24^{+0.41}_{-0.39}$	0.0
Single, $\lambda = 1$	$1.00^{+0.89}_{-0.85}$	1.2	$0.60^{+0.66}_{-0.63}$	1.0
Single, $\lambda = 2.5$	$9.1^{+6.5}_{-6.2}$	1.5	25^{+18}_{-17}	1.4
Nonres.	58^{+18}_{-17}	3.5	51^{+16}_{-15}	3.5
Total, $\lambda = 1$	$0.42^{+0.69}_{-0.66}$	0.6	$1.3^{+1.5}_{-1.4}$	0.5
Total, $\lambda = 2.5$	$12.2^{+7.1}_{-6.8}$	1.8	43^{+15}_{-14}	3.1

$\mathrm{CL_s}$ modified-frequentist criterion, as explained in Section 12.2. The observed and expected upper limits on the cross section of the different production modes and their combination are shown in Figs. 13.4–13.6 for scalar- and vector-LQ production at 95% CL, respectively. Note that the quantity of the vertical axis varies between the plots. In Fig. 13.7, I have rescaled the upper limits on the cross sections of each individual production mode to the upper limit on the total cross section using Eq. (12.1) in order to compare them directly. This illustrates how each of the three production modes (single, pair, and nonresonant) contributes to the upper limit on the total cross section, and therefore where the sensitivity lies. For the resonant signals, the observed data agree with the SM background expectation, as well as for the combined signal at $\lambda = 1$. The upper limits on the nonresonant signal, however, show an excess of about 3σ, resulting from several small excesses in the low χ bins and high $S_\mathrm{T}^\mathrm{MET}$ bins, where the S+B fit can better explain the data than the B-only fit. As expected from its relatively large cross section and hard kinematics, pair production dominates the sensitivity for an LQ signal at low coupling and low mass. At 95% confidence level, LQ masses below 1.25 TeV are excluded for the scalar model with $\lambda = 1$, and below 1.53 (1.86) GeV for the vector model with $\lambda = 1$ and nonminimal coupling $\kappa = 0$ (1). At $\lambda = 2.5$, the lower limits are 1.37 TeV for a scalar model, and 1.86 (1.96) GeV for a vector model with $\kappa = 0$ (1).

13.3 Exclusion of coupling & mass

As explained in Section 12.2, each production mode has a different dependency on λ, which allows us to exclude different regions of the λ-m_LQ phase space by setting an upper limit on λ and a lower limit on m_LQ at 95% CL. This is shown in Figs. 13.8 and 13.9 They include one line for each production mode, as well as their combination, which allows for the exclusion of a larger region at higher values of λ, where the single and nonresonant production start to contribute more significantly. Figure 13.10 shows the upper limit on the coupling strength for LQs exchanged in the t channel with an extended mass range. The region with blue shading shows the parameter space preferred by one of the models proposed to explain the anomalies in B hadron decays with leptons [113]. Thanks to the sensitivity to the LQ pair production, large part of this parameter space can already be excluded.

13.4 Impacts & pulls

Figure 13.11 shows how the profile of the negative logarithm of the likelihood (NLL) breaks down when including different uncertainties in the fit of the total vector-LQ signal. It shows that the measurement of the signal strength r is statistically dominated at smaller values of λ, where the total LQ signal is dominated by pair production in the high tail of $S_\mathrm{T}^\mathrm{MET}$. At higher values of the masses and λ, the LQ signal becomes more dominated by the nonresonant production, which is constrained by the low-χ bins and the whole $S_\mathrm{T}^\mathrm{MET}$ tail, which have relatively higher expected yield. As such, the statistical and systematic uncertainty in the signal strength becomes more comparable for a mass of 2000 GeV and $\lambda = 2.5$.

To study how nuisance parameters can affect the measurement of the signal strength r, we define the *impact* on r as the shift $\Delta\hat{r}$ that is induced in r by nuisance parameter θ if the fit is performed with θ fixed to

$$\theta = \hat{\theta} \pm \Delta\hat{\theta}, \tag{13.1}$$

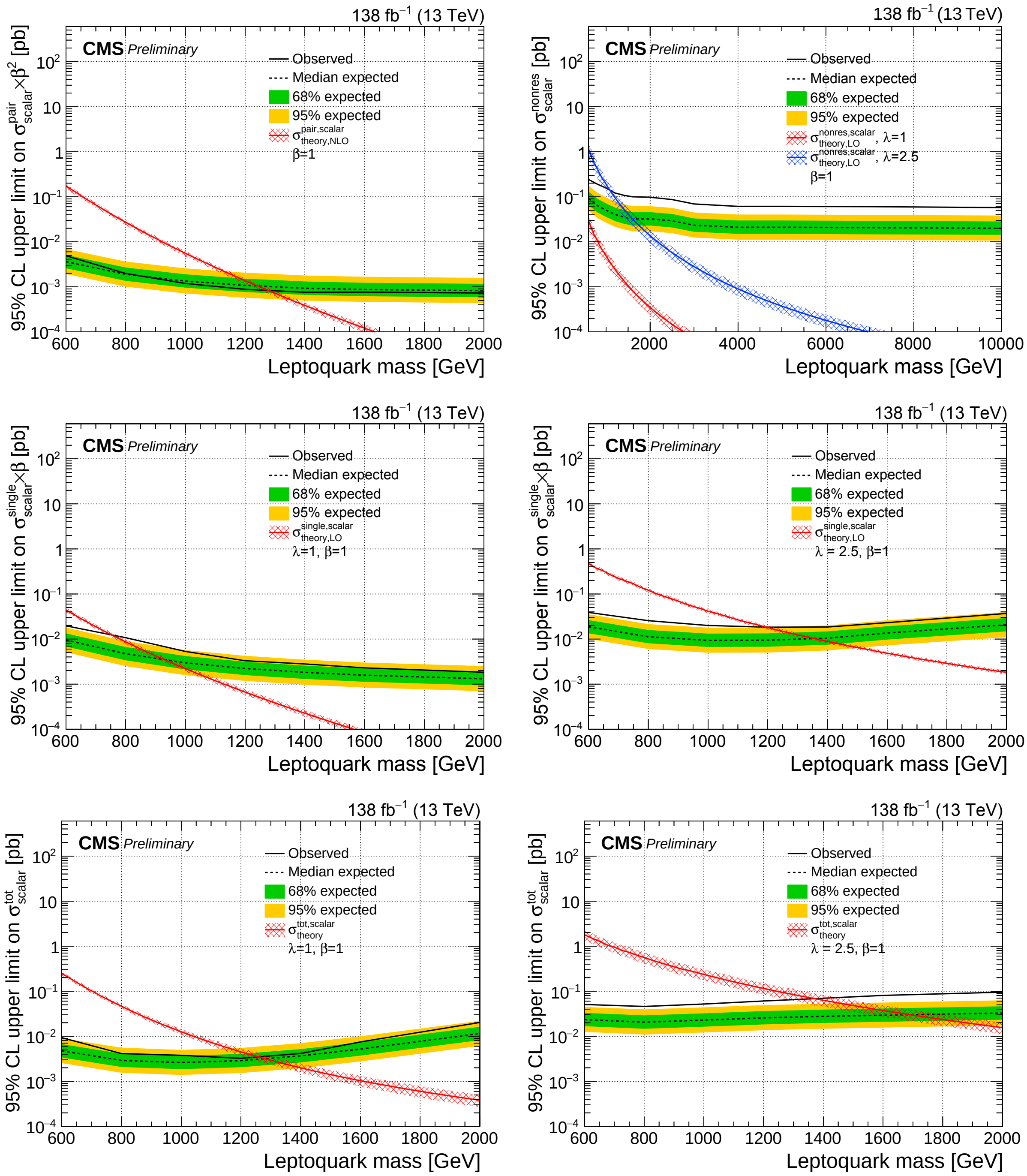

Figure 13.4: The observed and expected upper limit on the cross section of different scalar LQ $\rightarrow$ bτ signals at 95% CL. Shown are pair (top left), nonresonant (top right), and single production with $\lambda = 1$ (middle left) and $\lambda = 2.5$ (middle right), as well as the total signal with $\lambda = 1$ (bottom left) and $\lambda = 2.5$ (bottom right). The inner (green) band and the outer (yellow) band indicate the regions containing 68 and 95%, respectively, of the distribution of limits expected under the background-only hypothesis. The red line shows the cross section with the hatched band indicating the theoretical uncertainties.

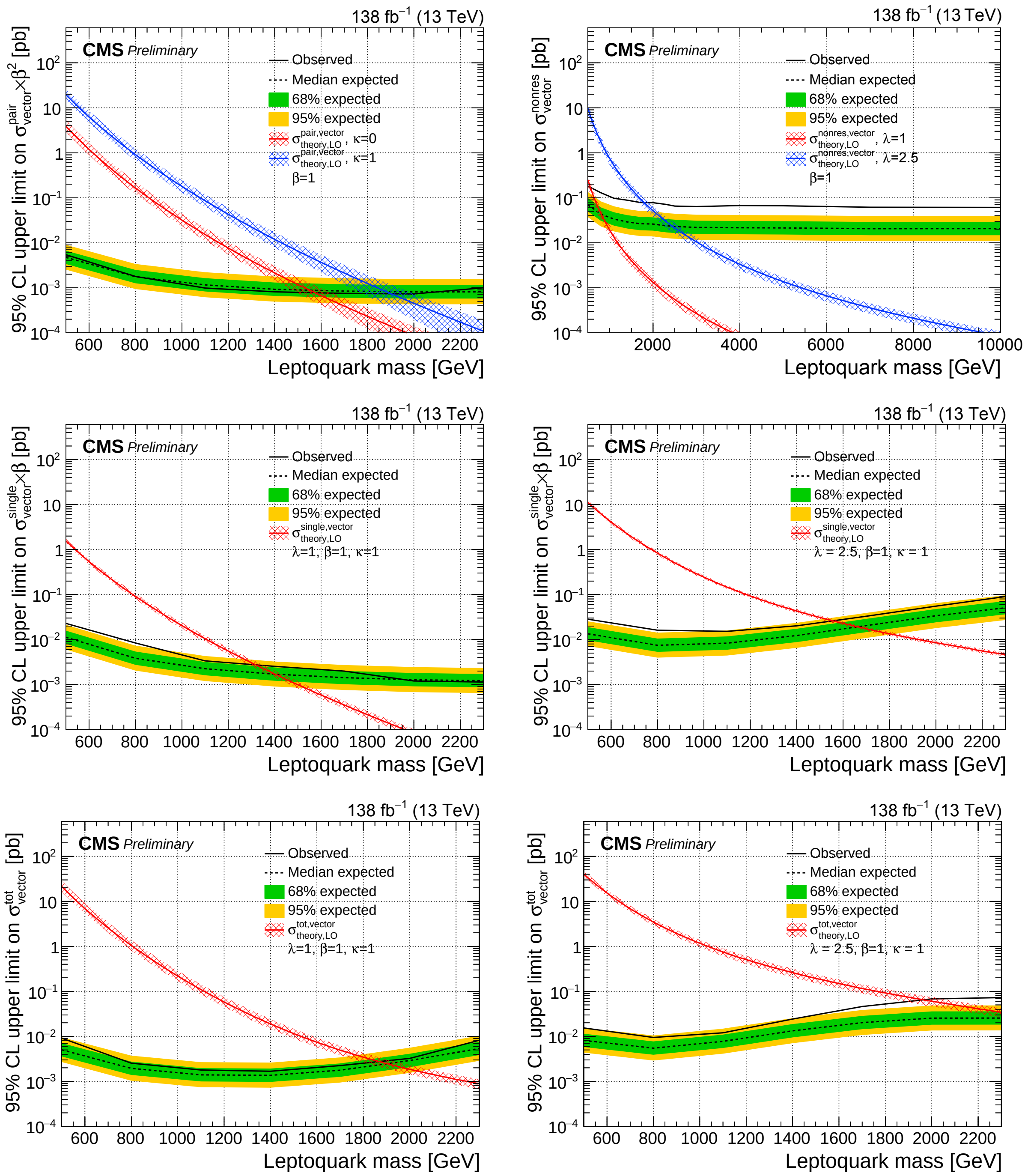

Figure 13.5: The observed and expected upper limit on the cross section of different vector LQ $\rightarrow$ bτ signals at 95% CL. Shown are pair (top left), nonresonant (top right), and single production with $\lambda = 1$ (second row left) or $\lambda = 2.5$ (second row right), as well as the total signal with $\lambda = 1$ (third row left) and $\lambda = 2.5$ (third row right), assuming a nonminimal coupling of $\kappa = 1$. The inner (green) band and the outer (yellow) band indicate the regions containing 68 and 95%, respectively, of the distribution of limits expected under the background-only hypothesis. The red line shows the cross section calculated at LO with the hatched band indicating the theoretical uncertainties.

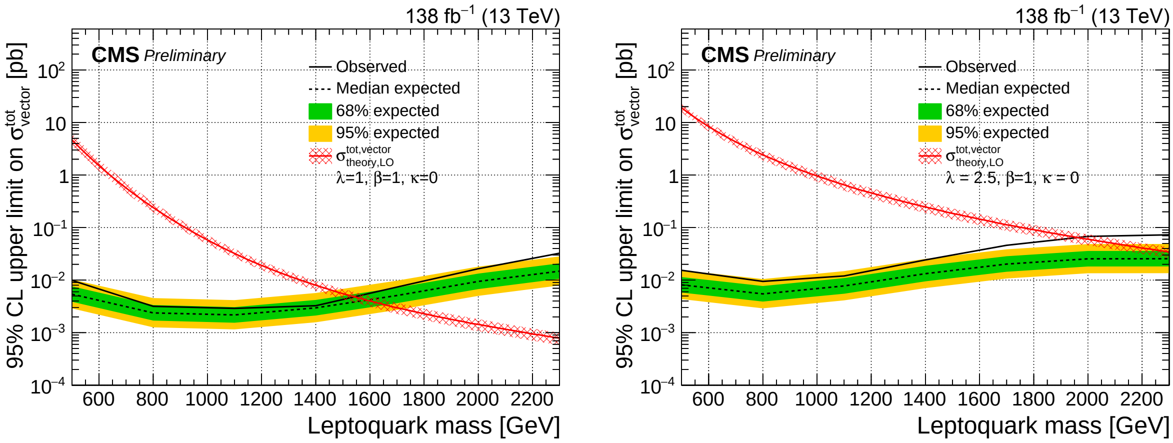

Figure 13.6: The observed and expected upper limit on the cross section of the total vector LQ $\rightarrow$ bτ signal at 95% CL, assuming a nonminimal coupling of $\kappa = 0$, and $\lambda = 0$ (left) or $\lambda = 2.5$ (right). The inner (green) band and the outer (yellow) band indicate the regions containing 68 and 95%, respectively, of the distribution of limits expected under the background-only hypothesis. The red line shows the cross section calculated at LO with the hatched band indicating the theoretical uncertainties.

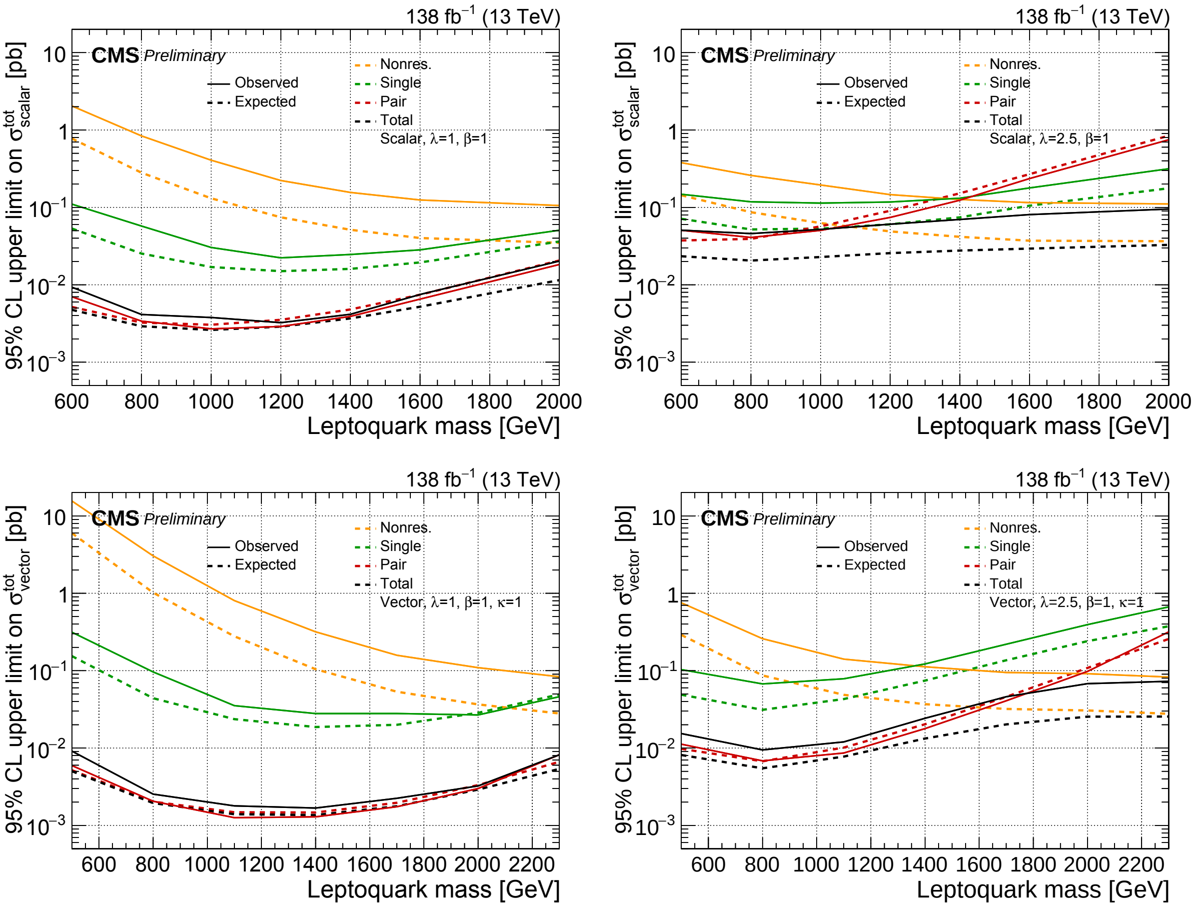

Figure 13.7: The expected upper limit on the total LQ production cross section at 95% CL comparing each production mode as a separate signal to illustrate their respective sensitivity and contribution to the total sensitivity. Single LQ production is shown in green, pair in red, nonresonant in orange, and the total black. All years and all channels in each category are combined. The top (bottom) plots are for scalar (vector) LQs, while the left (right) plots are for $\lambda = 1$ ($\lambda = 2.5$).

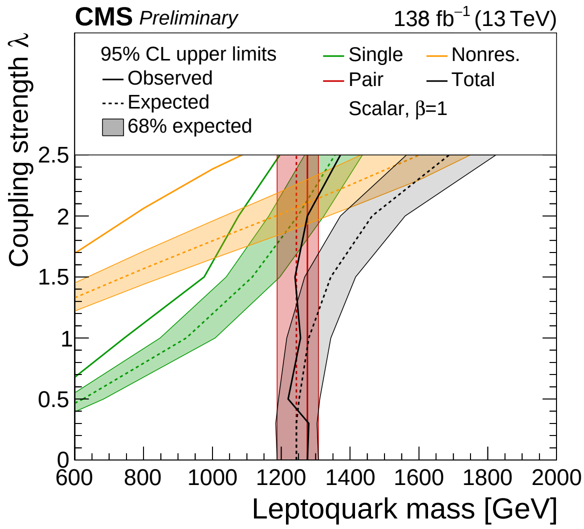

Figure 13.8: The observed and expected upper limits at 95% CL on the coupling strength λ of a scalar LQ. All years and all $\tau\tau$ decay channels in each category are combined. The limits derived for the single (green), pair (red), nonresonant (orange), and total LQ production (black) are shown. Bands around the expected limit lines correspond to the regions containing 68% of the distribution of limits expected under the background-only hypothesis.

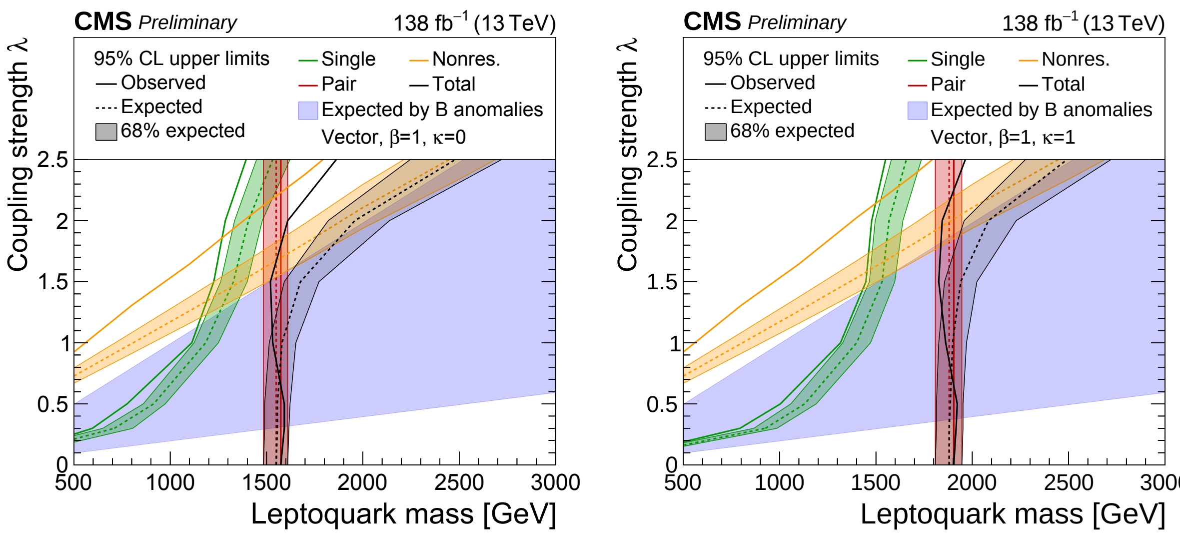

Figure 13.9: The observed and expected upper limits at 95% CL on the coupling strength λ of a vector-LQ model with $\kappa = 0$ (left) and $\kappa = 1$ (right). All years and all $\tau\tau$ decay channels in each category are combined. The limits derived for the single (green), pair (red), nonresonant (orange), and total LQ production (black) are shown. Bands around the expected limit lines correspond to the regions containing 68% of the distribution of limits expected under the background-only hypothesis. The region with blue shading shows the parameter space preferred by one of the models proposed to explain the anomalies observed in B hadron decays, see Eq. (7.11) and Ref. [113].

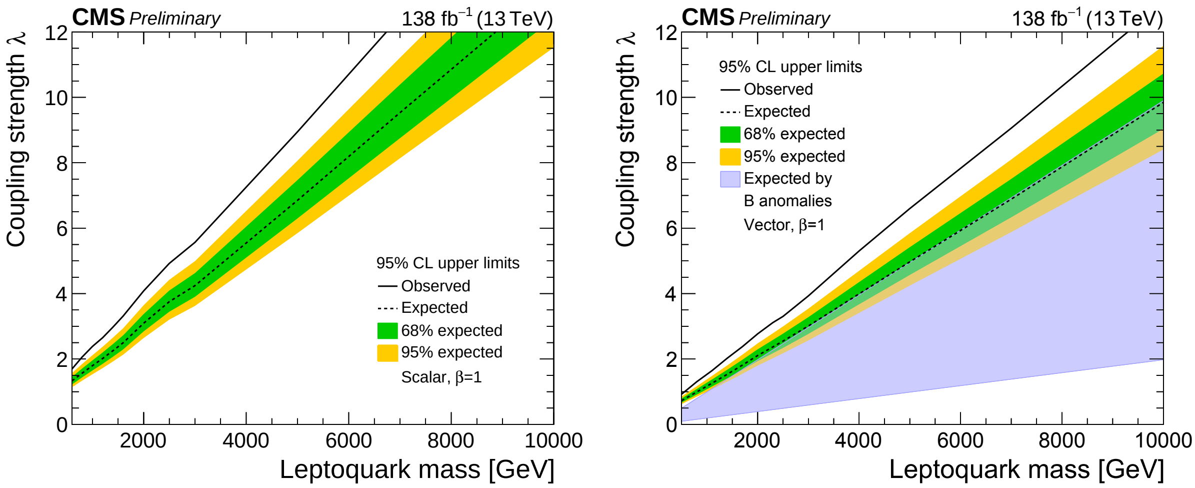

Figure 13.10: The observed and expected upper limits at 95% CL on the coupling strength λ of a scalar- (left) and vector-LQ model (right) determined by considering only the nonresonant production of two τ leptons through t-channel LQ exchange. The inner (green) band and the outer (yellow) band indicate the regions containing 68 and 95%, respectively, of the distribution of limits expected under the background-only hypothesis. The region with blue shading shows the parameter space preferred by one of the models proposed to explain anomalies observed in B physics, see Eq. (7.11) and Ref. [113].

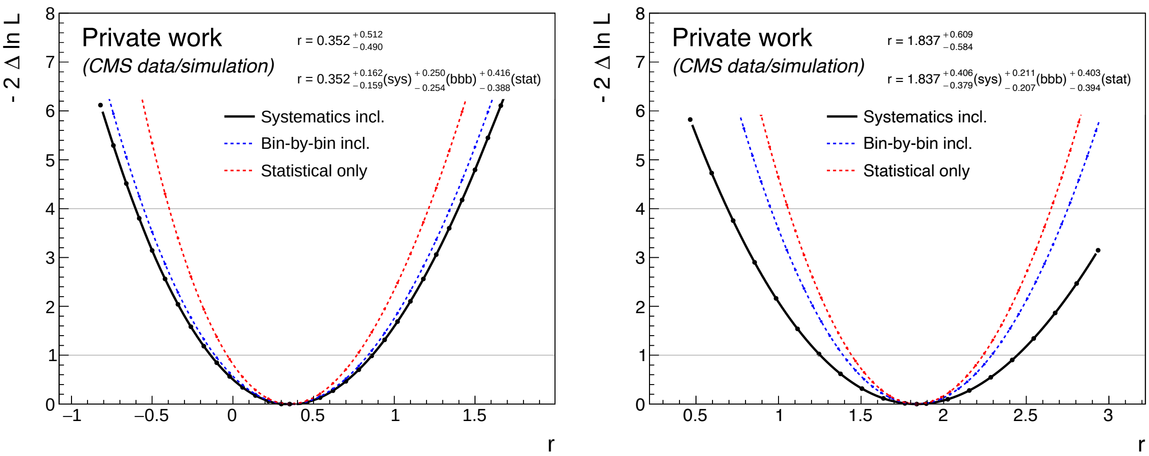

Figure 13.11: The negative log likelihood profiles in the signal strength r for the total vector-LQ signal assuming $\kappa = 1$. The total statistical and systematic uncertainty (black) is broken down into statistical without bin-by-bin uncertainties (red), and statistical with bin-by-bin uncertainties (blue). The statistical component is obtained by fixing all nuisance parameters in the fit to the best-fit value. **Left**: $m_{\mathrm{LQ}} = 1400\,\mathrm{GeV}$ and $\lambda = 1$. **Right**: $m_{\mathrm{LQ}} = 2000\,\mathrm{GeV}$ and $\lambda = 2.5$. The fit is performed with the signal templates normalized to the expected upper limit on the cross section.

where $\hat{\theta}$ is the post-fit value of θ, and $\Delta\hat{\theta}$ is the post-fit uncertainty of one standard deviation. Furthermore, to study how the nuisance parameter θ is shifted by a fit to the data and how its uncertainties are constrained in this fit, we define the post-fit central value of θ that is normalized to the pre-fit values of θ:

$$p(\hat{\theta}) = \frac{\hat{\theta} - \theta_0}{\Delta\theta}, \tag{13.2}$$

where θ_0 is the central pre-fit value, and $\Delta\theta$ is the pre-fit uncertainty in $\theta = \theta_0$. Within the CMS Collaboration, this quantity is often referred to as the *pull* of θ. The pulls and impacts of the most important nuisance parameters are shown in Fig. 13.12. At lower values of masses and λ, the parameters that have the largest impact are the bin-by-bin uncertainties of the last $S_{\mathrm{T}}^{\mathrm{MET}}$ bins that have the most sensitivity to single and pair production. These are statistical in nature. At higher values of masses and λ, however, nuisance parameters related to τ_{h} systematic uncertainties become more important.

To further investigate the excess, the pulls of the most important systematics in background-only (B-only) and background-plus-signal (S+B) fits are compared in Figs. 13.13. Little difference between the background-only and S+B fit pulls is observed. The backgrounds are therefore already strongly constrained by the numerous low-purity regions, such as the $\mathrm{e}\mu$ channel, the 0b and $200 < m_{\mathrm{vis}} < 400\,\mathrm{GeV}$ categories, and the side bands of each distribution (i.e. low $S_{\mathrm{T}}^{\mathrm{MET}}$ and high χ).

There are also no strong correlations found between the nuisance parameters and signal strength r in the S+B fit, as is shown in Fig. 13.14 for two representative m_{LQ}-λ points. At lower values of mass and λ, the nuisance parameters with the strongest correlations (ρ) have $\rho > -0.38$. These are related to the bin-by-bin uncertainties of the most sensitive $S_{\mathrm{T}}^{\mathrm{MET}}$ bins in the $\tau_{\mathrm{h}}\tau_{\mathrm{h}}$ channel of the $\geq$1b category and are anti-correlated to r, as expected. At large values of masses and λ, the strongest (anti-)correlations are related to systematic shape uncertainties related to the SFs and energy scale of the τ lepton. As mentioned above, the backgrounds can be well constrained. Figure 13.15 also presents the correlation matrix of the $S_{\mathrm{T}}^{\mathrm{MET}}$ bins in the 2018 data set as a representative example. The matrices reveal no strong correlation between different $S_{\mathrm{T}}^{\mathrm{MET}}$ distributions in the same event category of the same year, or between the bins of the same $S_{\mathrm{T}}^{\mathrm{MET}}$. Most of the largest correlations between bins in different channels or categories are still well below 20%.

13.5 Discussion

Figure 13.16 shows a summary of lower limits on LQ masses from searches by CMS. ATLAS has set similar limits. Roughly speaking, most types of LQ-fermion couplings for scalar-LQ masses below 1 TeV have been excluded. The strongest limits are set on vector scenarios, of which most types are excluded below 1.5 (1.8) TeV for $\kappa = 0$ (1) as the cross sections tends to be considerably larger than for the scalar case.

Up until now, the most stringent limits on the production of an LQ couplings to a τ lepton and a bottom quark come from an analysis by the ATLAS Collaboration, in which a scalar (vector) LQ with mass below 1.25 (1.8) TeV was excluded in a search for LQ pair production [384]. The LQ search presented in this analysis achieves very similar limits. Previously, a search for single production of a scalar LQ with the same decay mode was also performed by the CMS Collaboration with just 2016 data, and is now superseded by the present search [385]. Other

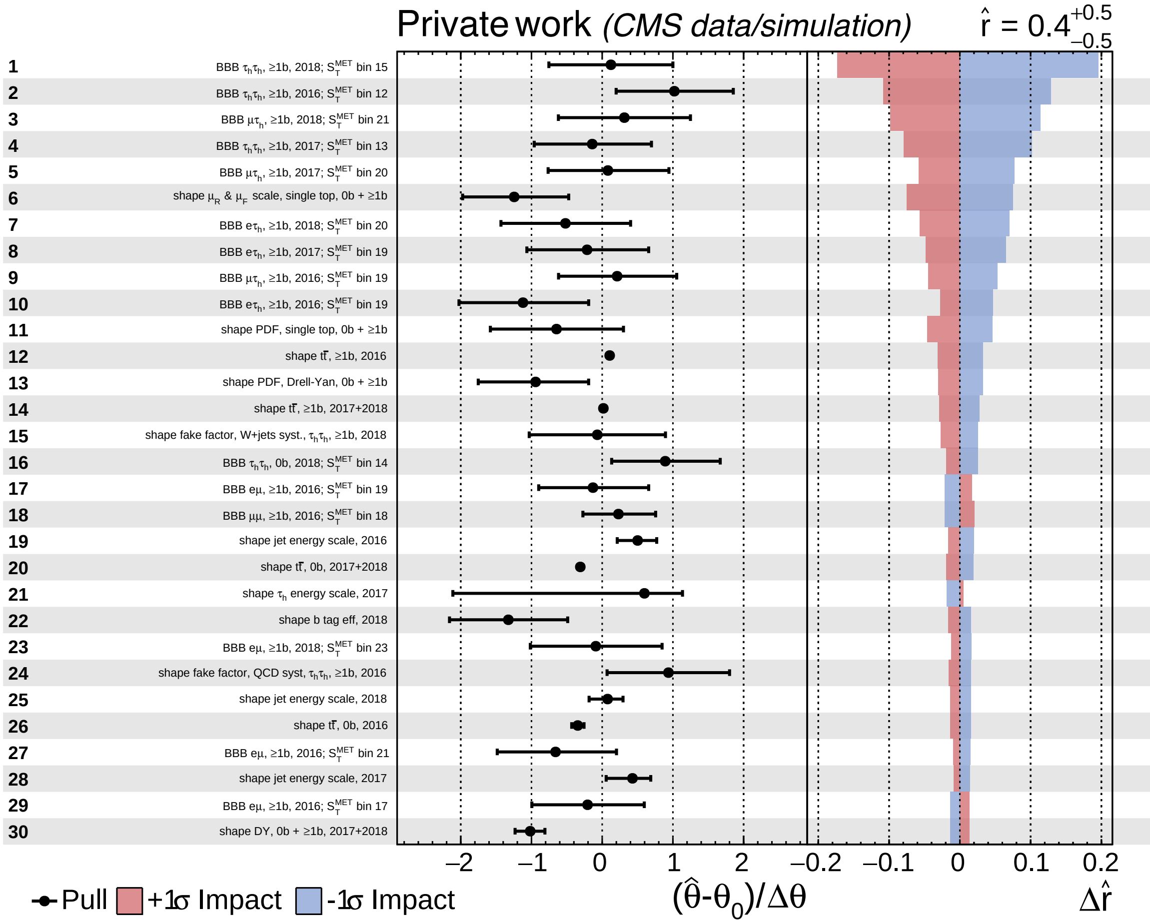

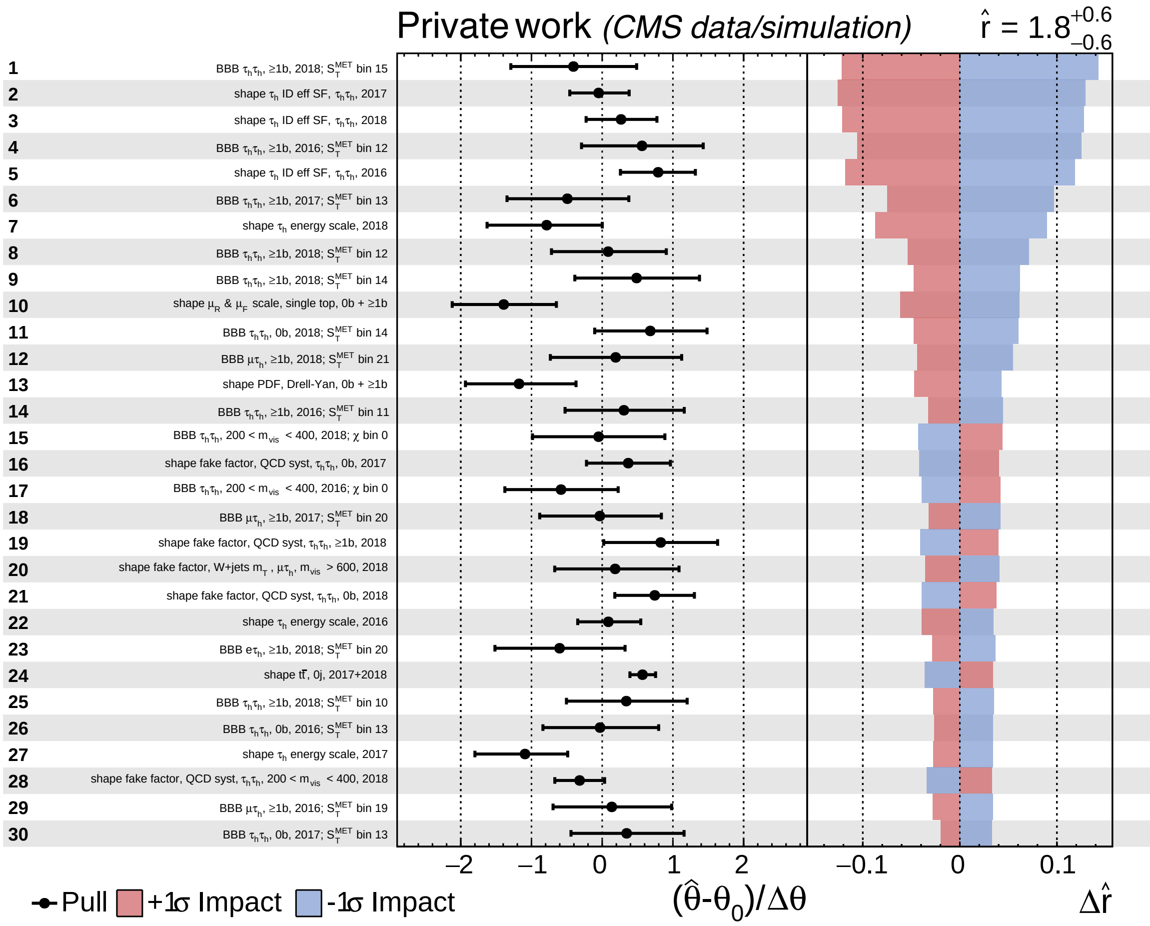

Figure 13.12: Pulls and impacts for the nuisance parameters with the largest impact in the measurement of the signal strength of the total vector-LQ signal in all categories. **Top**: $m_{\mathrm{LQ}} = 1400\,\mathrm{GeV}$ and $\lambda = 1$. **Bottom**: $m_{\mathrm{LQ}} = 2000\,\mathrm{GeV}$ and $\lambda = 2.5$. Note that the signal template is normalized to the expected upper limit on the cross section.

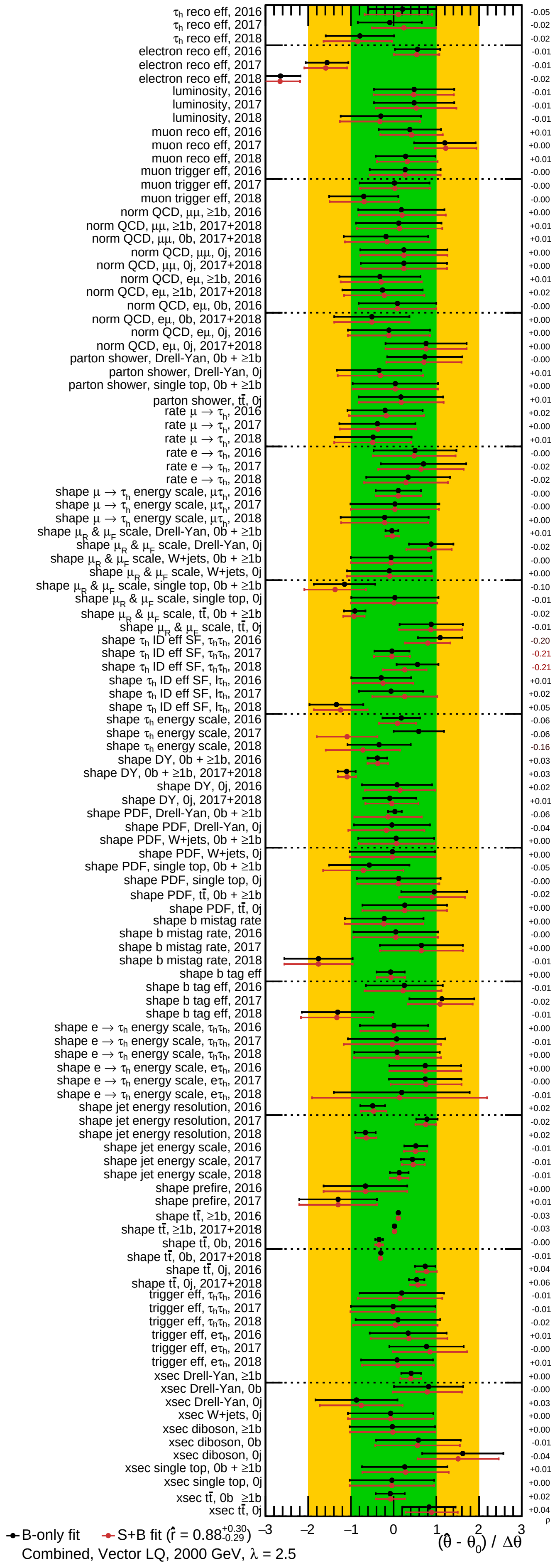

Figure 13.13: Background-only (black) and S+B pulls (red) of nuisance parameters representing systematic uncertainties in the fit of the signal strength of the total LQ signal in all categories observed with the full Run-2 data set. The values are shown for the vector model with mass 2000 GeV, $\lambda = 2.5$, and $\kappa = 1$. The signal template is normalized to the expected upper limit on the cross section.

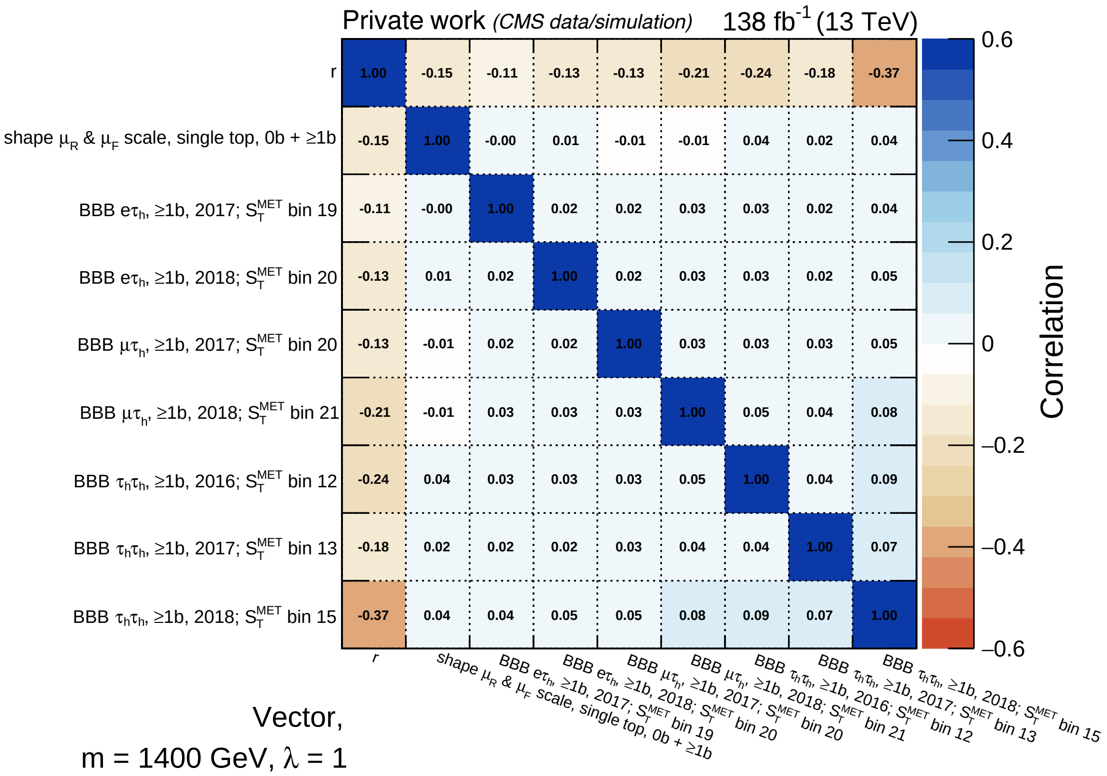

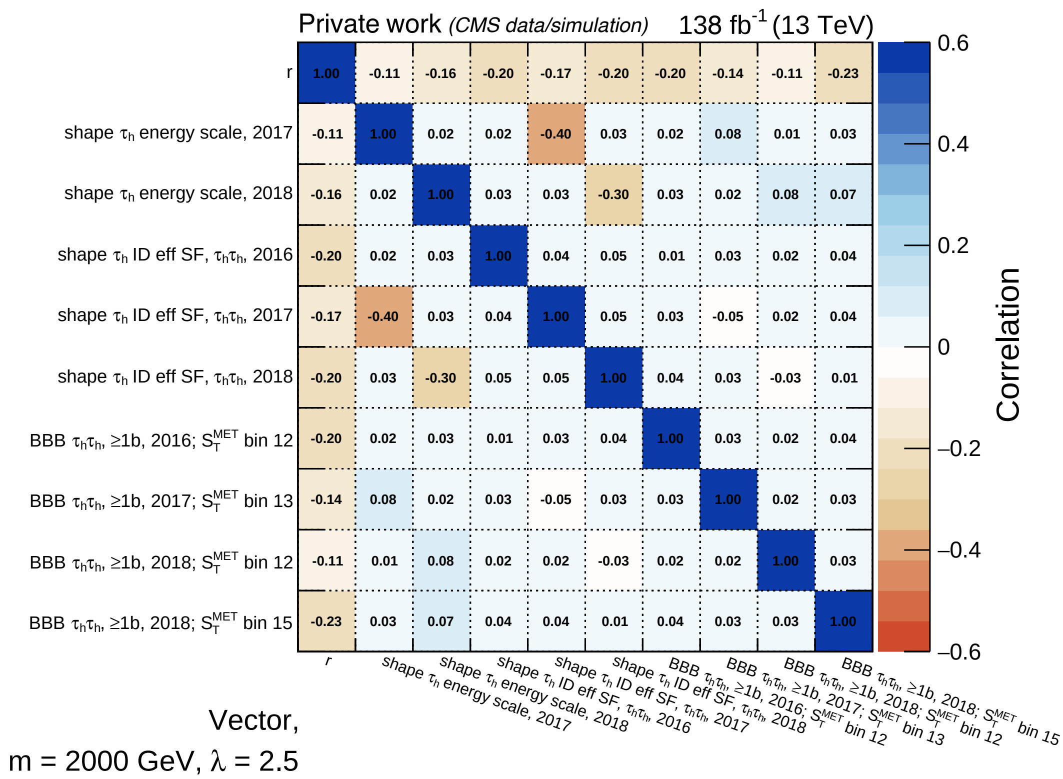

Figure 13.14: Correlation matrix of the nuisance parameters with the total signal strength r in all event categories. Only parameters with $\rho > 0.10$ are shown. **Top**: For $m_{\mathrm{LQ}} = 1400\,\mathrm{GeV}$ and $\lambda = 1$. **Bottom**: For $m_{\mathrm{LQ}} = 2000\,\mathrm{GeV}$ and $\lambda = 2.5$.

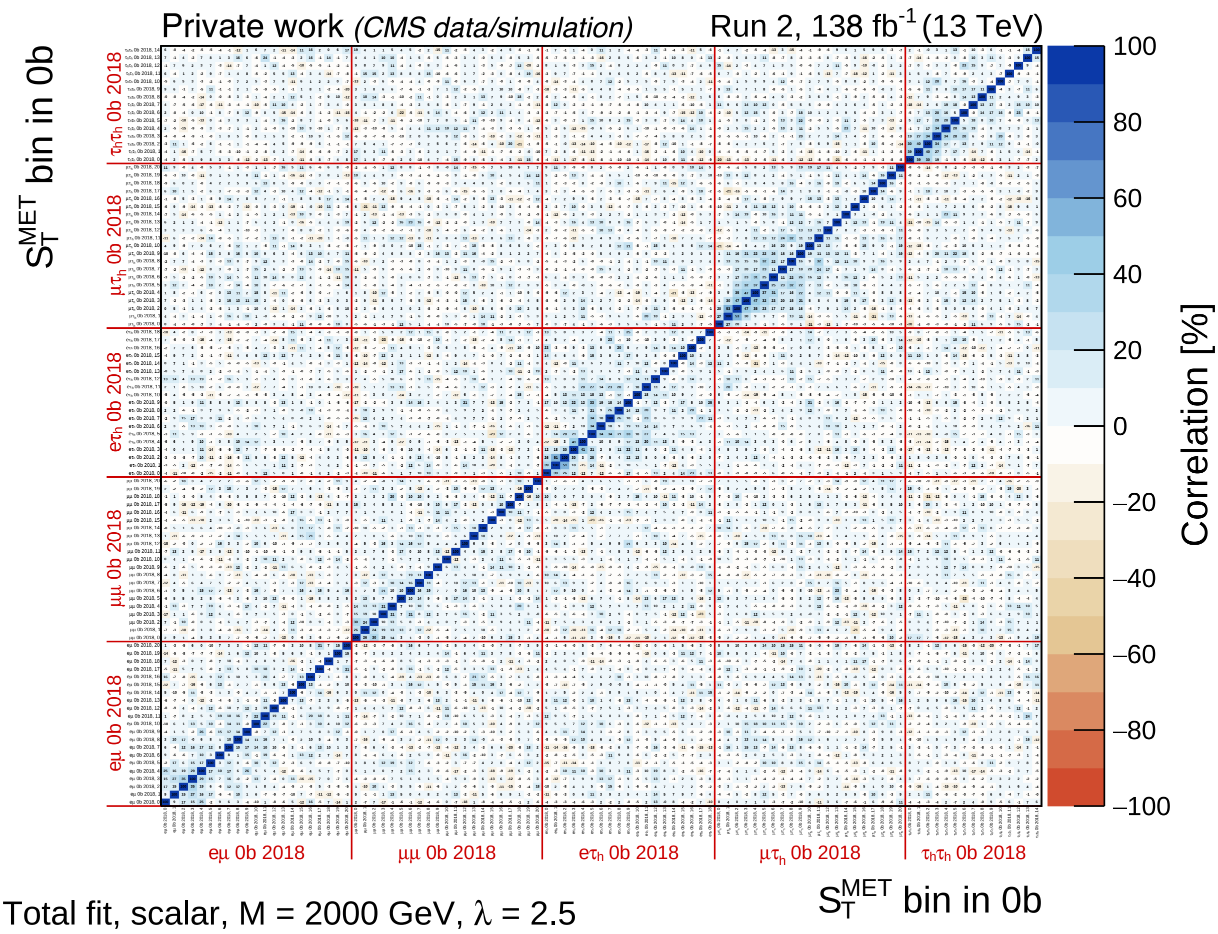

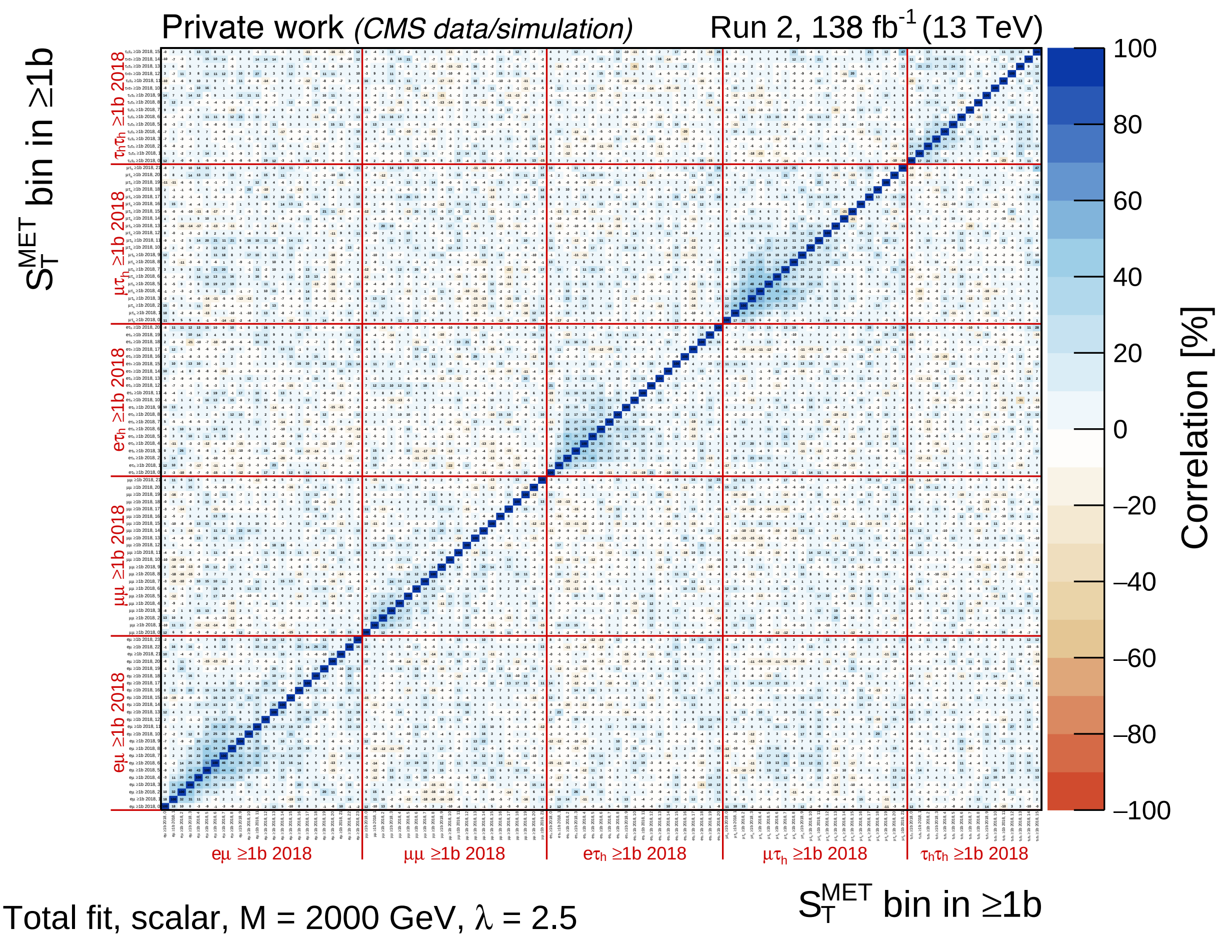

Figure 13.15: Correlation matrix between $S_{\mathrm{T}}^{\mathrm{MET}}$ bins in the same category of the 2018 data set for the fit of a scalar LQ with mass 2000 GeV and $\lambda = 2.5$. The correlation value between bins is written as a percentage in each cell.

searches for LQs decaying to a top quark and a τ lepton or neutrino exploiting the full LHC 2016–2018 data set have been performed by CMS [341, 386] and ATLAS [384, 387].

A search for a nonresonant $\tau\tau$ production through the t-channel exchange of a vector-LQ has also been performed in Ref. [371]. An important difference with the analysis presented in this thesis is the event categorization. Ref. [371] uses a "no b tag" category, which is inclusive in terms of jet selections and vetoes events with a b-tagged jet of $p_\mathrm{T} > 30\,\mathrm{GeV}$, while the "0b" category of the analysis presented in this thesis requires at least one jet with $p_\mathrm{T} > 50\,\mathrm{GeV}$, and also includes the "0j" category with a jet veto. The other difference is the signal model used; Ref. [371] uses two benchmarks for several LQ-fermion couplings as fitted to the B anomalies by Ref. [113], while the present analysis considers exclusively the LQ-bτ coupling. The independent analysis group has found consistent results in terms of the exclusion limits and the excess reported above when applying similar event categorization and selection, and using a similar LQ model.

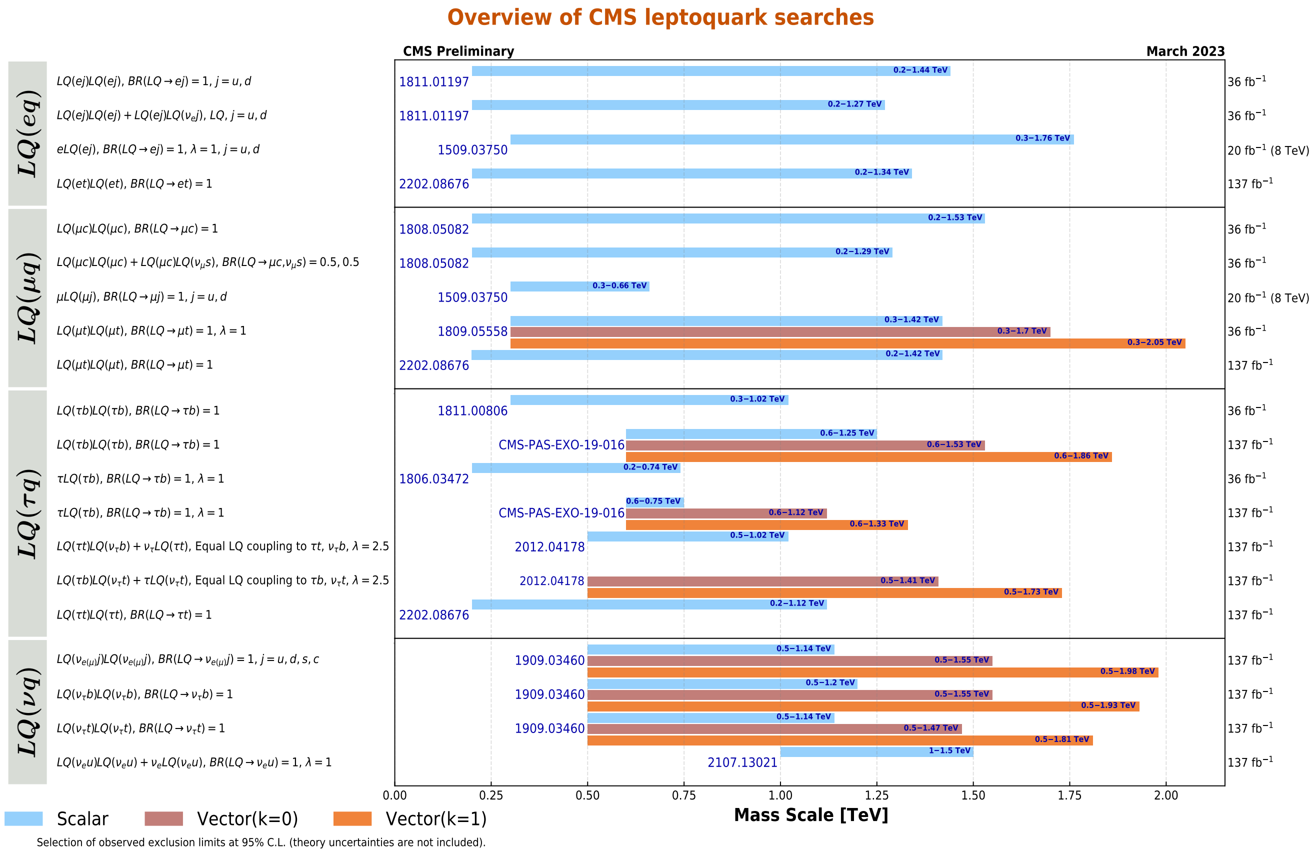

Figure 13.16: Summary plot of limits on LQ mass for various coupling scenarios, from searches by the CMS Collaboration using proton-proton collision data collected. Taken from Ref. [383].

14 Conclusions

Despite the many remarkable successes of the Standard Model (SM) of particle physics, there are both theoretical and experimental reasons that imply the SM is not the final and most fundamental theory of nature. One of the most striking features of the SM are the three generations of quarks and leptons, which on the one hand seem very symmetric, but on the other hand form a hierarchical mass pattern. This could suggest something about the underlying physics beyond the SM, which might preferentially couple to the third-generation fermions. Meanwhile, on the experimental side, some anomalies have emerged in tests of the universality of lepton flavor that could reveal the violation of lepton flavor universality. In particular, the experimental evidence from measurements of $R\big(\mathrm{D}^{(*)}\big)$ points to new physics interactions that couple preferentially to third-generation fermions like bottom quarks and τ leptons.

Models that propose a new particle called the leptoquark (LQ) are strongly motivated as a possible explanation for these flavor anomalies, and could be discovered directly in proton-proton (pp) collisions collected by the CMS or ATLAS experiments. This new type of boson emerges naturally from many extensions of the SM, such as grand unification theories, which unify the fermions under some larger symmetry group, or theories invoking technicolor, compositeness, or supersymmetry. They could therefore reveal the underlying connection between quarks and leptons and explain the observed flavor symmetries, as well as the hierarchical mass pattern.

This thesis presents a combined search targeting the signal of the single and pair production of an LQ that decay exclusively to a τ lepton and a bottom quark, as well as a novel search for the exchange of an LQ by b quarks that produces a τ lepton pair. This is done by targeting the $\tau\tau$ decay channels, and creating several event categories based on the number of jets and heavy-flavored jets. Preliminary results of this LQ $\to$ bτ search have been presented. These have been made public in Ref. [368], and the full analysis will soon be published.

The search for an LQ coupling to a τ lepton and b quark uses pp collision data corresponding to an integrated luminosity of $138\,\mathrm{fb}^{-1}$, collected at a center-of-mass energy of $13\,\mathrm{TeV}$, and recorded with the CMS detector. Upper limits are set on the production cross section of third-generation scalar and vector LQs as a function of the LQ mass, and results are compared with theoretical predictions to obtain lower limits on the LQ mass. At 95% confidence level, third-generation LQs decaying to a τ lepton and a b quark with unit coupling are excluded for masses below $1.25\,\mathrm{TeV}$ for a scalar model, and below 1.53 $(1.86)\,\mathrm{TeV}$ for a vector model with nonminimal coupling $\kappa = 0$ (1). At $\lambda = 2.5$, the lower limits are $1.37\,\mathrm{TeV}$ for a scalar model, and 1.86 $(1.96)\,\mathrm{TeV}$ for a vector model with $\kappa = 0$ (1). Upper limits are also set on the coupling strength of such LQs as a function of their mass. Due to the inclusion of the nonresonant LQ exchange processes, this analysis was able to set constraints on LQs with masses up to $10\,\mathrm{TeV}$, much higher than can be produced directly at the LHC.

The observed data agree with the standard model expectation within 2 standard deviations below a coupling strength of $\lambda = 1.5$. However, for a representative LQ mass of $2\,\mathrm{TeV}$ and a coupling strength of 2.5, an excess with a significance of 3.4 standard deviations above the standard model expectation is observed in the data. Consequently, the observed upper limits on the LQ production cross section are about three times larger than expected for this benchmark.

As hadronic decays of the τ lepton (τ_h) are an important part of physics analyses like the search for an LQ coupling to a b quark and a τ lepton, dedicated algorithms have been developed to reconstruct and identify τ_h decays with high efficiency, while suppressing the large background of objects that is misreconstructed or misidentified. This thesis has also presented the measurements of the corrections to simulated τ_h candidates that are needed to ensure sufficient modeling of the data in order to search for new physics.

References

[1] L. M. Brown, M. Dresden, L. H. Hoddeson, and M. West, eds., "Proceedings, 2nd International Symposium on on the History of Particle Physics in the 1950s: Pions to Quarks: Batavia, USA, May 1-4, 1985". Univ. Pr., Cambridge, UK, (1989).

[2] L. H. Hoddeson, L. Brown, M. Riordan, and M. Dresden, eds., "The Rise of the standard model: Particle physics in the 1960s and 1970s. Proceedings, Conference, Stanford, USA, June 24-27, 1992". (1997).

[3] D. Griffiths, "Introduction to Elementary Particles". Wiley-VCH, 2 edition, 2008. ISBN 978-3-527-40601-2.

[4] Mountain Empire High School, Pine Valley, California, "Particle Physics Timeline", `https://particleadventure.org/other/history/index.html`, 1996. (Retrieved Jul 20, 2017).

[5] A. Pais, "Some Remarks on the V-Particles", *Phys. Rev.* **86** (1952) 663, `doi:10.1103/PhysRev.86.663`.

[6] M. Gell-Mann, "A Schematic Model of Baryons and Mesons", *Phys. Lett.* **8** (1964) 214, `doi:10.1016/S0031-9163(64)92001-3`.

[7] G. Zweig, "An SU(3) model for strong interaction symmetry and its breaking. Version 1",.

[8] V. E. Barnes et al., "Observation of a Hyperon with Strangeness Minus Three", *Phys. Rev. Lett.* **12** (1964) 204, `doi:10.1103/PhysRevLett.12.204`.

[9] **E598** Collaboration, "Experimental Observation of a Heavy Particle J", *Phys. Rev. Lett.* **33** (1974) 1404, `doi:10.1103/PhysRevLett.33.1404`.

[10] **SLAC-SP-017** Collaboration, "Discovery of a Narrow Resonance in e^+e^- Annihilation", *Phys. Rev. Lett.* **33** (1974) 1406, `doi:10.1103/PhysRevLett.33.1406`.

[11] **E288** Collaboration, "Observation of a Dimuon Resonance at 9.5-GeV in 400-GeV Proton-Nucleus Collisions", *Phys. Rev. Lett.* **39** (1977) 252, `doi:10.1103/PhysRevLett.39.252`.

[12] **Super-Kamiokande** Collaboration, "Search for proton decay via $p \to e^+\pi^0$ and $p \to \mu^+\pi^0$ with an enlarged fiducial volume in Super-Kamiokande I-IV", *Phys. Rev. D* **102** (2020), no. 11, 112011, `doi:10.1103/PhysRevD.102.112011`, `arXiv:2010.16098`.

[13] **Particle Data** Group, "Review of Particle Physics", *PTEP* **2022** (2022) 083C01, `doi:10.1093/ptep/ptac097`.

[14] F. Reines and C. L. Cowan, "Detection of the free neutrino", *Phys. Rev.* **92** (1953) 830, `doi:10.1103/PhysRev.92.830`.

[15] S. Weinberg, "A Model of Leptons", *Phys. Rev. Lett.* **19** (1967) 1264, `doi:10.1103/PhysRevLett.19.1264`.

[16] **UA1** Collaboration, "Experimental Observation of Isolated Large Transverse Energy Electrons with Associated Missing Energy at $\sqrt{s} = 540$ GeV", *Phys. Lett. B* **122** (1983) 103, doi:10.1016/0370-2693(83)91177-2.

[17] **UA1** Collaboration, "Experimental Observation of Lepton Pairs of Invariant Mass Around 95 GeV/c^2 at the CERN SPS Collider", *Phys. Lett. B* **126** (1983) 398, doi:10.1016/0370-2693(83)90188-0.

[18] C. S. Wu et al., "Experimental Test of Parity Conservation in β Decay", *Phys. Rev.* **105** (1957) 1413, doi:10.1103/PhysRev.105.1413.

[19] G. Backenstoss et al., "Helicity of mu- Mesons from pi-Meson Decay", *Phys. Rev. Lett.* **6** (1961) 415, doi:10.1103/PhysRevLett.6.415.

[20] M. Bardon, P. Franzini, and J. Lee, "Helicity of μ^- Mesons: Mott Scattering of Polarized Muons", *Phys. Rev. Lett.* **7** (1961) 23, doi:10.1103/PhysRevLett.7.23.

[21] **TWIST** Collaboration, "Measurement of the Michel parameter rho in muon decay", *Phys. Rev. Lett.* **94** (2005) 101805, doi:10.1103/PhysRevLett.94.101805, arXiv:hep-ex/0409063.

[22] **PiENu** Collaboration, "Improved Measurement of the $\pi \to e\nu$ Branching Ratio", *Phys. Rev. Lett.* **115** (2015), no. 7, 071801, doi:10.1103/PhysRevLett.115.071801, arXiv:1506.05845.

[23] N. Cabibbo, "Unitary Symmetry and Leptonic Decays", *Phys. Rev. Lett.* **10** (1963) 531, doi:10.1103/PhysRevLett.10.531.

[24] S. L. Glashow, J. Iliopoulos, and L. Maiani, "Weak Interactions with Lepton-Hadron Symmetry", *Phys. Rev. D* **2** (1970) 1285, doi:10.1103/PhysRevD.2.1285.

[25] M. Gell-Mann and A. Pais, "Behavior of neutral particles under charge conjugation", *Phys. Rev.* **97** (1955) 1387, doi:10.1103/PhysRev.97.1387.

[26] J. H. Christenson, J. W. Cronin, V. L. Fitch, and R. Turlay, "Evidence for the 2π Decay of the K_2^0 Meson", *Phys. Rev. Lett.* **13** (1964) 138, doi:10.1103/PhysRevLett.13.138.

[27] M. Kobayashi and T. Maskawa, "CP Violation in the Renormalizable Theory of Weak Interaction", *Prog. Theor. Phys.* **49** (1973) 652, doi:10.1143/PTP.49.652.

[28] **CDF** Collaboration, "Observation of top quark production in $\bar{p}p$ collisions", *Phys. Rev. Lett.* **74** (1995) 2626, doi:10.1103/PhysRevLett.74.2626, arXiv:hep-ex/9503002.

[29] **D0** Collaboration, "Observation of the top quark", *Phys. Rev. Lett.* **74** (1995) 2632, doi:10.1103/PhysRevLett.74.2632, arXiv:hep-ex/9503003.

[30] **DONUT** Collaboration, "Observation of tau neutrino interactions", *Phys. Lett. B* **504** (2001) 218, doi:10.1016/S0370-2693(01)00307-0, arXiv:hep-ex/0012035.

[31] **ALEPH** Collaboration, "Determination of the Number of Light Neutrino Species", *Phys. Lett. B* **231** (1989) 519, doi:10.1016/0370-2693(89)90704-1.

[32] E. Eichten, K. D. Lane, and M. E. Peskin, "New Tests for Quark and Lepton Substructure", *Phys. Rev. Lett.* **50** (1983) 811, doi:10.1103/PhysRevLett.50.811.

[33] **CMS** Collaboration, "A portrait of the Higgs boson by the CMS experiment ten years after the discovery", *Nature* **607** (2022), no. 7917, 60,

doi:10.1038/s41586-022-04892-x, arXiv:2207.00043.

[34] **CMS** Collaboration, "CMS Higgs Physics Results", https://twiki.cern.ch/twiki/bin/view/CMSPublic/PhysicsResultsHIG, 2022. (Retrieved Jan 16, 2023).

[35] F. Englert and R. Brout, "Broken Symmetry and the Mass of Gauge Vector Mesons", *Phys. Rev. Lett.* **13** (1964) 321, doi:10.1103/PhysRevLett.13.321.

[36] P. W. Higgs, "Broken Symmetries and the Masses of Gauge Bosons", *Phys. Rev. Lett.* **13** (1964) 508, doi:10.1103/PhysRevLett.13.508.

[37] **CMS** Collaboration, "Observation of a new boson at a mass of 125 GeV with the CMS experiment at the LHC", *Phys. Lett. B* **716** (2012) 30, doi:10.1016/j.physletb.2012.08.021, arXiv:1207.7235.

[38] **ATLAS** Collaboration, "Observation of a new particle in the search for the Standard Model Higgs boson with the ATLAS detector at the LHC", *Phys. Lett. B* **716** (2012) 1, doi:10.1016/j.physletb.2012.08.020, arXiv:1207.7214.

[39] **CMS** Collaboration, "Observation of a new boson with mass near 125 GeV in pp collisions at $\sqrt{s} = 7$ and 8 TeV", *JHEP* **06** (2013) 081, doi:10.1007/JHEP06(2013)081, arXiv:1303.4571.

[40] **ATLAS** and **CMS** Collaborations, "Combined Measurement of the Higgs Boson Mass in pp Collisions at $\sqrt{s} = 7$ and 8 TeV with the ATLAS and CMS Experiments", *Phys. Rev. Lett.* **114** (2015) 114, doi:10.1103/PhysRevLett.114.191803, arXiv:1503.07589.

[41] A. Ferrari and N. Rompotis, "Exploration of Extended Higgs Sectors with Run-2 Proton–Proton Collision Data at the LHC", *Symmetry* **13** (2021), no. 11, 2144, doi:10.3390/sym14081546. [Erratum: Symmetry 14, 1546 (2022)].

[42] Wikimedia Commons, "File:Standard Model of Elementary Particles.svg — Wikimedia Commons, the free media repository", https://commons.wikimedia.org/wiki/File:Standard_Model_of_Elementary_Particles.svg, 2023. (Retrieved Jan 13, 2023).

[43] J. R. Ellis, G. L. Fogli, and E. Lisi, "The Top quark and Higgs boson masses in the standard model and the MSSM", *Phys. Lett. B* **333** (1994) 118, doi:10.1016/0370-2693(94)91016-2.

[44] **ALEPH**, **CDF**, **D0**, **DELPHI**, **L3**, **OPAL**, and **SLD** Collaborations, and LEP Electroweak Working Group, Tevatron Electroweak Working Group, and SLD Electroweak and Heavy Flavour Groups, "Precision Electroweak Measurements and Constraints on the Standard Model", arXiv:1012.2367.

[45] **ATLAS** Collaboration, "A detailed map of Higgs boson interactions by the ATLAS experiment ten years after the discovery", *Nature* **607** (2022), no. 7917, 52, doi:10.1038/s41586-022-04893-w, arXiv:2207.00092. [Erratum: Nature 612, E24 (2022)].

[46] E. J. Konopinski and H. M. Mahmoud, "The Universal Fermi interaction", *Phys. Rev.* **92** (1953) 1045, doi:10.1103/PhysRev.92.1045.

[47] B. Pontecorvo, "Electron and Muon Neutrinos", *Zh. Eksp. Teor. Fiz.* **37** (1959) 1751.

[48] T. D. Lee, "Intermediate boson hypothesis of weak interactions", in *Proceedings, 10th International Conference on High-Energy Physics (ICHEP 60)*, p. 567. U. Rochester, Rochester, 1960.

[49] **Super-Kamiokande** Collaboration, "Evidence for oscillation of atmospheric neutrinos", *Phys. Rev. Lett.* **81** (1998) 1562, `doi:10.1103/PhysRevLett.81.1562`, `arXiv:hep-ex/9807003`.

[50] J. Schwichtenberg, "Physics from Symmetry". Undergraduate Lecture Notes in Physics. Springer International Publishing, Cham, 2018. `doi:10.1007/978-3-319-66631-0`, ISBN 978-3-319-66630-3, 978-3-319-66631-0.

[51] A. Jain, "Notes on symmetries in particle physics", `arXiv:2109.12087`.

[52] **Super-Kamiokande** Collaboration, "Search for Differences in Oscillation Parameters for Atmospheric Neutrinos and Antineutrinos at Super-Kamiokande", *Phys. Rev. Lett.* **107** (2011) 241801, `doi:10.1103/PhysRevLett.107.241801`, `arXiv:1109.1621`.

[53] **BASE** Collaboration, "A parts-per-billion measurement of the antiproton magnetic moment", *Nature* **550** (2017), no. 7676, 371, `doi:10.1038/nature24048`.

[54] A. Di Domenico, "Testing CPT Symmetry with Neutral K Mesons: A Review", *Symmetry* **12** (2020), no. 12, 2063, `doi:10.3390/sym12122063`.

[55] M. S. Sozzi, "Tests of discrete symmetries", *J. Phys. G* **47** (2020), no. 1, 013001, `doi:10.1088/1361-6471/ab4822`.

[56] G. Isidori, "Lectures notes on Flavour physics", `https://www.physik.uzh.ch/en/groups/isidori/teaching.html`, 2016. (Retrieved Nov 16, 2022).

[57] R. S. Chivukula and H. Georgi, "Composite Technicolor Standard Model", *Phys. Lett. B* **188** (1987) 99, `doi:10.1016/0370-2693(87)90713-1`.

[58] G. D'Ambrosio, G. F. Giudice, G. Isidori, and A. Strumia, "Minimal flavor violation: An Effective field theory approach", *Nucl. Phys. B* **645** (2002) 155, `doi:10.1016/S0550-3213(02)00836-2`, `arXiv:hep-ph/0207036`.

[59] G. Isidori, Y. Nir, and G. Perez, "Flavor Physics Constraints for Physics Beyond the Standard Model", *Ann. Rev. Nucl. Part. Sci.* **60** (2010) 355, `doi:10.1146/annurev.nucl.012809.104534`, `arXiv:1002.0900`.

[60] G. 't Hooft, "Symmetry Breaking Through Bell-Jackiw Anomalies", *Phys. Rev. Lett.* **37** (1976) 8, `doi:10.1103/PhysRevLett.37.8`.

[61] M. Ardu and G. Pezzullo, "Introduction to Charged Lepton Flavor Violation", *Universe* **8** (2022), no. 6, 299, `doi:10.3390/universe8060299`, `arXiv:2204.08220`.

[62] M. E. Peskin and D. V. Schroeder, "An Introduction to quantum field theory". Addison-Wesley, Reading, USA, 1995. ISBN 978-0-201-50397-5.

[63] J. Heeck, "Interpretation of Lepton Flavor Violation", *Phys. Rev. D* **95** (2017), no. 1, 015022, `doi:10.1103/PhysRevD.95.015022`, `arXiv:1610.07623`.

[64] S. T. Petcov, "The Processes $\mu \to e + \gamma, \mu \to e + \overline{e}, \nu' \to \nu + \gamma$ in the Weinberg-Salam Model with Neutrino Mixing", *Sov. J. Nucl. Phys.* **25** (1977) 340. [Erratum:

Sov.J.Nucl.Phys. 25, 698 (1977), Erratum: Yad.Fiz. 25, 1336 (1977)].

[65] S. M. Bilenky, S. T. Petcov, and B. Pontecorvo, “Lepton Mixing, mu –> e + gamma Decay and Neutrino Oscillations”, *Phys. Lett. B* **67** (1977) 309, `doi:10.1016/0370-2693(77)90379-3`.

[66] T.-P. Cheng and L.-F. Li, “Muon Number Nonconservation Effects in a Gauge Theory with V A Currents and Heavy Neutral Leptons”, *Phys. Rev. D* **16** (1977) 1425, `doi:10.1103/PhysRevD.16.1425`.

[67] B. W. Lee and R. E. Shrock, “Natural Suppression of Symmetry Violation in Gauge Theories: Muon - Lepton and Electron Lepton Number Nonconservation”, *Phys. Rev. D* **16** (1977) 1444, `doi:10.1103/PhysRevD.16.1444`.

[68] R. H. Bernstein and P. S. Cooper, “Charged Lepton Flavor Violation: An Experimenter’s Guide”, *Phys. Rept.* **532** (2013) 27, `doi:10.1016/j.physrep.2013.07.002`, `arXiv:1307.5787`.

[69] **NNPDF** Collaboration, “Parton distributions from high-precision collider data”, *Eur. Phys. J. C* **77** (2017), no. 10, 663, `doi:10.1140/epjc/s10052-017-5199-5`, `arXiv:1706.00428`.

[70] E. D. Bloom et al., “High-Energy Inelastic e^{-}p Scattering at 6° and 10°”, *Phys. Rev. Lett.* **23** (1969) 930, `doi:10.1103/PhysRevLett.23.930`.

[71] M. Breidenbach et al., “Observed Behavior of Highly Inelastic Electron-Proton Scattering”, *Phys. Rev. Lett.* **23** (1969) 935, `doi:10.1103/PhysRevLett.23.935`.

[72] **ZEUS** and **H1** Collaborations, “Combination of measurements of inclusive deep inelastic $e^{\pm}$p scattering cross sections and QCD analysis of HERA data”, *Eur. Phys. J. C* **75** (2015), no. 12, 580, `doi:10.1140/epjc/s10052-015-3710-4`, `arXiv:1506.06042`.

[73] R. P. Feynman, “The Behavior of Hadron Collisions at Extreme Energies”, in *High Energy Collisions: Third International Conference*, p. 237. Stony Brook, N.Y., U.S.A., 1969.

[74] J. D. Bjorken and E. A. Paschos, “Inelastic Electron-Proton and γ-Proton Scattering and the Structure of the Nucleon”, *Phys. Rev.* **185** (1969) 1975, `doi:10.1103/PhysRev.185.1975`.

[75] J. M. Campbell, J. W. Huston, and W. J. Stirling, “Hard Interactions of Quarks and Gluons: A Primer for LHC Physics”, *Rept. Prog. Phys.* **70** (2007) 89, `doi:10.1088/0034-4885/70/1/R02`, `arXiv:hep-ph/0611148`.

[76] R. Placakyte, “Parton Distribution Functions”, in *Proceedings, 31st International Conference on Physics in collisions (PIC 2011)*. Vancouver, Canada, 2011. `arXiv:1111.5452`.

[77] **ALICE** Collaboration, “Parton distributions for the LHC”, *Eur. Phys. J. C* **63** (2009) 189, `doi:10.1140/epjc/s10052-009-1072-5`, `arXiv:0901.0002`.

[78] **ALICE** Collaboration, “Measurement of inelastic, single- and double-diffraction cross sections in proton–proton collisions at the LHC with ALICE”, *Eur. Phys. J. C* **73** (2013), no. 6, 2456, `doi:10.1140/epjc/s10052-013-2456-0`, `arXiv:1208.4968`.

[79] S. H. Stark, "Measurements of the elastic, inelastic and total pp cross sections with the ATLAS, CMS and TOTEM detectors", in *EPJ Web Conf.*, volume 141, p. 03007. 2017. doi:10.1051/epjconf/201714103007.

[80] **CMS** Collaboration, "Measurement of the inelastic proton-proton cross section at $\sqrt{s} = 13$ TeV", *JHEP* **07** (2018) 161, doi:10.1007/JHEP07(2018)161, arXiv:1802.02613.

[81] **ATLAS** Collaboration, "Measurement of the Inelastic Proton-Proton Cross Section at $\sqrt{s} = 13\,\text{TeV}$ with the ATLAS Detector at the LHC", *Phys. Rev. Lett.* **117** (2016) 182002, doi:10.1103/PhysRevLett.117.182002, arXiv:1606.02625.

[82] T. Regge, "Introduction to complex orbital momenta", *Il Nuovo Cimento Series 10* **14** (1959) 951.

[83] P. Collins, "An introduction to Regge theory and high energy physics". Cambridge University Press, Cambridge, 1977.

[84] O. Nachtmann, "Pomeron physics and QCD", in *Proceedings, Ringberg Workshop on New Trends in HERA Physics 2003*, p. 253. Ringberg Castle, Tegernsee, Germany, 2004. arXiv:0312279. doi:10.1142/9789812702722_0023.

[85] J. C. Collins and D. E. Soper, "The Theorems of Perturbative QCD", *Ann. Rev. Nucl. Part. Sci.* **37** (1987) 383, doi:10.1146/annurev.ns.37.120187.002123.

[86] J. C. Collins, D. E. Soper, and G. F. Sterman, "Factorization of Hard Processes in QCD", *Adv. Ser. Direct. High Energy Phys.* **5** (1989) 11, doi:10.1142/9789814503266_0001, arXiv:hep-ph/0409313.

[87] J. Stirling, "Parton Luminosity and Cross Section Plots". http://www.hep.ph.ic.ac.uk/~wstirlin/plots/plots.html. (Retrieved Jul 22, 2017).

[88] **CMS** Collaboration, "Summaries of CMS cross section measurements". https://twiki.cern.ch/twiki/bin/view/CMSPublic/PhysicsResultsCombined. (Retrieved Dec 30, 2022).

[89] J. M. Butterworth, G. Dissertori, and G. P. Salam, "Hard Processes in Proton-Proton Collisions at the Large Hadron Collider", *Ann. Rev. Nucl. Part. Sci.* **62** (2012) 387, doi:10.1146/annurev-nucl-102711-094913, arXiv:1202.0583.

[90] T. Aoyama, M. Hayakawa, T. Kinoshita, and M. Nio, "Tenth-Order QED Contribution to the Electron g-2 and an Improved Value of the Fine Structure Constant", *Phys. Rev. Lett.* **109** (2012) 111807, doi:10.1103/PhysRevLett.109.111807, arXiv:1205.5368.

[91] T. Aoyama, M. Hayakawa, T. Kinoshita, and M. Nio, "Tenth-Order Electron Anomalous Magnetic Moment — Contribution of Diagrams without Closed Lepton Loops", *Phys. Rev. D* **91** (2015), no. 3, 033006, doi:10.1103/PhysRevD.91.033006,10.1103/PhysRevD.96.019901, arXiv:1412.8284. [Erratum: Phys. Rev. D96, no.1, 019901 (2017)].

[92] M. Nio, "QED tenth-order contribution to the electron anomalous magnetic moment and a new value of the fine-structure constant", Fundamental Constants Meeting, Eltville, Germany, 2015. http://www.bipm.org/cc/CODATA-TGFC/Allowed/2015-02/Nio.pdf.

[93] D. Hanneke, S. Fogwell, and G. Gabrielse, "New Measurement of the Electron Magnetic Moment and the Fine Structure Constant", *Phys. Rev. Lett.* **100** (2008) 120801, doi:10.1103/PhysRevLett.100.120801, arXiv:0801.1134.

[94] S. Dimopoulos, "LHC, SSC and the universe", *Phys. Lett. B* **246** (1990), no. 3, 347, doi:10.1016/0370-2693(90)90612-A.

[95] **Planck** Collaboration, "Planck 2013 results", *Astron. Astrophys.* **571** (2014) A1, doi:10.1051/0004-6361/201321529, arXiv:1303.5062.

[96] **Planck** Collaboration, "Planck 2015 results", *Astron. Astrophys.* **594** (2016) A1, doi:10.1051/0004-6361/201527101, arXiv:1502.01582.

[97] L. Bergström, "Nonbaryonic dark matter: Observational evidence and detection methods", *Rept. Prog. Phys.* **63** (2000) 793, doi:10.1088/0034-4885/63/5/2r3, arXiv:hep-ph/0002126.

[98] V. C. Rubin, W. K. Ford, Jr., and N. Thonnard, "Rotational properties of 21 SC galaxies with a large range of luminosities and radii, from NGC 4605 ($R = 4$ kpc) to UGC 2885 ($R = 122$ kpc)", *Astrophysical J.* **283** (1980) 471, doi:10.1086/158003.

[99] K. G. Begeman, A. H. Broeils, and R. H. Sanders, "Extended rotation curves of spiral galaxies: Dark haloes and modified dynamics", *Mon. Not. Roy. Astron. Soc.* **249** (1991) 523.

[100] D. Clowe, A. Gonzalez, and M. Markevitch, "Weak lensing mass reconstruction of the interacting cluster 1E0657-558: Direct evidence for the existence of dark matter", *Astrophysical J.* **604** (2004), no. 2, 596, doi:10.1086/381970, arXiv:astro-ph/0312273.

[101] M. Markevitch et al., "Direct constraints on the dark matter self-interaction cross-section from the merging galaxy cluster 1E0657-56", *Astrophys. J.* **606** (2004), no. 2, 819, doi:10.1086/383178, arXiv:astro-ph/0309303.

[102] S. Weinberg, "The Cosmological Constant Problem", *Rev. Mod. Phys.* **61** (1989) 1, doi:10.1103/RevModPhys.61.1.

[103] **MEG** Collaboration, "Search for the lepton flavour violating decay $\mu^+ \to \mathrm{e}^+\gamma$ with the full dataset of the MEG experiment", *Eur. Phys. J. C* **76** (2016), no. 8, 434, doi:10.1140/epjc/s10052-016-4271-x, arXiv:1605.05081.

[104] **SINDRUM** Collaboration, "Search for the Decay $\mu^+ \to e^+e^+e^-$", *Nucl. Phys. B* **260** (1985) 1, doi:10.1016/0550-3213(85)90308-6.

[105] **Belle-II** Collaboration, "The Belle II Physics Book", *PTEP* **2019** (2019), no. 12, 123C01, doi:10.1093/ptep/ptz106, arXiv:1808.10567. [Erratum: PTEP 2020, 029201 (2020)].

[106] **LHCb** Collaboration, "Search for the lepton-flavour violating decays $\mathrm{B}^0_{(s)} \to e^\pm\mu^\mp$", *JHEP* **03** (2018) 078, doi:10.1007/JHEP03(2018)078, arXiv:1710.04111.

[107] **LHCb** Collaboration, "Search for the lepton-flavour-violating decays $B^0_s \to \tau^\pm\mu^\mp$ and $B^0 \to \tau^\pm\mu^\mp$", *Phys. Rev. Lett.* **123** (2019), no. 21, 211801, doi:10.1103/PhysRevLett.123.211801, arXiv:1905.06614.

[108] **LHCb** Collaboration, "Search for Lepton-Flavor Violating Decays $B^+ \to K^+\mu^\pm e^\mp$", *Phys. Rev. Lett.* **123** (2019), no. 24, 241802, `doi:10.1103/PhysRevLett.123.241802`, `arXiv:1909.01010`.

[109] **LHCb** Collaboration, "Search for the lepton-flavour violating decays $B^0 \to K^{*0}\mu^\pm e^\mp$ and $B_s^0 \to \phi\mu^\pm e^\mp$", `arXiv:2207.04005`.

[110] L. Calibbi, T. Li, X. Marcano, and M. A. Schmidt, "Indirect constraints on lepton-flavour-violating quarkonium decays", `arXiv:2207.10913`.

[111] **Belle** Collaboration, "Experimental review of Lepton Flavor Violation searches", in *20th Conference on Flavor Physics and CP Violation* . 8, 2022. `arXiv:2208.02723`.

[112] I. Doršner et al., "Physics of leptoquarks in precision experiments and at particle colliders", *Phys. Rept.* **641** (2016) 1, `doi:10.1016/j.physrep.2016.06.001`, `arXiv:1603.04993`.

[113] C. Cornella et al., "Reading the footprints of the B-meson flavor anomalies", *JHEP* **08** (2021) 050, `doi:10.1007/JHEP08(2021)050`, `arXiv:2103.16558`.

[114] **Muon** Collaboration, "Final Report of the Muon E821 Anomalous Magnetic Moment Measurement at BNL", *Phys. Rev. D* **73** (2006) 072003, `doi:10.1103/PhysRevD.73.072003`, `arXiv:hep-ex/0602035`.

[115] **Muon** Collaboration, "Measurement of the Positive Muon Anomalous Magnetic Moment to 0.46 ppm", *Phys. Rev. Lett.* **126** (2021), no. 14, 141801, `doi:10.1103/PhysRevLett.126.141801`, `arXiv:2104.03281`.

[116] **Budapest-Marseille-Wuppertal** Collaboration, "Hadronic vacuum polarization contribution to the anomalous magnetic moments of leptons from first principles", *Phys. Rev. Lett.* **121** (2018), no. 2, 022002, `doi:10.1103/PhysRevLett.121.022002`, `arXiv:1711.04980`.

[117] **UKQCD** Collaboration, "Calculation of the hadronic vacuum polarization contribution to the muon anomalous magnetic moment", *Phys. Rev. Lett.* **121** (2018), no. 2, 022003, `doi:10.1103/PhysRevLett.121.022003`, `arXiv:1801.07224`.

[118] H. B. Meyer and H. Wittig, "Lattice QCD and the anomalous magnetic moment of the muon", *Prog. Part. Nucl. Phys.* **104** (2019) 46, `doi:10.1016/j.ppnp.2018.09.001`, `arXiv:1807.09370`.

[119] D. Bryman, V. Cirigliano, A. Crivellin, and G. Inguglia, "Testing Lepton Flavor Universality with Pion, Kaon, Tau, and Beta Decays", `doi:10.1146/annurev-nucl-110121-051223`, `arXiv:2111.05338`.

[120] **KLOE** Collaboration, "Precise measurement of $\Gamma(K \to e\nu(\gamma))/\Gamma(K \to \mu\nu(\gamma))$ and study of $K \to e\nu\gamma$", *Eur. Phys. J. C* **64** (2009) 627, `doi:10.1140/epjc/s10052-009-1217-6`, `arXiv:0907.3594`. [Erratum: Eur.Phys.J. 65, 703 (2010)].

[121] **NA62** Collaboration, "Precision Measurement of the Ratio of the Charged Kaon Leptonic Decay Rates", *Phys. Lett. B* **719** (2013) 326, `doi:10.1016/j.physletb.2013.01.037`, `arXiv:1212.4012`.

[122] **FlaviaNet Working Group** Collaboration, "An Evaluation of $|V_{us}|$ and precise tests of the Standard Model from world data on leptonic and semileptonic kaon decays", *Eur.*

Phys. J. C **69** (2010) 399, doi:10.1140/epjc/s10052-010-1406-3, arXiv:1005.2323.

[123] A. Pich, "Precision Tau Physics", *Prog. Part. Nucl. Phys.* **75** (2014) 41, doi:10.1016/j.ppnp.2013.11.002, arXiv:1310.7922.

[124] **BESIII** Collaboration, "Precision measurements of $\mathcal{B}[\psi(3686) \to \pi^+\pi^- J/\psi]$ and $\mathcal{B}[J/\psi \to l^+l^-]$", *Phys. Rev. D* **88** (2013), no. 3, 032007, doi:10.1103/PhysRevD.88.032007, arXiv:1307.1189.

[125] **BESIII** Collaboration, "Measurement of the total and leptonic decay widths of the J/ψ resonance with an energy scan method at BESIII", arXiv:2206.13674.

[126] **BESIII** Collaboration, "Measurement of the absolute branching fractions for purely leptonic D_s^+ decays", *Phys. Rev. D* **104** (2021), no. 5, 052009, doi:10.1103/PhysRevD.104.052009, arXiv:2102.11734.

[127] **BESIII** Collaboration, "Measurement of the branching fraction for the semi-leptonic decay $D^{0(+)} \to \pi^{-(0)}\mu^+\nu_\mu$ and test of lepton universality", *Phys. Rev. Lett.* **121** (2018), no. 17, 171803, doi:10.1103/PhysRevLett.121.171803, arXiv:1802.05492.

[128] **BESIII** Collaboration, "Study of the $D^0 \to K^-\mu^+\nu_\mu$ dynamics and test of lepton flavor universality with $D^0 \to K^-\ell^+\nu_\ell$ decays", *Phys. Rev. Lett.* **122** (2019), no. 1, 011804, doi:10.1103/PhysRevLett.122.011804, arXiv:1810.03127.

[129] **BESIII** Collaboration, "Observation of the decay $D^0 \to \rho^-\mu^+\nu_\mu$", *Phys. Rev. D* **104** (2021), no. 9, L091103, doi:10.1103/PhysRevD.104.L091103, arXiv:2106.02292.

[130] **ALEPH**, **DELPHI**, **L3**, **OPAL**, and **SLD** Collaborations, and LEP Electroweak Working Group, and SLD Electroweak and Heavy Flavour Groups, "Precision electroweak measurements on the Z resonance", *Phys. Rept.* **427** (2006) 257, doi:10.1016/j.physrep.2005.12.006, arXiv:hep-ex/0509008.

[131] **ALEPH**, **DELPHI**, **L3**, and **OPAL** Collaborations, and LEP Electroweak Working Group, "Electroweak Measurements in Electron-Positron Collisions at W-Boson-Pair Energies at LEP", *Phys. Rept.* **532** (2013) 119, doi:10.1016/j.physrep.2013.07.004, arXiv:1302.3415.

[132] **ATLAS** Collaboration, "Test of the universality of τ and μ lepton couplings in W-boson decays with the ATLAS detector", *Nature Phys.* **17** (2021), no. 7, 813, doi:10.1038/s41567-021-01236-w, arXiv:2007.14040.

[133] **CMS** Collaboration, "Precision measurement of the W boson decay branching fractions in proton-proton collisions at $\sqrt{s} = 13$ TeV", *Phys. Rev. D* **105** (2022), no. 7, 072008, doi:10.1103/PhysRevD.105.072008, arXiv:2201.07861.

[134] **BaBar** Collaboration, "The BaBar detector", *Nucl. Instrum. Meth. A* **479** (2002) 1, doi:10.1016/S0168-9002(01)02012-5, arXiv:hep-ex/0105044.

[135] **Belle** Collaboration, "The Belle Detector", *Nucl. Instrum. Meth. A* **479** (2002) 117, doi:10.1016/S0168-9002(01)02013-7.

[136] **LHCb** Collaboration, "The LHCb Detector at the LHC", *JINST* **3** (2008) S08005, doi:10.1088/1748-0221/3/08/S08005.

[137] **LHCb** Collaboration, "Roadmap for selected key measurements of LHCb",

arXiv:0912.4179.

[138] **LHCb** Collaboration, “LHCb Detector Performance”, *Int. J. Mod. Phys. A* **30** (2015), no. 07, 1530022, doi:10.1142/S0217751X15300227, arXiv:1412.6352.

[139] P. Koppenburg, “Flavour Anomalies”, https://www.nikhef.nl/~pkoppenb/anomalies.html, 2022. (Retrieved Jan 23, 2023).

[140] “Average of R(D) and R(D*) for End 2022”. https://hflav-eos.web.cern.ch/hflav-eos/semi/fall22/html/RDsDsstar/RDRDs.html. (Retrieved Nov 17, 2022).

[141] M. Bordone, G. Isidori, and A. Pattori, “On the Standard Model predictions for R_K and R_{K^*}”, *Eur. Phys. J. C* **76** (2016), no. 8, 440, doi:10.1140/epjc/s10052-016-4274-7, arXiv:1605.07633.

[142] G. Hiller and F. Kruger, “More model-independent analysis of $b \to s$ processes”, *Phys. Rev. D* **69** (2004) 074020, doi:10.1103/PhysRevD.69.074020, arXiv:hep-ph/0310219.

[143] **Belle** Collaboration, “Measurement of the Differential Branching Fraction and Forward-Backward Asymmetry for $B \to K^{(*)}\ell^+\ell^-$”, *Phys. Rev. Lett.* **103** (2009) 171801, doi:10.1103/PhysRevLett.103.171801, arXiv:0904.0770.

[144] **Belle** Collaboration, “Test of Lepton-Flavor Universality in $B \to K^*\ell^+\ell^-$ Decays at Belle”, *Phys. Rev. Lett.* **126** (2021), no. 16, 161801, doi:10.1103/PhysRevLett.126.161801, arXiv:1904.02440.

[145] **BELLE** Collaboration, “Test of lepton flavor universality and search for lepton flavor violation in $B \to K\ell\ell$ decays”, *JHEP* **03** (2021) 105, doi:10.1007/JHEP03(2021)105, arXiv:1908.01848.

[146] **BaBar** Collaboration, “Measurement of Branching Fractions and Rate Asymmetries in the Rare Decays $B \to K^{(*)}l^+l^-$”, *Phys. Rev. D* **86** (2012) 032012, doi:10.1103/PhysRevD.86.032012, arXiv:1204.3933.

[147] **LHCb** Collaboration, “Test of lepton universality with $B^0 \to K^{*0}\ell^+\ell^-$ decays”, *JHEP* **08** (2017) 055, doi:10.1007/JHEP08(2017)055, arXiv:1705.05802.

[148] **LHCb** Collaboration, “Test of lepton universality in beauty-quark decays”, *Nature Phys.* **18** (2022), no. 3, 277, doi:10.1038/s41567-021-01478-8, arXiv:2103.11769.

[149] **LHCb** Collaboration, “Tests of lepton universality using $B^0 \to K^0_S\ell^+\ell^-$ and $B^+ \to K^{*+}\ell^+\ell^-$ decays”, *Phys. Rev. Lett.* **128** (2022), no. 19, 191802, doi:10.1103/PhysRevLett.128.191802, arXiv:2110.09501.

[150] **LHCb** Collaboration, “Differential branching fractions and isospin asymmetries of $B \to K^{(*)}\mu^+\mu^-$ decays”, *JHEP* **06** (2014) 133, doi:10.1007/JHEP06(2014)133, arXiv:1403.8044.

[151] **LHCb** Collaboration, “Search for lepton-universality violation in $B^+ \to K^+\ell^+\ell^-$ decays”, *Phys. Rev. Lett.* **122** (2019), no. 19, 191801, doi:10.1103/PhysRevLett.122.191801, arXiv:1903.09252.

[152] **LHCb** Collaboration, “Test of lepton universality in $b \to s\ell^+\ell^-$ decays”, arXiv:2212.09152.

[153] **LHCb** Collaboration, "Measurement of lepton universality parameters in $B^+ \to K^+\ell^+\ell^-$ and $B^0 \to K^{*0}\ell^+\ell^-$ decays", `arXiv:2212.09153`.

[154] **LHCb** Collaboration, "Measurements of the S-wave fraction in $B^0 \to K^+\pi^-\mu^+\mu^-$ decays and the $B^0 \to K^*(892)^0\mu^+\mu^-$ differential branching fraction", *JHEP* **11** (2016) 047, `doi:10.1007/JHEP11(2016)047`, `arXiv:1606.04731`. [Erratum: `doi:10.1007/JHEP04(2017)142`].

[155] **LHCb** Collaboration, "Angular analysis and differential branching fraction of the decay $B_s^0 \to \phi\mu^+\mu^-$", *JHEP* **09** (2015) 179, `doi:10.1007/JHEP09(2015)179`, `arXiv:1506.08777`.

[156] **LHCb** Collaboration, "Branching Fraction Measurements of the Rare $B_s^0 \to \phi\mu^+\mu^-$ and $B_s^0 \to f_2'(1525)\mu^+\mu^-$- Decays", *Phys. Rev. Lett.* **127** (2021), no. 15, 151801, `doi:10.1103/PhysRevLett.127.151801`, `arXiv:2105.14007`.

[157] **Belle** Collaboration, "Lepton-Flavor-Dependent Angular Analysis of $B \to K^*\ell^+\ell^-$", *Phys. Rev. Lett.* **118** (2017) 111801, `doi:10.1103/PhysRevLett.118.111801`, `arXiv:1612.05014`.

[158] **LHCb** Collaboration, "Angular analysis of the $B^0 \to K^{*0}\mu^+\mu^-$ decay using 3 fb^{-1} of integrated luminosity", *JHEP* **02** (2016) 104, `doi:10.1007/JHEP02(2016)104`, `arXiv:1512.04442`.

[159] **LHCb** Collaboration, "Measurement of CP-Averaged Observables in the $B^0 \to K^{*0}\mu^+\mu^-$ Decay", *Phys. Rev. Lett.* **125** (2020), no. 1, 011802, `doi:10.1103/PhysRevLett.125.011802`, `arXiv:2003.04831`.

[160] **LHCb** Collaboration, "Angular Analysis of the $B^+ \to K^{*+}\mu^+\mu^-$ Decay", *Phys. Rev. Lett.* **126** (2021), no. 16, 161802, `doi:10.1103/PhysRevLett.126.161802`, `arXiv:2012.13241`.

[161] **Belle** Collaboration, "Measurement of the CKM matrix element $|V_{cb}|$ from $B^0 \to D^{*-}\ell^+\nu_\ell$ at Belle", *Phys. Rev. D* **100** (2019), no. 5, 052007, `doi:10.1103/PhysRevD.100.052007`, `arXiv:1809.03290`. [Erratum: Phys.Rev.D 103, 079901 (2021)].

[162] **BaBar** Collaboration, "Evidence for an excess of $\bar{B} \to D^{(*)}\tau^-\bar{\nu}_\tau$ decays", *Phys. Rev. Lett.* **109** (2012) 101802, `doi:10.1103/PhysRevLett.109.101802`, `arXiv:1205.5442`.

[163] **BaBar** Collaboration, "Measurement of an excess of $\bar{B} \to D^{(*)}\tau^-\bar{\nu}_\tau$ decays and implications for charged Higgs bosons", *Phys. Rev. D* **88** (2013) 072012, `doi:10.1103/PhysRevD.88.072012`, `arXiv:1303.0571`.

[164] **Belle** Collaboration, "Observation of $B^0 \to D^{*-}\tau^+\nu_\tau$ decay at Belle", *Phys. Rev. Lett.* **99** (2007) 191807, `doi:10.1103/PhysRevLett.99.191807`, `arXiv:0706.4429`.

[165] **Belle** Collaboration, "Observation of $B^+ \to \bar{D}^{*0}\tau^+\nu_\tau$ and Evidence for $B^+ \to \bar{D}^0\tau^+\nu_\tau$ at Belle", *Phys. Rev. D* **82** (2010) 072005, `doi:10.1103/PhysRevD.82.072005`, `arXiv:1005.2302`.

[166] **Belle** Collaboration, "Measurement of the branching ratio of $\bar{B} \to D^{(*)}\tau^-\bar{\nu}_\tau$ relative to $\bar{B} \to D^{(*)}\ell^-\bar{\nu}_\ell$ decays with hadronic tagging at Belle", *Phys. Rev. D* **92** (2015) 072014, `doi:10.1103/PhysRevD.92.072014`, `arXiv:1507.03233`.

[167] **Belle** Collaboration, "Measurement of the branching ratio of $\bar{B}^0 \to D^{*+}\tau^-\bar{\nu}_\tau$ relative to $\bar{B}^0 \to D^{*+}\ell^-\bar{\nu}_\ell$ decays with a semileptonic tagging method", *Phys. Rev. D* **94** (2016) 072007, doi:10.1103/PhysRevD.94.072007, arXiv:1607.07923.

[168] **Belle** Collaboration, "Measurement of the τ lepton polarization and $R(D^*)$ in the decay $\bar{B} \to D^*\tau^-\bar{\nu}_\tau$", *Phys. Rev. Lett.* **118** (2017) 211801, doi:10.1103/PhysRevLett.118.211801, arXiv:1612.00529.

[169] **Belle** Collaboration, "Measurement of the τ lepton polarization and $R(D^*)$ in the decay $\bar{B} \to D^*\tau^-\bar{\nu}_\tau$ with one-prong hadronic τ decays at Belle", *Phys. Rev. D* **97** (2018) 012004, doi:10.1103/PhysRevD.97.012004, arXiv:1709.00129.

[170] **Belle** Collaboration, "Measurement of $\mathcal{R}(D)$ and $\mathcal{R}(D^*)$ with a semileptonic tagging method", *Phys. Rev. Lett.* **124** (2020), no. 16, 161803, doi:10.1103/PhysRevLett.124.161803, arXiv:1910.05864.

[171] **LHCb** Collaboration, "Measurement of the ratio of branching fractions $\mathcal{B}(\bar{B}^0 \to D^{*+}\tau^-\bar{\nu}_\tau)/\mathcal{B}(\bar{B}^0 \to D^{*+}\mu^-\bar{\nu}_\mu)$", *Phys. Rev. Lett.* **115** (2015) 111803, doi:10.1103/PhysRevLett.115.159901, arXiv:1506.08614. [Erratum: doi:10.1103/PhysRevLett.115.111803].

[172] **LHCb** Collaboration, "Measurement of the ratio of the $B^0 \to D^{*-}\tau^+\nu_\tau$ and $B^0 \to D^{*-}\mu^+\nu_\mu$ branching fractions using three-prong τ-lepton decays", *Phys. Rev. Lett.* **120** (2018), no. 17, 171802, doi:10.1103/PhysRevLett.120.171802, arXiv:1708.08856.

[173] **LHCb** Collaboration, "Test of Lepton Flavor Universality by the measurement of the $B^0 \to D^{*-}\tau^+\nu_\tau$ branching fraction using three-prong τ decays", *Phys. Rev. D* **97** (2018), no. 7, 072013, doi:10.1103/PhysRevD.97.072013, arXiv:1711.02505.

[174] B. Dumont, K. Nishiwaki, and R. Watanabe, "LHC constraints and prospects for S_1 scalar leptoquark explaining the $\bar{B} \to D^{(*)}\tau\bar{\nu}$ anomaly", *Phys. Rev. D* **94** (2016) 034001, doi:10.1103/PhysRevD.94.034001, arXiv:1603.05248.

[175] A. V. Manohar, "Effective field theories", *Lect. Notes Phys.* **479** (1997) 311, doi:10.1007/BFb0104294, arXiv:hep-ph/9606222.

[176] W. Buchmuller and D. Wyler, "Effective Lagrangian Analysis of New Interactions and Flavor Conservation", *Nucl. Phys. B* **268** (1986) 621, doi:10.1016/0550-3213(86)90262-2.

[177] B. Grzadkowski, M. Iskrzynski, M. Misiak, and J. Rosiek, "Dimension-Six Terms in the Standard Model Lagrangian", *JHEP* **10** (2010) 085, doi:10.1007/JHEP10(2010)085, arXiv:1008.4884.

[178] T. Appelquist and J. Carazzone, "Infrared Singularities and Massive Fields", *Phys. Rev. D* **11** (1975) 2856, doi:10.1103/PhysRevD.11.2856.

[179] K. G. Wilson, "The renormalization group and critical phenomena", *Rev. Mod. Phys.* **55** (1983) 583, doi:10.1103/RevModPhys.55.583.

[180] A. Angelescu et al., "Single leptoquark solutions to the B-physics anomalies", *Phys. Rev. D* **104** (2021), no. 5, 055017, doi:10.1103/PhysRevD.104.055017, arXiv:2103.12504.

[181] W. Buchmuller, R. Ruckl, and D. Wyler, "Leptoquarks in Lepton - Quark Collisions",

Phys. Lett. B **191** (1987) 442, doi:10.1016/0370-2693(87)90637-X. [Erratum: Phys.Lett.B 448, 320–320 (1999)].

[182] H. Georgi and S. L. Glashow, "Unity of All Elementary Particle Forces", *Phys. Rev. Lett.* **32** (1974) 438, doi:10.1103/PhysRevLett.32.438.

[183] J. C. Pati and A. Salam, "Unified lepton-hadron Symmetry and a Gauge Theory of the Basic Interactions", *Phys. Rev. D* **8** (1973) 1240, doi:10.1103/PhysRevD.8.1240.

[184] J. C. Pati and A. Salam, "Lepton Number as the Fourth Color", *Phys. Rev. D* **10** (1974) 275, doi:10.1103/PhysRevD.10.275. [Erratum: doi:10.1103/PhysRevD.11.703.2].

[185] H. Murayama and T. Yanagida, "A viable SU(5) GUT with light leptoquark bosons", *Mod. Phys. Lett. A* **7** (1992) 147, doi:10.1142/S0217732392000070.

[186] H. Fritzsch and P. Minkowski, "Unified Interactions of Leptons and Hadrons", *Annals Phys.* **93** (1975) 193, doi:10.1016/0003-4916(75)90211-0.

[187] G. Senjanovic and A. Sokorac, "Light Leptoquarks in SO(10)", *Z. Phys. C* **20** (1983) 255, doi:10.1007/BF01574858.

[188] P. H. Frampton and B.-H. Lee, "SU(15) grand unification", *Phys. Rev. Lett.* **64** (1990) 619, doi:10.1103/PhysRevLett.64.619.

[189] P. H. Frampton and T. W. Kephart, "Higgs sector and proton decay in SU(15) grand unification", *Phys. Rev. D* **42** (1990) 3892, doi:10.1103/PhysRevD.42.3892.

[190] S. Dimopoulos and L. Susskind, "Mass Without Scalars", *Nucl. Phys. B* **155** (1979) 237, doi:10.1016/0550-3213(79)90364-X.

[191] S. Dimopoulos, "Technicolored Signatures", *Nucl. Phys. B* **168** (1980) 69, doi:10.1016/0550-3213(80)90277-1.

[192] E. Farhi and L. Susskind, "Technicolor", *Phys. Rept.* **74** (1981) 277, doi:10.1016/0370-1573(81)90173-3.

[193] L. F. Abbott and E. Farhi, "Are the Weak Interactions Strong?", *Phys. Lett. B* **101** (1981) 69, doi:10.1016/0370-2693(81)90492-5.

[194] B. Schrempp and F. Schrempp, "Light leptoquarks", *Phys. Lett. B* **153** (1985) 101, doi:10.1016/0370-2693(85)91450-9.

[195] J. Wudka, "Composite leptoquarks", *Phys. Lett. B* **167** (1986) 337, doi:10.1016/0370-2693(86)90356-4.

[196] L. J. Hall and M. Suzuki, "Explicit R-Parity Breaking in Supersymmetric Models", *Nucl. Phys. B* **231** (1984) 419, doi:10.1016/0550-3213(84)90513-3.

[197] S. Dawson, "R-Parity Breaking in Supersymmetric Theories", *Nucl. Phys. B* **261** (1985) 297, doi:10.1016/0550-3213(85)90577-2.

[198] G. F. Giudice and R. Rattazzi, "R-parity violation and unification", *Phys. Lett. B* **406** (1997) 321, doi:10.1016/S0370-2693(97)00702-8, arXiv:hep-ph/9704339.

[199] C. Csaki, Y. Grossman, and B. Heidenreich, "MFV SUSY: A Natural Theory for R-Parity Violation", *Phys. Rev. D* **85** (2012) 095009, doi:10.1103/PhysRevD.85.095009, arXiv:1111.1239.

[200] V. D. Angelopoulos et al., "Search for New Quarks Suggested by the Superstring", *Nucl. Phys. B* **292** (1987) 59, doi:10.1016/0550-3213(87)90637-7.

[201] J. K. Elwood and A. E. Faraggi, "Exotic leptoquarks from superstring derived models", *Nucl. Phys. B* **512** (1998) 42, doi:10.1016/S0550-3213(97)00757-8, arXiv:hep-ph/9704363.

[202] M. J. Baker, J. Fuentes-Martín, G. Isidori, and M. König, "High-p_T signatures in vector–leptoquark models", *Eur. Phys. J. C* **79** (2019), no. 4, 334, doi:10.1140/epjc/s10052-019-6853-x, arXiv:1901.10480.

[203] P. Langacker, "Parity violation in muonic atoms and cesium", *Phys. Lett. B* **256** (1991) 277, doi:10.1016/0370-2693(91)90688-M.

[204] M. J. Baker et al., "The Coannihilation Codex", *JHEP* **12** (2015) 120, doi:10.1007/JHEP12(2015)120, arXiv:1510.03434.

[205] M. Carpentier and S. Davidson, "Constraints on two-lepton, two quark operators", *Eur. Phys. J. C* **70** (2010) 1071, doi:10.1140/epjc/s10052-010-1482-4, arXiv:1008.0280.

[206] E. Gabrielli, "Model independent constraints on leptoquarks from rare muon and tau lepton processes", *Phys. Rev. D* **62** (2000) 055009, doi:10.1103/PhysRevD.62.055009, arXiv:hep-ph/9911539.

[207] M. Tanaka and R. Watanabe, "New physics in the weak interaction of $\bar{B} \to D^{(*)}\tau\bar{\nu}$", *Phys. Rev. D* **87** (2013) 034028, doi:10.1103/PhysRevD.87.034028, arXiv:1212.1878.

[208] Y. Sakaki, M. Tanaka, A. Tayduganov, and R. Watanabe, "Testing leptoquark models in $\bar{B} \to D^{(*)}\tau\bar{\nu}$", *Phys. Rev. D* **88** (2013) 094012, doi:10.1103/PhysRevD.88.094012, arXiv:1309.0301.

[209] I. Doršner, S. Fajfer, N. Košnik, and I. Nišandžić, "Minimally flavored colored scalar in $\bar{B} \to D^{(*)}\tau\bar{\nu}$ and the mass matrices constraints", *JHEP* **11** (2013) 084, doi:10.1007/JHEP11(2013)084, arXiv:1306.6493.

[210] B. Gripaios, M. Nardecchia, and S. A. Renner, "Composite leptoquarks and anomalies in B-meson decays", *JHEP* **05** (2015) 006, doi:10.1007/JHEP05(2015)006, arXiv:1412.1791.

[211] R. Alonso, B. Grinstein, and J. Martin Camalich, "Lepton universality violation and lepton flavor conservation in B-meson decays", *JHEP* **10** (2015) 184, doi:10.1007/JHEP10(2015)184, arXiv:1505.05164.

[212] L. Calibbi, A. Crivellin, and T. Ota, "Effective Field Theory Approach to $b \to s\ell\ell^{(\prime)}$, $B \to K^{(*)}\nu\bar{\nu}$ and $B \to D^{(*)}\tau\nu$ with Third Generation Couplings", *Phys. Rev. Lett.* **115** (2015) 181801, doi:10.1103/PhysRevLett.115.181801, arXiv:1506.02661.

[213] M. Bauer and M. Neubert, "Minimal Leptoquark Explanation for the $R_{D^{(*)}}$, R_K , and $(g-2)_\mu$ Anomalies", *Phys. Rev. Lett.* **116** (2016) 141802, doi:10.1103/PhysRevLett.116.141802, arXiv:1511.01900.

[214] R. Barbieri, G. Isidori, A. Pattori, and F. Senia, "Anomalies in B-decays and $U(2)$ flavour symmetry", *Eur. Phys. J. C* **76** (2016), no. 2, 67, doi:10.1140/epjc/s10052-016-3905-3, arXiv:1512.01560.

[215] D. Bečirević and O. Sumensari, "A leptoquark model to accommodate $R_K^{\rm exp} < R_K^{\rm SM}$ and $R_{K^*}^{\rm exp} < R_{K^*}^{\rm SM}$", *JHEP* **08** (2017) 104, doi:10.1007/JHEP08(2017)104, arXiv:1704.05835.

[216] D. Buttazzo, A. Greljo, G. Isidori, and D. Marzocca, "B-physics anomalies: a guide to combined explanations", *JHEP* **11** (2017) 044, doi:10.1007/JHEP11(2017)044, arXiv:1706.07808.

[217] E. Coluccio Leskow, G. DAmbrosio, A. Crivellin, and D. Muller, "$(g-2)_\mu$, lepton flavor violation, and Z decays with leptoquarks: Correlations and future prospects", *Phys. Rev. D* **95** (2017) 055018, doi:10.1103/PhysRevD.95.055018, arXiv:1612.06858.

[218] A. Crivellin, D. Müller, and T. Ota, "Simultaneous explanation of $R(D^{(*)})$ and $\mathrm{b} \to \mathrm{s}\mu^+\mu^-$: the last scalar leptoquarks standing", *JHEP* **09** (2017) 040, doi:10.1007/JHEP09(2017)040, arXiv:1703.09226.

[219] G. Hiller and I. Nišandžić, "R_K and R_{K^*} beyond the standard model", *Phys. Rev. D* **96** (2017) 035003, doi:10.1103/PhysRevD.96.035003, arXiv:1704.05444.

[220] I. Doršner, S. Fajfer, D. A. Faroughy, and N. Košnik, "The role of the S_3 GUT leptoquark in flavor universality and collider searches", *JHEP* **10** (2017) 188, doi:10.1007/JHEP10(2017)188, arXiv:1706.07779.

[221] L. Di Luzio, A. Greljo, and M. Nardecchia, "Gauge leptoquark as the origin of B-physics anomalies", *Phys. Rev. D* **96** (2017), no. 11, 115011, doi:10.1103/PhysRevD.96.115011, arXiv:1708.08450.

[222] L. Calibbi, A. Crivellin, and T. Li, "Model of vector leptoquarks in view of the B-physics anomalies", *Phys. Rev. D* **98** (2018), no. 11, 115002, doi:10.1103/PhysRevD.98.115002, arXiv:1709.00692.

[223] M. Bordone, C. Cornella, J. Fuentes-Martín, and G. Isidori, "A three-site gauge model for flavor hierarchies and flavor anomalies", *Phys. Lett. B* **779** (2018) 317, doi:10.1016/j.physletb.2018.02.011, arXiv:1712.01368.

[224] G. Hiller, D. Loose, and I. Nišandžić, "Flavorful leptoquarks at hadron colliders", *Phys. Rev. D* **97** (2018) 075004, doi:10.1103/PhysRevD.97.075004, arXiv:1801.09399.

[225] D. Bečirević et al., "Scalar leptoquarks from grand unified theories to accommodate the B-physics anomalies", *Phys. Rev. D* **98** (2018), no. 5, 055003, doi:10.1103/PhysRevD.98.055003, arXiv:1806.05689.

[226] J. Kumar, D. London, and R. Watanabe, "Combined Explanations of the $b \to s\mu^+\mu^-$ and $b \to c\tau^-\bar{\nu}$ Anomalies: a General Model Analysis", *Phys. Rev. D* **99** (2019), no. 1, 015007, doi:10.1103/PhysRevD.99.015007, arXiv:1806.07403.

[227] L. Di Luzio et al., "Maximal Flavour Violation: a Cabibbo mechanism for leptoquarks", *JHEP* **11** (2018) 081, doi:10.1007/JHEP11(2018)081, arXiv:1808.00942.

[228] R. Barbieri and A. Tesi, "B-decay anomalies in Pati-Salam SU(4)", *Eur. Phys. J. C* **78** (2018), no. 3, 193, doi:10.1140/epjc/s10052-018-5680-9, arXiv:1712.06844.

[229] D. Marzocca, "Addressing the B-physics anomalies in a fundamental Composite Higgs Model", *JHEP* **07** (2018) 121, doi:10.1007/JHEP07(2018)121, arXiv:1803.10972.

[230] A. Angelescu, D. Bečirević, D. A. Faroughy, and O. Sumensari, "Closing the window on single leptoquark solutions to the B-physics anomalies", *JHEP* **10** (2018) 183, doi:10.1007/JHEP10(2018)183, arXiv:1808.08179.

[231] C. Cornella, J. Fuentes-Martín, and G. Isidori, "Revisiting the vector leptoquark explanation of the B-physics anomalies", *JHEP* **07** (2019) 168, doi:10.1007/JHEP07(2019)168, arXiv:1903.11517.

[232] G. Isidori, D. Lancierini, P. Owen, and N. Serra, "On the significance of new physics in $b \to s\ell^+\ell^-$ decays", *Phys. Lett. B* **822** (2021) 136644, doi:10.1016/j.physletb.2021.136644, arXiv:2104.05631.

[233] J. Aebischer et al., "Confronting the vector leptoquark hypothesis with new low- and high-energy data", arXiv:2210.13422.

[234] L. Buonocore et al., "Lepton-Quark Collisions at the Large Hadron Collider", *Phys. Rev. Lett.* **125** (2020), no. 23, 231804, doi:10.1103/PhysRevLett.125.231804, arXiv:2005.06475.

[235] L. Buonocore, P. Nason, F. Tramontano, and G. Zanderighi, "Leptons in the proton", *JHEP* **08** (2020), no. 08, 019, doi:10.1007/JHEP08(2020)019, arXiv:2005.06477.

[236] D. A. Faroughy, A. Greljo, and J. F. Kamenik, "Confronting lepton flavor universality violation in B decays with high-p_T tau lepton searches at LHC", *Phys. Lett. B* **764** (2017) 126, doi:10.1016/j.physletb.2016.11.011, arXiv:1609.07138.

[237] M. Schmaltz and Y.-M. Zhong, "The leptoquark Hunter's guide: large coupling", *JHEP* **01** (2019) 132, doi:10.1007/JHEP01(2019)132, arXiv:1810.10017.

[238] L. Forthomme (Wikimedia Commons), "File:Cern-accelerator-complex.svg — Wikimedia Commons, the free media repository", https://commons.wikimedia.org/wiki/File:Cern-accelerator-complex.svg, 2016. (Retrieved Jul 24, 2017).

[239] S. Holmes, R. S. Moore, and V. Shiltsev, "Overview of the Tevatron Collider Complex: Goals, Operations and Performance", *JINST* **6** (2011) T08001, doi:10.1088/1748-0221/6/08/T08001, arXiv:1106.0909.

[240] L. Evans and P. Bryant, "LHC Machine", *JINST* **3** (2008), no. 08, S08001, doi:10.1088/1748-0221/3/08/S08001.

[241] **CMS** Collaboration, "Public CMS Luminosity Information". https://twiki.cern.ch/twiki/bin/view/CMSPublic/LumiPublicResults. (Retrieved Dec 6, 2022).

[242] W. Herr and B. Muratori, "Concept of luminosity", in *CAS - CERN Accelerator School: Intermediate Course on Accelerator Physics*, CERN. CERN, Zeuthen, Germany, 2003. doi:10.5170/CERN-2006-002.361.

[243] C. Pralavorio and C. Pralavorio, "The LHC racks up records", http://home.cern/about/updates/2017/06/lhc-racks-records, 2017. (Archived at http://cds.cern.ch/record/2272474).

[244] I. Efthymiopoulos et al., "Bunch Luminosity Variations in LHC Run 2. BUNCH LUMINOSITY VARIATIONS IN LHC RUN 2", *JACoW IPAC* **2021** (2021) 4094,

doi:10.18429/JACoW-IPAC2021-THPAB172.

[245] **CMS** Collaboration, "The CMS experiment at the CERN LHC", *JINST* **3** (2008) S08004, doi:10.1088/1748-0221/3/08/S08004.

[246] **CMS** Collaboration, "Performance of the CMS Drift Tube Chambers with Cosmic Rays", *JINST* **5** (2010) T03015, doi:10.1088/1748-0221/5/03/T03015, arXiv:0911.4855.

[247] **CMS** Collaboration, "CMS Tracker Detector Performance Results", https://twiki.cern.ch/twiki/bin/view/CMSPublic/DPGResultsTRK, 2022. (Retrieved Dec 2, 2022).

[248] **CMS Tracker** Group, "The CMS Phase-1 Pixel Detector Upgrade", *JINST* **16** (2021), no. 02, P02027, doi:10.1088/1748-0221/16/02/P02027, arXiv:2012.14304.

[249] **CMS** Collaboration, "Precise Mapping of the Magnetic Field in the CMS Barrel Yoke using Cosmic Rays", *JINST* **5** (2015) T03021, doi:10.1088/1748-0221/5/03/T03021, arXiv:0910.5530.

[250] **CMS** Collaboration, "Description and performance of track and primary-vertex reconstruction with the CMS tracker", *JINST* **9** (2014) P10009, doi:10.1088/1748-0221/9/10/P10009, arXiv:1405.6569.

[251] **CMS** Collaboration, "The Phase-1 upgrade of the CMS pixel detector", *JINST* **12** (2017), no. 07, C07009, doi:10.1088/1748-0221/12/07/C07009.

[252] **CMS** Collaboration, "CMS Tracking POG Performance Plots For 2017 with PhaseI pixel detector", https://twiki.cern.ch/twiki/bin/view/CMSPublic/TrackingPOGPerformance2017MC#Vertex_Resolutions, 2022. (Retrieved Dec 8, 2022).

[253] **CMS** Collaboration, "The CMS electromagnetic calorimeter project: Technical Design Report", Technical Design Report CMS. CERN, Geneva, 1997.

[254] **CMS** Collaboration, "Jet energy scale and resolution in the CMS experiment in pp collisions at 8 TeV", *JINST* **12** (2017), no. 02, P02014, doi:10.1088/1748-0221/12/02/P02014, arXiv:1607.03663.

[255] **CMS** Collaboration, "CMS Physics: Technical Design Report Volume 1: Detector Performance and Software", Technical Design Report CMS. CERN, Geneva, 2006.

[256] E. Manca, "Validation of the muon momentum resolution in view of the W mass measurement with the CMS experiment". PhD thesis, INFN, Pisa, 2016. CMS-TS-2016-024, CERN-THESIS-2016-173.

[257] **CMS** Collaboration, "Performance of CMS muon reconstruction in pp collision events at $\sqrt{s} = 7\,\mathrm{TeV}$", *JINST* **7** (2012) P10002, doi:10.1088/1748-0221/7/10/P10002, arXiv:1206.4071.

[258] **CMS** Collaboration, "The CMS muon project : Technical Design Report", Technical Design Report CMS. CERN, Geneva, 1997.

[259] **CMS** Collaboration, "The CMS trigger system", *JINST* **12** (2017) P01020, doi:10.1088/1748-0221/12/01/P01020, arXiv:1609.02366.

[260] L. Lee, C. Ohm, A. Soffer, and T.-T. Yu, "Collider Searches for Long-Lived Particles Beyond the Standard Model", *Prog. Part. Nucl. Phys.* **106** (2019) 210,

doi:10.1016/j.ppnp.2019.02.006, arXiv:1810.12602. [Erratum: Prog.Part.Nucl.Phys. 122, 103912 (2022)].

[261] D. Barney, “CMS Slice”, https://cds.cern.ch/record/2628641/, 2015. (Retrieved Dec 8, 2022).

[262] **CDF** Collaboration, “Measurement of $B(t \to Wb)/B(t \to Wq)$ in Top-Quark-Pair Decays Using Dilepton Events and the Full CDF Run II Data Set”, *Phys. Rev. Lett.* **112** (2014) 221801, doi:10.1103/PhysRevLett.112.221801.

[263] T. J. Humanic, “Extracting the hadronization timescale in $\sqrt{s} = 7$ TeV proton-proton collisions from pion and kaon femtoscopy”, *J. Phys. G* **41** (2014) 075105, doi:10.1088/0954-3899/41/7/075105, arXiv:1312.2303.

[264] S. Ferreres-Solé and T. Sjöstrand, “The space–time structure of hadronization in the Lund model”, *Eur. Phys. J. C* **78** (2018), no. 11, 983, doi:10.1140/epjc/s10052-018-6459-8, arXiv:1808.04619.

[265] **CMS** Collaboration, “Commissioning of the Particle-flow Event Reconstruction with the first LHC collisions recorded in the CMS detector”, CMS Physics Analysis Summary CMS-PAS-PFT-10-001, CERN, 2010.

[266] **CMS** Collaboration, “Particle-flow reconstruction and global event description with the CMS detector”, *JINST* **12** (2017) P10003, doi:10.1088/1748-0221/12/10/P10003, arXiv:1706.04965.

[267] W. Adam, B. Mangano, T. Speer, and T. Todorov, “Track Reconstruction in the CMS tracker”, technical report, CERN, Geneva, 2006.

[268] R. Fruhwirth, “Application of Kalman filtering to track and vertex fitting”, *Nucl. Instrum. Meth. A* **262** (1987) 444, doi:10.1016/0168-9002(87)90887-4.

[269] K. Rose, “Deterministic annealing for clustering, compression, classification, regression, and related optimization problems”, *IEEE Proc.* **86** (1998), no. 11, 2210, doi:10.1109/5.726788.

[270] R. Frühwirth, W. Waltenberger, and P. Vanlaer, “Adaptive Vertex Fitting”, technical report, CERN, Geneva, 2007.

[271] **CMS** Collaboration, “Technical proposal for the Phase-II upgrade of the Compact Muon Solenoid”, CMS Technical Proposal CERN-LHCC-2015-010, CMS-TDR-15-02, CERN, 2015.

[272] W. Adam, R. Frühwirth, A. Strandlie, and T. Todorov, “Reconstruction of electrons with the Gaussian-sum filter in the CMS tracker at the LHC”, *Journal of Physics G: Nuclear and Particle Physics* **31** (2005), no. 9, N9, doi:10.1088/0954-3899/31/9/n01.

[273] **CMS** Collaboration, “Electron and photon reconstruction and identification with the CMS experiment at the CERN LHC”, *JINST* **16** (2021) P05014, doi:10.1088/1748-0221/16/05/P05014, arXiv:2012.06888.

[274] **CMS** Collaboration, “ECAL 2016 refined calibration and Run2 summary plots”, CMS Detector Performance Summary CMS-DP-2020-021, CERN, 2020.

[275] H. Voss, A. Höcker, J. Stelzer, and F. Tegenfeldt, “TMVA, the Toolkit for Multivariate

Data Analysis with ROOT", in *XI Int. Workshop on Advanced Computing and Analysis Techniques in Physics Research*. 2007. arXiv:physics/0703039. PoS ACAT:040.

[276] **CMS** Collaboration, "Performance of electron reconstruction and selection with the CMS detector in proton-proton collisions at $\sqrt{s} = 8\,\text{TeV}$", *JINST* **10** (2015) P06005, doi:10.1088/1748-0221/10/06/P06005, arXiv:1502.02701.

[277] M. Cacciari and G. P. Salam, "Pileup subtraction using jet areas", *Phys. Lett. B* **659** (2008) 119, doi:10.1016/j.physletb.2007.09.077, arXiv:0707.1378.

[278] **CMS** Collaboration, "Performance of the CMS muon detector and muon reconstruction with proton-proton collisions at $\sqrt{s} = 13$ TeV", *JINST* **13** (2018) P06015, doi:10.1088/1748-0221/13/06/P06015, arXiv:1804.04528.

[279] M. Cacciari, G. P. Salam, and G. Soyez, "The anti-$\mathrm{k_t}$ jet clustering algorithm", *JHEP* **04** (2008) 063, doi:10.1088/1126-6708/2008/04/063, arXiv:0802.1189.

[280] M. Cacciari and G. P. Salam, "Dispelling the N^3 myth for the k_T jet-finder", *Phys. Lett. B* **641** (2006) 57, doi:10.1016/j.physletb.2006.08.037, arXiv:hep-ph/0512210.

[281] M. Cacciari, G. P. Salam, and G. Soyez, "FastJet user manual", *Eur. Phys. J. C* **72** (2012) 1896, doi:10.1140/epjc/s10052-012-1896-2, arXiv:1111.6097.

[282] **CMS** Collaboration, "Determination of jet energy calibration and transverse momentum resolution in CMS", *JINST* **6** (2011) P11002, doi:10.1088/1748-0221/6/11/P11002, arXiv:1107.4277.

[283] **CMS** Collaboration, "Pileup Jet Identification", CMS Physics Analysis Summary CMS-PAS-JME-13-005, CERN, 2013.

[284] **CMS** Collaboration, "Jet algorithms performance in 13 TeV data", CMS Physics Analysis Summary CMS-PAS-JME-16-003, CERN, 2017.

[285] D. Guest et al., "Jet Flavor Classification in High-Energy Physics with Deep Neural Networks", *Phys. Rev. D* **94** (2016), no. 11, 112002, doi:10.1103/PhysRevD.94.112002, arXiv:1607.08633.

[286] **CMS** Collaboration, "Identification of heavy-flavour jets with the CMS detector in pp collisions at 13 TeV", *JINST* **13** (2018), no. 05, P05011, doi:10.1088/1748-0221/13/05/P05011, arXiv:1712.07158.

[287] **CMS** Collaboration, "Performance of missing energy reconstruction in 13 TeV pp collision data using the CMS detector", CMS Physics Analysis Summary CMS-PAS-JME-16-004, CERN, 2016.

[288] **CMS** Collaboration, "Performance of missing transverse momentum in pp collisions at $\sqrt{s} = 13$ TeV using the CMS detector", CMS Physics Analysis Summary CMS-PAS-JME-17-001, CERN, 2018.

[289] **CMS** Collaboration, "Identification of hadronic tau lepton decays using a deep neural network", *JINST* **17** (2022), no. 07, P07023, doi:10.1088/1748-0221/17/07/p07023, arXiv:2201.08458.

[290] P. R. Burchat, "Decays of the Tau Lepton". PhD thesis, Stanford Linear Accelerator Center, 1986. SLAC-292 UC-34D (E).

[291] M. Davier, A. Hocker, and Z. Zhang, "The Physics of hadronic tau decays", *Rev. Mod. Phys.* **78** (2006) 1043, `doi:10.1103/RevModPhys.78.1043`, `arXiv:hep-ph/0507078`.

[292] Y. Takahashi and M. Tomoto, "Measurement of the top-quark pair production cross-section in *pp* collisions at $\sqrt{s} = 7\,\text{TeV}$ using final states with an electron or a muon and a hadronically decaying τ-lepton". PhD thesis, Nagoya University, 2012. CERN-THESIS-2012-252.

[293] **CHORUS** Collaboration, "Observation of neutrino induced diffractive D_s^{*+} production and subsequent decay $D_s^{*+} \to D_s^+ \to \tau^+ \to \mu^+$", *Phys. Lett. B* **435** (1998) 458, `doi:10.1016/S0370-2693(98)00914-9`.

[294] A. Stahl, "Physics with tau leptons", volume 160. Springer, 2000. `doi:10.1007/BFb0109630`.

[295] **CLEO** Collaboration, "Resonant structure of $\tau \to 3\pi\pi^0\nu_\tau$ and $\tau \to \omega\pi\nu_\tau$ decays", *Phys. Rev. D* **61** (2000) 072003, `doi:10.1103/PhysRevD.61.072003`, `arXiv:hep-ex/9908024`.

[296] A. E. Bondar et al., "Novosibirsk hadronic currents for $\tau \to 4\pi$ channels of τ decay library TAUOLA", *Comput. Phys. Commun.* **146** (2002) 139, `doi:10.1016/S0010-4655(02)00262-X`, `arXiv:hep-ph/0201149`.

[297] H. Czyz, J. H. Kuhn, and A. Wapienik, "Four-pion production in tau decays and e+e- annihilation: An Update", *Phys. Rev. D* **77** (2008) 114005, `doi:10.1103/PhysRevD.77.114005`, `arXiv:0804.0359`.

[298] **CMS** Collaboration, "Performance of τ-lepton reconstruction and identification in CMS", *JINST* **7** (2012), no. 01, P01001, `doi:10.1088/1748-0221/7/01/P01001`, `arXiv:1109.6034`.

[299] **CMS** Collaboration, "Performance of reconstruction and identification of τ leptons decaying to hadrons and ν_τ in pp collisions at $\sqrt{s} = 13$ TeV", *JINST* **13** (2018) P10005, `doi:10.1088/1748-0221/13/10/P10005`, `arXiv:1809.02816`.

[300] **CMS** Collaboration, "Performance of reconstruction and identification of tau leptons in their decays to hadrons and tau neutrino in LHC Run-2", CMS Physics Analysis Summary CMS-PAS-TAU-16-002, CERN, 2016.

[301] A. Cardini, "Measurement of the CP properties of the Higgs boson in its decays to τ leptons with the CMS experiment". PhD thesis, Universität Hamburg, 2021. DESY-THESIS-2021-015, `doi:10.3204/PUBDB-2021-03550`.

[302] E. Bols et al., "Jet Flavour Classification Using DeepJet", *JINST* **15** (2020), no. 12, P12012, `doi:10.1088/1748-0221/15/12/P12012`, `arXiv:2008.10519`.

[303] D. Bertolini, P. Harris, M. Low, and N. Tran, "Pileup Per Particle Identification", *JHEP* **10** (2014) 059, `doi:10.1007/JHEP10(2014)059`, `arXiv:1407.6013`.

[304] I. Goodfellow, Y. Bengio, and A. Courville, "Deep Learning". MIT Press, 2016. `http://www.deeplearningbook.org`.

[305] T.-Y. Lin et al., "Focal Loss for Dense Object Detection", `arXiv:1708.02002`.

[306] G. Cowan, K. Cranmer, E. Gross, and O. Vitells, "Asymptotic formulae for likelihood-based tests of new physics", *Eur. Phys. J. C* **71** (2011)

doi:10.1140/epjc/s10052-011-1554-0, arXiv:1007.1727. [Erratum: doi:10.1140/epjc/s10052-013-2501-z].

[307] **SLAC** Collaboration, "Simulations". https://theory.slac.stanford.edu/our-research/simulations. (Retrieved Jul 25, 2017).

[308] T. Sjöstrand, S. Mrenna, and P. Z. Skands, "PYTHIA 6.4 Physics and Manual", *JHEP* **05** (2006) 026, doi:10.1088/1126-6708/2006/05/026, arXiv:hep-ph/0603175.

[309] **CMS** Collaboration, "Event generator tunes obtained from underlying event and multiparton scattering measurements", *Eur. Phys. J. C* **76** (2016) 155, doi:10.1140/epjc/s10052-016-3988-x, arXiv:1512.00815.

[310] **CMS** Collaboration, "Extraction and validation of a new set of CMS PYTHIA8 tunes from underlying-event measurements", *Eur. Phys. J. C* **80** (2020) 4, doi:10.1140/epjc/s10052-019-7499-4, arXiv:1903.12179.

[311] **CMS** Collaboration, "Investigations of the impact of the parton shower tuning in Pythia 8 in the modelling of $\mathrm{t\bar{t}}$ at $\sqrt{s} = 8$ and 13 TeV", CMS Physics Analysis Summary CMS-PAS-TOP-16-021, CERN, 2016.

[312] S. Marzani and R. D. Ball, "High Energy Resummation of Drell-Yan Processes", *Nucl. Phys. B* **814** (2009) 246, doi:10.1016/j.nuclphysb.2009.01.029, arXiv:0812.3602.

[313] E. S. Shcherbakova, "Quantum corrections to Drell-Yan production of Z bosons". PhD thesis, Universität Hamburg, 2011.

[314] J. R. Incandela, A. Quadt, W. Wagner, and D. Wicke, "Status and Prospects of Top-Quark Physics", *Prog. Part. Nucl. Phys.* **63** (2009) 239, doi:10.1016/j.ppnp.2009.08.001, arXiv:0904.2499.

[315] F.-P. Schilling, "Top Quark Physics at the LHC: A Review of the First Two Years", *Int. J. Mod. Phys. A* **27** (2012) doi:10.1142/S0217751X12300165, arXiv:1206.4484.

[316] **GEANT4** Collaboration, "GEANT4 — a simulation toolkit", *Nucl. Instrum. Meth. A* **506** (2003) 250, doi:10.1016/S0168-9002(03)01368-8.

[317] M. H. Seymour and M. Marx, "Monte Carlo Event Generators", in *Proceedings, 69th Scottish Universities Summer School in Physics: LHC Phenomenology (SUSSP69) 2012*, p. 287. St.Andrews, Scotland, U.K., 2013. arXiv:1304.6677. doi:10.1007/978-3-319-05362-2_8.

[318] F. Maltoni and T. Stelzer, "MadEvent: Automatic event generation with MadGraph", *JHEP* **02** (2003) 027, doi:10.1088/1126-6708/2003/02/027, arXiv:hep-ph/0208156.

[319] J. Alwall et al., "Comparative study of various algorithms for the merging of parton showers and matrix elements in hadronic collisions", *Eur. Phys. J. C* **53** (2008) 473, doi:10.1140/epjc/s10052-007-0490-5, arXiv:0706.2569.

[320] J. Alwall et al., "The automated computation of tree-level and next-to-leading order differential cross sections, and their matching to parton shower simulations", *JHEP* **07** (2014) 079, doi:10.1007/JHEP07(2014)079, arXiv:1405.0301.

[321] P. Nason, "A new method for combining NLO QCD with shower Monte Carlo

algorithms”, *JHEP* **11** (2004) 040, doi:10.1088/1126-6708/2004/11/040, arXiv:hep-ph/0409146.

[322] S. Frixione, P. Nason, and C. Oleari, “Matching NLO QCD computations with parton shower simulations: the POWHEG method”, *JHEP* **11** (2007) 070, doi:10.1088/1126-6708/2007/11/070, arXiv:0709.2092.

[323] S. Alioli, P. Nason, C. Oleari, and E. Re, “A general framework for implementing NLO calculations in shower Monte Carlo programs: the POWHEG BOX”, *JHEP* **06** (2010) 043, doi:10.1007/JHEP06(2010)043, arXiv:1002.2581.

[324] S. Frixione, P. Nason, and G. Ridolfi, “A positive-weight next-to-leading-order Monte Carlo for heavy flavour hadroproduction”, *JHEP* **09** (2007) 126, doi:10.1088/1126-6708/2007/09/126, arXiv:0707.3088.

[325] J. M. Campbell, R. K. Ellis, P. Nason, and E. Re, “Top-Pair Production and Decay at NLO Matched with Parton Showers”, *JHEP* **04** (2015) 114, doi:10.1007/JHEP04(2015)114, arXiv:1412.1828.

[326] S. Alioli, P. Nason, C. Oleari, and E. Re, “NLO single-top production matched with shower in POWHEG: s- and t-channel contributions”, *JHEP* **09** (2009) 111, doi:10.1088/1126-6708/2009/09/111, arXiv:0907.4076. [Erratum: doi:10.1007/JHEP02(2010)011].

[327] E. Re, “Single-top Wt-channel production matched with parton showers using the POWHEG method”, *Eur. Phys. J. C* **71** (2011) 1547, doi:10.1140/epjc/s10052-011-1547-z, arXiv:1009.2450.

[328] T. Sjöstrand, S. Mrenna, and Z. S., Peter, “A Brief Introduction to PYTHIA 8.1”, *Comput. Phys. Commun.* **178** (2008) 852, doi:10.1016/j.cpc.2008.01.036, arXiv:0710.3820.

[329] T. Sjöstrand et al., “An introduction to PYTHIA 8.2”, *Comput. Phys. Commun.* **191** (2015) 159, doi:10.1016/j.cpc.2015.01.024, arXiv:1410.3012.

[330] R. D. Ball et al., “Parton distributions for the LHC Run II”, *JHEP* **15** (2015) 40, doi:10.1007/JHEP04(2015)040, arXiv:1410.8849.

[331] K. Melnikov and F. Petriello, “Electroweak gauge boson production at hadron colliders through O(alpha(s)**2)”, *Phys.Rev. D* **74** (2006) 114017, doi:10.1103/PhysRevD.74.114017, arXiv:hep-ph/0609070.

[332] M. Czakon and A. Mitov, “Top++: A Program for the Calculation of the Top-Pair Cross-Section at Hadron Colliders”, *Comput. Phys. Commun.* **185** (2014) 2930, doi:10.1016/j.cpc.2014.06.021, arXiv:1112.5675.

[333] “NNLO+NNLL top-quark-pair cross sections – ATLAS-CMS recommended predictions for top-quark-pair cross sections using the Top++v2.0 program (M. Czakon, A. Mitov, 2013)”, https://twiki.cern.ch/twiki/bin/view/LHCPhysics/TtbarNNLO, 2022. (Retrieved Dec 21, 2020).

[334] “LQ_UFO.tar.gz”, https://cms-project-generators.web.cern.ch/cms-project-generators/LQ_UFO.tar.gz, 2017. (Retrieved November 15, 2018).

[335] **CMS** Collaboration, "Search for single production of scalar leptoquarks in proton-proton collisions at $\sqrt{s} = 8\ TeV$", *Phys. Rev. D* **93** (2016), no. 3, 032005, doi:10.1103/PhysRevD.95.039906,10.1103/PhysRevD.93.032005, arXiv:1509.03750. [Erratum: Phys. Rev.D95,no.3,039906(2017)].

[336] I. Doršner and A. Greljo, "Leptoquark toolbox for precision collider studies", *JHEP* **05** (2018) 126, doi:10.1007/JHEP05(2018)126, arXiv:1801.07641.

[337] "VectorLQ_UFO.tar.gz", https://cms-project-generators.web.cern.ch/cms-project-generators/VectorLQ_UFO.zip, 2017. (Retrieved November 15, 2018).

[338] "LQ_NLO", https://lqnlo.hepforge.org, 2017. (Retrieved May 12, 2019).

[339] "SingleVectorLQ/PdfLo", https://github.com/cms-sw/genproductions/tree/master/bin/MadGraph5_aMCatNLO/cards/production/2017/13TeV/SingleVectorLQ/PdfLo, 2019. (Retrieved May 12, 2019).

[340] "VectorLQ/PdfLo", https://github.com/cms-sw/genproductions/tree/master/bin/MadGraph5_aMCatNLO/cards/production/2017/13TeV/VectorLQ/PdfLo, 2019. (Retrieved May 12, 2019).

[341] **CMS** Collaboration, "Search for singly and pair-produced leptoquarks coupling to third-generation fermions in proton-proton collisions at $\sqrt{s} = 13$ TeV", *Phys. Lett. B* **819** (2021) 136446, doi:10.1016/j.physletb.2021.136446, arXiv:2012.04178.

[342] "VectorLQ_tchannel_UFO.tar.gz", https://cms-project-generators.web.cern.ch/cms-project-generators/VectorLQ_tchannel_UFO.zip, 2017. (Retrieved November 15, 2018).

[343] **CMS** Collaboration, "Measurements of Inclusive W and Z Cross Sections in pp Collisions at $\sqrt{s} = 7$ TeV", *JHEP* **01** (2011) 080, doi:10.1007/JHEP01(2011)080, arXiv:1012.2466.

[344] **CMS** Collaboration, "Performance of the CMS muon trigger system in proton-proton collisions at $\sqrt{s} = 13$ TeV", *JINST* **16** (2021) P07001, doi:10.1088/1748-0221/16/07/P07001, arXiv:2102.04790.

[345] **CMS** Collaboration, "Measurement of differential cross sections for top quark pair production using the lepton+jets final state in proton-proton collisions at 13 TeV", *Phys. Rev. D* **95** (2017), no. 9, 092001, doi:10.1103/PhysRevD.95.092001, arXiv:1610.04191.

[346] **CMS** Collaboration, "Measurement of the differential cross section for $\mathrm{t\bar{t}}$ production in the dilepton final state at $\sqrt{s} = 13$ TeV", CMS Physics Analysis Summary CMS-PAS-TOP-16-011, CERN, 2016.

[347] **CMS** Collaboration, "Performance of the CMS Level-1 trigger in proton-proton collisions at $\sqrt{s} = 13$ TeV", *JINST* **15** (2020), no. 10, P10017, doi:10.1088/1748-0221/15/10/P10017, arXiv:2006.10165.

[348] **CDF** Collaboration, "Search for neutral MSSM Higgs bosons decaying to tau pairs in $p\bar{p}$ collisions at $\sqrt{s} = 1.96$ TeV", *Phys. Rev. Lett.* **96** (2006) 011802, doi:10.1103/PhysRevLett.96.011802, arXiv:hep-ex/0508051.

[349] R. Raja, "A General theory of goodness of fit in likelihood fits", `arXiv:physics/0509008`.

[350] D. Jang, "Search for MSSM Higgs decaying to tau pairs in $p\bar{p}$ collision at $\sqrt{s} = 1.96$ TeV at CDF". PhD thesis, Rutgers University, 2006. FERMILAB-THESIS-2006-11, UMI-32-40224.

[351] R. J. Barlow and C. Beeston, "Fitting using finite Monte Carlo samples", *Comput. Phys. Commun.* **77** (1993) 219, `doi:10.1016/0010-4655(93)90005-W`.

[352] J. S. Conway, "Incorporating Nuisance Parameters in Likelihoods for Multisource Spectra", in *PHYSTAT 2011*, p. 115. 2011. `arXiv:1103.0354`. `doi:10.5170/CERN-2011-006.115`.

[353] **CMS** Collaboration, "Search for third-generation scalar leptoquarks and heavy right-handed neutrinos in final states with two tau leptons and two jets in proton-proton collisions at $\sqrt{s} = 13$ TeV", *JHEP* **07** (2017) 121, `doi:10.1007/JHEP07(2017)121`, `arXiv:1703.03995`.

[354] **CMS** Collaboration, "Search for heavy neutrinos and third-generation leptoquarks in hadronic states of two τ leptons and two jets in proton-proton collisions at $\sqrt{s} = 13$ TeV", *JHEP* **03** (2019) 170, `doi:10.1007/JHEP03(2019)170`, `arXiv:1811.00806`.

[355] **D0** Collaboration, "High-p_T jets in $\bar{p}p$ collisions at $\sqrt{s} = 630$ GeV and 1800 GeV", *Phys. Rev. D* **64** (2001) 032003, `doi:10.1103/PhysRevD.64.032003`, `arXiv:hep-ex/0012046`.

[356] **D0** Collaboration, "Measurement of dijet angular distributions at s**(1/2) = 1.96-TeV and searches for quark compositeness and extra spatial dimensions", *Phys. Rev. Lett.* **103** (2009) 191803, `doi:10.1103/PhysRevLett.103.191803`, `arXiv:0906.4819`.

[357] **CDF** Collaboration, "Measurement of dijet angular distributions at CDF", *Phys. Rev. Lett.* **77** (1996) 5336, `doi:10.1103/PhysRevLett.78.4307,10.1103/PhysRevLett.77.5336`, `arXiv:hep-ex/9609011`. [Erratum: Phys. Rev. Lett.78,4307(1997)].

[358] **ATLAS** Collaboration, "Search for New Physics in Dijet Mass and Angular Distributions in pp Collisions at $\sqrt{s} = 7$ TeV Measured with the ATLAS Detector", *New J. Phys.* **13** (2011) 053044, `doi:10.1088/1367-2630/13/5/053044`, `arXiv:1103.3864`.

[359] **ATLAS** Collaboration, "Search for quark contact interactions in dijet angular distributions in pp collisions at $\sqrt{s} = 7$ TeV measured with the ATLAS detector", *Phys. Lett. B* **694** (2011) 327, `doi:10.1016/j.physletb.2010.10.021`, `arXiv:1009.5069`.

[360] **ATLAS** Collaboration, "ATLAS search for new phenomena in dijet mass and angular distributions using pp collisions at $\sqrt{s} = 7$ TeV", *JHEP* **01** (2013) 029, `doi:10.1007/JHEP01(2013)029`, `arXiv:1210.1718`.

[361] **ATLAS** Collaboration, "Search for New Phenomena in Dijet Angular Distributions in Proton-Proton Collisions at $\sqrt{s} = 8$ TeV Measured with the ATLAS Detector", *Phys. Rev. Lett.* **114** (2015), no. 22, 221802, `doi:10.1103/PhysRevLett.114.221802`, `arXiv:1504.00357`.

[362] **ATLAS** Collaboration, "Search for new phenomena in dijet mass and angular distributions from pp collisions at $\sqrt{s} = 13$ TeV with the ATLAS detector", *Phys. Lett.*

B **754** (2016) 302, doi:10.1016/j.physletb.2016.01.032, arXiv:1512.01530.

[363] **CMS** Collaboration, "Measurement of Dijet Angular Distributions and Search for Quark Compositeness in pp Collisions at $sqrts = 7$ TeV", *Phys. Rev. Lett.* **106** (2011) 201804, doi:10.1103/PhysRevLett.106.201804, arXiv:1102.2020.

[364] **CMS** Collaboration, "Search for Quark Compositeness with the Dijet Centrality Ratio in *pp* Collisions at $\sqrt{s} = 7$ TeV", *Phys. Rev. Lett.* **105** (2010) 262001, doi:10.1103/PhysRevLett.105.262001, arXiv:1010.4439.

[365] **CMS** Collaboration, "Search for quark compositeness in dijet angular distributions from *pp* collisions at $\sqrt{s} = 7$ TeV", *JHEP* **05** (2012) 055, doi:10.1007/JHEP05(2012)055, arXiv:1202.5535.

[366] **CMS** Collaboration, "Search for quark contact interactions and extra spatial dimensions using dijet angular distributions in proton-proton collisions at $\sqrt{s} = 8$ TeV", *Phys. Lett. B* **746** (2015) 79, doi:10.1016/j.physletb.2015.04.042, arXiv:1411.2646.

[367] D. Savoiu, "Triple-Differential Measurement of the Dijet Cross Section at $\sqrt{s} = 13$ TeV with the CMS Detector". PhD thesis, Karlsruher Institut für Technologie, 2021. doi:10.5445/IR/1000129970.

[368] **CMS** Collaboration, "The search for a third-generation leptoquark coupling to a τ lepton and a b quark through single, pair and nonresonant production at $\sqrt{s} = 13$ TeV", CMS Physics Analysis Summary CMS-PAS-EXO-19-016, CERN, 2022.

[369] J. W. Andrejkovic, "Data-Driven Background Modeling for Precision Studies of the Higgs Boson and Searches for New Physics with the CMS Experiment". PhD thesis, Technische Universität Wien, 2022. Presented 06-07-2022. CERN-THESIS-2022-098.

[370] **CMS** Collaboration, "Search for additional neutral MSSM Higgs bosons in the $\tau\tau$ final state in proton-proton collisions at $\sqrt{s} = 13$ TeV", *JHEP* **09** (2018) 007, doi:10.1007/JHEP09(2018)007, arXiv:1803.06553.

[371] **CMS** Collaboration, "Searches for additional Higgs bosons and for vector leptoquarks in $\tau\tau$ final states in proton-proton collisions at $\sqrt{s} = 13$ TeV", arXiv:2208.02717.

[372] **CMS** Collaboration, "Measurement of the $Z/\gamma^* \to \tau\tau$ cross section in pp collisions at $\sqrt{s} = 13$ TeV and validation of τ lepton analysis techniques", *Eur. Phys. J. C* **78** (2018), no. 9, 708, doi:10.1140/epjc/s10052-018-6146-9, arXiv:1801.03535.

[373] "CombineHarvester: ch::BinByBinFactory Class Reference", https://cms-analysis.github.io/CombineHarvester/classch_1_1_bin_by_bin_factory.html, 2020.

[374] T. Junk, "Confidence level computation for combining searches with small statistics", *Nucl. Instrum. Meth. A* **434** (1999) 435, doi:10.1016/S0168-9002(99)00498-2, arXiv:hep-ex/9902006.

[375] A. L. Read, "Presentation of search results: The CL_s technique", *J. Phys. G* **28** (2002) 2693, doi:10.1088/0954-3899/28/10/313.

[376] ATLAS and CMS Collaborations, "Procedure for the LHC Higgs boson search combination in Summer 2011", Technical Report CMS-NOTE-2011-005, ATL-PHYS-PUB-2011-011, CERN, 2011.

[377] J. Bendavid, "Implications of Bias Threshold in Pull Definition", Presentation in the Higgs Working Meeting, CERN, 2013. https://indico.cern.ch/event/255493/contributions/1584346/attachments/447909/621085/bias-Jun26.pdf.

[378] **CMS** Collaboration, "Precision luminosity measurement in proton-proton collisions at $\sqrt{s} = 13$ TeV in 2015 and 2016 at CMS", *Eur. Phys. J. C* **81** (2021) 800, doi:10.1140/epjc/s10052-021-09538-2, arXiv:2104.01927.

[379] **CMS** Collaboration, "CMS luminosity measurement for the 2017 data-taking period at $\sqrt{s} = 13$ TeV", CMS Physics Analysis Summary CMS-PAS-LUM-17-004, CERN, 2018.

[380] **CMS** Collaboration, "CMS luminosity measurement for the 2018 data-taking period at $\sqrt{s} = 13$ TeV", CMS Physics Analysis Summary CMS-PAS-LUM-18-002, CERN, 2019.

[381] **CMS** Collaboration, "Observation of the Higgs boson decay to a pair of τ leptons with the CMS detector", *Phys. Lett. B* **779** (2018) 283, doi:10.1016/j.physletb.2018.02.004, arXiv:1708.00373.

[382] J. Butterworth et al., "PDF4LHC recommendations for LHC Run II", *J. Phys. G* **43** (2016) 023001, doi:10.1088/0954-3899/43/2/023001, arXiv:1510.03865.

[383] **CMS** Collaboration, "CMS Exotica Summary plots for 13 TeV data", https://twiki.cern.ch/twiki/bin/view/CMSPublic/SummaryPlotsEXO13TeV#Leptoquark_summary_plot, 2022. (Retrieved Nov 24, 2022).

[384] **ATLAS** Collaboration, "Search for new phenomena in *pp* collisions in final states with tau leptons, b-jets, and missing transverse momentum with the ATLAS detector", *Phys. Rev. D* **104** (2021), no. 11, 112005, doi:10.1103/PhysRevD.104.112005, arXiv:2108.07665.

[385] **CMS** Collaboration, "Search for a singly produced third-generation scalar leptoquark decaying to a τ lepton and a bottom quark in proton-proton collisions at $\sqrt{s} = 13$ TeV", *JHEP* **07** (2018) 115, doi:10.1007/JHEP07(2018)115, arXiv:1806.03472.

[386] **CMS** Collaboration, "Searches for physics beyond the standard model with the M_{T2} variable in hadronic final states with and without disappearing tracks in proton-proton collisions at $\sqrt{s} = 13$ TeV", *Eur. Phys. J. C* **80** (2020), no. 1, 3, doi:10.1140/epjc/s10052-019-7493-x, arXiv:1909.03460.

[387] **ATLAS** Collaboration, "Search for pair production of third-generation scalar leptoquarks decaying into a top quark and a τ-lepton in *pp* collisions at $\sqrt{s} = 13$ TeV with the ATLAS detector", *JHEP* **06** (2021) 179, doi:10.1007/JHEP06(2021)179, arXiv:2101.11582.